Università degli Studi della Basilicata

Dottorato di Ricerca in
Ingegneria per l’innovazione e lo sviluppo sostenibile

Investigation of ozone assisted combustion for internal combustion engines applications

Settore Scientifico-Disciplinare
ING-IND/08 – Macchine a Fluido

Coordinatrice del Dottorato:
Prof.ssa Aurelia Sole

Dottorando:
Dott. Marco D’Amato

Relatrice:
Prof.ssa Annarita Viggiano

Correlatore:
Prof. Vinicio Magi

Ciclo XXXV

Abstract

In this work, the potential of using ozone for possible applications in both unconventional engines, in particular Homogeneous Charge Compression Ignition (HCCI) engines, and conventional Spark Ignition engines was investigated. For this purpose, simulations were conducted by employing 0-D, 1-D numerical models and Computational Fluid Dynamics (CFD). The iso-octane/air/ozone mixture was the one mainly investigated; however, analyses were also carried out considering the methane/air/ozone mixture. First, the chemical kinetics of ozone-assisted combustion were studied, evaluating the effect of ozone on Laminar Flame Speed (LFS), Ignition Delay Time (IDT), flame structure and reaction paths. Then CFD simulations of both an HCCI engine and a Spark Ignition engine were carried out to evaluate the effect of ozone on performance, fuel economy and specific fuel consumption under different operating conditions (mixture composition, engine speed, spark advance). The main results show that the ozone addition leads to an increase in LFS, however, different behaviour was found for methane and iso-octane. Specifically, for relatively low temperatures (T<540 K) the effect of ozone is similar on the two fuels, while for temperatures higher than about 540 K only in the case of iso-octane a cool flame occurs, leading to a significantly greater increase in LFS than in methane. Furthermore, in the presence of a cool flame and with ozone addition, the increase in pressure leads to an increase in LFS, unlike with methane and unlike without ozone. The formation of a cool flame is due to the chemical reactions in the Low-Temperature Combustion (LTC) regime and the change in reaction pathways enabled by the ozone. The results show that ozone decomposes, producing oxygen atoms that oxidise the fuel, producing OH radicals that continue the oxidation. Ozone decomposition occurs faster the higher the temperature and pressure, with an acceleration of ozone chemical kinetics for temperatures higher than about 540 K. Enabling the LTC regime through ozone leads to a reduction in IDT. Specifically, the results show that as ozone concentration increases IDT decreases, with a greater impact at low temperatures. However, the reduction of IDT with ozone addition is less as ozone concentration increases, especially at low temperatures. These results encourage the use of ozone in HCCI engines where the combustion phase is mainly governed by chemical kinetics. In particular, the HCCI engine simulations suggest that the ozone addition, by reducing the IDT and enabling reactions in the LTC regime, is able to anticipate the mixture auto-ignition, reduce the combustion duration and reduce the cycle-to-cycle variation which characterises these engines especially at low load. Furthermore, the ozone effect is higher in the case with a higher percentage of residual gas, leading to a reduction of the Specific Fuel Consumption (SFC) from 1.54% to 4.96% under some conditions for the case without residual gas and the case with 10% by mass of residual gas. Another interesting factor suggesting the results of the simulations is that the ozone effect could be reduced in the presence of reactive species, especially nitrogen oxide, due to a direct reaction between the two species. However, this effect is limited in an HCCI engine since combustion takes place at low temperatures and the formation of NO_x is relatively low. As regards the ozone applications in Spark Ignition engines, simulation results suggest that the flame propagates faster with ozone addition and this effect is more pronounced the longer the residence time of the mixture. The delay in spark advance or the lower engine speed gives more time to ozone to decompose and enable LTC reactions in both compression and end gas, leading to an increase in flame speed. However, the interaction between the parameters influencing the residence time in the end gases (flame propagation speed, engine speed, spark advance) and those influencing the IDT in the end gases (temperature, pressure, mixture composition) must be carefully investigated, because in some cases mixture auto-ignition can occur, resulting in loss of performance and possible structural damage due to detonation and high maximum pressure rise rates. For this reason, ozone can have interesting applications in Spark Ignition engines operating under lean conditions. Simulation results on LFS show an increase in LFS under lean conditions with ozone addition to higher values than those obtained in stoichiometric conditions without ozone. Furthermore, the reduction of the equivalence ratio leads to an increase in IDT, reducing the risk of mixture auto-ignition. Indeed, the results of CFD simulations in lean conditions show that the flame propagation speed, which without ozone is lower than in the stoichiometric case, benefits more than in the stoichiometric case from the presence of ozone, increasing engine performance: in some conditions with ozone addition, a maximum increase in gross indicated work per cycle of 4% and 14% was obtained for the stoichiometric and lean cases, respectively.

Summary

Nomenclature

Acronyms

ARP	Absolute Rate of Production
ATDC	After Top Dead Center
BTDC	Before Top Dead Center
CA	Crank Angle
CA10	Crank Angle when 10% of the total heat has been released
CA50	Crank Angle when 50% of the total heat has been released
CA90	Crank Angle when 90% of the total heat has been released
CAD	Crank Angle Degrees
CFD	Computational Fluid Dynamics
CFR	Cooperative Fuel Research
CI	Compression Ignition
CR	Compression Ratio
DISI	Direct Injection Spark Ignition
DME	Dimethyl Ether
DNS	Direct Numerical Simulations
EDC	Eddy Dissipation Concept
EGR	Exhaust Gas Recirculation
EU	European Union
EVO	Exhaust Valve Opening
GHG	Greenhouse Gas
HCCI	Homogeneous Charge Compression Ignition
HRR	Heat Release Rate
HTC	High Temperature Combustion
ICEs	Internal Combustion Engines
IDT	Ignition Delay Time
IMEP	Indicated Mean Effective Pressure
IVC	Intake Valve Closure
LES	Large Eddy Simulations
LFS	Laminar Flame Speed
LTC	Low Temperature Combustion
LTR	Low Temperature Regime
MILD	Moderate or Intense Low-oxygen Dilution
MPRR	Maximum Pressure Rise Rate
NSD	NanoSecond pulsed Discharge
NTC	Negative Temperature Coefficient
OECD	Organisation for Economic Cooperation and Development
PAC	Plasma Assisted Combustion
PCCI	Premixed Charge Compression Ignition
PFI	Port Fuel Injection

PFRs	Plug Flow Reactors
PISO	Pressure-Implicit with Splitting of Operators
PLIF	Planar Laser-Induced Fluorescence
PPCI	Partially Premixed Compression Ignition
PRF0	Primary Reference Fuel with 0% (by volume) iso-octane
PRF100	Primary Reference Fuel with 100% (by volume) iso-octane
PRFs	Primary Reference Fuels
PSRs	Perfectly Stirred Reactors
RANS	Reynolds Averaged Navier Stokes
RCM	Rapid Compression Machine
RNG	Re-Normalisation Group
RON	Research Octane Number
RPM	Round Per Minute
RRP	Relative Rate of Production
SA	Spark Advance
SACI	Spark Assisted Compression Ignition
SCR	Selective Catalytic Reduction
SFC	Specific Fuel Consumption
SI	Spark Ignition
SOC	Start of Combustion
SOI	Start of Injection
TDC	Top Dead Center
UHCs	Unburnt Hydrocarbons

Latin symbols

A	cross-sectional area
A_{in}	maximum open intake area
A_{pist}	piston area
A_w	chamber surface area
A'	polynomial coefficient for c_p evaluation in the first temperature range
a_A	coefficient in Annand correlation
a^{EVO}	ratio between the mass fractions at EVO
B'	polynomial coefficient for c_p evaluation in the second temperature range
b_A	coefficient in Annand correlation
$\mathrm{CA_{Pmax}}$	crank angle at which the pressure peak occurs
C_{1s}, C_{2s}	coefficients in Sutherland correlation
$C_{1\varepsilon}$, $C_{2\varepsilon}$	constants in the ε-transport equation
C_{D1}, C_{D2}	EDC model constants
C	Arrhenius pre-exponential factor
C_γ	EDC model constant for the fine-structures length fraction evaluation
C_μ	constant for the turbulent viscosity evaluation
C_τ	EDC model constant for the fine-structures characteristic time evaluation

c_p	constant pressure specific heat
c_v	constant volume specific heat
D_B	bore length
D	diffusion coefficient
D_T	thermal diffusivity
D_t	turbulent diffusivity coefficient
E_a	activation energy
E	total internal energy
e	specific internal energy
G_k	generation term of turbulent kinetic energy
$H_{i,fuel}$	lower calorific value of the fuel
H°	standard state molar enthalpy
h_c	convective heat-transfer coefficient
h_{cell}	cell height corresponding to the layer to be added/removed
h	specific enthalpy
h_{ideal}	ideal cell height
h^0	enthalpy of formation
h_s	mixture sensible enthalpy
$\bar{\bar{I}}$	unit tensor
$\vec{J}$	mass diffusion flux
K_c	equilibrium constants in concentration units
K_p	equilibrium constant in pressure units
k	turbulent kinetic energy
k_b	backward rate constant
k_f	forward rate constant
k_{wc}	turbulence kinetic energy at the wall-adjacent cell centroid
L_A	crank arm length
L_C	connecting rode length
l_t	integral length scale
M	mass
$M_{fuel_{IVC}}$	mass of fuel at IVC
$\dot{M}$	mass flow rate
N_r	number of reactions
N_s	number of gas species
N_s^{EVO}	number of gas species at EVO with a concentration greater than 1 ppm
n_{rc}	number of revolutions per cycle
$\bar{P}_{MAX}$	maximum volume-averaged in-cylinder pressure
$\dot{P}_I^g$	gross indicated power output
P_{atm}	pressure of one standard atmosphere
Pr	Prandtl number
Pr_t	turbulent Prandtl number
p	pressure

Q_{ch}	chemical energy released by the combustion
Q_s	heat transfer across the system boundary
Q_w	heat transfer to the walls
q	rate of progress variable
R	universal gas constant
R_{rr}	volumetric mean reaction rate
R_ε	additional term in in the RNG ε-transport equation
RG	normalised value of the residual gas mass with respect to the total mass
r_t	size of generic turbulence scale
Re	Reynolds number
Re_t	integral Reynolds number
Re_k	Kolmogorov Reynolds number
S	modulus of the mean rate of strain tensor
S°	standard state molar entropy
$S_{h,rxn}$	source energy term
Sc_t	turbulent Schmidt number
S_L	laminar flame speed
S_{L_0}	laminar flame speed without ozone addition
$S_{L_{X_{O_3}}}$	laminar flame speed with X_{O_3} ppm of ozone addition
T	temperature
$\bar{T}_{MAX}$	maximum mass-averaged in-cylinder temperature
T_w	wall temperature
t	time
u	mean velocity
u'	fluctuating velocity
$\bar{u}_p$	mean piston speed
V	volume
V_c	engine displaced volume
V_D	volume at TDC
V_{max}	maximum volume
V_{min}	minimum volume
V_{dif}	diffusion velocity
V'	ordinary diffusion velocity
V''	thermal diffusion velocity
V_c'''	correction velocity
v_s	specific volume
$\vec{v}$	gas velocity vector
$\overline{W}$	mean molecular weight of the mixture
W	molecular weight
$W_{c,I}^{g}$	gross indicated work per cycle
X	molar fraction
$[X]$	molar concentration

X_{O_3}	ozone concentration in ppm
x	spatial coordinate
Y	mass fraction
Y°	surrounding mass fraction
Y^{*}	fine structure mass fraction
Y'	mass fraction in residuals composition
y_{wc}	distance from the centroid of the wall-adjacent cell to the wall
y^{+}	dimensionless distance from the wall
y^{*}	dimensionless distance from the wall referred to the wall-adjacent cell
Z	generic chemical species

Greek symbols

α_c	collapse factor
α_s	split factor
α_{S_L}	angular coefficient of the linear relationship of LFS vs ozone concentration
α_{IVC}	constant for the k evaluation at IVC
α	third body efficiency
β_{IVC}	constant for the ε evaluation at IVC
β	Arrhenius temperature exponent
γ	specific heat ratio
γ^{*}	dimensionless fine structures length fraction
γ_{curv}	solution curvature parameter
$\Delta\theta_{in}$	angle during which the intake valve remains open
δ_{grad}	solution gradient parameter
ε	dissipation rate of turbulent kinetic energy
ε_{IDT}	ignition delay time relative variation
ε_{LFS}	laminar flame speed relative enhancement
$\vec{\zeta}$	unknowns vector
η_{th}^{g}	gross thermodynamic efficiency
η_k	Kolmogorov length scale
θ	crank angle
θ_{MPRR}	crank angle at which the MPRR occurs
$\theta_{\bar{P}_{MAX}}$	crank angle at which $\bar{P}_{MAX}$ occurs
$\theta_{\bar{T}_{MAX}}$	crank angle at which $\bar{T}_{MAX}$ occurs
λ	thermal conductivity of the mixture
λ_{eff}	effective thermal conductivity
λ_t	turbulent thermal conductivity
μ	dynamic viscosity
μ_t	turbulent viscosity
ν	kinematic viscosity
ν'	stoichiometric coefficient of the reactant species

ν''	stoichiometric coefficient of the produced species
ρ	mixture mass density
σ_ε	constant in the ε-transport equation
σ_k	constant in the k-transport equation
τ^*	characteristic time scale of the fine structures
$\bar{\bar{\tau}}$	stress tensor
Φ	generic fluid property
φ, ϕ	equivalence ratio
χ	reaction probability in fine scales
ψ	scalar coefficient of mutual interaction between species
Ω	characteristic swirl number
$\dot{\omega}$	molar rate of production/consumption

Chemical species

Ar	argon
CH_2O	formaldehyde
CH_3	methyl radical
CH_3O	methoxy radical
CH_4	methane
CO	carbon monoxide
CO_2	carbon dioxide
C_2H_4	ethylene
C_3H_8	propane
C_7H_{16}	n-heptane
C_8H_{18}	iso-octane
H	atomic hydrogen
HO_2	hydroperoxyl radical
H_2	molecular hydrogen
H_2O	water
H_2O_2	hydrogen peroxide
M	third-body
N	atomic nitrogen
NO	nitrogen monoxide
NO_2	nitrogen dioxide
NO_3	nitrogen trioxide
NO_x	nitrogen oxides
O	atomic oxygen
OH	hydroxyl radical
$OQ'O$	ketoalkyloxy radical
$OQ'OOH$	ketohydroperoxide
O_2	molecular oxygen
O_2QOOH	peroxy-hydroperoxyl-alkyl radical

O_3	ozone
$QOOH$	hydroperoxyl-alkyl radical
R	alkyl radical
RH	alkane fuel
RO_2	alkylperoxyl radical

Introduction

I. Energy and environmental context

Over the past decades, world energy consumption has continued to rise significantly, going from 87,933 TWh in 1980 to 176,431 TWh in 2021, an increase of about 74% [1,2]. Only in 2009 (due to the financial crisis) and 2020 (due to the Covid-19 pandemic) energy demand decreased compared to the previous year. Figure I.1 shows the world energy consumption by source and it can be seen that most energy is produced from fossil sources. In 2019, about 84% of energy came from fossil sources (about 33% from oil, 27% from coal and 24% from gas), a reduction of only 2% compared to 2000. Only 16%, therefore, came from low-carbon sources, including nuclear energy (4.3%), hydropower (6.4%), wind (2.2%), solar (1.1%), biofuels (0.7%) and other renewables (0.9%). Despite producing more and more energy from renewable sources every year, the global energy mix is still dominated by fossil fuels, which, moreover, are increasing globally: total production has increased from 116,214 to 136,761 TWh in the last 10 years.

In International Energy Outlook 2021 (IEO2021), the U.S. Energy Information Administration stated that global energy consumption will increase by almost 50% over the next 30 years. As shown in Figure I.2, the majority of that increase will be driven by non-OECD (Organisation for Economic Cooperation and Development) countries, mainly due to the continuing population growth and the development needs of poorer, less technological countries. According to these projections, falling technology costs and government policies that incentivise renewables will lead to growth in renewable electricity generation to meet growing demand. On the other hand, even if coal and nuclear energy use will decrease in OECD countries, this reduction will be more than compensated by increased coal and nuclear energy use in non-OECD countries. Renewable energy sources, such as solar and wind energy, have strong fluctuations and are not always available and sufficient to meet energy demand. Therefore, combustion still plays a fundamental role in society, for both transport and energy production. In 2050, therefore, oil and other liquid fuels will remain the world's main source of energy, despite the renewable energy sources, which include solar and wind, growing at almost the same level.

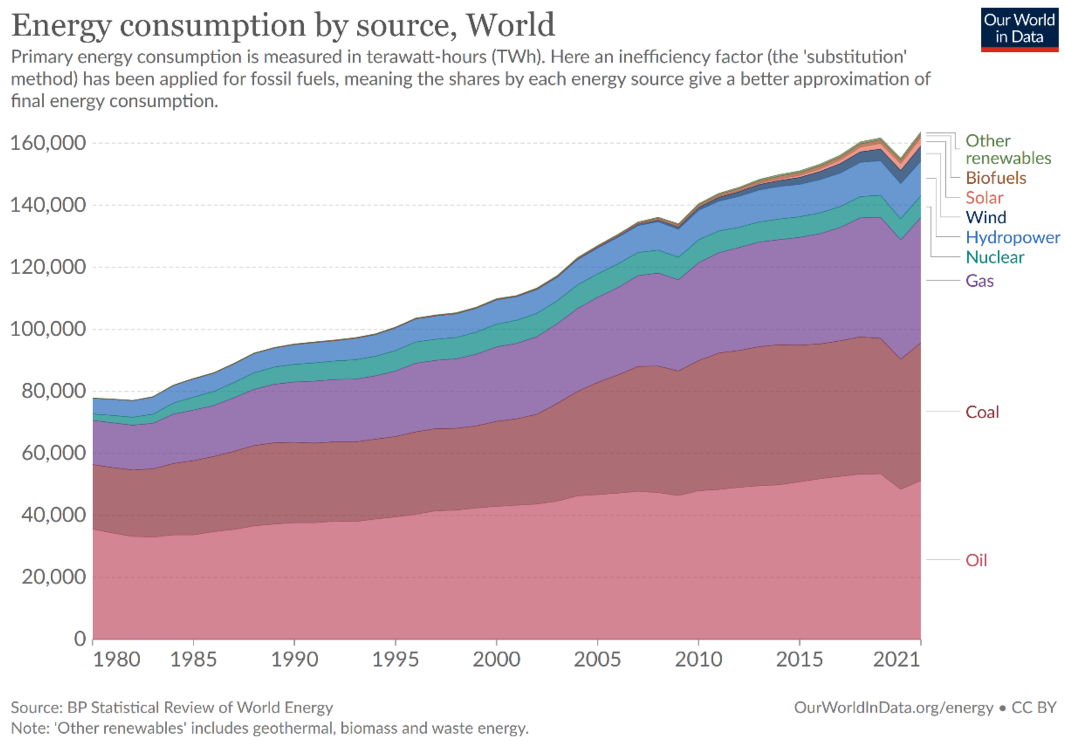
Energy consumption by source, World

Primary energy consumption is measured in terawatt-hours (TWh). Here an inefficiency factor (the 'substitution' method) has been applied for fossil fuels, meaning the shares by each energy source give a better approximation of final energy consumption.

Source: BP Statistical Review of World Energy

OurWorldInData.org/energy • CC BY

Note: 'Other renewables' includes geothermal, biomass and waste energy.

Figure I.1. Global Energy Consuption by source. [1].

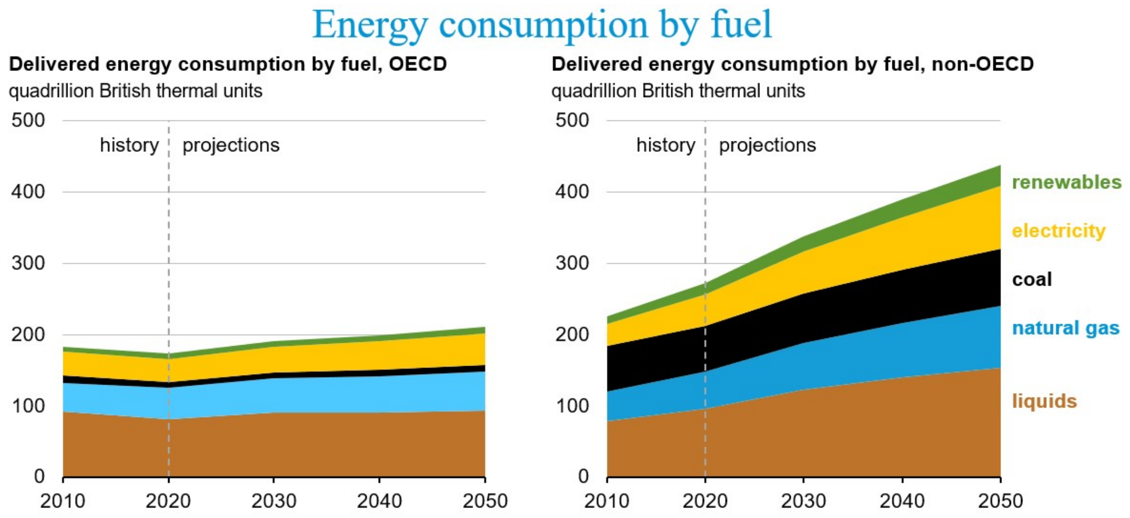
Energy consumption by fuel

Delivered energy consumption by fuel, OECD
quadrillion British thermal units

Delivered energy consumption by fuel, non-OECD
quadrillion British thermal units

Figure I.2. Global Energy Consuption by fuel. [2].

The increase in global energy demand, however, conflicts with the need to reduce polluting emissions in order to safeguard the environment and human health. The Kyoto Protocol, negotiated in December 1997, was the first international treaty that looked to limit Greenhouse Gas (GHG) emissions, requiring signatory countries to reduce their greenhouse gas emissions by 5% compared to 1990 levels between 2008 and 2012 [3]. More recently at COP 21 in Paris, the Paris Agreement was adopted by 196 Parties who, in a legally binding international climate change treaty, set themselves the goal of limiting global warming to well below 2°C, preferably to 1.5°C, compared to pre-industrial levels [4]. To contrast climate change, the European Union (EU) has employed a series of laws to achieve a number of targets by 2020: 20% cut in greenhouse gas emissions (compared to 1990 levels); 20% of EU energy from renewables; 20% improvement in energy efficiency. Later, for the period 2021-2030, the EU set itself the following key targets: at least 40% cuts in greenhouse gas emissions (compared to 1990 levels); at least 32% share for renewable energy; at least 32.5% improvement in energy efficiency. The EU declared the long-term goal is to become climate neutral by 2050, i.e. to have an economy with zero net greenhouse gas emissions. [5-7].

Figure I.3, shows global GHG emissions by sector [8]. As can be seen around three-quarters of GHG come from energy (about 73.2%) with transport contributing 16.2% of global GHG emissions, i.e. about 22% of GHG emissions due to energy production. Road travel accounts for three-quarters of transport emissions, most of this comes from passenger vehicles (cars and buses), which contribute 45.1%, and the other 29.4% comes from trucks carrying freight [8, 9].

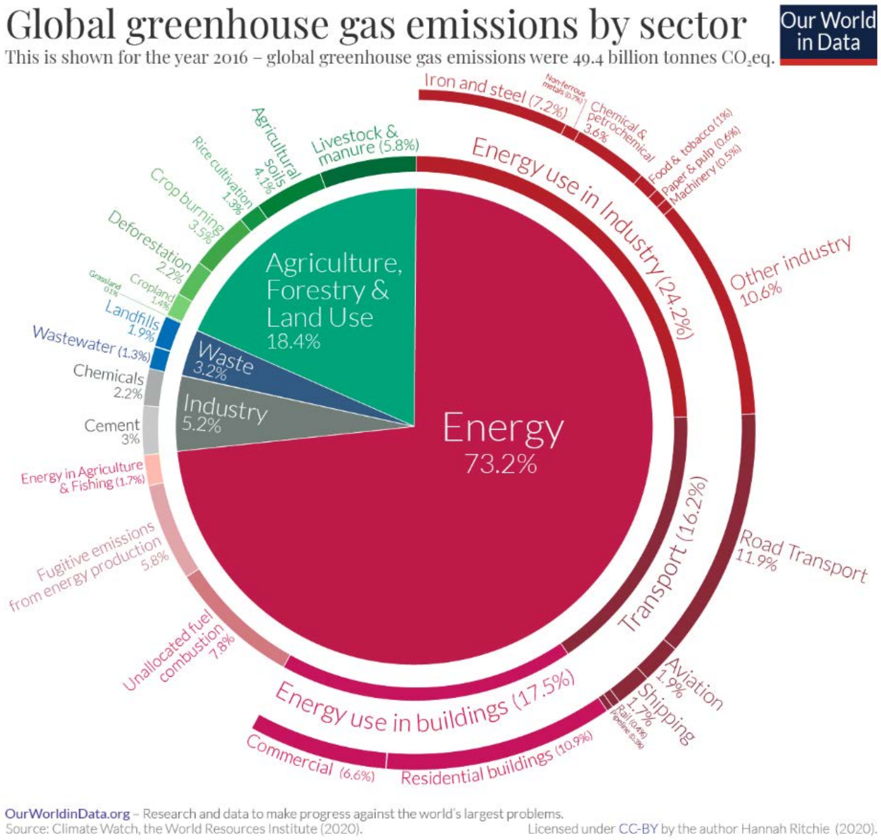

Figure I.3. Global Greenhouse gas emissions (GHG) by sector. [8].

This means that, if we could electrify the whole road transport sector, with a transition to a fully decarbonized electricity mix, we could feasibly reduce GHG emissions by 11.9%. Moreover, considering that, as mentioned above, energy demand is set to grow very significantly with the increase in global population and prosperity, particularly in developing countries, and that currently more than 80% (in 2050 probably about 50%) of energy comes from fossil sources, if this increase in demand is not offset by improvements in energy efficiency, the challenge of the transition of our energy systems from fossil fuels to low-carbon energy sources will be very difficult.

In the transport sector, which is dominated by internal combustion engines, several strategies have been studied in recent years. These include the electric or hybrid supply of vehicles, fuel cell electric vehicles, the use of biofuels, and the adoption of conventional or unconventional thermal engines. The choice of the different solutions, together or separately, depends on several factors such as the consumer acceptance (e.g. cost), the country considered (technological or developing), and the specific application (city, country, personal, freight, etc.). Furthermore, stationary internal combustion engines (e.g. generators, not those for transport or off-road applications) are ubiquitous in industries and power generation facilities. Therefore, the combustion engine will continue to play a central role, whether it is used for power generation or to power the vehicle itself.

II. Objectives and organization of the manuscript

Considering both the energy and the climate context described above, there is a need to find increasingly efficient strategies and technologies in terms of both performance and reduction of pollutant emissions for internal combustion engines. To achieve these goals, engineering research is focusing on several aspects, including: improving the combustion process, better after-treatment and control systems, exhaust gas heat recovery, exhaust gas recirculation, use of biofuel, employment of unconventional engines, use of a bi-fuel (gasoline and gas).

The aim of this work was to investigate ozone-assisted combustion for internal combustion engines applications, evaluating the possible increases in performance, energy efficiency and reduction of fuel consumption. The influence of ozone on combustion has been studied in recent decades and still represents one of the possibilities for improving and controlling the combustion process and reducing pollutant emissions in internal combustion engines. Most of the studies on ozone-assisted combustion in the scientific literature have concerned applications with methane and, as regards internal combustion engines, in HCCI engines. In this work, however, the mixture mainly studied was iso-octane/air/ozone. By employing 0-D, 1-D numerical models and CFD, the ozone effect on combustion was investigated considering various aspects useful for possible applications in internal combustion engines. Specifically, chemical kinetics was studied by coupling, comparing and validating several reaction kinetics mechanisms taken from the scientific literature and calculating some characteristic combustion parameters, such as laminar flame speed and ignition delay time. In addition, the work cycles of both an HCCI engine and a Spark Ignition engine were simulated using CFD with a model that solves chemical kinetics in detail, evaluating the effect of ozone on both the thermo-fluid-dynamic evolution of the mixture during compression and on some performance parameters (such as work per cycle, specific fuel consumption, combustion speed, etc.) under different operating conditions.

The present work is based on the following scientific publications (in addition, part of this thesis is being submitted for further publication):

- M. D’Amato, A. Viggiano, V. Magi, On the Turbulence-Chemistry Interaction of an HCCI Combustion Engine, Energies, 13 (2020) 5876. https://doi.org/10.3390/en13225876;
- M. D’Amato, A. Viggiano, V. Magi, A numerical investigation on the laminar flame speed of methane/air and iso-octane/air mixtures with ozone addition, Combust. Flame, 241 (2022) 112145. https://doi.org/10.1016/j.combustflame.2022.112145;
- M. D’Amato, A. Cantiani, V. Magi, A. Viggiano, The Laminar Flame Speed of Iso-Octane/Air/Ozone Lean Mixtures under Engine-Like Thermo-chemical Conditions, IOP Conf. Ser.: Earth Environ. Sci., 1106 (2022). https://doi.org/10.1088/1755-1315/1106/1/012005;

- M. D'Amato, V. Magi, A. Viggiano, On Iso-octane Combustion with Ozone Addition under HCCI Engine-Like Conditions, J. Phys.: Conf. Ser., 2385 (2022) 012086. https://doi.org/10.1088/1742-6596/2385/1/012086.

This manuscript is organised as follows.

The first chapter presents the literature review on ozone-assisted combustion, with particular interest for applications in both conventional and unconventional internal combustion engines.

The second chapter discusses the mathematical and numerical models used for the variety of investigations that were carried out.

The third chapter concerns the study of the chemical kinetics of combustion of iso-octane/air/ozone mixtures. The different kinetic mechanisms used in the successive analyses are described, compared and validated, and a comparison is made with methane for which there are experimental results in the literature. In addition, a parametric study is carried out to calculate the laminar flame speed and ignition delay time under different thermodynamic conditions and mixture composition.

The fourth chapter presents the results of the analyses concerning the possible applications of ozone in HCCI engines. Specifically, a parametric analysis of the ignition delay time under typical HCCI engine conditions is performed; in addition, CFD simulations of an HCCI engine are performed in order to assess how the interaction between residual gases and ozone can alter the chemical composition and the combustion process in this type of engine.

The fifth chapter presents the results of the analyses concerning the possible applications of ozone in Spark Ignition engines. Specifically, a parametric analysis of the laminar flame speed under typical Spark Ignition engine conditions is performed; in addition, CFD simulations of a Spark Ignition engine are performed in order to assess how ozone alters the performance of these engines under different conditions of engine speed, ignition timing and equivalence ratio.

Finally, the last chapter summarises the main conclusions that can be drawn from the analyses performed.

1. Chapter 1: Literature review

1.1 Ozone chemical kinetics and effects on combustion

In recent decades, many studies were conducted to understand the properties of ozone and investigate its effects within combustion systems [10]. There are several characteristics of ozone that have captured the attention of researchers for its use in combustion processes. One of these characteristics is that ozone, due to its relatively long lifetime (about 25 hours at room conditions and zero humidity) [11], could be transported to the combustion region, thus promoting fuel oxidation. Another relevant aspect is the simplicity of its efficient and economical production even under high-pressure conditions, i.e. the operating conditions of most combustion devices.

Since ozone is a molecule consisting of three oxygen atoms, most commercial O_3 generators operate with electrical discharges (typically corona discharge or dielectric barrier discharge), which are used to break the molecular bond of O_2, producing atomic oxygen, which then recombines with O_2 to form ozone via the reaction:

R1.1) $O_2 + O + M \rightleftarrows O_3 + M$,

where M is a third-body and represents all collision species. However, if air is used to produce ozone, species such as N, NO and NO_2 NO_x are also produced [12,13], which could consume some of ozone through the reactions:

R1.2) $N + O_2 \rightleftarrows NO + O$,

R1.3) $NO + O_3 \rightleftarrows NO_2 + O_2$,

R1.4) $NO_2 + O_3 \rightleftarrows NO_3 + O_2$.

Due to the direct reactions between ozone and nitrogen oxides, the possibility of using ozone to convert NO, which has a low solubility in water, into NO_2 or NO_3, which being more soluble can be captured, was also investigated [14,15].

Most studies concerning the chemical reactions involving ozone were focused on atmospheric chemistry, as ozone is not usually present in conventional combustion processes. However, already in the first studies concerning ozone-assisted combustion [16-20], it was realised that one of the fundamental reactions to utilise ozone in combustion systems is the backword R1.1 reaction, through which ozone decomposes releasing an oxygen atom that is highly oxidising. Due to its importance, the R1.1 reaction was extensively studied [21-28], and it was observed that, away from its high-pressure limit (above 100 bar), it is a bimolecular reaction, therefore dependent on both temperature and pressure. Other important reactions involving ozone in combustion processes are ozone oxidation reactions ($O_3 + X \rightleftarrows O_2 + XO$) and production of HO_2 ($O_3 + XH \rightleftarrows HO_2 + product$).

Concerning the interaction between ozone and hydrocarbons, a significant difference was found between saturated hydrocarbons (alkanes) and unsaturated hydrocarbons (alkenes) [29]. The idea behind the use of ozone with hydrocarbons is that, through the R1.1 reaction, ozone produces oxygen atoms that can accelerate reactions involving fuel molecules. However, this interpretation is based on the assumption that oxygen atoms are always produced, a condition that may not occur. While reactions between ozone and alkanes are very slow [30,31], those with alkenes are approximately one million times faster [32,33,34]. The alkenes therefore undergo ozone cycloaddition by exothermal reactions, generally called ozonolysis reactions, such as:

R1.5) $O_3 + Fuel \rightleftarrows Products + Q$,

where Q is the heat release. Ozonolysis reactions occur very quickly at low temperatures, unlike most fuel oxidation reactions, which require high temperatures instead. For this reason, for mixtures containing ozone and alkenes, ozone decomposition is the dominant mechanism of O_3 consumption only at high temperatures, whereas at low temperatures (approximately below 700 K), ozonolysis reactions are the dominant mechanism [10].

Studies conducted on ozone assisted combustion have covered several aspects such as: mixture ignition, flame propagation speed, flame structure and stability. Lucas *et al.* [35] investigated the influence of pressure, initial temperature, and equivalence ratio on the minimum ozone concentration to produce ignition with a laser in $H_2/O_2/O_3$ mixtures at pressure below 13.3 kPa. The results showed that only the initial temperature had a significant effect, specifically as the temperature increased, the minimum ozone concentration decreased. Other photolysis experiments were conducted by Liu *et al.* [36] comparing the growth speed of the flame kernel obtained in $H_2/O_2/Ar$ and $H_2/O_2/Ar/O_3$ mixtures, finding that with ozone addition the growth speed of the flame kernel was much higher.

Nomaguchi and Koda [37] employed methane and methanol as fuels and found that the ignition time, defined as the minimum spark time duration to ensure a stable kernel, was significantly reduced with partially ozonized air. In addition, they made measurements on the burning velocity at room and stoichiometric conditions. The results showed that the addition of 5000 ppm ozone to the CH_4/Air mixture increased the combustion speed by 5%. Ombrello *et al.* [38] investigated the thermal and kinetic effects of O_3 on flame propagation by using $C_3H_8/O_2/N_2$ laminar lifted flames. They observed an acceleration of chemical kinetics with ozone by comparing flame stabilization locations with and without O_3 production. In particular, taking into account hydrodynamic and kinetic effects, experiments at atmospheric pressure showed a 4% enhancement of the flame propagation speed with the addition of 1260 ppm O_3 to the oxidant O_2/N_2 under stoichiometric conditions. Halter *et al.* [39] examined the combustion and laminar flame speed of methane with ozone addition using both an experimental and a numerical approach. Ozone was produced using a dielectric barrier discharge device. Equivalence ratios between 1.0 and 1.3 were investigated. The laminar flame speed measured at atmospheric pressure and room temperature is presented in Table 1.1.

Table 1.1. Laminar flame speed measurements for CH_4/Air/Ozone mixture, $P = 0.1\ MPa, T = 300\ K$. [39]

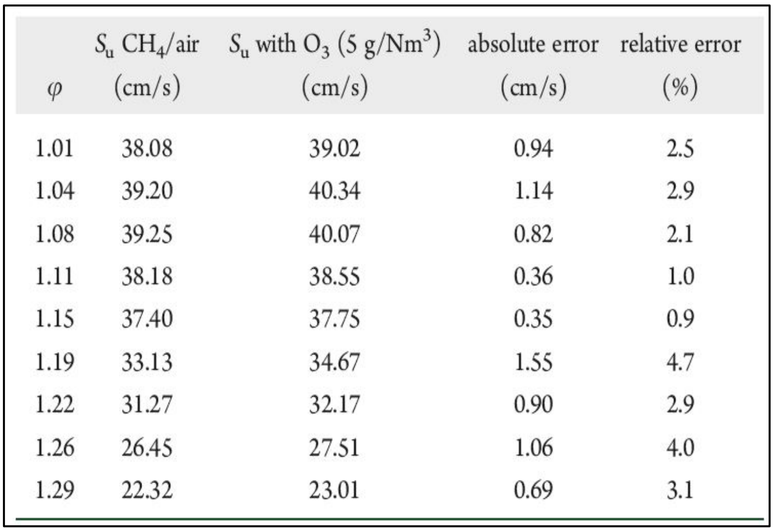

φ	S_u CH_4/air (cm/s)	S_u with O_3 (5 g/Nm^3) (cm/s)	absolute error (cm/s)	relative error (%)
1.01	38.08	39.02	0.94	2.5
1.04	39.20	40.34	1.14	2.9
1.08	39.25	40.07	0.82	2.1
1.11	38.18	38.55	0.36	1.0
1.15	37.40	37.75	0.35	0.9
1.19	33.13	34.67	1.55	4.7
1.22	31.27	32.17	0.90	2.9
1.26	26.45	27.51	1.06	4.0
1.29	22.32	23.01	0.69	3.1

Table 1.1 shows that the laminar flame speed increased for all examined equivalence ratios. These results were also confirmed by simulations with other ozone concentrations, as shown in Figure 1.1.

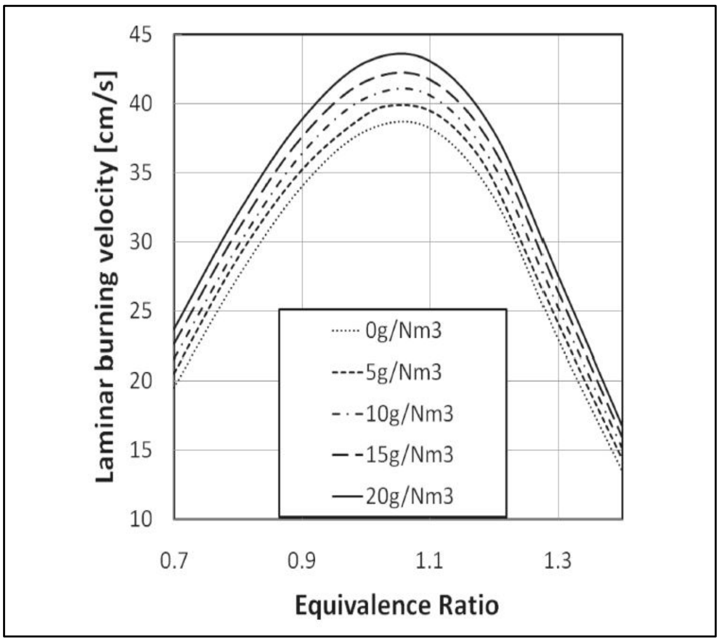

Figure 1.1. Laminar flame speed simulations for CH_4/Air/Ozone mixture, $P = 0.1\ MPa$, $T = 300\ K$. [39]

In addition, a detailed kinetic analysis was performed to evaluate the normalised production and consumption rates of each species under certain flame conditions. Reaction pathways were compared in the presence and absence of ozone at the maximum concentration of HO_2 and the kinetic analyses showed that, with ozone addition, the methane rate of consumption increased by 40% at stoichiometric conditions, 394% at $\varphi = 0.6$ and 977% at $\varphi = 1.4$, where φ is the equivalence ratio. A comparison of the main reaction pathways of methane in the cases with and without ozone is shown in Figure 1.2. In both cases, methane is mostly consumed by the reaction with OH, however, with ozonated air, the reaction rate with oxygen atoms increased by 23 times and consumed 15% methane, whereas under pure conditions (without ozone), consumption was only 3%. Then, the thermal flame thickness was also calculated, using both the experimental and numerical temperature profiles. The authors found, for both profiles, that with ozone addition the flame thickness was reduced, with a higher effect under stoichiometric conditions.

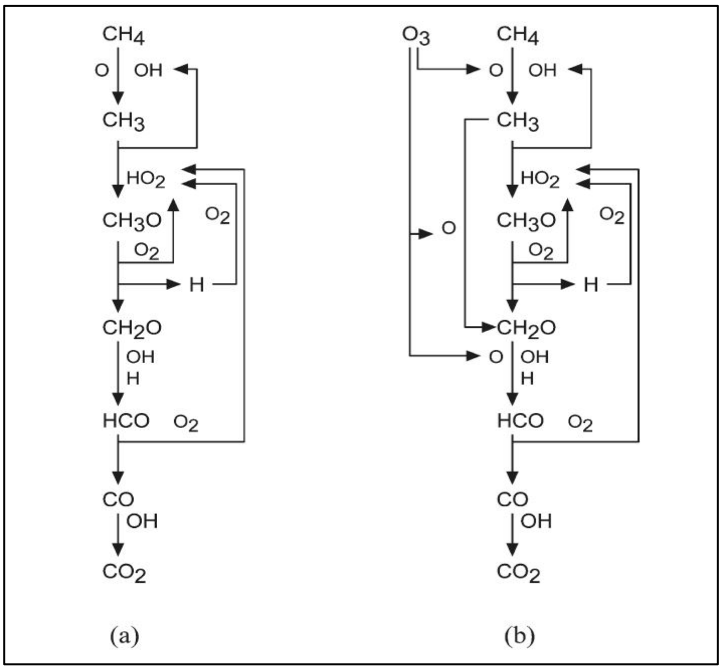

Figure 1.2. Main reaction pathways at $\varphi = 0.6$ for: (a) CH_4/Air; (b) $CH_4/Air/O_3$. [39]

Similar results were obtained by Wang *et al.* [40], who measured a laminar flame in a mixture of methane and ozonized air using a heat-flux burner, founding that the laminar flame speed increases as the concentration of ozone increases. The authors also conducted a sensitivity analysis, finding that ozone releases oxygen atoms in the preheating zone, promoting early fuel oxidation, but without changing the methane reaction pathways. Ji *et al.* [41] conducted experiments with ozonized methane-air mixture in a constant volume combustion bomb, finding that the O atoms obtained from ozone increased the concentration of active species, which promoted combustion, raised the flame temperature and thus enhanced the laminar flame speed. Ji *et al.* [42] conducted both experiments with a constant volume combustion bomb and simulations on the Ignition Delay Time (IDT) to study the influence of ozone on the combustion of a lean methane/air mixture. The numerical results showed that the time when the pressure peak occurs advances with increasing ozone addition. Xie *et al.* [43], on the other hand, used a Rapid Compression Machine to measure the IDT of a $CH_4/O_2/O_3/Ar$ mixture and found a reduction of IDT in the presence of ozone. Jiang *et al.* [44] conducted experiments and simulations to study the effect of ozone on a methane/oxygen mixture in meso-scale channels. In particular, they studied the flammability limits and the influence of ozone concentration on the combustion process near the limits. The results showed that ozone can extend the flammability limits and shift the combustion zone towards the inlet. In addition, after mixing with 2.3% of ozone, the maximum outer wall temperature increased by 30 K, with a greater effect at lower equivalence ratio.

Gao *et al.* [45] examined the effect of ozone on three different fuels: methane (CH_4), propane (C_3H_8) and ethylene (C_2H_4). Measurements were performed using a Bunsen burner under different conditions of pressure and mixture composition. Numerical simulations helped to understand the main reactions involving ozone and fuel within the flame, as shown in Figure 1.3 for methane. The effect of ozone begins with the release of oxygen atoms in the preheating zone by

R1.6) $O_3 + N_2 \rightleftarrows O_2 + O + N_2$,

which react with the fuel. For example, as shown in Figure 1.3(b), the rate of reaction of $CH_4 + O \rightarrow CH_3 + OH$ increased by 10.2% after ozone addition. This accelerated the production of OH species, that reacts with fuel via $CH_4 + OH \rightarrow CH_3 + H_2O$. These reactions promoted the production of CH_3 and, as a result, the product CH_2O increased. As shown in Figure 1.3(a), another relevant reaction for ozone consumption was:

R1.7) $O_3 + H \rightleftarrows O_2 + OH$,

which is a chain propagation or termination reaction and is unfavourable for laminar flame speed. The reaction R1.7 is associated with the diffusion process of hydrogen atoms, which tend to diffuse very quickly in the preheating zone. Since, with increasing pressure, the dissociation of species containing H is suppressed, the diffusion and concentration of H atoms from the pre-heating zone is reduced, so the authors found that the reaction R1.7 is also suppressed and consequently the decomposition of ozone via R1.6 becomes the dominant pathway for ozone consumption.

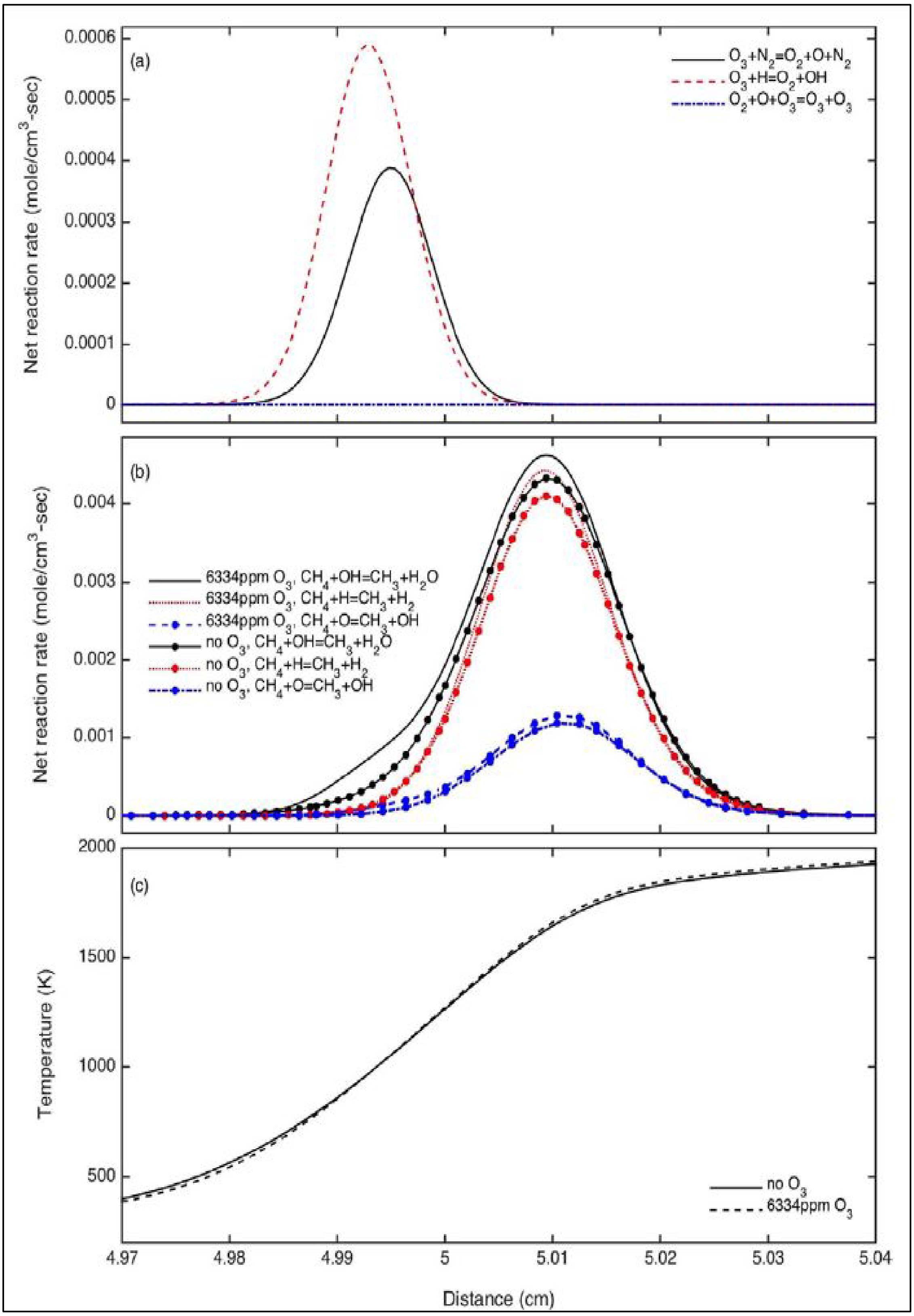

Figure 1.3. Flame Simulations for $CH_4/Air/O_3$ mixtures, P= 1 atm, T= 300 K, φ=1; (a) main reactions of O_3; (b) main reaction of CH_4; (c) temperature profiles. [45]

Similar results were obtained for propane, while, in the case of ethylene, the effects of ozone on laminar flame speed were opposite. Gluckstein *et al.* [46] already observed in 1955 a decrease in the laminar flame speed of ethylene with ozone addition at room conditions, and they hypothesised that the reason was due to the production of CH_2O, but this explanation was inadequate since the laminar flame speed of CH_2O is higher than that of C_2H_4. Pinchak *et al.* [47], on the other hand, found an increase in laminar flame speed, at sub-atmospheric pressure, for ethylene with ozone addition, attributing this effect to early heat release. An in-depth study to understand the effect of ozone on the laminar flame speed of ethylene was conducted by Gao *et al.* [45]. The authors found that at room conditions the laminar flame speed of ethylene with ozone addition decreased due to ozonolysis reactions. As these reactions take place very fast at room conditions, the ozone molecules and the ethylene molecules reacted during mixing, dissipating heat and causing the decrease of the laminar flame speed, as shown in Figure 1.4. Conducting experiments by lowering the temperature of the reactants to 200 K, the authors found a 5.7% increase in the laminar flame speed of ethylene with 3910 ppm ozone addition. The increase in laminar flame speed was also found when operating at sub-atmospheric pressure, which is consistent with a previous work [48], showing that, at low temperatures or pressures, ozonolysis reactions are significantly reduced.

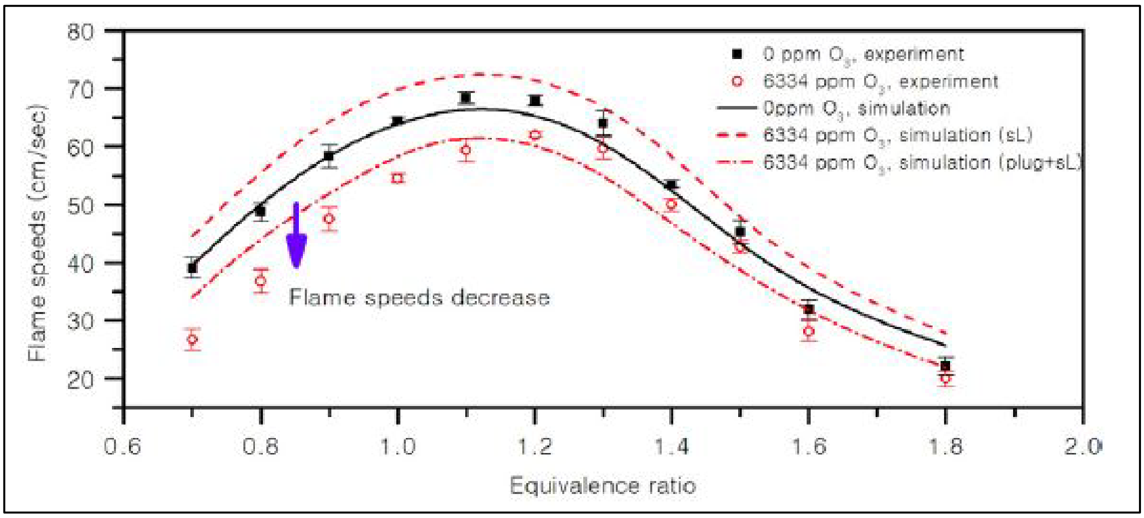

Figure 1.4. Ozone effect on C_2H_4 laminar flame speed at room conditions. [45]

Ozone was also used to investigate the possibility of flame stabilisation. Vu *et al.* [49] carried out experiments with methane/air and propane/air mixtures, thus showing that the addition of ozone was able to stabilise an initially unstable flame, due to an increase in laminar flame speed. Similar results were also obtained by Zhang *et al.* [50], finding that the flammability limits of syngas were extended with ozone addition. Weng *et al.* [51], investigating the effect of ozone on a methane/air Bunsen flame, found an increase in the concentration of formaldehyde (CH_2O), which the authors link to flame stability, when ozone was added, with a greater effect under rich mixture conditions. The increase in formaldehyde was due to the reactions of the CH_3O:

R1.8) $CH_3O + M \rightleftarrows CH_2O + H + M$,

R1.9) $CH_3O + O_2 \rightleftarrows CH_2O + HO_2$,

and the CH_3O radical is produced by the reaction:

R1.10) $CH_3 + HO_2 \rightleftarrows CH_3O + OH$,

but with ozone addition CH_3O is also produced by:

R1.11) $CH_3 + O_3 \rightleftarrows CH_3O + O_2$,

as also shown by the reaction pathways in Figure 1.2. To understand the influence of ozone on the production of CH_3O, the authors conducted experiments by simply heating the reactants (without flame) to limit the production of HO_2 and to inhibit the R1.10 reaction. The results showed that CH_3O was still produced due to the R1.11 reaction, demonstrating that it is possible to produce formaldehyde at much lower temperatures with ozone than in the case without ozone.

Ehn *et al.* [52] conducted Planar Laser-Induced Fluorescence (PLIF) measurements on methane/air/ozone flames and saw an increase in formaldehyde concentration with the addition of ozone, due to the acceleration of $CH_3 + O \rightleftarrows CH_2O + H$ reaction. Sensitivity analyses also showed an extension of the extinction strain rate due to the acceleration of the atomic oxygen reactions produced by ozone, indicating that O_3 can sustain flame burning in more turbulent conditions than without ozone. Weng *et al.* [51] also investigated the effect of ozone in turbulent CH_4/Air flames. The authors observed that, by adding the same amount of ozone as in the laminar case, CH_2O production was greater in the turbulent case, attributing this effect to the expansion of the pre-heating zone and to turbulent transport, leading to an increased mixing between burned and unburned gases. Khan *et al.* [53] investigated the effects of O_3, H, CO and Exhaust Gas Recirculation (EGR) addition to Haltermann gasoline by evaluating laminar and turbulent flame speeds using spherically propagating premixed flames in a constant volume combustion vessel. The authors found that for the stoichiometric mixture, the addition of 10% H_2, 5% CO and 1000 ppm O_3 resulted in an increase in laminar flame speed of 80%. In addition, increasing the initial temperature and pressure of the mixture resulted in a significant increase in laminar flame speed, suggesting that the ternary additives suppress the pressure-reducing effect on laminar flame speed found at high pressures with pure Haltermann gasoline. Reuter and Ombrello [54] conducted numerical simulations in the counterflow twin premixed flame configuration to study the effect of ozone addition on strained laminar flames under different ethylene/methane ratios, pressures and initial temperatures. The results showed that ozone addition increased the extinction strain rate more than the freely-propagating flame speed for all of the conditions studied. Recently, the effect of ozone on flame ignition and propagation, detonation and explosion limits for H_2/O_2 mixtures was also investigated [55-58]. The main conclusions were that ozone increased flame speed and influenced both reaction and preferential diffusion, mainly due to the reaction of ozone with H: $H + O_3 \rightleftarrows O_2 + OH.$

Since ozone plays its role from the beginning of the oxidation process, by influencing the Low-Temperature Chemistry (LTC), it was also used to induce the formation of a cool flames. The study of LTC (below 1000 K), and thus of cool flames, is particularly important in ignition timing, burning rate, burning limits, emissions and engine knocking in conventional and unconventional combustion engines [59]. The low-temperature ignition timescales can be comparable to the timescales of combustion processes in engines, so understanding and controlling low-temperature ignition, cool flames and the transition from cool to hot flames is a critical aspect for improving engine performance. Cool flames are hardly stable because they depend on low-temperature oxidation reactions, which have long induction times, avoiding radical chain branching. Won *et al.* [60] used ozone to enhance low-temperature combustion and successfully stabilized a n-heptane$/O_2/O_3$ non-premixed cool flame in a counterflow burner. When ozone was added, they successfully obtained a stable cool flame, as shown in Figure 1.5(a), proving that ozone addition is an effective way to ignite non-premixed cool flames without the need to first sustain a hot flame.

Ozone, by releasing the oxygen atom via R1.6 reaction, enables direct access to the cool flame branch, initiated the following low-temperature reaction pathways:

R1.12) $C_7H_{16} + O \rightleftarrows C_7H_{15} + OH,$

R1.13) $C_7H_{16} + OH \rightleftarrows C_7H_{15} + H_2O,$

R1.14) $C_7H_{15} + O_2 \rightleftarrows C_7H_{15}O_2$.

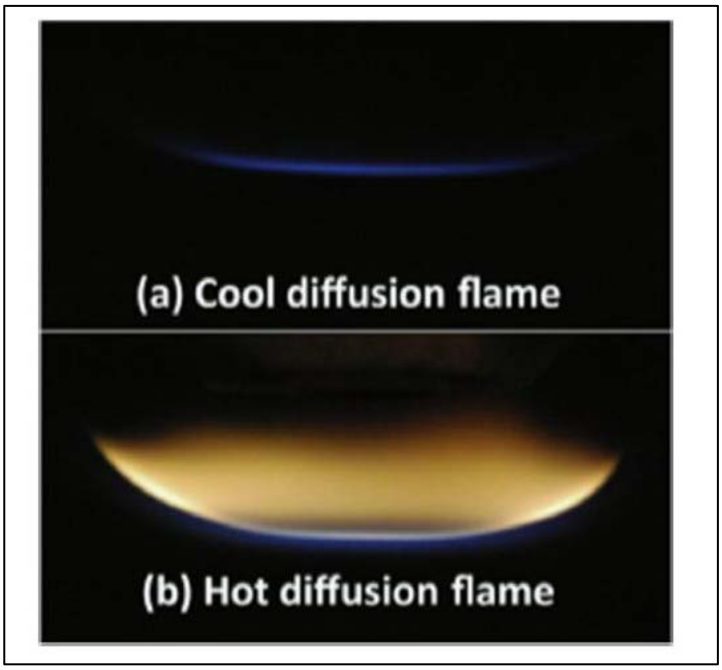

Figure 1.5. Direct photos of n-heptane: (a) ozone-activated cool diffusion flame; (b) normal high temperature diffusion flame. [60]

Similar effects were also obtained by Brown and Belmont [61] who measured cool flame propagation speeds using a broadband chemiluminescence-based lift-off height technique. The authors found a linear increase in propagation speeds with increasing O_3 concentrations. Reuter *et al.* [62] investigated the effect of ozone on n-alkanes (from n-heptane to n-tetradecane). They compared cool flames generated in the presence of ozone and cool flames "without ozone" (by turning off the O_3 generator after the formation of the cool flame). In both cases the cool flames were self-sustaining but with ozone addition they were much more intense in terms of chemiluminescence, as shown in Figure 1.6 for n -dodecane.

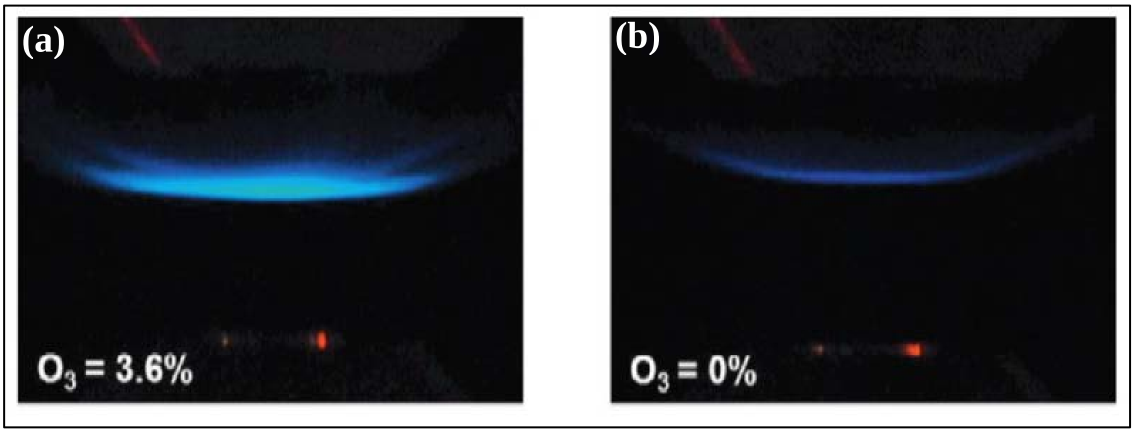

Figure 1.6. Direct photographs of *n* -dodecane cool flames: (a) with ozone addition; (b) without ozone addition. [62]

Liu *et al.* [63], on the other hand, investigated the effect of ozone on the cool flame and the Negative Temperature Coefficients (NTC) region of a propane/oxygen mixture and found that, with ozone, the cool flame occurs over a wider range of temperature, which extends towards lower temperatures.

Yehia *et al.* [64] experimentally investigated dibutyl ether/oxygen/ozone flames. They observed a self-sustaining low-temperature non-premixed warm flame, between the cool flame and hot flame, at atmospheric pressure. However, simulations showed that ozone played a different role between the different flame regimes: the hot flame was insensitive to the presence of ozone due to the high concentrations of radicals and the high heat release, whereas both the cool flame and the warm flame were sensitive to the ozone addition due to the formation of useful radicals at low temperatures. To understand the dynamics of near-limit steady-state cool flames and their relationship to hot flames, Ju *et al.* [65] conducted numerical simulations of one dimensional premixed freely-propagating dimethyl ether (DME) flames. The results showed that for freely propagating flames, at an initial temperature of 300 K, purely hot flames were observed, whereas to observe cool flames or the temperature of the reactants had to be increased to 530 K, or O_3 had to be added to the reactants. Between the two possibilities, the addition of ozone increased the reactivity of the flame more significantly than simply heating the reactants.

Reuter *et al.* [66] conducted experiments at atmospheric pressure with a counterflow burner to investigate premixed flame regimes in DME/O_2/O_3 ultra-lean mixture. The ozone-assisted counterflow burner setup was successful in establishing self-sustained premixed cool flames, as shown in Figure 1.7(a), and conducting CH_2O PLIF measurements, the authors observed that the cool flame's CH_2O signal profile is significantly thicker than that of the hot flame, as shown in Figure 1.7(c) and Figure 1.7(d). However, in contrast to the cool n-heptane diffusion flames obtained by Won *et al.* [60], ozone was absolutely necessary for the premixed cool flame, at the experimental conditions used, to remain self-sustained. Indeed, by carrying out path flow analyses, the DME fuel molecules feeding the cool flame were almost always (>96%) decomposed through H-abstraction reactions by O or OH-radicals. O radicals were almost exclusively (>97%) produced by ozone molecules, while 42% of OH radicals were produced by reactions involving O or OH. For these reasons, the cool flame extinguished immediately if the ozone generator was switched off.

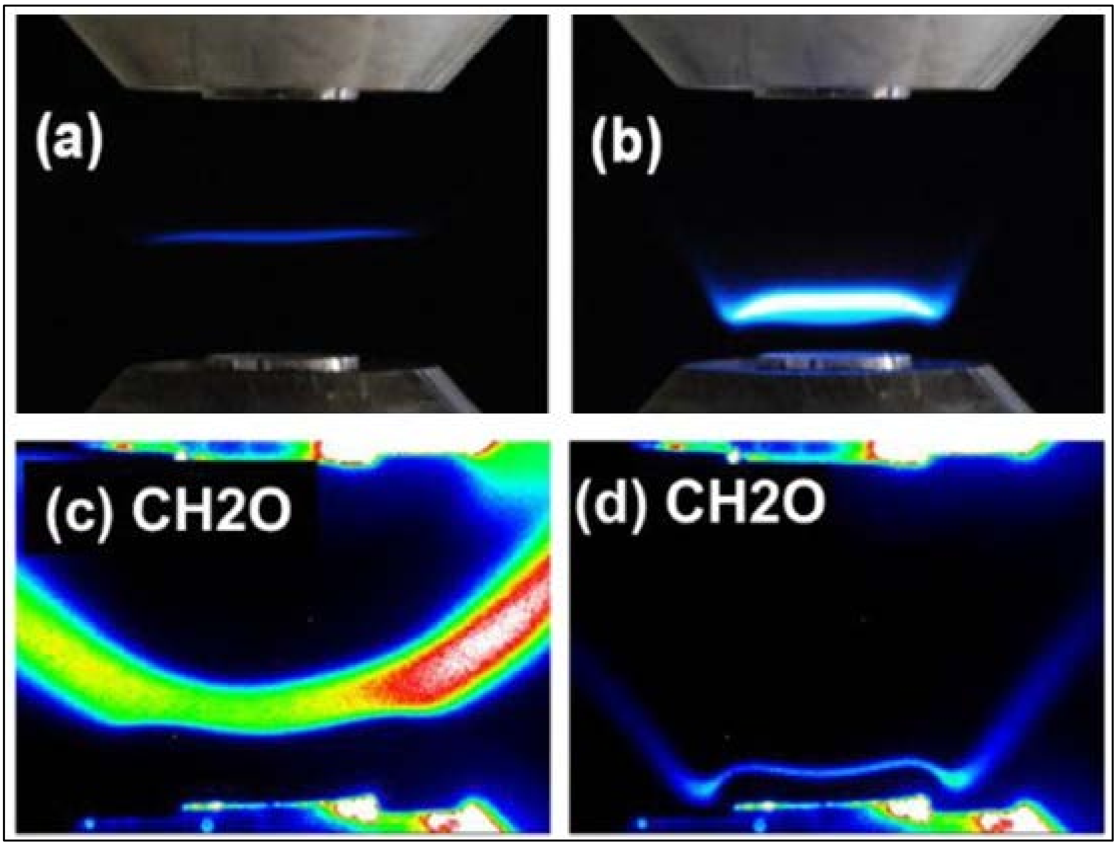

Figure 1.7. Images of: (a) cool flame; (b) hot flame; (c) cool flame CH_2O PLIF; (d) hot flame CH_2O PLIF. [66]

1.2 Ozone in internal combustion engines

Since ozone is able to modify ignition timing, accelerate and stabilise the flame, it could influence several performance parameters of Internal Combustion Engines (ICEs), such as ignition timing control, heat release rate, operating range, pollutant emissions. Therefore, ozone-assisted combustion within internal combustion engines may have different scopes depending on the engine technology considered. For this reason, the main aspects that characterise the different engine technologies, both conventional and unconventional, are first discussed, and then the state of the art on the use of ozone in internal combustion engines is presented.

1.2.1 Conventional and unconventional combustion engines

One of the historical classifications of internal combustion engines concerns the technology with which combustion occurs. There are two dominant modalities of combustion in internal combustion engines and therefore they characterise the so-called "conventional combustion engines": Spark Ignition (SI) engines based on Otto cycle, and Compression Ignition (CI) engines based on Diesel cycle.

In traditional Spark Ignition (SI) engines, well-mixed, near-stoichiometric fuel/air mixture is ignited by a spark plug. The fuel used is gasoline, which is injected within the intake pipe upstream of the intake valve, therefore this technology is called Port Fuel Injection (PFI). The mixture of vaporised fuel and air is aspirated into the cylinder during the engine's intake stroke and then compressed. A spark plug ignites the mixture and a turbulent flame propagates from the ignition site towards the walls of the combustion chamber, as shown in Figure 1.8. The equivalence ratio is near to stoichiometric for several reasons, including increasing performance, reducing pollutant emissions from combustion and ensuring efficient exhaust gas post-treatment. Carbon monoxide (CO) emissions increase with equivalence ratio, due to fuel-rich mixtures leading to incomplete combustion. Emissions of unburnt hydrocarbons (UHCs) are lower with a slight excess of air (fuel-lean mixture), but for excessively low equivalence ratios UHCs increase considerably due to the reduced flammability of the mixture. The main sources of these emissions are the crevices between the piston and cylinder and the flame quenching layer, where the flame is extinguished by cold boundaries. NO_x production, on the other hand, depends on several factors, the most important of which is temperature, which leads to the dissociation of molecular oxygen and nitrogen in the air. For this reason, nitrogen oxides increase significantly with increasing flame temperature, but NO_x concentrations also depend on the flame propagation speed: lower flame speeds in lean mixtures allow more time for NO_x formation reactions to take place [67,68]. For these engines, it is very important to avoid knocking phenomena, which could occur when pockets of unburned mixture (End Gases) auto-ignite before the flame reaches them. In this case there are very rapid and irregular increases of in-cylinder pressure, which could lead to structural damage of the engine. To avoid these undesired auto-ignitions, fuel with a high-octane number is used and the compression ratio is deliberately limited, which also restricts engine efficiency. In addition to the compression ratio, efficiency in Spark Ignition engines is influenced by the flame temperature and flame propagation speed, which determine the in-cylinder pressure and pollutant emissions.

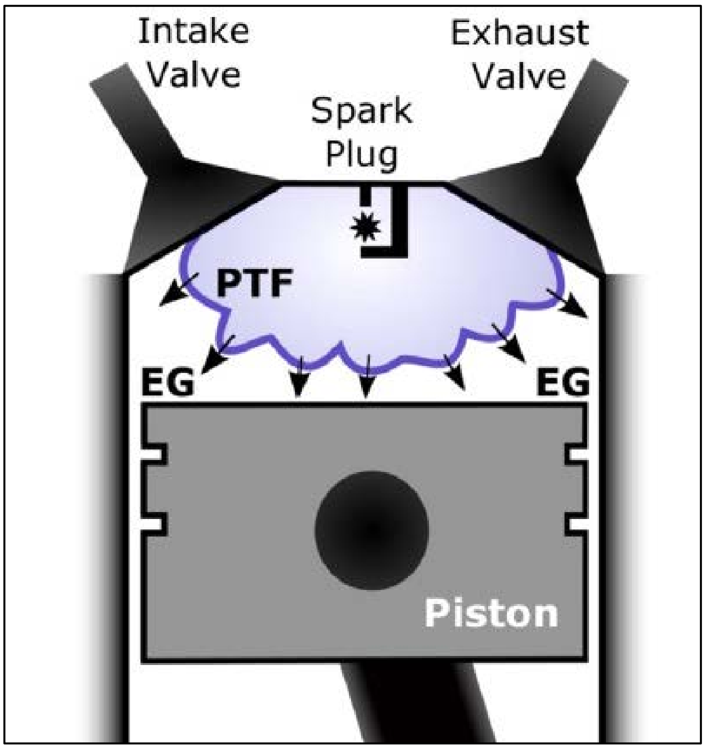

Figure 1.8. Schematic illustration of the combustion process in a traditional Spark Ignition engine. PTF= Premixed Turbulent Flame, EG=End Gases. [71]

An additional drop of efficiency is due to the loss of pressure through the throttling valve required to control the air flow. One strategy to increase the efficiency of Spark Ignition engines is to inject the fuel directly into the chamber to eliminate throttle losses, and therefore these engines are called Direct Injection Spark Ignition (DISI) engines. The direct injection of fuel, which vaporises in the cylinder, reduces the knock potential and allows the use of slightly higher compression ratios than in PFI engines. However, a stratified mixture is produced in the cylinder, with a higher equivalence ratio near the injector and lower near the walls, with emissions also depending on the size of fuel droplets that could impinge the walls causing high concentrations of UHCs and soot [69,70].

In traditional Compression Ignition (CI) engines, only air is aspirated and compressed, while fuel (diesel) is injected as a fine spray inside the combustion chamber, where it vaporises and mixes with the gases at high pressure and temperature (air and recirculated burned gases). With this strategy, there is no risk of knock and therefore higher compression ratios are used than in Spark Ignition (SI) engines. The in-cylinder fluid dynamics and injection pressure control the mixing of fresh gases with fuel, then the mixture auto-ignites where the equivalence ratio is close to stoichiometric generating a diffusive flame [67,68], as shown in Figure 1.9.

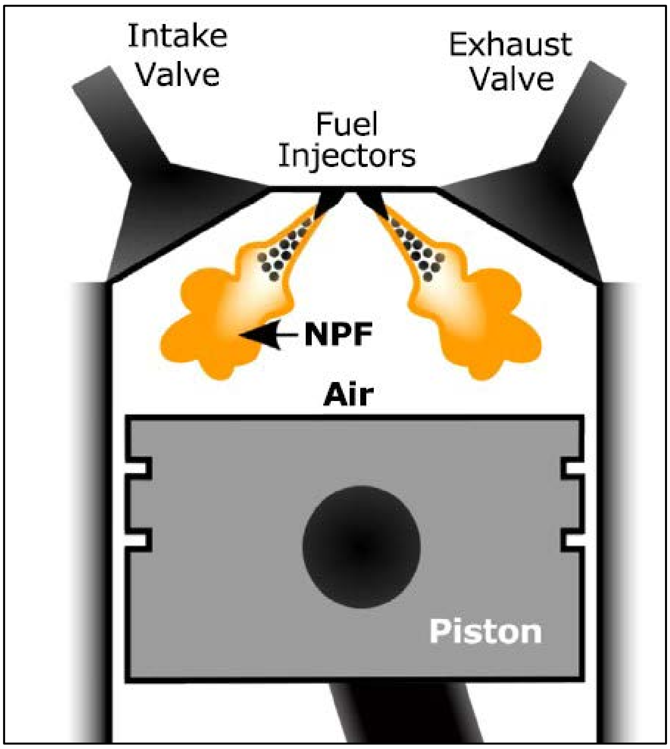

Figure 1.9. Schematic illustration of the combustion process in a traditional Compression Ignition engine. NPF= Non-Premixed Flame. [71]

Once ignition has occurred and combustion of the premixed charge has initiated, the flame propagates towards the centre of the spray where it finds larger fuel droplets. These receive heat from the flame front, evaporate quickly and the vapours diffuse into the surrounding air. Many droplets, especially those in the jet centre, are surrounded by the flame front while still liquid. It is important that the fuel droplets vaporise and mix quickly with the air to reduce soot emissions. The amount of premixed charge that is formed influences the pressure rate and its maximum value. In addition, the mixture must burn quickly enough to avoid emissions of unburned hydrocarbons (UHCs). The fuel molecules located in the spray centre are in a high oxygen deficit, but before they are diluted, they are heated up to flame temperature by the combustion process that takes place around them leading to high soot emissions. Later, when the fuel vapours are diluted, and are in a near-stoichiometric condition, they burn, but the temperature has reached such high values ($T > 2500\ K$) that it leads to high NO_x production [67,68,71]. For this reason, diesel engines are equipped with a particulate filter and NO_x trap or Selective Catalytic Reduction (SCR) devices.

With a focus on improving fuel economy and limiting pollutant emissions, several innovative forms of combustion were experimented in recent years, which attempt to combine the benefits of Spark Ignition (SI) engines with those of Compression Ignition (CI) engines, trying as far as possible to reduce the negative aspects of both technologies. In most cases, these unconventional engines are based on Low Temperature Combustion (LTC) techniques [72,73,74]. Some of the most promising technologies, which could also be enhanced by the use of ozone, include:

- Homogeneous Charge Compression Ignition (HCCI);
- Premixed Charge Compression Ignition (PCCI);
- Partially Premixed Compression Ignition (PPCI);
- Spark Assisted Compression Ignition (SACI).

Since PCCI, PPCI and SACI technologies actually derive from HCCI in an attempt to overcome its operational and control limitations, the operations of HCCI combustion engines will be described in more detail below.

Homogeneous Charge Compression Ignition (HCCI) combustion engines are positioned in between Compression Ignition (CI) and Spark Ignition (SI) engines, since they meet the main advantages of both combustion strategies (i.e., the high thermodynamic efficiency typical of CI engines, due to their high compression ratios, and the low emissions typical of SI engines). Specifically, HCCI engines are characterized by a quasi-constant volume combustion, and exploit the benefits of a charge composed by a highly diluted fuel vapor/air mixture. Fuel can be either indirectly or directly injected into the combustion chamber. Then, the fuel/air mixture is compressed until auto-ignition occurs at several locations in the combustion chamber, as shown in Figure 1.10. In this way, the main benefit of HCCI is achieved, namely low soot and low NO_x emissions when compared with conventional engines. Indeed, the combustion temperature is relatively low in HCCI engines, thus avoiding the formation of thermal NO_x. Soot formation, on the other hand, is strongly restrained due to the use of a highly diluted fuel/air mixture. Moreover, such a poor mixture provides a condition to avoid detonation, especially for gasoline, since a very fast Heat Release Rate (HRR) occurs [74,75,76].

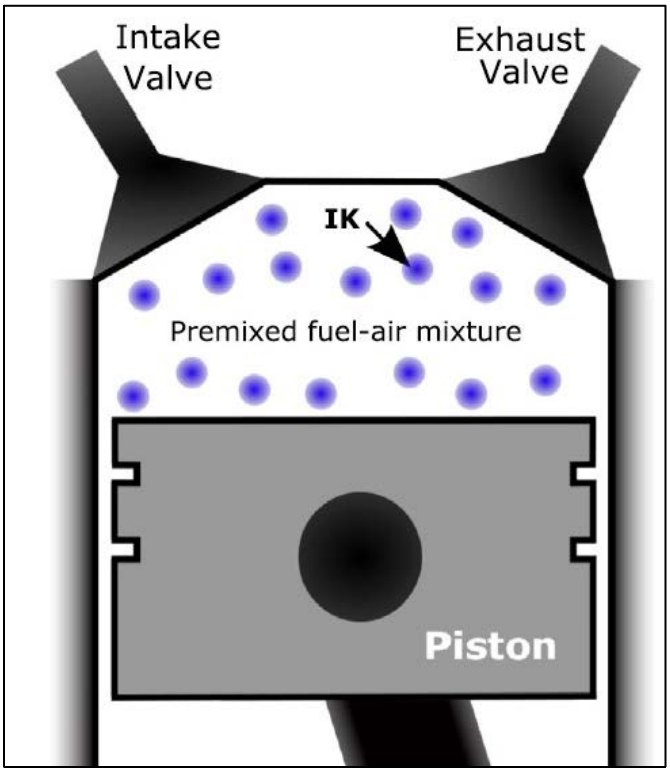

Figure 1.10. Schematic illustration of the combustion process in a Homogeneous Charge Compression Ignition Engine. IK= Ignition Kernels. [71]

A very important issue with HCCI engines is the control of the combustion phasing. In SI engines, the combustion process is easily controlled by a spark ignition timing, whereas, in CI engines, such a process is controlled by the fuel injection timing. In HCCI, auto-ignition and the entire combustion process are mainly governed by both the turbulence/chemistry interaction and complex chemical kinetics. Specifically, kinetics is influenced by several factors [77-79], such as mixture composition and temperature [80], which in turn are related to fuel properties, equivalence ratio, amount of EGR [81,82], wall heat transfer, combustion chamber geometry [83-85] and lubricant oil contamination [86]. The control and optimization of all these factors are challenging questions that limit the production of HCCI engines on a large scale. In particular, the main limitations concern:

- the control of the auto-ignition timing and heat release rate;
- the narrow engine operating range. Under high loads, high pressure peaks caused by the instantaneous combustion could lead to structural damages of the engine. At low loads, it is cumbersome to keep the engine running, due to the highly diluted mixture;
- the sudden rise in pressure due to a large number of quasi-simultaneous ignition spots in the combustion chamber, which can cause high noise or even structural damage;
- the non-perfect homogeneity of the charge. In order to obtain low pollutant emissions and an excellent fuel economy, a good charge homogeneity is requested. Thus, the Port Fuel Injection (PFI) strategy is beneficial to increase the time duration for mixing between fresh air and fuel. However, in this case, it is necessary to operate at low loads and under Low Temperature Regime (LTR) conditions with very lean mixtures, leading to an increase of Unburnt Hydrocarbons (UHCs) and CO. In addition, it is difficult to extend the engine speed range, which would depend solely on the characteristics of the mixture and on the thermo-fluid-dynamic parameters. On the other hand, direct injection provides an improvement of the control on combustion (in particular on the auto-ignition time), but with a less homogeneity of the charge and consequences on combustion quality and emissions, especially in terms of soot and NO_x;
- the high emissions of UHCs and CO, which are typically high both because the mixture is far from stoichiometric conditions and because the Low Temperature Combustion (LTC) reduces the conversion of CO to CO_2.

Several strategies were accomplished and are being studied to address all of these issues. The engine Compression Ratio (CR), the intake gas mixture temperature and the EGR need to be properly adjusted to improve the control over the combustion process. For instance, by reducing the CR, the auto-ignition timing is delayed, and therefore a wider time interval for fuel injection is available that will improve the charge homogeneity before auto-ignition [87]. As regards the intake gas mixture temperature, an increase in the charge temperature provides a decrease in the ignition delay. The sensitivity to this parameter mainly depends on the equivalence ratio and on the type of fuel, with consequences on emissions [80,88]. Wide load conditions are highly dependent on HRR, which may be either too slow or too fast to lead to knock. One approach to limit HRR is the use of a mixture temperature stratification within the combustion chamber [89]. With this strategy, the reactions occur at different rates and time instants, and therefore the combustion rate slows down as well as the pressure rise rate, which extends the engine operating range [90-92].

Premixed Charge Compression Ignition (PCCI) and Partially Premixed Compression Ignition (PPCI) are very close to the combustion occurring in CI engines and are based on HCCI combustion with the objective to have more control on the Start of Combustion (SOC). As discussed above, in an HCCI engine operating with a perfectly homogeneous charge, it is difficult to have control on the combustion process, as it is governed by the quasi-simultaneous auto-ignition of several spots within the chamber that cause a very fast heat release. Differently from the HCCI mode, PCCI and PPCI combustions use a charge that is not perfectly homogeneous. The combustion process is controlled by delaying the auto-ignition timing of the mixture through the massive use of EGR and by using an appropriate high-pressure fuel injection strategy (one or more injection events) that promotes rapid mixing in the chamber. This results in a more homogeneous mixture than that of traditional CI engines that will burn in premixed or partially premixed mode, extending and distributing the reaction zone and reducing the flame temperature as in HCCI mode, leading to a reduction of soot and $NO_x$with respect to conventional Compression Ignition (CI) engines, as shown in Figure 1.11 where the emissions of the main CI combustion technologies are given [93,73,94,71]. There are different injection strategies. Early injection promotes air/fuel mixing by giving the charge more time to tend towards homogeneity, leading to a reduction in soot and NO_x. However, some of the fuel may deposit on the walls resulting in increased UHCs and CO. Delaying injection, on the other hand, returns to conventional CI combustion, which is useful when operating with high loads. Another approach is to use dual injection: the first is an early injection to obtain a mixture that is as homogeneous as possible and to have a lower temperature when the piston approaches the Top Dead Center (TDC), then a late injection is carried out to control combustion. In fact, the fuel-rich area of the late injection burns earlier than the fuel-lean homogeneous mixture, so simultaneous ignition spots within the charge are avoided, resulting in an improved control on heat release.

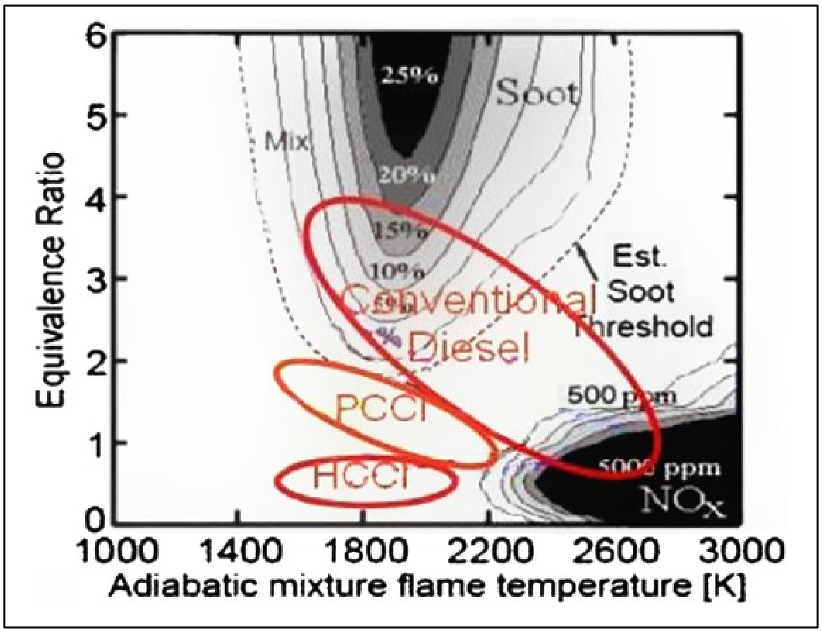

Figure 1.11. Plot of local equivalence ratio as function of flame temperature with different combustion strategies. [73]

Spark Assisted Compression Ignition (SACI) engines are based on HCCI technology, except that a spark plug is used to control the ignition timing. The spark produces a flame that consumes a portion of the charge by releasing energy. The propagation of the flame increases the temperature in the surrounding charge, anticipating auto-ignition. Essentially, in this kind of engine, combustion begins as in a Spark Ignition (SI) engine, with the flame propagation phase limiting the Heat Release Rate (HRR), while auto-ignition by compression quickly completes combustion. This mode limits the rate of in-cylinder pressure rise typical of an HCCI engine while maintaining high thermal efficiency and low NO_x emissions [95,96,97]. In order to maintain appropriate reaction rates, high dilution charge is required, but this could lead to problems for the spark ignition phase. Due to the slow flame propagation rate in a highly diluted mixture, the reactions in the flame front are strongly influenced by the temperature of the End Gases [98]. The difficulty in producing stable flame fronts in ultra-lean conditions results from the lack of time for the reaction front to achieve stable propagation before auto-ignition [99].

1.2.2 Ozone in Compression Ignition (CI) engines

One of the early studies investigating the use of ozone within Compression Ignition engines was that of Tachibana *et al.* [100], using a Cooperative Fuel Research (CFR) diesel engine. Based on these results, the researchers began to consider ozone as a way to control the auto-ignition timing and as a way to assist cold starting.

Nishida and Tachibana in [101] investigated the possibility of using ozone to control the auto-ignition timing in an HCCI engine by conducting both experimental and numerical analyses. The numerical results encouraged the use of ozone for this purpose, showing that it was possible to change the auto-ignition timing in relation to the ozone concentration, as shown in Figure 1.12. Furthermore, the authors found that the ozone addition to the mixture was more efficient than the addition of OH-radicals and was comparable to the addition of oxygen atoms. Experiments have also given similar results: with the addition of 1200 ppm ozone, the auto-ignition timing advanced by approximately 18 Crank Angle Degrees (CAD).

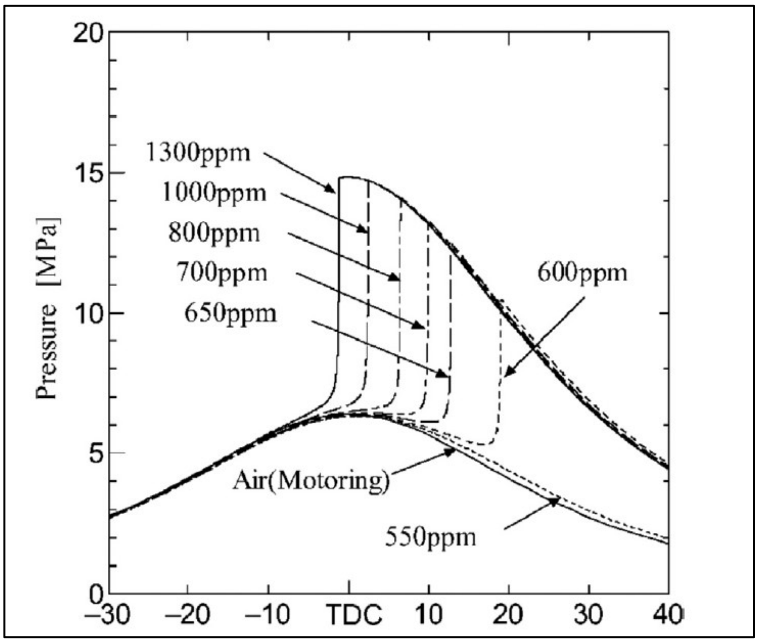

Figure 1.12. Calculated ignition process in HCCI for different ozone concentrations. [101]

Similar results were also obtained by Foucher *et al.* [102], who studied the effect of ozone in an n-heptane-fuelled HCCI engine and observed that 50 ppm addition of O_3 was able to anticipate ignition by about 15 CAD. Masurier *et al.* [103] investigated the use of ozone for the control of HCCI engines powered with alcohol fuels and found that ozone is useful to control combustion phasing and to improve combustion. Yamada *et al.* [104]

investigated the addition of different additives in a mixture with DME as fuel operating in an HCCI engine, finding that ozone in addition to anticipating the auto-ignition timing reduced the ignition temperature of the cool flame.

Masurier *et al.* [105] considered different Primary Reference Fuels (PRFs), from PRF0 to PRF100, and carried out experiments on a single cylinder of an HCCI engine powered with a mixture of PRF and ozonized air. The results showed that ozone promotes the formation of the cool flame and advances the entire combustion process. Masurier *et al.* [106], also evaluated the effect of different oxidising species, i.e. nitric oxide, nitrogen dioxide and ozone, within an iso-octane fuelled HCCI engine and found that ozone was the species that most advanced and accelerated combustion resulting in an advance and an increase in the maximum in-cylinder pressure, as shown in Figure 1.13. The authors also considered the performance of the HCCI engine in the case of simultaneous injection of oxidising chemical species. Specifically, 47 ppm NO was fixed in the chamber, while the ozone concentration was varied. The results showed that the only addition of nitrogen monoxide anticipated auto-ignition. By adding also ozone, first a delay was obtained and then, by increasing the ozone concentration to values comparable to those of NO, an advanced combustion phase was again achieved. These trends were due to the interaction between NO and O_3 via the reaction R1.3) $NO + O_3 \rightleftarrows NO_2 + O_2$, through which ozone and nitrogen monoxide react directly, producing NO_2, which is the species that has the minor effect on combustion, as also shown in Figure 1.13. Masurier *et al.* [107] focused their attention on the HCCI engine with regard to the addition of ozone alone, varying both the ozone generator supply gas and the method of injecting ozone in the combustion chamber. The results showed that the best conditions were achieved when the ozone generator was supplied with pure oxygen. However, despite the oxygen contained in air is five times lower, the ozone produced by using air was high enough to observe an impact almost similar to that with a pure oxygen supply. The authors also compared the case of injecting ozone into a plenum placed on the intake duct, where iso-octane and air were also supplied to produce a perfectly homogeneous mixture, with the case of injection into the intake duct directly. No differences were found between the two injection modes in terms of effects on the combustion process, probably because in both cases the fluid dynamics inside the cylinder produced a perfectly homogeneous distribution of ozone as in the case of plenum injection.

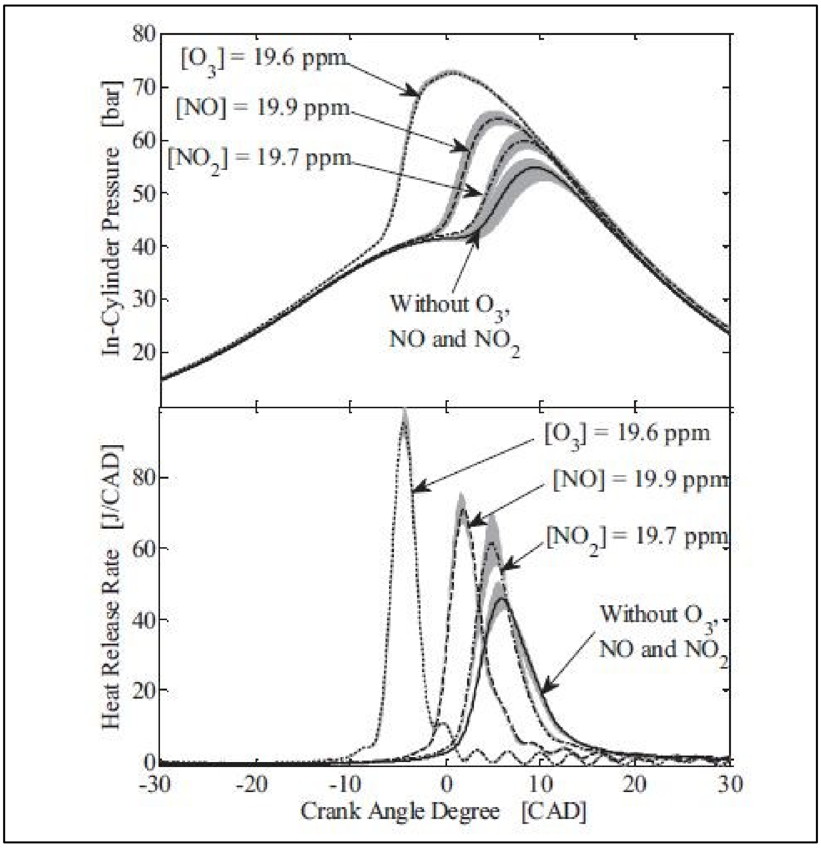

Figure 1.13. In-cylinder pressure and heat release rate without any oxidants and with 20 ppm of each oxidant separately injected. [106]

Pinazzi and Foucher [108,109] investigated the effect of ozone in a diesel engine operating in Partially Premixed Compression Ignition (PPCI) mode with direct gasoline injection of a commercial gasoline 95 RON (Research Octane Number). Experimental campaigns were conducted by investigating different injector geometries, different injection strategies and different gasoline Start of Injection (SOI). The authors found that in the case of single fuel injection, ozone had a greater impact on the engine performance if fuel injection was advanced, because, without fuel, ozone decomposes during compression, producing oxygen atoms, which then recombine into oxygen molecules. Using a double injection, the first at the beginning of the intake stroke, to maximise the residence time of ozone with fuel, and the second to control the combustion phase, analyses were carried out by varying ozone concentration. The authors found that the intake temperature, which should be high enough for gasoline auto-ignition and low-load operation, can be progressively reduced with the addition of ozone, resulting in a significant energy efficiency in heating the intake air, as shown in Figure 1.14.

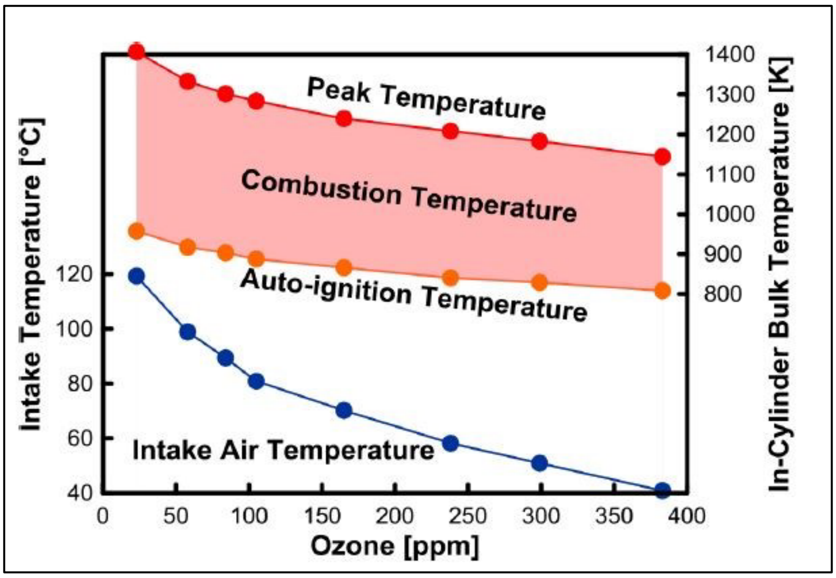

Figure 1.14. Intake temperature as a function of the intake ozone concentration. [109]

Seignour *et al.* [110] conducted experiments using an ultraviolet light absorption diagnostic to understand the effects of certain parameters and species on ozone decomposition in an HCCI engine. They found that iso-octane and water vapour had a greater effect on ozone decomposition. Seignour *et al.* [111] examined ozone-assisted combustion in an HCCI engine comparing hydrogen with isooctane. Analyses were conducted on the effect of intake pressure, intake temperature and ozone on combustion for both fuels. They found that ozone had the greatest impact, which was also used to shift the combustion region of isooctane in order to make a valid comparison between the two fuels.

Other studies examined the use of ozone in Spark Assisted Combustion Ignition (SACI) engines [112,113]. Biswas and Ekoto [112] have investigated the effect of ozone on the performance and emissions of a lean SACI engine. They found that ozone addition stabilised combustion compared to the case without O_3, increasing the reactivity of the end gases. Ozone addition extended the SACI operating range and was more advantageous at lower engine speeds due to the longer residence time for heat release.

1.2.3 Ozone in Spark Ignition (SI) engines

Compared to Compression Ignition engines, only few studies have investigated the use of ozone in conventional Spark Ignition (SI) engines. Gong *et al.* [114,115] carried out numerical investigations of an ozone-assisted, methanol-fuelled Direct Injection Spark Ignition (DISI) engine. The results showed that the maximum in-cylinder pressure increased with increasing ozone addition for both cold start and steady state modes. In addition, they found that ozone was able to reduce emissions of both formaldehyde and unburnt methanol with a stronger effect under cold engine start.

Golke *et al.* [116] tested the addition of ozone as an ignition enhancer for increased de-throttling to reduce part-load pumping losses in a Spark Ignition (SI) engine. The authors conducted an experimental investigation of efficiency and emissions in a turbocharged direct-injected engine. Different concentrations of ozone in the intake air were used to overcome the limitations of low-load operation. The results showed that it was possible to increase the gas exchange efficiency with ozone addition by promoting de-throttling operation with residual gases. In addition, ozone showed the potential to promote combustion even at low compression ratio and residual gas fraction higher than 30%.

In addition to the intake of an air/ozone mixture, it is possible for ozone to be produced in the cylinder: this is the case of Plasma Assisted Combustion (PAC). In spark ignition (SI) engines, the growth of the initial spark kernel significantly influences the emissions characteristics and lean burn limit. In order to improve the ignition of Spark Ignition engines, the idea is to replace or integrate the conventional spark plug with devices generating plasma, such as microwave, gliding arc or NanoSecond pulsed Discharge (NSD). Due to its properties, plasma interacts with combustion in several ways, among which the most important pathways are thermal, kinetic, and transport [117], shown in Figure 1.15. The production of ozone results from the kinetic pathway: the plasma, produces high-energy electrons and ions, which produce active radicals, ions, electronically and vibrationally excited molecules, catalytic intermediate species and long-lifetime reactive species including O_3. Several studies [118,119,120] on plasma activation in SI engines have shown that the operating range of the engine is extended towards leaner mixtures, with increased fuel efficiency and CO reduction [121], thus allowing to work in intermediate conditions between HCCI and traditional SI.

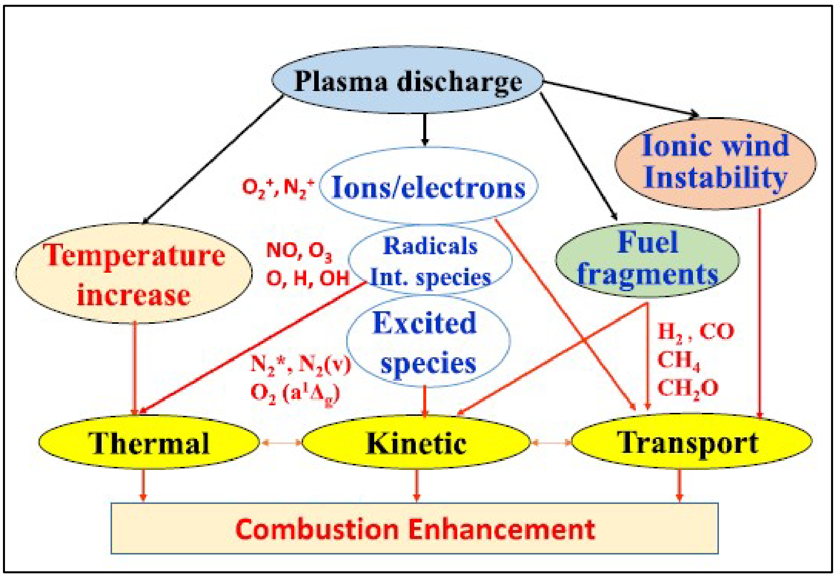

Figure 1.15. Schematic diagram of the main pathways of plasma-assisted combustion. [117]

2. Chapter 2: The models

2.1 Mathematical models

In a numerical investigation, the results obtained are the consequence of the particular mathematical models used, which cannot be separated from the knowledge of the specific problem to be studied. The equations to be solved, in fact, may be more or less complex depending on both the types and the level of detail of the physical phenomena considered. In this chapter the chemical kinetics of hydrocarbons combustion will be summarised and the reaction kinetic mechanisms used will be introduced, with a focus on the ozone kinetic sub-mechanism. Then, the governing equations of the phenomena studied will be described.

2.1.1 Hydrocarbons combustion and reaction kinetic mechanisms

2.1.1.1 Hydrocarbons combustion

Combustion, even of a simple hydrocarbon such as methane (CH_4), is described by a very complex reaction mechanism involving a large number of different species and reactions that increase with the complexity of the fuel composition. For a hydrocarbon, the general combustion reaction is:

R2.1) $C_xH_y + \left(x + \frac{y}{4}\right) O_2 \longrightarrow xCO + \frac{y}{2} H_2O.$

The global combustion reaction, however, only provides approximate estimation of the heat released and changes in composition, but cannot provide accurate information on the oxidation processes of intermediate species, which are crucial for the formation of pollutants and, in this case, for understanding the interaction with oxidants such as ozone.

In Internal Combustion Engines (ICEs), the pressure, and consequently the temperature, already change during the compression stroke of the engine, without combustion initiating. For this reason, it is useful to describe which reactions are involved in the various temperature ranges (defined by the properties of the specific fuel), i.e. the

Low Temperature Combustion (LTC) regime, the Negative Temperature Coefficient (NTC) regime and the High Temperature Combustion (HTC) regime [122-124,59].

Combustion in the Low Temperature Regime (LTR) involves an abstraction of H atoms from the fuel through the following initiation reaction, which generally takes place at temperatures below 800 K:

R2.2) $RH + O_2 \longrightarrow R + HO_2$,

where RH is the fuel considered and R is an alkyl radical. The alkyl radical then reacts with other molecular oxygen to produce an alkylperoxyl radical (RO_2), via reaction R2.3, which contributes to the beginning of a chain branching. Then, RO_2 isomerizes into hydroperoxyl-alkyl radical ($QOOH$) with R2.4, i.e. an H atom is transferred from carbon atom to O_2:

R2.3) $R + O_2 \longrightarrow RO_2$,

R2.4) $RO_2 \longrightarrow QOOH$.

The hydroperoxyl-alkyl radical ($QOOH$), depending on its size and structure, is consumed via four different propagation reactions leading to the production of stable species (olefin, cyclic ether or carbonyl) and hydroperoxyl (HO_2), hydroxyl (OH) or peroxy-hydroperoxyl-alkyl (O_2QOOH) radicals:

R2.5) $QOOH \longrightarrow olefin + HO_2$,

R2.6) $QOOH \longrightarrow cyclic\ ether + OH$,

R2.7) $QOOH \longrightarrow olefin + carbonyl + OH$,

R2.8) $QOOH + O_2 \longrightarrow O_2QOOH$.

The R2.8 reaction, which is similar to R2.3, is responsible for the formation of the cool flame chain branching reactions. The subsequent decomposition of O_2QOOH produces ketohydroperoxide ($OQ'OOH$) and an OH radical via reaction R2.9, then $OQ'OOH$ decomposes to form a ketoalkyloxy radical ($OQ'O$) and another OH radical through reaction R2.10:

R2.9) $O_2QOOH \longrightarrow OQ'OOH + OH$,

R2.10) $OQ'OOH \longrightarrow OQ'O + OH$.

The two OH molecules continue the oxidation of the fuel through the reaction:

R2.11) $RH + X \longrightarrow R + XH$,

where X is a radical (mainly OH and HO_2) and XH is a stable species (H_2O and H_2O_2) in this temperature regime.

The Low Temperature Regime (LTR) is followed by a Negative Temperature Coefficient (NTC) regime, which is characterised by a reduction in reactivity while the temperature increases. In this range, the reaction rates change and the reaction pathways are altered: the production of $QOOH$ decreases and the R2.5 reaction dominates the R2.8 reaction, so the chain branching, which leads to heat release, is broken. Specifically, the R2.3 reaction is replaced by the reaction:

R2.12) $R + O_2 \longrightarrow olefin + HO_2$.

The R2.5 and R2.12 reactions result in significant HO_2 production, while OH radicals are mainly consumed by R2.11. As a result, the formation of OH is interrupted and HO_2, which is a less reactive species than OH and does not lead to exothermic reactions, reacts with the fuel through R2.11 and with itself through R2.13, producing H_2O_2, which is a stable species in this temperature regime that limits reactivity.

R2.13) $HO_2 + HO_2 \longrightarrow H_2O_2 + O_2$.

The continuous temperature increase leads to new changes in the reaction pathways and results in the High Temperature Regime (HTR). In this regime, the bonds of the previously formed H_2O_2 are broken, producing two OH molecules resulting in a strongly increased reactivity:

R2.14) $H_2O_2 + M \longrightarrow 2OH + M$.

OH radicals oxidise the fuel and lead to the formation of more OH radicals following the R2.11-2.14 pathway. The large amount of OH and the reactivation of chain branching lead to an exponential increase in temperature and reactivity. When the temperature is high enough, additional OH radicals are produced by the reactions:

R2.15) $H + O_2 \longrightarrow O + OH$,

R2.16) $H_2 + O \longrightarrow H + OH$, R2.17) $H_2O + O \longrightarrow 2OH,$

while the fuel and other species decompose into smaller species. Finally, OH radicals consume all the fuel via the R2.11 reaction, and then contribute to the production of the final products.

2.1.1.2 Reaction kinetic mechanisms

Four different reaction mechanisms are employed. The first one refers to the oxidation of methane [125], whereas the other mechanisms refer to the oxidation of iso-octane [126,127,123]. The reaction mechanism of Cai & Pitsch [127] also accounts for NO_x formation, whereas the Saxena sub-mechanism for NO_x [128] is added to the remaining mechanisms. Moreover, all the mechanisms are modified by adding the ozone sub-mechanism proposed by Halter et al. [39] and given in Table 2.1.

The resulting mechanisms are:

- “CurranModif” for iso-octane with 889 species and 3866 reactions [123,128,39];
- “Cai&PitschModif” for iso-octane with 340 species and 1707 reactions [127,39];
- “YooModif” for iso-octane with 187 species and 931 reactions [126,128,39];
- “GRI3.0Modif” for methane with 54 species and 342 reactions [125,128,39].

Both detailed and reduced mechanisms are used for iso-octane oxidation. The most detailed mechanism [123] is used to infer the chemical phenomena involved in combustion with ozone addition. However, this mechanism may not be adequate for the analysis of multi-dimensional fluid-dynamic problems within a practical computational time. Hence, it is also important to test the accuracy of skeletal [126] and reduced [127] mechanisms to predict the main features of ozone-assisted combustion.

Table 2.1. Ozone kinetic sub-mechanism [39]. $k_{f,r} = C_r T^{\beta_r} e^{-\frac{E_{a_r}}{RT}}$ **.**

N.	Reaction	C_r	β_r	$E_{a,r}$ [cal/mol]	Ref.
1	$O_3 + N_2 \rightarrow O_2 + O + N_2$	4.00E+14	0	22667	[129]
2	$O_2 + O + N_2 \rightarrow O_3 + N_2$	1.60E+14	-0.4	-1391	[129]
3	$O_3 + O_2 \rightarrow O_2 + O + O_2$	1.54E+14	0	23064	[129]
4	$O_2 + O + O_2 \rightarrow O_3 + O_2$	3.26E+19	-2.1	0	[129]
5	$O_3 + O_3 \rightarrow O_2 + O + O_3$	4.40E+14	0	23064	[129]
6	$O_2 + O + O_3 \rightarrow O_3 + O_3$	1.67E+15	-0.5	-1391	[129]
7	$O_3 + H \rightleftarrows O_2 + OH$	8.43E+13	0	934	[130]
8	$O_3 + O \rightleftarrows O_2 + O_2$	4.82E+12	0	4094	[131]
9	$O_3 + OH \rightleftarrows O_2 + HO_2$	1.85E+11	0	831	[132]
10	$O_3 + HO_2 \rightleftarrows O_2 + OH + O_2$	6.02E+09	0	938	[129]
11	$O_3 + H_2O \rightleftarrows O_2 + H_2O_2$	6.62E+01	0	0	[133]
12	$O_3 + CH_3 \rightleftarrows O_2 + CH_3O$	3.07E+12	0	417	[134]
13	$O_3 + NO \rightleftarrows O_2 + NO_2$	8.43E+11	0	2603	[131]
14	$O_3 + N \rightleftarrows O_2 + NO$	6.03E+07	0	0	[134]
15	$O_3 + H \rightleftarrows O + HO_2$	4.52E+11	0	0	[135]
16	$O_3 + H_2 \rightleftarrows OH + HO_2$	6.00E+10	0	19840	[136]
17	$O_3 + CH_4 \rightleftarrows CH_3O + HO_2$	8.13E+10	0	15280	[136]

For the ozone sub-mechanism, the one by Halter et al. [39] was chosen both because it is the most commonly used coupled to hydrocarbon mechanisms and because many other sub-mechanisms are based on that, with at most minor modifications [10,40,45,102,105,106]. Indeed, the mechanism of Wang *et al.* [40] includes the same reactions and constants as the one considered. The difference between the two mechanisms consists of the exclusion of the reaction between methane and ozone in Wang *et al.* [40], because direct reactions between saturated hydrocarbons and ozone occur very slowly [30,31]. The most recent mechanism by Sun *et al.* [10], also employs the reactions and constants of Halter *et al.* [39] but also considering ozonolysis reactions, which are not of interest for the cases of the present work. As can be seen in Table 2.1, reactions involving ozone include: ozone decomposition and production reactions ($O_3 + M \rightleftarrows O_2 + O + M$), ozone oxidation reactions ($O_3 + X \rightleftarrows O_2 + XO$) and hydroperoxyl radical (HO_2) production and consumption reactions ($O_3 + XH \rightleftarrows HO_2 + product$). Although direct reaction of ozone with methane is generally considered negligible, it has been included in the mechanism. The reactions of ozone with H and OH species, that play a key role during combustion, are included. In addition, the reaction between O_3 and H_2O is also included due to the branching generation of OH through H_2O_2, as discussed in the previous paragraph.

2.1.2 Governing equations for Laminar Flame Speed (LFS) calculation

Laminar Flame Speed (LFS) is a physical-chemical property of a given premixed fuel-oxidizer mixture and depends on the thermo-dynamic conditions (pressure and temperature) and on the diffusivity and exothermicity of the mixture. The LFS provides a measure of the reactivity of the mixture and is used to characterise the combustion of various fuel-oxidizer combinations and to determine flammability limits. It is also used to validate kinetic reaction mechanisms, since it plays a key role in combustion systems, such as gas turbines, furnaces and Internal Combustion Engines (ICEs), because it has a direct impact on efficiency, Heat Release Rate (HRR) and pollutant emissions. The interest in quantifying the premixed laminar flame speed of various mixtures with different fuels and under different operating conditions has led to many experimental and numerical works in the literature [137] and to the development of several experimental techniques [138-140,39]. Based on experimental evidence, various correlations for the LFS have been developed for different mixtures [141-143]. From the numerical point of view, several one-dimensional models have been developed [144,145] to analyse the chemical progress of the mixture composition, the heat and mass diffusion and the influence of various parameters (pressure, temperature, equivalence ratio, dilution, etc.) on the LFS. Among hydrocarbon fuels, the most widely investigated is methane [139,146,147]. However, due to their importance for many combustion systems, especially for ICEs, gasoline surrogates, such as iso-octane and Primary Reference Fuels (PRFs), have also been extensively taken into consideration [148]. Davis and Law [149] compared the LFS of hydrocarbons from C1 to C8, showing that the LFS of such alkanes was similar for all the equivalence ratios under consideration, with the exception of methane, which is characterized by lower values.

From a mathematical aspect, the calculation of the LFS involves a resolution of a system of differential governing equations of a one-dimensional, freely propagating flame under steady-state conditions.

The governing equations read

Continuity equation:

$$\dot{M} = \rho u A, \tag{Eq2.1}$$

Energy equation:

$$\dot{M}\frac{dT}{dx} - \frac{1}{c_p}\frac{d}{dx}\left(\lambda A \frac{dT}{dx}\right) + \frac{A}{c_p}\sum_{i=1}^{N_s} \rho Y_i V_{dif,i} c_{p,i}\frac{dT}{dx} + \frac{A}{c_p}\sum_{i=1}^{N_s} \dot{\omega}_i\, h_i W_i = 0, \tag{Eq2.2}$$

Chemical species equation:

$$\dot{M}\frac{dY_i}{dx} + \frac{d}{dx}\left(\rho A Y_i V_{dif,i}\right) - A\dot{\omega}_i W_i = 0, \quad i = 1, \dots, N_s, \tag{Eq2.3}$$

Equation of State:

$$\rho = \frac{p\overline{W}}{RT}, \tag{Eq2.4}$$

where x is the spatial coordinate, $\dot{M}$ is the mass flow rate, ρ is the mass density, u is the fluid mixture velocity, A is the cross-sectional area of the stream tube enclosing the flame, T is the temperature, c_p and $c_{p,i}$ are the constant pressure specific heat of the mixture and of the *i*-th chemical species, respectively, λ is the thermal conductivity of the mixture, N_s is the number of gas species, Y_i is the mass fraction of the species *i* in the mixture, $V_{dif,i}$ is the diffusion velocity of the species i, $\dot{\omega}_i$ is the molar rate of production/consumption by chemical reactions of the *i*-th species per unit volume, h_i is the specific enthalpy of the *i*-th species, W_i is the molecular weight of the *i*-th species and $\overline{W}$ is the mean molecular weight of the mixture, p is the pressure and R is the universal gas constant.

The net chemical production/consumption rate depends on all reactions involving the *i*-th species. Specifically, a generic chemical reaction can be written in the form:

$$\sum_{i=1}^{N_s} \nu'_{i,r} Z_i \rightleftarrows \sum_{i=1}^{N_s} \nu''_{i,r} Z_i, \tag{Eq2.5}$$

where $\nu'_{i,r}$ and $\nu''_{i,r}$ are the stoichiometric coefficients in the reaction *r* of the reactant and produced species *i* respectively, and Z_i is the generic chemical species. For the law of mass action, it is possible to write $\dot{\omega}_i$ as:

$$\dot{\omega}_i = \sum_{r=1}^{N_r} \left(\nu''_{i,r} - \nu'_{i,r}\right) q_r \qquad \text{(Eq2.6)}$$

where N_r is the number of reactions and q_r is the rate of progress variable for the reaction *r* computed as:

$$q_r = k_{f,r} \prod_{j=1}^{N_s} \left[X_j\right]^{\nu'_{i,r}} - k_{b,r} \prod_{j=1}^{N_s} \left[X_j\right]^{\nu''_{j,r}} \qquad \text{(Eq2.7)}$$

where $k_{f,r}$ and $k_{b,r}$ are the forward and backward rate constants of the reaction *r* and $\left[X_j\right]$ is molar concentration of the species *j*. In reactions that require the 'third body' to occur (typically in dissociation and recombination reactions), the concentration of the third body must be taken into account, so Equation Eq2.7 is modified as follows:

$$q_r = \left(\sum_{j=1}^{N_s} \left(\alpha_{j,r}\right)\left[X_j\right]\right)\left(k_{f,r} \prod_{j=1}^{N_s} \left[X_j\right]^{\nu'_{i,r}} - k_{b,r} \prod_{j=1}^{N_s} \left[X_j\right]^{\nu''_{j,r}}\right) \qquad \text{(Eq2.8)}$$

where $\alpha_{j,r}$ is the third body efficiency of the species *j* in the reaction *r*.

The forward rate coefficients, $k_{f,r}$, are assumed to have the Arrhenius temperature dependence:

$$k_{f,r} = C_r T^{\beta_r} e^{\frac{-E_{a_r}}{RT}}, \qquad \text{(Eq2.9)}$$

where C_r is the pre-exponential factor, β_r is the temperature exponent and E_{a_r} is the activation energy related to the reaction *r*. The backward rate constants $k_{b,r}$ are related to the forward rate constants through the equilibrium constants in concentration units $K_{c,r}$

$$k_{b,r} = \frac{k_{f,r}}{K_{c,r}}, \qquad \text{(Eq2.10)}$$

and $K_{c,r}$ is related to the thermodynamic properties through:

$$K_{c,r} = K_{p,r}\left(\frac{P_{atm}}{RT}\right)^{\sum_{i=1}^{N_s}(\nu''_{i,r}-\nu'_{i,r})}, \tag{Eq2.11}$$

where P_{atm} is the pressure of one standard atmosphere and $K_{p,r}$ is the equilibrium constant in pressure units and is obtained with the following relationships:

$$K_{p,r} = e^{\left(\frac{\Delta S_r^{\circ}}{R}-\frac{\Delta H_r^{\circ}}{RT}\right)}, \tag{Eq2.12}$$

$$\frac{\Delta S_r^{\circ}}{R} = \sum_{i=1}^{N_s} \frac{(\nu''_{i,r}-\nu'_{i,r})S_i^{\circ}}{R}, \tag{Eq2.13}$$

$$\frac{\Delta H_r^{\circ}}{RT} = \sum_{i=1}^{N_s} \frac{(\nu''_{i,r}-\nu'_{i,r})H_i^{\circ}}{R}, \tag{Eq2.14}$$

where S_i° and H_i° are the standard state molar entropy and the standard state molar enthalpy of the species *i*, respectively. The constant pressure specific heat of the mixture c_p is computed as:

$$c_p = \sum_i Y_i c_{p,i}, \tag{Eq2.15}$$

and the constant pressure specific heat of the generic species *i* is calculated as a polynomial function of the temperature:

$$c_{p,i}(T) = \begin{cases} R\sum_{j=0}^{4} A'_{j,i}T^j, & T_{min,1} \le T \le T_{max,1} \\ R\sum_{j=0}^{4} B'_{j,i}T^j, & T_{min,2} \le T \le T_{max,2} \end{cases}, \tag{Eq2.16}$$

where $A'_{j,i}$ and $B'_{j,i}$ are the polynomial coefficients and are given in the related kinetic mechanics, together with $T_{min,1}$, $T_{min,2}$, $T_{max,1}$ and $T_{max,2}$ values. Similarly, the thermal conductivity of individual species λ_i is also determined as a function of temperature in order to calculate the thermal conductivity of the mixture λ.

The transport properties of each species in Equation Eq2.2 are evaluated by using the mixture-averaged formulation. This model assumes that the diffusion rate has three contributions:

$$V_{dif,i} = V_i' + V_i'' + V_c''', \tag{Eq2.17}$$

V_i' is the ordinary diffusion velocity and is computed by the Curtiss-Hirschfelder approximation [150], V_i'' is the thermal diffusion velocity [151], and V_c''' is the correction velocity [152], which ensures that the mass fractions sum is unity.

The inlet conditions are given in terms of temperature, pressure and mixture composition. No heat losses are considered.

2.1.3 Governing equations for Ignition Delay Time (IDT) calculation

Similar to Laminar Flame Speed (LFS), Ignition Delay Time (IDT) is also a key parameter in combustion processes and its calculation is also crucial for the validation of detailed kinetic mechanisms. In many applications, auto-ignition phenomena must be avoided to protect the integrity of the technology or to prevent efficiency losses, as in the case of Spark Ignition (SI) engines. In other cases, the auto-ignition timing is the fundamental parameter that determines the correct functioning of the technology, as in the case of Compression Ignition (CI) engines and, especially, in HCCI engines where the whole combustion process is governed by the auto-ignition of the mixture.

There are various definitions of IDT, in both the experimental and the numerical fields, some of which are:

- time required for a certain temperature value to occur;
- time required for a certain temperature increase to occur;
- time required for the first emission of light radiation to occur;
- time required for the peak of a chemical species concentration to occur (usually OH);
- time required for the maximum slope of the temperature or pressure profile to occur.

Experimentally, one of the most employed methods of determining the IDT is to use a Rapid Compression Machine (RCM) [153-155], whose operation is illustrated in Figure 2.1.

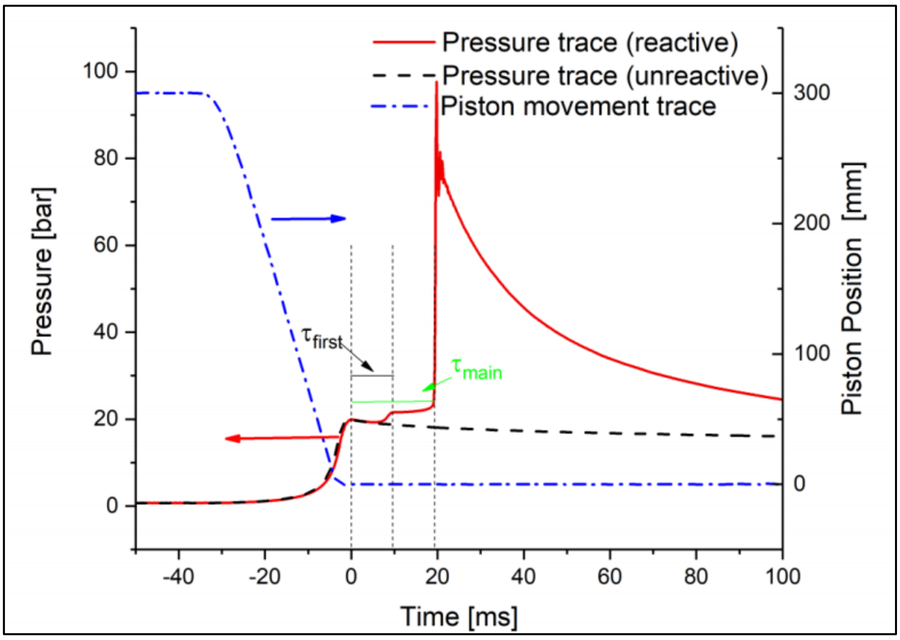

Figure 2.1. Representation of the operation and pressure trace of a Rapid Compression Machine. [153]

By setting the intake conditions and the compression ratio of the RCM, the mixture is compressed very quickly, in order to minimise heat exchange with the walls, up to the pressure and temperature of interest (time $t = 0$ in Figure 2.1). Under the desired conditions, the piston stops, and the system, at constant volume, evolves with auto-ignition and combustion of the mixture, detected with increasing pressure in the cylinder. Then, the IDT is identified as the time at which the derivative of the pressure curve is maximum (time $t = \tau_{main}$ in Figure 2.1). As can be seen from Figure 2.1 before the main pressure rise, there is a smaller one representing the first-stage of combustion (time $t = \tau_{first}$ in Figure 2.1).

From a mathematical perspective, the calculation of IDT involves the resolution of the balance equations for each chemical species and the energy conservation equation, considering a closed 0-D, constant-volume, adiabatic reactor.

Since the system is closed, the mass is constant, which means that the change in the mass of each chemical species is equal to the change in its mass fraction due to chemical reactions:

$$\frac{dY_i}{dt} = \frac{\dot{\omega}_i W_i}{\rho}, \tag{Eq2.18}$$

where t is the time. The first law of thermodynamics for closed systems reads:

$$\frac{de}{dt} = \frac{dQ_s}{dt} - p\frac{dv_s}{dt}, \tag{Eq2.19}$$

where e, Q_s and v_s are the internal energy, heat-transfer across the system boundary and volume, referred to the mass unit (i.e. specific), respectively. Since the system is adiabatic and the volume is constant, it remains:

$$\frac{de}{dt} = 0, \tag{Eq2.20}$$

Considering the ideal gas, the internal energy is the sum of the internal energies of the individual species, and deriving with respect to time gives:

$$\frac{de}{dt} = \sum_{i=1}^{N_s} Y_i \frac{de_i}{dt} + \sum_{i=1}^{N_s} e_i \frac{dY_i}{dt}, \tag{Eq2.21}$$

$$\frac{de_i}{dt} = c_{v,i}\frac{dT}{dt}, \tag{Eq2.22}$$

where e_i and $c_{v,i}$ are the internal energy and the constant volume specific heat of the species *i* respectively. Similarly to the calculation of the constant pressure specific heat, the constant volume specific heat of the mixture c_v is equal to:

$$c_v = \sum_i Y_i c_{v,i}. \tag{Eq2.23}$$

Finally, by inserting Eq2.18, Eq2.21, Eq2.22 and Eq2.23 into Eq2.20, the energy equation is obtained:

$$c_v \frac{dT}{dt} + \frac{1}{\rho}\sum_{i=1}^{N_s} e_i \dot{\omega}_i W_i = 0. \tag{Eq2.24}$$

The mass equation Eq2.18 and the energy equation Eq2.20, together with the equation of state Eq2.4 and the calculation of the molar rate of production (Eq2.6-2.9) close the problem.

2.1.4 Governing equations for engines 0-D simulations

Depending on the type of engine to be simulated, the mathematical model describing the thermodynamic evolution of the mixture inside the cylinder changes. In this work, zero-dimensional modelling of an engine was used for two scopes: the first was to simulate the thermo-chemical evolution of the mixture with ozone addition during the compression stroke, up to the ignition time; the second was to calculate the heat released by combustion, from experimental pressure traces taken from the literature, in order to validate CFD models. For these purposes, the evolution of the system was modelled mathematically as a closed 0-D reactor, with variable volume, as shown in Figure 2.2.

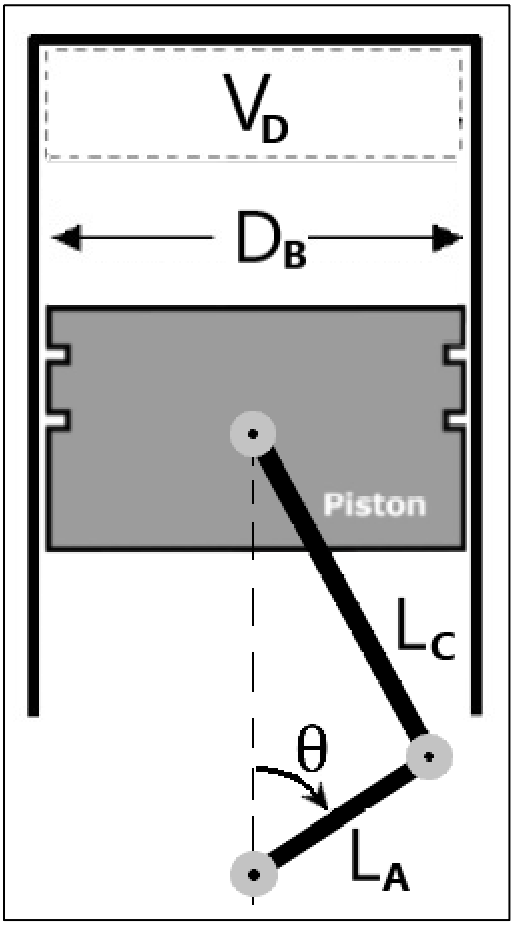

Figure 2.2. Schematic representation of the cylinder of an internal combustion engine. L_A= length of crank arm; θ= crank angle; L_C= length of connecting rod; D_B= length of Bore; V_D= Top Dead Center Volume.

From the geometric quantities of the engine, it is possible to derive the engine displaced volume and volume variation law as a function of Crank Angle (CA) θ:

$$V_c = \pi \frac{D_B^2}{2} L_A \,, \tag{Eq2.25}$$

$$V = V_D + \pi \frac{D_B^2}{4} \left(L_C + L_A(1 - cos\theta) - \sqrt{L_C^2 - (L_A sin\theta)^2} \right), \tag{Eq2.26}$$

where V_c is the engine displaced volume, L_A is the crank arm length, V_D is the volume at Top Dead Center (TDC), D_B is the bore length and L_C is connecting rode length. The TDC volume V_D is derived from the engine displacement and compression ratio CR:

$$V_D = \frac{V_c}{CR - 1}, \tag{Eq2.27}$$

with

$$CR = \frac{V_{max}}{V_{min}}. \tag{Eq2.28}$$

The mass trapped in the cylinder is constant, so Equation Eq2.18 can be written. Furthermore, by applying the first law of thermodynamics (Eq2.19), taking into account both the contribution of the work done by the piston and the heat transfer to the chamber walls, differentiating by $d\theta$ instead dt, the following is obtained:

$$c_v \frac{dT}{d\theta} + \frac{1}{\rho} \sum_{i=1}^{N_s} e_i \dot{\omega}_i W_i = -\frac{dQ_w}{d\theta} - p \frac{dv_s}{d\theta}, \tag{Eq2.29}$$

where Q_w is the heat transfer to the chamber walls (the negative sign is due to the thermodynamic convention used, since in engines the heat transfer is from the system to the walls). In order to calculate the total heat released by combustion, instead, it is useful to write the first law of thermodynamics in the following form:

$$\frac{dQ_{ch}}{d\theta} - \frac{dQ_w}{d\theta} = \frac{\gamma}{\gamma - 1} p \frac{dV}{d\theta} + \frac{1}{\gamma - 1} V \frac{dp}{d\theta}, \tag{Eq2.30}$$

where Q_{ch} represent the chemical energy released by the combustion, and γ is the specific heat ratio:

$$\gamma = \frac{c_p}{c_v}. \tag{Eq2.31}$$

For the resolution of the Equations Eq2.29 and Eq2.30, it is necessary to calculate the heat transferred to the walls, which can be written in the following form:

$$\frac{dQ_w}{dt} = A_w h_c (T - T_w)\,, \qquad \text{(Eq2.32)}$$

where A_w is the chamber surface area (sum of piston area, head area and cylinder area which is a function of CA), T_w is the wall temperature and h_c is the convective heat-transfer coefficient. Different correlations can be used to calculate the convective heat-transfer coefficient h_c [156-159]. The following Hohenberg correlation [158] was used for the computation of Q_w in Equation Eq2.30:

$$h_c = 130 V^{-0.06} p^{0.8} T^{-0.4} \left(\bar{u}_p + 1.4\right)^{0.8}\,, \qquad \text{(Eq2.33)}$$

where $\bar{u}_p$ is the mean piston speed and p is expressed in bar.

Then it is possible to change dt of Equation Eq2.32 in $d\theta$ using the engine speed RPM (Round Per Minute):

$$\frac{dt}{d\theta} = \frac{60}{2\pi RPM} \left[\frac{s}{rad}\right], \qquad \text{(Eq2.34)}$$

Finally, by combining the Equations Eq2.30,32-34, knowing the experimental pressure trace, volume, in cylinder mass and gas composition at the Intake Valve Closure (IVC) CA, the gas temperature T can be calculated from the equation of state, so the only unknown in the Eq2.30 is the heat released by combustion, which is the Heat Release Rate (HRR).

On the other hand, Annand correlation [156] was also used for the computation of Q_w in in Equation Eq2.29:

$$h_c = \lambda \frac{a_A}{D_B} \left(\frac{\rho \bar{u}_p D_B}{\mu}\right)^{b_A}\,, \qquad \text{(Eq2.35)}$$

where a_A and b_A are two constants which, in four-stroke engines, assume the typical values of 0.26 and 0.75 ± 0.15, respectively. The viscosity μ is computed with Sutherland law:

$$\mu = \frac{C_{1s} T^{\frac{3}{2}}}{T + C_{2s}}\,, \qquad \text{(Eq2.36)}$$

with $C_{1s} = 1.42 \times 10^{-6} \frac{kg}{msK^{\frac{1}{2}}}$ and $C_{2s} = 100\ K$, and finally λ is calculated by using the Prandtl number: $\lambda = \frac{\mu c_p}{Pr}$.

2.1.5 Governing equations for engines CFD simulations

The thermo-fluid dynamic analysis of the processes occurring in an internal combustion engine (ICE) and characterising its operation is very complex: the flow inside the combustion chamber is turbulent, thousands of chemical reactions take place and there are heat exchanges. Therefore, the behaviour of a multi-component reactant mixture must be studied, which, under the assumption of a continuous fluid, is governed by the following balance laws:

- the mass conservation law;
- the momentum conservation law;
- the energy conservation equation.

2.1.5.1 Balance equations

The first balance equation is the mass conservation equation (or continuity equation), which, for multi-component reactant flow, can be written either for the total mass (Eq2.37) or for individual chemical species (Eq2.38):

$$\frac{\partial}{\partial t}(\rho) + \vec{\nabla} \cdot (\rho \vec{v}) = 0\,, \tag{Eq2.37}$$

$$\frac{\partial}{\partial t}(\rho Y_i) + \vec{\nabla} \cdot (\rho \vec{v} Y_i) = -\vec{\nabla} \cdot \vec{J_i} + R_{rr,i}\,, \tag{Eq2.38}$$

where $\vec{v}$ is the gas velocity vector, $R_{rr,i}$ is the volumetric mean reaction rate of the species *i* and $\vec{J_i}$ is the mass diffusion flux of species *i* in the mixture, computed as:

$$\vec{J_i} = -\left(\rho D_{i,m} + \frac{\mu_t}{Sc_t}\right)\vec{\nabla} Y_i - D_{T,i}\frac{\vec{\nabla} T}{T}, \tag{Eq2.39}$$

where $D_{T,i}$ is thermal diffusivity of the species i, μ_t is the turbulent viscosity, Sc_t is the turbulent Schmidt number, and $D_{i,m}$ is the diffusion coefficient of species *i* in the mixture, with:

$$Sc_t = \frac{\mu_t}{\rho D_t}, \tag{Eq2.40}$$

$$D_{i,m} = \frac{1 - X_i}{\sum_{j,j\neq i} \frac{X_j}{D_{ij}}}, \qquad \text{(Eq2.41)}$$

where D_t is the turbulent diffusivity coefficient, X_i is the molar fraction of species *i*, and D_{ij} is the diffusion coefficient of species *i* in species *j*, modelled using the Chapman-Enskog formulation [160].

The thermal conductivity λ and the dynamic diffusivity μ of the mixture were calculated taking into account the mutual interactions between the chemical species using the scalar ψ_{ij}, defined as:

$$\psi_{ij} = \frac{\left[1 + \left(\frac{\mu_i}{\mu_j}\right)^{\frac{1}{2}} \left(\frac{W_j}{W_i}\right)^{\frac{1}{4}}\right]^2}{\left[8\left(1 + \frac{W_i}{W_j}\right)\right]^{\frac{1}{2}}}, \qquad \text{(Eq2.42)}$$

and therefore:

$$\lambda = \sum_i \frac{X_i \lambda_i}{\sum_j X_j \psi_{ij}}, \qquad \text{(Eq2.43)}$$

$$\mu = \sum_i \frac{X_i \mu_i}{\sum_j X_j \psi_{ij}}, \qquad \text{(Eq2.44)}$$

where λ_i and μ_i are the thermal conductivity and the dynamic diffusivity of the species *i*, respectively.

As a consequence of the second law of dynamics, it is possible to write the momentum equation (also called Navier-Stokes equation). Neglecting the contribution due to buoyancy forces (negligible in Internal Combustion Engine) the following equation is obtained:

$$\frac{\partial}{\partial t}(\rho\vec{v}) + \vec{\nabla} \cdot (\rho\vec{v}\vec{v}) = -\vec{\nabla}p + \vec{\nabla} \cdot \bar{\bar{\tau}}, \qquad \text{(Eq2.45)}$$

where $\bar{\bar{\tau}}$ is the stress tensor given by

$$\bar{\bar{\tau}} = \mu\left[\left(\vec{\nabla}\vec{v} + \vec{\nabla}\vec{v}^T\right) - \frac{2}{3}\vec{\nabla} \cdot \vec{v}\bar{\bar{I}}\right], \qquad \text{(Eq2.46)}$$

where $\bar{\bar{I}}$ is the unit tensor.

By using the first law of thermodynamics, it is possible to write the energy conservation equation. Depending on the type of energy referred to (internal, total, etc.), it is possible to obtain different formulations. The one presented below is the total energy conservation equation, which includes all the terms necessary to model the phenomena involved in multi-component reactant mixtures (chemical reactions and diffusive transport):

$$\frac{\partial}{\partial t}(\rho E) + \vec{\nabla} \cdot \left(\vec{v}(\rho E + p)\right) = \\ = \vec{\nabla} \cdot \left(\lambda_{eff} \vec{\nabla} T - \sum_i h_{s,i} \vec{J}_i + \left(\bar{\bar{\tau}}_{eff} \cdot \vec{v} \right) \right) + S_{h,rxn} \,, \tag{Eq2.47}$$

where $\lambda_{eff} = \lambda + \lambda_t$ is the effective thermal conductivity (where λ_t is the turbulent thermal conductivity, defined according to the turbulence model used), $h_{s,i}$ is the sensible enthalpy of the species i and $S_{h,rxn}$ is the source term that includes the heat released by chemical reactions and E is the total internal energy defined as:

$$E = h_s - \frac{p}{\rho} + \frac{v^2}{2} \,. \tag{Eq2.48}$$

the term h_s is the mixture sensible enthalpy, calculated with:

$$h_s = \sum_i Y_i h_{s,i} \,, \tag{Eq2.49}$$

where $h_{s,i}$ sensible enthalpy of species i, i.e. the part of enthalpy that includes only the changes in the enthalpy due to specific heat:

$$h_{s,i} = \int_{T_{ref}}^{T} c_{p,i} dT \,, \tag{Eq2.50}$$

with $T_{ref} = 298.15\ K$.

In Equation Eq2.47, the terms $\vec{\nabla} \cdot (\lambda_{eff} \vec{\nabla} T)$, $\vec{\nabla} \cdot (\sum_i h_{s,i} \vec{J}_i)$ and $\vec{\nabla} \cdot \left(\bar{\bar{\tau}}_{eff} \cdot \vec{v} \right)$ represent energy transfer due to conduction, species diffusion and viscous dissipation, respectively. The term $S_{h,rxn}$ is computed with the following expression:

$$S_{h,rxn} = -\sum_i \frac{h_i^0}{M_i} R_{rr,i} \,, \tag{Eq2.51}$$

where h_i^0 and M_i are the enthalpy of formation and the mass of species i, respectively. The term $R_{rr,i}$, which appears in both the mass conservation equation and the energy conservation equation, will be described in detail in the section concerning the combustion model.

2.1.5.2 Turbulence model

Turbulence is characterised by fluctuations in all local flow properties and occurs for sufficiently large Reynolds numbers, depending on the system geometry, and is responsible for the mixing of transported quantities, such as momentum, energy and chemical species, resulting in random behaviour, in instantaneous values of all quantities. Any property f is usually decomposed into the mean (ensemble-averaged or time averaged) $\bar{f}$, and fluctuating f' contributions:

$$f = \bar{f} + f' , \tag{Eq2.52}$$

Therefore, by applying the Equation Eq2.52 to the velocity, gives $v = u + u'$ where u is the mean velocity and u' is the fluctuating velocity. The average is usually defined as an ensemble average, i.e. an average of a large number of realizations at the same instant of the same flow field; for steady mean flow fields, this average is replaced by time averages over a sufficiently long period.

Turbulent fluctuations are associated with different scales ranging from the integral length scale l_t (i.e. the largest), to the Kolmogorov length scale η_k (i.e. the smallest). Under the assumption of homogeneous and isotropic turbulence, the energy of the large scales flows to the smaller scales through the Kolmogorov cascade [161]. Specifically, the flow of energy from one scale to another, which occurs due to the non-linear term in the momentum equation, is constant and is given by the dissipation ε of the turbulent kinetic energy k. Then it is possible to introduce the Reynolds number $Re(r_t)$ associated with each scale of turbulence r_t:

$$Re(r_t) = \frac{u_{r_t}(r_t) r_t}{\nu} , \tag{Eq2.53}$$

where ν is the fluid kinematic viscosity and $u_{r_t}(r_t)$ is the characteristic velocity of the motion of size r_t, therefore when r_t corresponds to the largest scale l_t, $Re(r_t) = Re(l_t) = Re_t$, where Re_t is the integral Reynolds number, i.e. the Reynolds number associated with the turbulence integral scales; on the other hand, when r_t corresponds to the Kolmogorov length scale η_k, $Re(r_t) = Re(\eta_k) = Re_k$, where Re_k is the Kolmogorov Reynolds number. Along the energy cascade, the Reynolds number $Re(r_t)$ goes down from Re_t to values close to unity, where inertia and viscous forces balance. This limit determines the smallest scale found in the turbulent flow, the Kolmogorov scale η_k, controlled by viscosity and by the dissipation rate ε of the turbulent kinetic energy k, obtaining the following relationship between integral and Kolmogorov scales [161]:

$$\frac{l_t}{\eta_k} = Re_t^{\frac{3}{4}}. \tag{Eq2.54}$$

The Equation Eq2.54 shows that for high Reynolds numbers there are turbulent structures several orders of magnitude smaller compared to that of the characteristic size of the problem. It may be very expensive in terms of computational cost to solve all scales of turbulence, so three different approaches can be used to treat turbulence, depending on the level of detail desired: RANS, LES, DNS. An example of the difference between the three approaches is shown in Figure 2.3.

With the Reynolds Averaged Navier Stokes (RANS) approach, the governing equations are Reynolds-averaged, losing the information on the instantaneous properties of the flow and resolving the average values of all quantities. The effect of turbulence appears in a non-linear term (the Reynolds stress tensor) that introduces a number of unknowns greater than the number of available equations. Therefore, it is necessary to use a turbulence model for fluid dynamics in combination with a combustion model for the conversion of chemical species, to close the problem.

With the Large Eddy Simulations (LES) approach, large scales of turbulence are solved explicitly, while smaller scales are modelled with closure equations. The idea is to apply a filter, manipulating the balance equations to remove scales smaller than the chosen filter size. In this way, in contrast to the RANS approach, a part of the turbulence (the large scales) is solved, so more accurate results are obtained than the RANS approach, but with an increase in calculation time. Also in this case, the modification of the exact equations introduces a term (the stress tensor of the sub-grid scales) that takes into account the effect of the filtered scales and must be modelled for the closure of the problem.

The approach with the highest level of detail is Direct Numerical Simulations (DNS), where all balance equations written for instantaneous quantities are solved without modification. In this way, all scales of turbulence are solved explicitly and their effects on combustion are captured. This approach, however, is too expensive in the industrial environment for solving engineering problems, since for each physical dimension (including time) the Equation Eq2.54 must be considered in the generation of the computational grid.

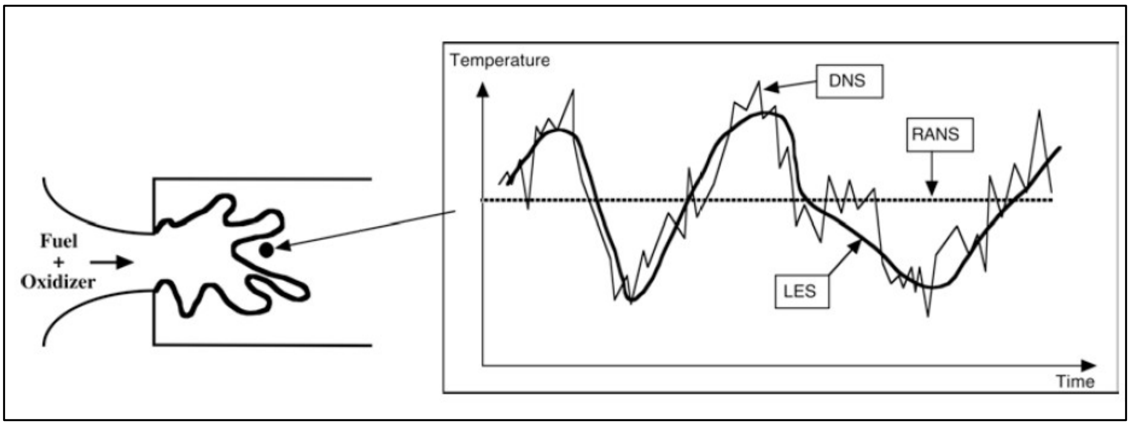

Figure 2.3. Time evolutions of local temperature computed with RANS, LES or DNS in a turbulent flame brush. [162]

In this work, the RANS approach was used, which gives the Reynolds-averaged momentum balance equation the following form (the Einstein summation convention is used):

$$\frac{\partial}{\partial t}(\rho u_i) + \frac{\partial}{\partial x_j}(\rho u_i u_j) = \\ = -\frac{\partial p}{\partial x_i} + \frac{\partial}{\partial x_j}\left[\mu\left(\frac{\partial u_i}{\partial x_j} + \frac{\partial u_j}{\partial x_i} - \frac{2}{3}\delta_{i,j}\frac{\partial u_k}{\partial x_k}\right)\right] + \frac{\partial}{\partial x_j}\left(-\rho\overline{u_i' u_j'}\right), \tag{Eq2.55}$$

where u_i and u_j are the *i*-th and *j*-th Reynolds-averaged velocity component, respectively, and the term $-\rho\overline{u_i' u_j'}$ is the Reynolds stress tensor.

Both the standard $k - \varepsilon$ model and the RNG $k - \varepsilon$ model were used to close the problem. The two models are very similar, they are based on the same assumptions and are described below.

The standard $k - \varepsilon$ model, was proposed by Launder and Spalding [163] and is based on the following assumptions:

- fully turbulent flow, where the effects of molecular viscosity are marginal;
- Boussinesq hypothesis for modelling the Reynolds stress tensor as a function of mean velocity gradients.

Using the Boussinesq hypothesis, the turbulent stress tensor is expressed as the sum of an isotropic and a deviatoric part (where the deviatoric part is modelled in analogy with that of the stress tensor) in the following form:

$$-\rho\overline{u_i'u_j'} = \mu_t\left(\frac{\partial u_i}{\partial x_j}+\frac{\partial u_j}{\partial x_i}\right)-\frac{2}{3}\left(\rho k+\mu_t\frac{\partial u_k}{\partial x_k}\right)\delta_{i,j}\,. \qquad \text{(Eq2.56)}$$

In addition, turbulent viscosity is calculated as:

$$\mu_t = \rho C_\mu\frac{k^2}{\varepsilon}\,. \qquad \text{(Eq2.57)}$$

The six scalar unknowns from the Reynolds stress tensor are reduced to two scalar unknowns, k and ε, and then the following transport equations are written to close the problem:

$$\frac{\partial}{\partial t}(\rho k)+\frac{\partial}{\partial x_i}(\rho k u_i) = \frac{\partial}{\partial x_j}\left[\left(\mu+\frac{\mu_t}{\sigma_k}\right)\frac{\partial k}{\partial x_j}\right]+G_k-\rho\varepsilon\,, \qquad \text{(Eq2.58)}$$

$$\frac{\partial}{\partial t}(\rho\varepsilon)+\frac{\partial}{\partial x_i}(\rho\varepsilon u_i) = \frac{\partial}{\partial x_j}\left[\left(\mu+\frac{\mu_t}{\sigma_\varepsilon}\right)\frac{\partial \varepsilon}{\partial x_j}\right]+C_{1\varepsilon}\frac{\varepsilon}{k}G_k-C_{2\varepsilon}\rho\frac{\varepsilon^2}{k}\,. \qquad \text{(Eq2.59)}$$

where $k=\frac{1}{2}\overline{u_i'u_i'}$ and $\varepsilon=\nu\overline{\frac{\partial u_i'}{\partial x_k}\frac{\partial u_i'}{\partial x_k}}$, with $i,k=1,2,3$ as the indexes associated with the three spatial dimensions; on the other hand, $C_{1\varepsilon}$, $C_{2\varepsilon}$, C_μ, σ_k and σ_ε are constants determined with the assistance of experiments in order to give the model characteristics of validity and universality for a wide range of problems and assume the following values:

$$C_{1\varepsilon}=1.44,\qquad C_{2\varepsilon}=1.92,\qquad C_\mu=0.09,\qquad \sigma_k=1,\qquad \sigma_\varepsilon=1.3\,.$$

The G_k term represents the generation of turbulent kinetic energy due to the mean velocity gradient and is defined as:

$$G_k=-\rho\overline{u_i'u_j'}\frac{\partial u_j}{\partial x_i}\,, \qquad \text{(Eq2.60)}$$

which under the assumption of Boussinesq can be calculated more simply as:

$$G_k = \mu_t S^2, \tag{Eq2.61}$$

where S is the modulus of the mean rate of strain tensor (i.e. the symmetrical part of the Reynolds-averaged velocity gradient tensor), defined as $S \equiv \sqrt{2S_{ij}S_{ij}}$.

Finally, the turbulent thermal conductivity in the energy conservation equation (Eq2.47) takes the form:

$$\lambda_t = \frac{c_p \mu_t}{Pr_t}, \tag{Eq2.62}$$

where Pr_t is the turbulent Prandtl number, set equal to $Pr_t = 0.85$.

The RNG $k - \varepsilon$ model is very similar to the standard one with some differences, including:

- an additional term in the transport equation for ε. Specifically, the term $R_\varepsilon = -\frac{C_\mu \rho \varepsilon^3 \left(1-\frac{\eta}{\eta_0}\right)}{1+\beta_\varepsilon \eta^3}\frac{\varepsilon^3}{k}$ is added to the second member of the transport equation for epsilon (Eq2.59), with $\eta = Sk/\varepsilon,\ \eta_0 = 4.38$ and $\beta_\varepsilon = 0.012$;
- the effect of swirl motion on turbulence. Turbulent viscosity μ_t is calculated as a function of the characteristic swirl number Ω: $\mu_t = \mu_{t0} f(\Omega, \frac{k}{\varepsilon})$, where μ_{t0} is the turbulent viscosity without the swirl modification computed with the Equation Eq2.57.

The values of some constants change with respect to the standard model, in particular:

$$C_{1\varepsilon} = 1.42, \qquad C_{2\varepsilon} = 1.68, \qquad C_\mu = 0.0845\,.$$

Since swirl motion was included in the HCCI model, which will be discussed in detail in section 4.2, the RNG $k - \varepsilon$ model was used, whereas in the Spark Ignition model, where swirl was not considered, the standard $k - \varepsilon$ model was used.

Since in an Internal Combustion Engine (ICE) the fluid is confined by the walls, it must be considered that both the mean velocity field and the turbulence are affected through the no-slip condition that has to be satisfied at the wall. Close to the walls, viscous stresses predominate with respect to turbulent ones, resulting in a region of fluid, the viscous sublayer, in which the flow can be considered laminar. Therefore, close to the walls the assumption of fully turbulent flow, which is necessary to obtain acceptable results with standard and RNG $k - \varepsilon$ models, is not satisfied. To take into account the effect of walls, standard wall functions were used [164], which are a set of semi-empirical formulas and functions that 'link' the thermo-fluid-dynamic properties of the flow with those of the walls.

2.1.5.3 Combustion model

In this work, the Eddy Dissipation Concept (EDC) combustion model was used. This model was proposed by Magnussen [165] and subsequently amended to adapt it to various conditions [166]. The model assumes that fluid can be separated into two regions: a first region where chemical reactions occur (fine-scales), and a second region that is non-reacting (surrounding fluid mixture). The fine-scales are turbulent structures of the same order of magnitude as Kolmogorov's scales. At these scales, the turbulence leads to a mixture of the chemical species at a molecular level, then dissipates its kinetic energy into heat due to viscous forces. From the energy cascade occurring from the large turbulent structures up to Kolmogorov's and consequently the fine-scales [165,167], it follows that the characteristic size of the fine-scales can be related to that of turbulence [168].

The fraction of the region occupied by the fine-scales can be expressed as a dimensionless fine structures length fraction [169]:

$$\gamma^* = \left(\frac{3C_{D2}}{4C_{D1}^2}\right)^{\frac{1}{4}} \left(\frac{\nu\varepsilon}{k^2}\right)^{\frac{1}{4}} = C_\gamma \left(\frac{\nu\varepsilon}{k^2}\right)^{\frac{1}{4}}, \qquad \text{(Eq2.63)}$$

whereas the characteristic time scale of the fine structures (i.e., the mean residence time of the fluid within the fine structures) is expressed as:

$$\tau^* = \left(\frac{C_{D2}}{3}\right)^{\frac{1}{2}} \left(\frac{\nu}{\varepsilon}\right)^{\frac{1}{2}} = C_\tau \left(\frac{\nu}{\varepsilon}\right)^{\frac{1}{2}}, \qquad \text{(Eq2.64)}$$

where C_{D1} and C_{D2} are model constants. In the original version of the model, the constants C_{D1} and C_{D2} are equal to 0.134 and 0.50, respectively. It follows that C_γ and C_τ are equal to 2.1377 and 0.4082, respectively. These values have been assumed on the basis of both theoretical reasoning and experimental data, and represent a compromise in order to extend the range of validity of the model [167]. Recently, some researchers have modified such constants to apply the EDC model to other combustion strategies. For instance, in the case of Moderate or Intense Low-oxygen Dilution (MILD) combustion, Parente et al. [170] modified the original values of the constants C_γ and C_τ. Further, they computed the constants locally as functions of the turbulent Reynolds number and Damköhler number. A similar approach has also been employed by Bao [171].

The term τ^* is the inverse of the mass transfer rate between fine structures (denoted with *) and surroundings (denoted with °), divided by the fine structure mass. A schematic representation of the EDC model is shown in Figure 2.4.

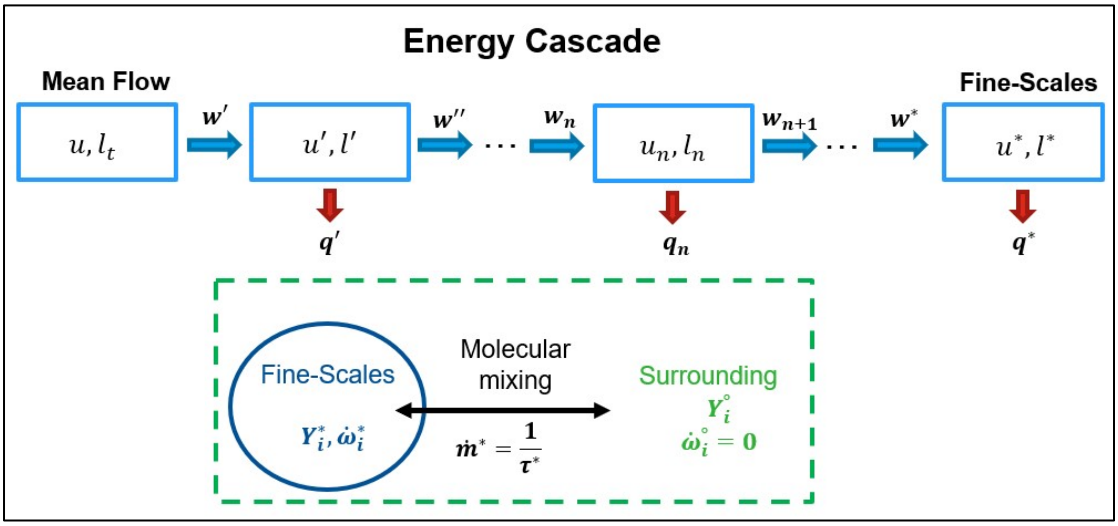

Figure 2.4. Schematic representation of the EDC combustion model. *u*= characteristic velocity of the turbulence structure; *l*= characteristic turbulent dimension; *w*= rate of mechanical energy transfer from a turbulent structure to a smaller one; *q*= rate of dissipation of energy into heat due to viscous forces.

Furthermore, the characteristic quantities of the fine structures (*) and those of the surroundings (°) can be combined together to compute the average flow properties (denoted with an over bar) by using the following equation:

$$\bar{\Phi} = \Phi^\circ[1 - \chi(\gamma^*)^3] + \Phi^*\chi(\gamma^*)^3, \qquad \text{(Eq2.65)}$$

where Φ is a generic fluid property and χ represents a probability that not all the fine structure volumes react. Generally, χ is assumed to be unity.

The mean reaction rate of the species *i* is expressed as:

$$\bar{R}_{rr,i} = \frac{\bar{\rho}\chi(\gamma^*)^2}{\tau^*}\left(Y_i^{\circ} - Y_i^*\right), \qquad \text{(Eq2.66)}$$

where $\bar{\rho}$ is the mean density of the fluid, and Y_i° and Y_i^* are the surrounding and fine structure mass fractions of species i, respectively. By applying Equation Eq2.65 to the species mass fractions, and combining Equations Eq2.65 and Eq2.66, the following expression of the mean reaction rate of i-th species is obtained:

$$\bar{R}_{rr,i} = \frac{\bar{\rho}\chi(\gamma^*)^2}{\tau^*[1-\chi(\gamma^*)^3]}(\bar{Y}_i - Y_i^*), \qquad \text{(Eq2.67)}$$

In the original version of the EDC model, the fine structures are modelled as Perfectly Stirred Reactors (PSRs). However, PSRs should be solved at a steady state to get the composition of the fine structures. To overcome this limitation and save computational time, the fine structures are modelled as Plug Flow Reactors (PFRs), described by the following equations:

$$\frac{dp}{dt} = 0, \qquad \text{(Eq2.68)}$$

$$\frac{dh}{dt} = 0, \qquad \text{(Eq2.69)}$$

$$\frac{dY_i^*}{dt} = \dot{\omega}_i, \qquad \text{(Eq2.70)}$$

and $\dot{\omega}_i$ is the instantaneous net chemical production/consumption rate computed with Equations Eq2.6-2.9. The Equation Eq2.70 is integrated over the characteristic residence time of the fine structures, τ^*, to get Y_i^*. Finally, the term $\bar{R}_{rr,i}$ of Equation Eq2.67 is included in the Reynolds-averaged transport equation of the i-th species:

$$\frac{\partial}{\partial t}(\bar{\rho}\bar{Y}_i) + \vec{\nabla}\cdot(\bar{\rho}\vec{u}\bar{Y}_i) = -\vec{\nabla}\cdot\vec{J}_i + \bar{R}_{rr,i}\,, \qquad \text{(Eq2.71)}$$

and in the source term of Reynolds-averaged energy equation:

$$\bar{S}_{h,rxn} = -\sum_i \frac{h_i^0}{M_i}\bar{R}_{rr,i}\,. \qquad \text{(Eq2.72)}$$

2.2 Numerical methods

The following section describes the numerical methods used for the simulations of the different phenomena taken into account. For the parametric analyses on the Laminar Flame Speed (LFS), all the kinetic mechanisms presented in section 2.1.1.2 were investigated, also to understand the differences and accuracies of the different mechanisms chosen and coupled with ozone and nitrogen oxides sub-mechanisms. The 0-D simulations concerning the compression stroke of the engine were carried out with the most detailed kinetic mechanism, i.e. the one called 'CurranModif' in section 2.1.1.2.

The CFD analyses, on the other hand, were only carried out with the mechanism called "YooModif" in section 2.1.1.2. The motivation is that since the EDC combustion model was used, the calculation times would have been too high if an excessive detailed mechanism had been used. However, as discussed in the chapter on model validation, the modified Yoo mechanism was also valid for the analyses performed.

The simulations for the calculation of the LFS and IDT were carried out by using Chemkin-Pro solver within Ansys® Academic Research CFD package, Release 20.1 [172]. Simulations of the compression stroke of the 0-D engine were carried out with the REC-2000 software [173] used in 0-D configuration. Finally, CFD calculations of the engine were performed by using Fluent solver within Ansys® Academic Research CFD package, Release 20.1 [174].

2.2.1 Numerical methods for 1-D and 0-D simulations

For the Laminar Flame Speed (LFS) calculation a one-dimensional domain of length 10 cm was considered. As regards boundary conditions, the pressure, temperature, and composition of the mixture were given at the cold boundary, whereas, the zero-gradient condition was set at the hot boundary. A first guess-value value was set for both the flame position, by defining an initial temperature profile, and the mass flow rate. The governing equations (Eq2.1-2.4) were discretized by using first order and second order finite differences for the convective and diffusive terms, respectively, and iteratively solved. The computational grid was dynamically adaptive. The numerical domain was discretized into a number of grid points and this number increased till specific criteria on the flow gradients and curvature of the numerical solution were satisfied. In particular, the criteria for each point *j* of the mesh were:

$$\left|\zeta_{n,j} - \zeta_{n,j-1}\right| \leq \delta_{grad}(\max\zeta_n - \min\zeta_n)\,, \tag{Eq2.73}$$

$$\left|\left(\frac{d\zeta_n}{dx}\right)_j - \left(\frac{d\zeta_n}{dx}\right)_{j-1}\right| \leq \gamma_{curv}\left(\max\frac{d\zeta_n}{dx} - \min\frac{d\zeta_n}{dx}\right), \tag{Eq2.74}$$

where ζ_n is the *n*-th component of the unknowns vector $\vec{\zeta}$, and δ_{grad} and γ_{curv} are user-specified parameters. If Equations Eq2.73-2.74 were not satisfied between two subsequent grid points, then a new grid point was added at the midpoint of such subinterval, and a new iteration was carried out. Absolute and relative tolerance values of 10^{-9} and 10^{-4}, respectively, were chosen for the converged solution. The computation was carried out with several successive continuations: starting with fairly high values of δ_{grad} and γ_{curv}, the solution of a previous continuation was assumed to be the starting condition for a new continuation with smaller values of δ_{grad} and γ_{curv} and so on.

The computational time is strongly dependent on the values of δ_{grad} and γ_{curv}, and on the number of species and chemical reactions of the mechanism. For the mechanism of methane, with a relatively low number of species and reactions, the minimum values of δ_{grad} and γ_{curv} were set to 0.01 and 0.05, respectively. For the iso-octane mechanisms, in order to reduce the computational time, the values of δ_{grad} and γ_{curv} were slightly increased compared to the methane case and are set to 0.035 and 0.075, respectively. Finally, for all computations, the minimum time-step was $10^{-10}s$. With these settings, the numerical method converged for all cases. The difference between the converged solution, in terms of LFS, and the solution of the previous continuation was within 1% and 1.5% for the simulations with methane and iso-octane, respectively, for all the selected thermodynamic conditions.

Regarding the calculation of the Ignition Delay Time (IDT), IDT was defined as the time when the slope of the temperature profile reaches its maximum value:

$$IDT = t : \max\left\{\frac{dT(t)}{dt}\right\}. \tag{Eq2.75}$$

The iso-octane/air/ozone kinetic reaction mechanism called “YooModif” and presented in section 2.1.1.2 was used, since the validation of the kinetic model with ozone addition was carried out with CFD simulations on experimental measurements of pressure traces in an HCCI engine (by using only the “YooModif” kinetic mechanism for the reasons discussed above). A 2-second-long simulation was considered with a backward-differencing method for the time integration. For the solution convergence, a relative tolerance of 10^{-8} was imposed.

0-D engine calculations covered the mixture evolution from Intake Valve Closing (IVC) to Spark Advance (SA), considering the engine geometric characteristics of a test case [175] and presented in Table 2.2, used to calculate the law of volume variation. The numerical time-step was set to 0.006 Crank Angle Degree (CAD).

Table 2.2. Reference engine specifications for 0-D and 2-D SI Engine simulations. [175]

Bore	79 mm
Stroke	81.3 mm
Rod length	143 mm
Displaced Volume	399 cc
Geometric compression ratio (CR)	10:1
Intake Valve Closure (IVC)	144 CAD BTDC
Exhaust Valve Opening (EVO)	153 CAD ATDC
Spark Advance	3 CAD BTDC
Engine Speed	1000 rpm

2.2.2 Numerical methods for engines CFD Simulations

CFD simulations were conducted by using two axial-symmetrical geometries, developed considering the main geometric characteristics of two reference engines taken from the scientific literature [175,107]. Closed-valve numerical simulations were carried out: started at Intake Valve Closing (IVC) and ended at Exhaust Valve Opening (EVO). The choice to simulate only the closed-valve phase with 2-D axial-symmetric geometries was necessary in order to have acceptable computational times considering the use of the EDC combustion model. Indeed, the EDC model solves the chemical kinetics in detail in each computational cell and at each numerical time-step, integrating the Equations Eq2.68-2.70 with the initial conditions relative to the specific computational cell at that time. In this way, it was possible to simulate the thermo-fluid-dynamic evolution of the mixture with ozone addition by solving the chemistry in detail in each temperature range.

The geometric characteristics of the engine for Spark Ignition applications are the same presented in Table 2.2 [175] for 0-D engine simulations, while the computational domain is shown in Figure 2.5.

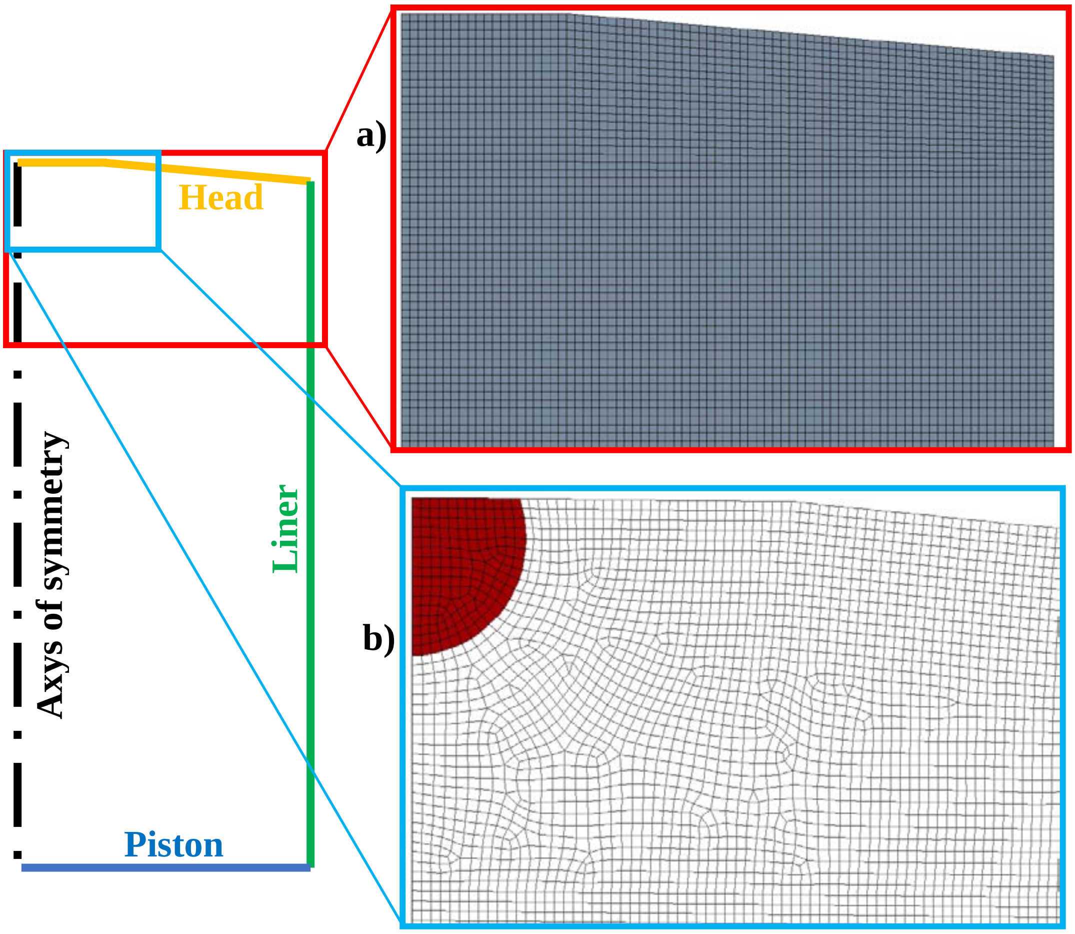

Figure 2.5. Computational domain and grid blow-up for 2-D SI engine simulations: a) mesh for the IVC-SA simulations; b) mesh for the IVC-EVO simulations, red area represents the spark zone.

As shown in Figure 2.5, a flat piston and a truncated cone-shaped head were considered, while two different computational grids were generated. The calculations involving only the compression phase (IVC-SA), which were aimed to identify the mixture composition and thermodynamic conditions at the ignition timing for LFS calculations, were carried out by using the grid in Figure 2.5(a). On the other hand, the simulations of the closed-valve cycle (IVC-EVO) with combustion were carried out with a higher resolution in order to more accurately simulate the flame propagation in the chamber. The ignition model consisted of a temperature increase in the spark zone, i.e. where the spark plug was assumed to be located (red area in Figure 2.5(b). Only at ignition time, the temperature in the spark zone was increased to 2800 K, then combustion (with flame formation and propagation) evolved with chemical reactions according to the EDC combustion model.

The grid in Figure 2.5(a) was completely structured and uniform, consisting of quadrilateral elements with a nominal cell size of 0.5 mm. The numerical domain, at IVC, consisted of 13,667 numerical cells and 13,920 grid points. On the other hand, the grid in Figure 2.5(b) was structured and uniform, with the exception of a few cells in the TDC volume to adapt the circular region to the spark zone boundary. The numerical domain, at IVC, consisted of 53,181 numerical cells and 53,671 grid points and was generated by imposing an average cell size equal to 0.25 mm. The minimum value of orthogonal quality was 0.82, while the maximum value of skewness was 0.43, however these values were only relative to approximately ten cells, in fact the average values were 0.9997 and 0.003 for orthogonal quality and skewness, respectively.

The main engine characteristics for HCCI applications are given in Table 2.3 [107] and the computational grid at 30 CAD BTDC is shown in Figure 2.6.

Table 2.3. Reference engine specifications for 2-D HCCI Engine simulations. [107]

Bore	85 mm
Stroke	88 mm
Rod length	145 mm
Displaced volume	499 cc
Geometric compression ratio (CR)	16:1
Intake valve closure IVC	157° BTDC
Exhaust valve opening EVO	140° ATDC
Engine Speed	1500 rpm

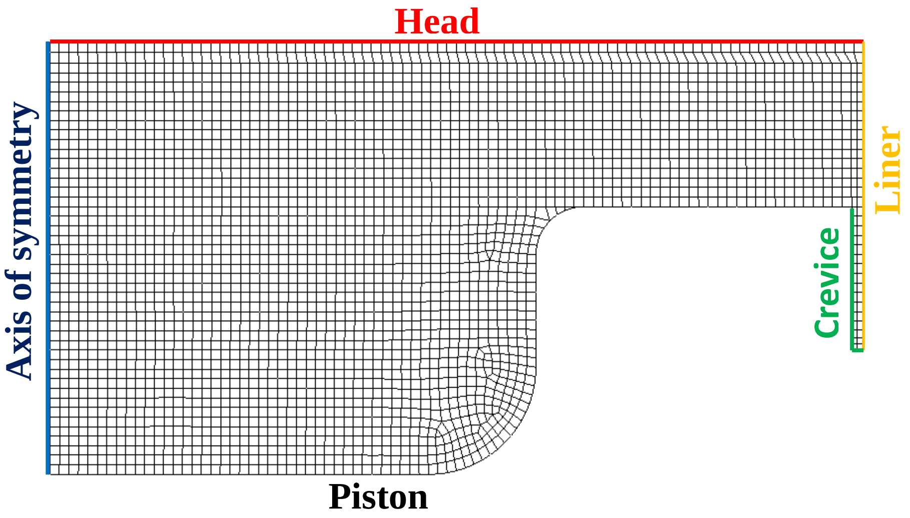

Figure 2.6. Computational grid at 30 CAD BTDC for 2-D HCCI engine simulations.

As shown in Figure 2.6, since the engine of the test case [107] was a PSA DW10 Diesel engine, a cup in the piston was considered, while the head was considered flat. A crevice volume equal to 3.46% of the TDC volume was also considered. Based on the chamber's geometry, the grid employed between the head of the piston and the cylinder head was fully structured by using quadrilateral elements, whereas differently shaped elements were used to adapt to the piston bowl profile. The numerical domain, at the IVC, was composed of 16,346 numerical cells and 16,645 grid points and was generated by imposing an average cell size equal to 0.5 mm. The crevice, with a thickness of 0.6 mm, consisted of two rows of 0.3-mm numerical cells to guarantee a good accuracy. The minimum value of orthogonal quality was 0.16, while the maximum value of skewness was 0.84. However, these values occur in only one cell, which is located on the fitting between the top and the piston cup. The average values were 0.9998 and 0.003 for orthogonal quality and skewness, respectively.

The resolution of the grids was chosen to ensure both acceptable calculation times and acceptable values of y^+ on the wall boundaries for the use of wall functions. Specifically, the aim was to have $y^+ \geq 15$ for the wall-adjacent cell, in order to have the second wall-distant cell within the fully turbulent region. However, due to the non-stationarity and complexity of the phenomena occurring in the combustion chamber, it was very difficult to control the y^+ at all times and in every wall-adjacent cell. For the mean velocity law at the wall, the value of $y^* \equiv \frac{\rho C_\mu^{1/4} k_{wc}^{1/2} y_{wc}}{\mu}$ was evaluated, where k_{wc} is the turbulence kinetic energy at the wall-adjacent cell centroid and y_{wc} is the distance from the centroid of the wall-adjacent cell to the wall. Specifically, for $y^* < 11.225$, the laminar stress-strain relationship was applied; on the other hand, for $y^* \geq 11.225$, the log-law was employed.

Furthermore, for both geometries the grid motion was carried out by means of a layering technique. Specifically, the mesh was modified by adding or removing cell layers adjacent to a moving boundary using the following relationships:

$$h_{cell} < \alpha_c h_{ideal} \,, \tag{Eq2.76}$$

$$h_{cell} > (1 + \alpha_s) h_{ideal} \,, \tag{Eq2.77}$$

where h_{cell} is the cell height corresponding to the layer to be added/removed (which is a function of the spatial increment for each time-step), h_{ideal} is the ideal (imposed) cell height, α_c and α_s are two constants called split factor and collapse factor, respectively.

During the compression phase, the height h_{cell} of the wall-adjacent cell layer is reducing and when the Relationship Eq2.76 is satisfied the boundary layer is merged with the second-last one, generating a new boundary layer of height $h_{cell} + h_{ideal}$. During the expansion phase, on the other hand, the height of the wall-adjacent cell layer increases and when the Relationship Eq2.77 is satisfied, the layer of height h_{cell} is divided into two layers: the inner with height h_{ideal} and the other with height $h_{cell} - h_{ideal}$. The constants α_c and α_s were set equal to 0.2 and 0.4, respectively. For all grids shown, layering was performed within the TDC volume.

Since the motion field at IVC is turbulent due to the intake phase, which has not been simulated, the following semi-empirical formulations were used to account the initial values of the turbulent kinetic energy k and its dissipation rate ε:

$$k = \alpha_{IVC} \left(\frac{A_{pist}}{A_{in}} \right)^2 \frac{\bar{u}_p^2}{(\Delta\theta_{\mathrm{in}})^2} \,, \tag{Eq2.78}$$

$$\varepsilon = \beta_{IVC} \left(\frac{A_{pist}}{A_{in}} \right)^3 \frac{\bar{u}_p^3}{(\Delta\theta_{\mathrm{in}})^3} \frac{1}{\sqrt{A_{in}}} \,, \tag{Eq2.79}$$

where α_{IVC} and β_{IVC} are constants equal to 0.0762 and 0.0294, respectively; $\Delta\theta_{in}$ is the angle, in radians, during which the intake valve remains open; and A_{pist} and A_{in} are the piston area and the maximum open intake area, respectively.

A time-dependence analysis was also carried out for the numerical time-step for all cases. For simulations concerning the compression phase only (Figure 2.5(a)), a numerical time-step of 0.5 CAD was used. For HCCI simulations, a value equal to 0.1 CAD was used, with the exception of the range from 80 CAD BTDC to 40 CAD ATDC when the time step was set to 0.01 CAD to improve the numerical accuracy at the end of the compression stroke and during combustion. Finally, the following numerical time-steps were used for closed-valve SI simulations:

- 0.1 CAD from IVC to SA, because during compression of an SI engine, temperatures are relatively low and chemical kinetics are minor;
- 10^{-4} CAD from SA for a period of 1000 time-step, because at SA ignition is simulated with the temperature rise in the spark zone, so the gradients are very high and a very low time-step is required to ensure convergence;
- 10^{-3} CAD for the next 1000 time-step, because after the previous 1000 time-steps it was possible to increase the time increment ensuring convergence and without losing accuracy;
- 10^{-2} CAD during combustion, up to 80 CAD ATDC;
- 0.125 CAD from 80 CAD ATDC to EVO, because in this range of the expansion phase, combustion is over and the flame is extinguished.

The solution convergence was ensured by checking the absolute globally scaled residuals (for more details see the User's Guide of the software [174]), set equal to 10^{-6} for energy, and 10^{-3} for the other quantities. Pressure-Implicit with Splitting of Operators (PISO) algorithm was used for pressure-velocity coupling. A spatial second-order upwind discretization and a first order implicit scheme for transient discretization were used. Least squares cell-based method for the gradient evaluation was used and chemistry was solved by direct integration.

3. Chapter 3: Investigation of ozone assisted combustion

This chapter will discuss the results of the simulations concerning the study of the chemical kinetics of ozone-assisted combustion. These analyses concerned: the calculation of the Laminar Flame Speed (LFS); the Ignition Delay Time (IDT) calculation; the study of flame structure and chemical kinetics under stationary and transient conditions.

3.1 Ozone effect on the laminar flame speed of methane/air and iso-octane/air mixtures

The aim of the following analyses was to provide a comprehensive investigation of the influence of ozonized air on the LFS of iso-octane and to highlight differences and similarities of such a fuel with respect to methane by using one-dimensional numerical simulations. Indeed, differently to methane, no experiments on iso-octane LFS in ozonized air have been found in the scientific literature, so this numerical investigation may be useful to understanding the ozone effects in this kind of mixture.

Combustion with ozone was investigated for different equivalence ratios and for a wide range of temperatures and pressures, since ozone may have a different impact on the combustion process depending on the chemical composition of the fuel/air mixture and on the thermodynamic conditions. In addition, three iso-octane reaction mechanisms, presented in section 2.1.1.2, have been considered, in order to assess if, with ozone addition, they provide the same results.

At first the model has been validated against experimental data, then several simulations have been performed, for both methane and iso-octane as fuels, by varying ozone concentrations, temperature, pressure and equivalence ratio of the fresh mixtures from 2330 to 7000 ppm referred to oxygen, from 300 K to 700 K, from 1 bar to 20 bar, and from 0.6 to 1.4, respectively.

3.1.1 Model validation

For methane as a fuel, the validation has been carried out against experimental data, both in absence of ozone [39,40,45,138,139,146,147] and with the addition of ozone [40]. On the other hand, for iso-octane as a fuel, the model has been validated against available data obtained in absence of ozone [140,176-183], since, in the literature, there are no data in terms of LFS for $C_8H_{18}/Air/O_3$ mixtures.

3.1.1.1 Methane

Figure 3.1 shows the numerical results obtained in terms of LFS for methane/air mixtures as a function of the equivalence ratio ϕ under ambient conditions (1 bar, 300 K), compared with several measurements. The figure shows that the model is able to reproduce the experimental data with a very good accuracy in the entire range of equivalence ratio from 0.6 to 1.4.

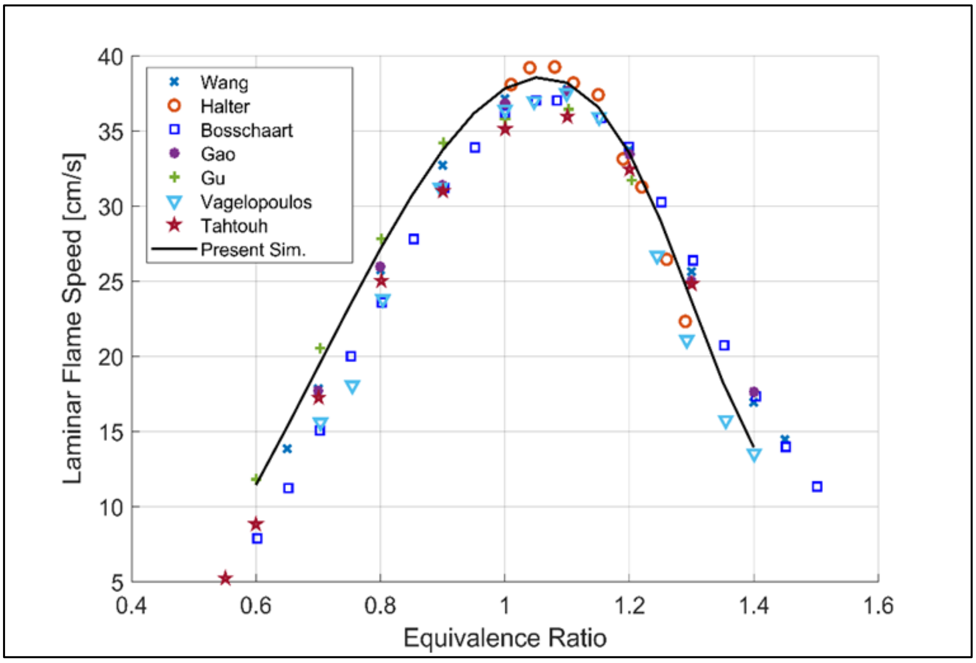

Figure 3.1. Comparison between experimental [39,40,45,138,139,146,147] and numerical results in terms of LFS vs equivalence ratio for CH_4/Air mixtures at ambient conditions (1 bar, 300 K).

The model validation with ozone addition has been carried out against the data of Wang *et al.* [40], who measured, at ambient conditions, the LFS of a mixture of methane, air and ozone with different concentrations of ozone in oxygen, i.e. 2330, 3730, 5130 and

7000 ppm. The comparison between the numerical results and measurements is shown in Figure 3.2(a) as a function of the equivalence ratio. Figure 3.2(b) shows the comparison in terms of the LFS relative enhancement defined as:

$$\varepsilon_{LFS} = \frac{S_{L_{X_{O_3}}} - S_{L_0}}{S_{L_0}}, \tag{Eq3.1}$$

where S_{L_0} is the LFS in absence of O_3, and $S_{L_{X_{O_3}}}$ is the LFS with X_{O_3} ppm of ozone addition.

Figure 3.2 shows that the simulations are able to provide the trends observed in the experiments. The maximum measurement uncertainty in the experiments in Figure 3.2(a) is about 0.8 cm/s and occurs at $\phi = 0.65$ for the case without ozone. As the ozone concentration increases, there is an increase of the LFS for all the equivalence ratios. The LFS enhancement is mostly within the range of the measurement uncertainty for all equivalence ratios. As shown in Figure 3.2(b), the simulations under-predict the LFS enhancement for both 2330 and 3730 ppm cases with $\phi = 1.4$ and for 3730 ppm case with $\phi = 0.65$. The differences between the simulations and the measurements are likely due to the kinetic mechanism. A similar trend is also found by Wang *et al.* [40].

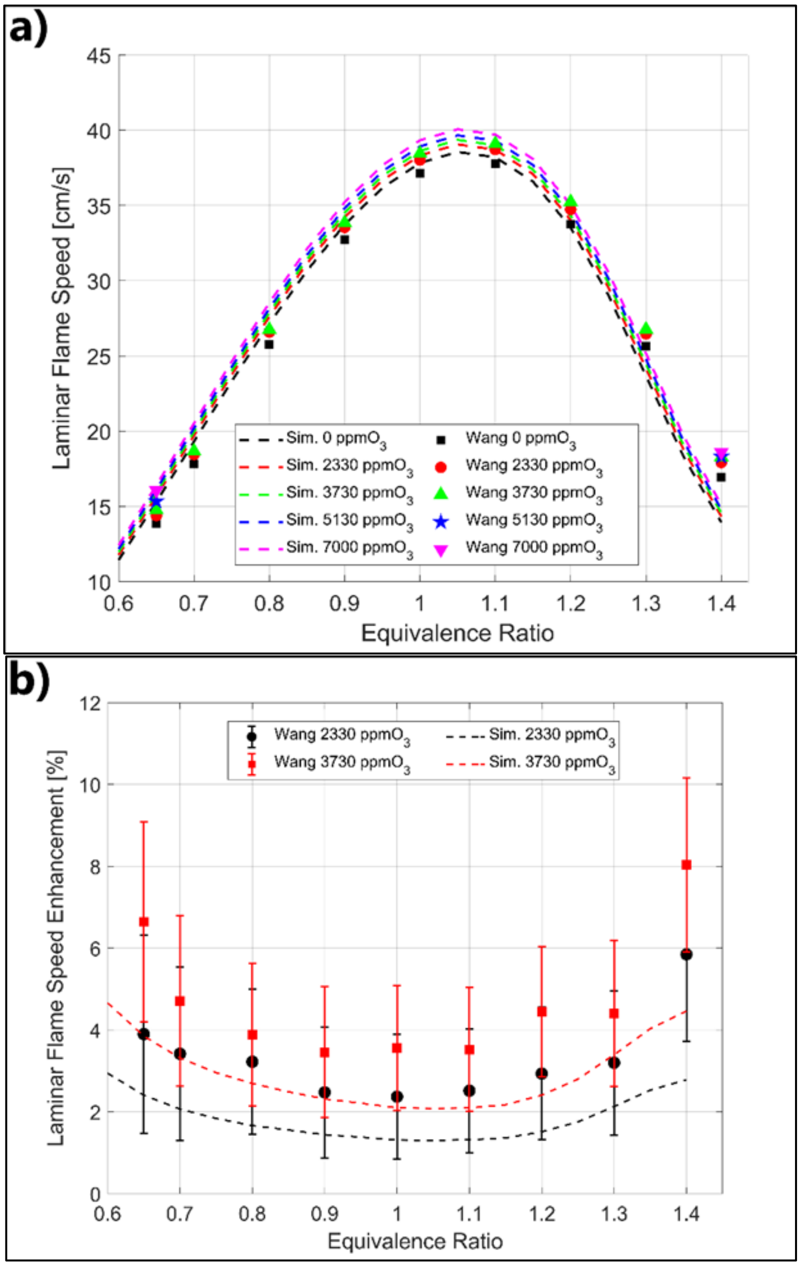

Figure 3.2. Comparison between experimental [40] and numerical results in terms of: a) LFS vs equivalence ratio; b) LFS relative enhancement vs equivalence ratio for $CH_4/Air/O_3$ mixtures at ambient conditions (1 bar, 300 K) with different O_3 concentrations.

3.1.1.2 Iso-octane

The three reaction mechanisms for iso-octane are validated by comparing the numerical results, in terms of LFS, with measurements available in the scientific literature for mixtures of iso-octane and air with different equivalence ratios, since experimental results with mixtures of iso-octane and ozonized air are not available in the literature.

Figure 3.3 shows the comparison between the numerical results in terms of LFS and the experimental data available in the literature [140,176-183], as a function of equivalence ratio, both at ambient conditions and considering higher values of pressure and temperature. The results show that the three mechanisms are able to accurately reproduce the experimental data at ambient conditions for all the equivalence ratios. The results at $p = 5\ bar$ fall in the experimental data range for $\phi < 1.1$, but for higher equivalence ratios, the simulations underestimate the LFS measured by Mandilas *et al.* [183]. Besides, compared to ambient conditions, a larger dispersion of the numerical results is observed, depending on the specific reaction mechanism. Under stoichiometric conditions, at $p = 1\ bar$ and $T = 300\ K$ a LFS between 34.34 and 34.89 cm/s is obtained for all the three mechanisms, whereas at $5\ bar$ and $355\ K$ the LFS varies from 27.45 cm/s, with the modified Yoo mechanism, to 31.49 cm/s, with the modified Cai&Pitsch mechanism.

The numerical results at 25 bar and 373 K are compared with the experimental data of Jerzembeck *et al.* [140] and are shown in Figure 3.3(c). A good match of the simulated results with the experimental data is observed, except for rich mixtures. Specifically, for $\phi < 0.8$ all the three mechanisms provide values of the LFS within the uncertainty range of the measurements. For higher equivalence ratios, the modified Yoo mechanism underestimates the LFS and for $\phi = 1.2$ all the three mechanisms underestimate the LFS between 11% and 27%.

In summary, the modified mechanisms are able to provide a LFS which is comparable to that observed in the measurements, even under high pressure conditions, for lean and stoichiometric mixtures, which are the conditions of interest for SI engines.

LFS sensitivity analyses have also been carried out for the three mechanisms at room conditions (1 bar, 300 K) for lean, stoichiometric and rich mixtures without ozone addition. Figure 3.4 shows the main LFS sensitivity coefficients, for each mechanism and equivalence ratio. The sensitivity analysis shows very similar results for the modified Curran and Yoo mechanisms for each equivalence ratio. On the other hand, for the modified Cai&Pitsch mechanism, LFS is more affected by reactions that are less important for the other two mechanisms. However, for all the three mechanisms, LFS shows large sensitivity to the kinetics of the main chain-branching reaction, $H + O_2 \rightleftarrows$

$O + OH$. The reactions $H + O_2\ (+M) \rightleftarrows HO_2\ (+M)$, $CO + OH \rightleftarrows CO_2 + H$ and $CH_3 + H\ (+M) \rightleftarrows CH_4\ (+M)$ also have a significant role for all the three mechanisms.

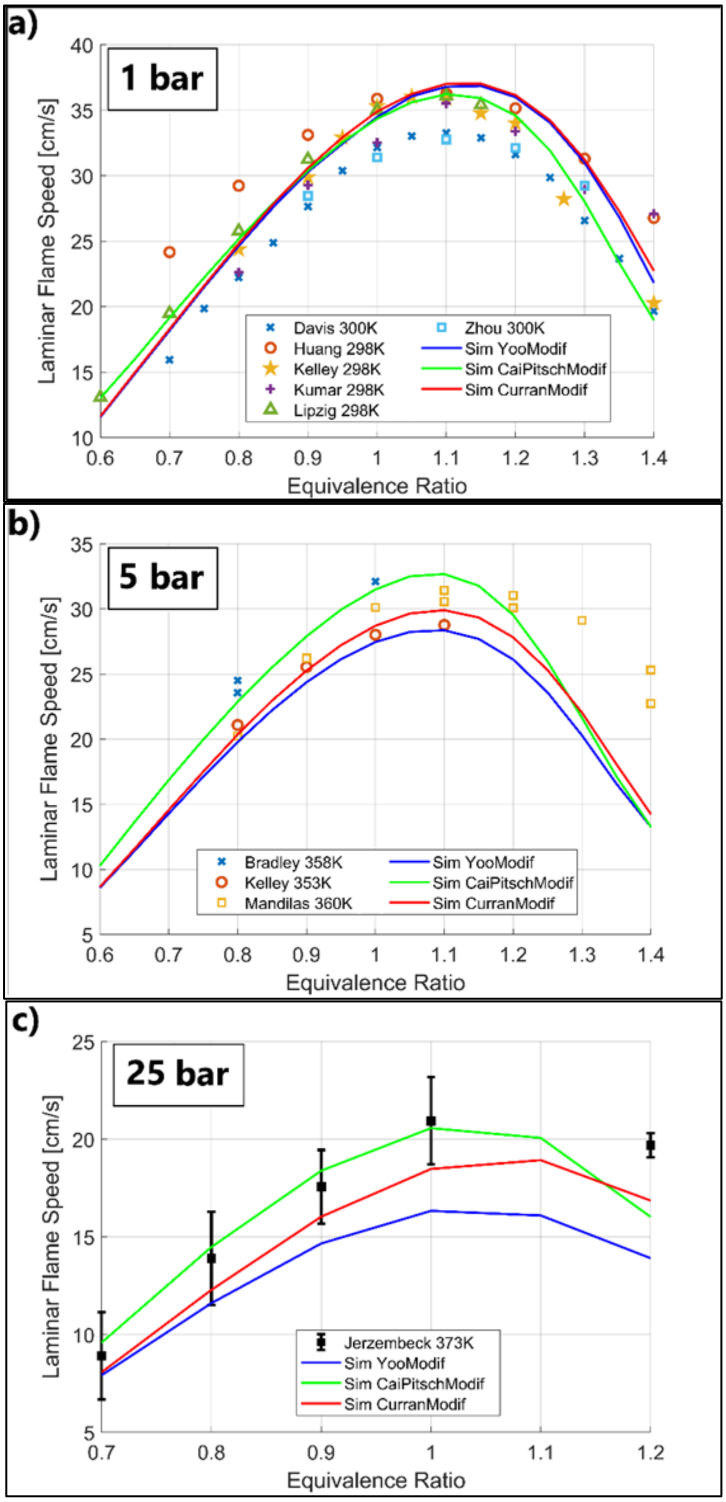

Figure 3.3. Comparison between experimental [140,176-183] and numerical results in terms of LFS vs equivalence ratio for C_8H_{18}/Air mixtures at: a) 1bar, 300 K; b) 5 bar, 355 K; c) 25 bar, 373 K. For the experimental data, the mixture temperature is given in the legend.

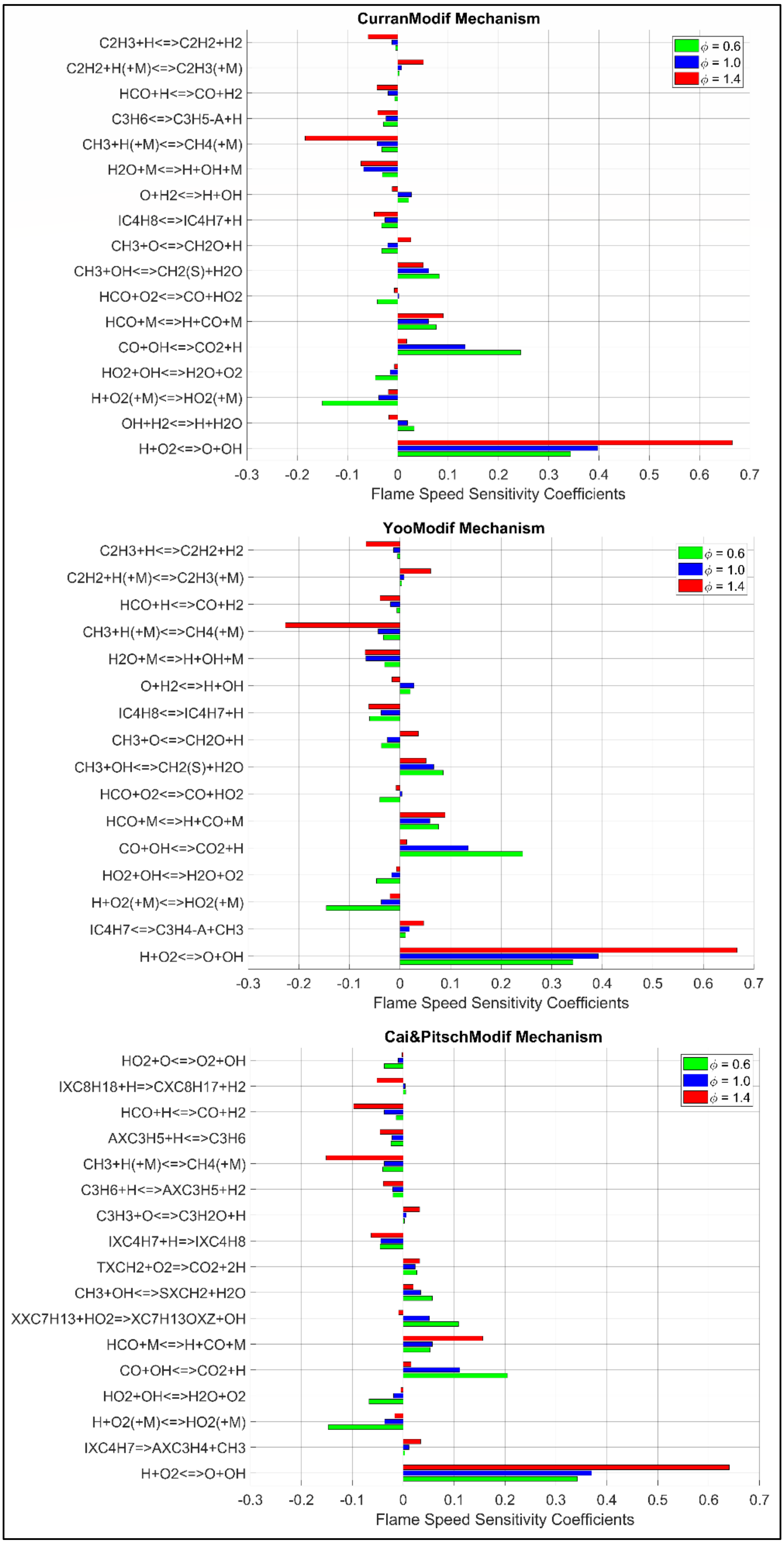

Figure 3.4. LFS sensitivity coefficients for the modified Curran, Yoo and Cai&Pitsch mechanisms at 1 bar, 300 K and for three different equivalence ratios.

3.1.2 LFS for iso-octane/air/ozone mixtures

The same thermodynamic conditions used for methane in section 3.1.1.1 are considered for iso-octane/air/ozone mixtures, such that a direct comparison between the two fuels can be carried out. Figure 3.5(a) shows the LFS, obtained with the modified Curran mechanism, as a function of equivalence ratio. With increasing ozone concentrations, an increase in the LFS is observed for all investigated equivalence ratios. This trend is also observed by the other two reaction mechanisms and, for the sake of conciseness, is not shown.

The relative enhancement of the LFS obtained with 2330 and 7000 ppm O_3 is shown in Figure 3.5(b) for both iso-octane and methane by using all the selected kinetic mechanisms. The results show that the trends are the same for both methane and iso-octane, and are in agreement with the experimental data [40], available only for methane (Figure 3.2(b)). The relative enhancement of the LFS increases with ozone concentration, especially for lean and rich mixtures, whereas a lower benefit is observed under near-stoichiometric conditions.

As regards iso-octane, the three reaction mechanisms give similar results, especially for lean mixtures and with lower ozone concentration. With the addition of 2330 ppm O_3, for all equivalence ratios, the values of the LFS enhancement with the three iso-octane reaction mechanisms differ by less than 0.4%. For 7000 ppm O_3 concentrations, the maximum difference is less than 0.5% for $\phi < 1.3$, while at $\phi = 1.4$ the relative enhancement ranges from about 6% with the modified Curran mechanism to about 8% with the modified Cai&Pitsch mechanism.

Moreover, for 2330 ppm ozone concentration, the results show that for $\phi < 1.1$ the LFS enhancement for methane is comparable to that for iso-octane, whereas, for higher equivalence ratios, the maximum enhancement is obtained with methane. For higher ozone concentrations, the LFS enhancement obtained for methane is very close to that obtained with the modified Cai&Pitsch mechanism for iso-octane, except for low equivalence ratios.

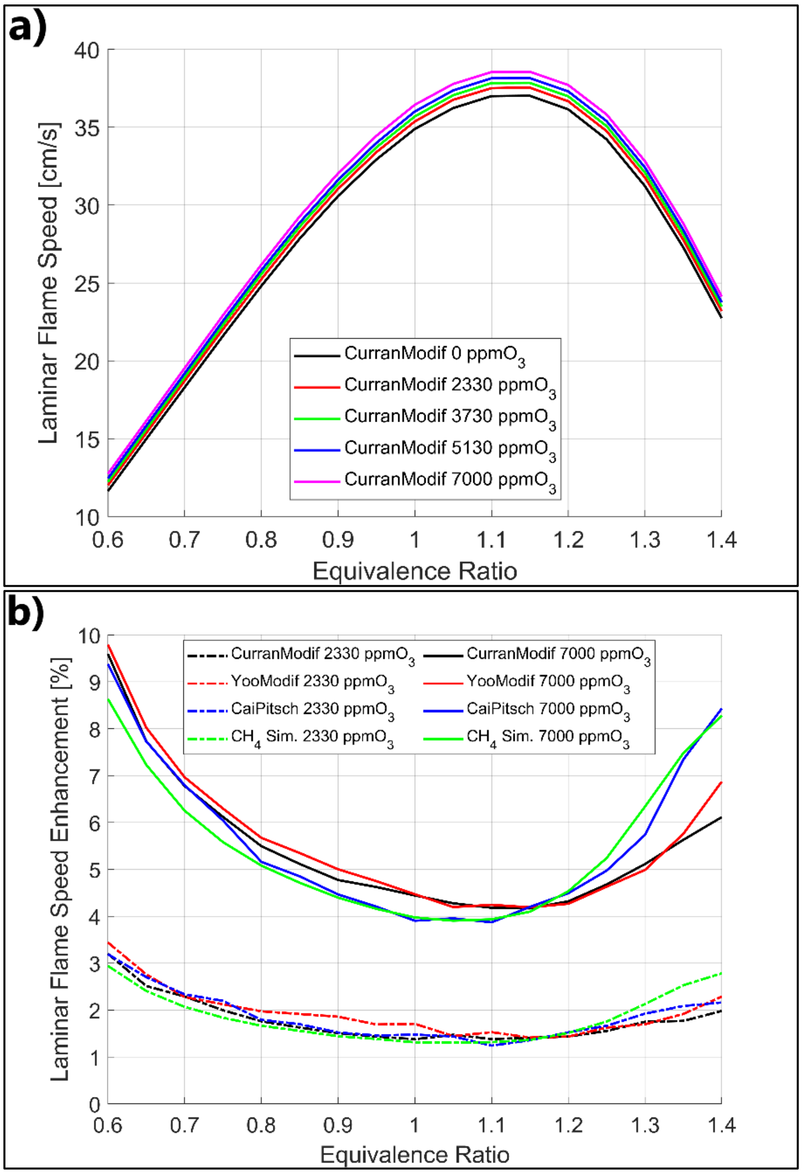

Figure 3.5. Numerical results in terms of LFS vs equivalence ratio at ambient conditions (1 bar, 300 K): a) LFS (with the modified Curran mechanism) for $C_8H_{18}/Air/O_3$ mixture; b) LFS relative enhancement for $C_8H_{18}/Air/O_3$ and for CH_4Air/O_3 mixtures.

LFS increases linearly with ozone concentration for both methane and iso-octane mixtures, as shown in Figure 3.6, where three equivalence ratios, i.e. 0.6, 1 and 1.4, are considered. By using a linear fit, the following expression can be written:

$$S_{L_{X_{O_3}}} = S_{L_0} + \alpha_{S_L} X_{O_3}\,, \qquad \text{(Eq3.2)}$$

where X_{O_3} is the ozone concentration. The α_{S_L} coefficients for all cases are also given in Figure 3.6, with LFS given in cm/s and ozone concentration in thousands of ppm.

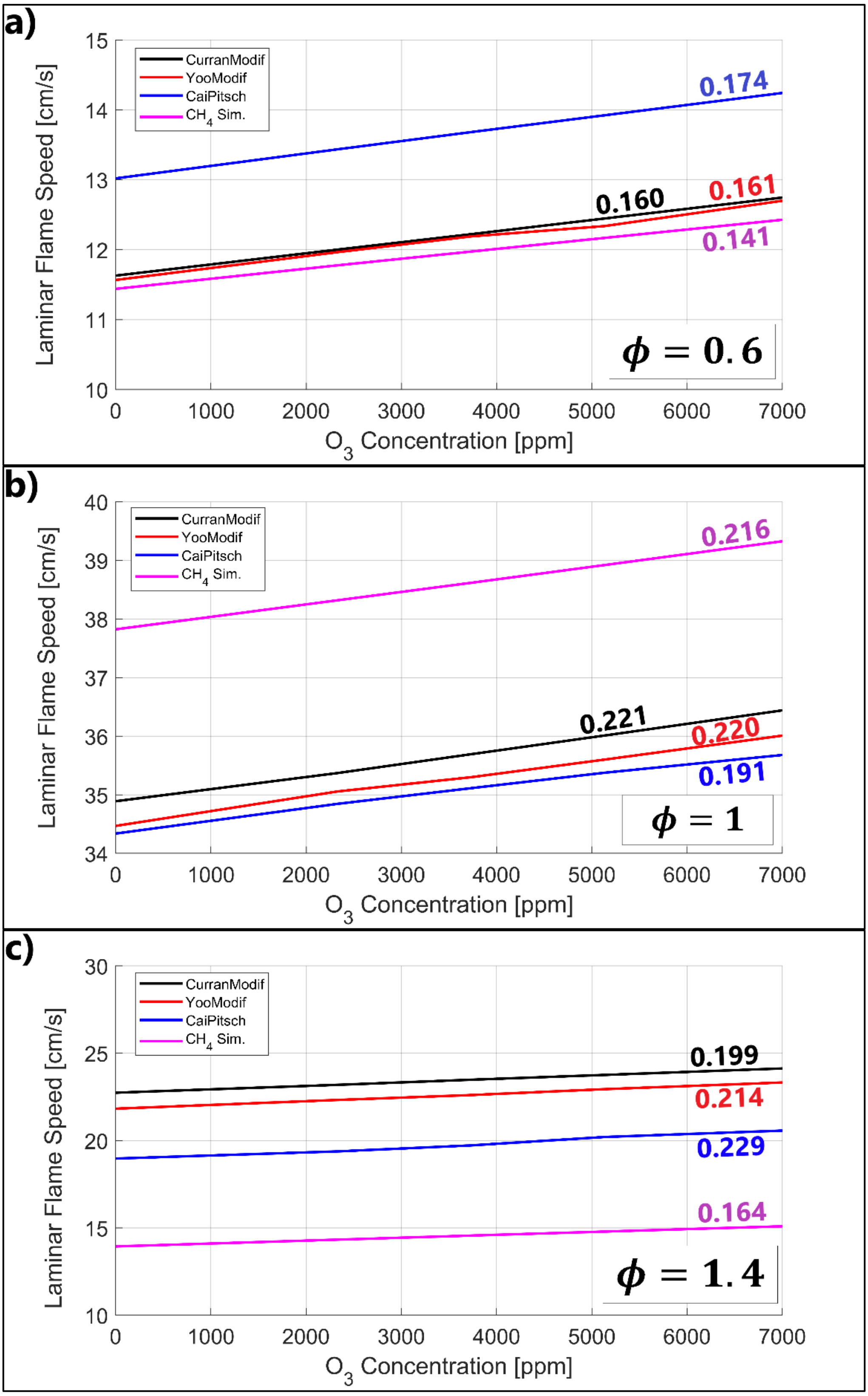

Figure 3.6. Numerical results in terms of LFS vs ozone concentration for $C_8H_{18}/Air/O_3$ and $CH_4/Air/O_3$ mixtures at ambient conditions (P=1 bar, T=300 K) and for different equivalence ratios, with α_{S_L} coefficients expressed in cm/(s*1000ppm$_{O_3}$): a) $\phi = 0.6$; b) $\phi = 1$; c) $\phi = 1.4$.

The highest value of α_{S_L} is obtained under stoichiometric conditions for all mechanisms except for the modified Cai&Pitsch mechanism, which predicts a maximum value at $\phi = 1.4$. The lowest α_{S_L} values are observed in the case of methane for both lean and rich mixtures, whereas under stoichiometric conditions α_{S_L} values are comparable for the two fuels. For iso-octane mixtures, the influence of the addition of ozone on the absolute speed enhancement is significantly lower for lean mixtures with respect to stoichiometric and rich mixtures.

3.1.3 Influence of mixture temperature

Simulations are carried out by varying by 20 K the temperature of the reactant mixture, in the range 300 - 700 K, with the aim of investigating the case of ozonized air at higher temperatures, which are of interest for SI engines. Such simulations have been carried out by setting the equivalence ratio to 1 and the pressure to 1 bar.

Figure 3.7(a) shows the LFS of $CH_4/Air/O_3$ mixtures as a function of reactants temperature for different ozone concentrations. Figure 3.7(b) and Figure 3.7(c) show the absolute and relative LFS enhancement, respectively. As expected, the results show that the LFS increases with temperature for all cases, and that this trend is enhanced by adding ozone to the mixture. By increasing the temperature in the range 300-540 K, the absolute value of the LFS enhancement for the cases with ozone (Figure 3.7(b)) increases linearly with a slope that is proportional to the ozone concentration; above 540 K ozone addition has a stronger effect and the slope of the profiles increases the greater the ozone concentration.

As regards the relative LFS enhancement (Figure 3.7(c)), in the range 300-520 K, for a given ozone concentration, the relative LFS enhancement slightly decreases with increasing temperature, whereas for temperatures in the range 520-680 K the relative enhancement increases with temperature and, finally, over about 680 K it approaches a constant, temperature-independent value. This trend indicates that, as long as the temperature is relatively low, ozone addition has a minor effect with respect to the increase of temperature; starting from about 520 K, instead, ozone has a major influence and an opposite trend is achieved.

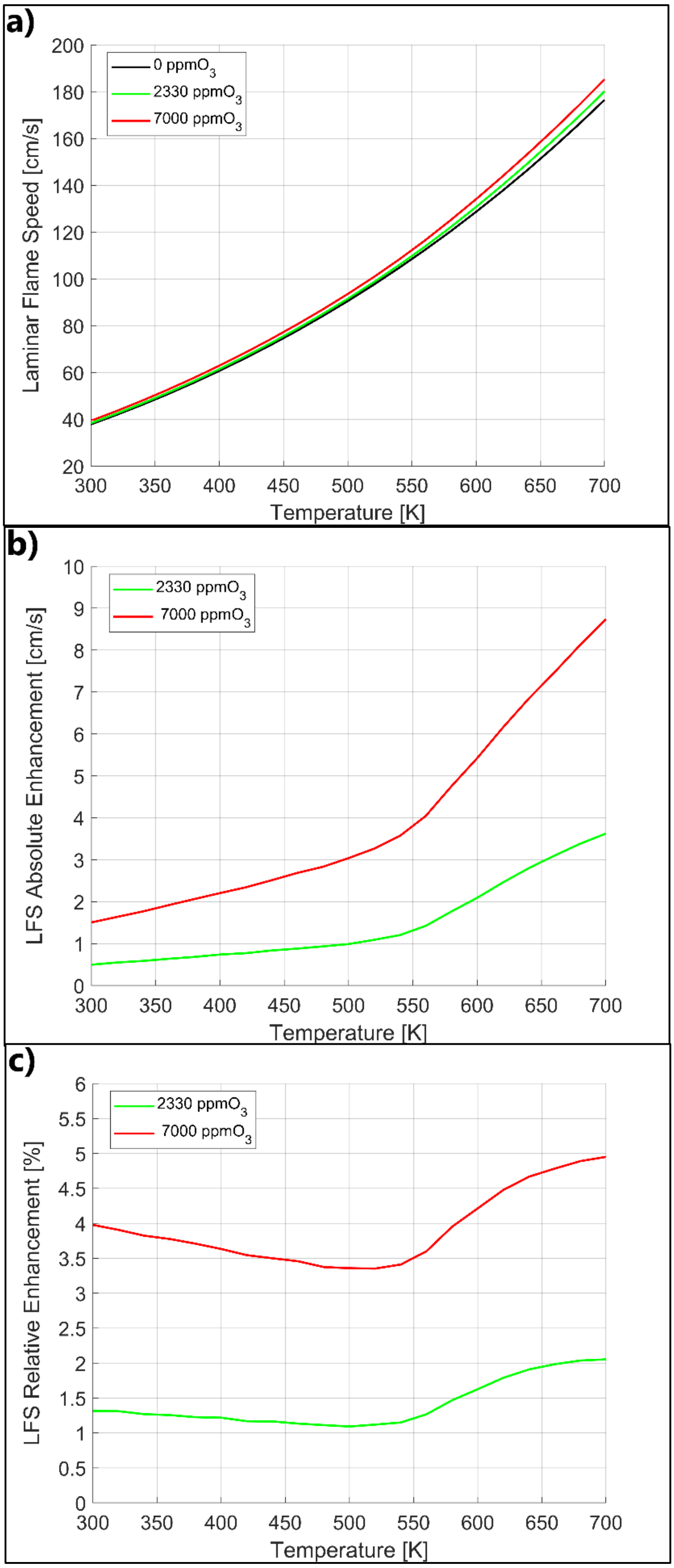

Figure 3.7. Numerical results in terms of LFS vs mixture temperature for $CH_4/Air/O_3$ for different ozone concentrations at P=1 bar and $\phi = 1$: a) LFS; b) absolute enhancement; c) relative enhancement.

The same analysis has also been performed for a mixture of iso-octane/air/ozone. Figure 3.8(a) shows the LFS as a function of mixture temperature for different ozone concentrations by using the modified Yoo mechanism, whereas Figure 3.8(b) shows the derivative of the LFS with respect to temperature, i.e. $\frac{dS_L(T)}{dT}$, obtained with 0, 2330 and 7000 ppm of ozone. Similar trends have been found by using both the modified Curran and the modified Cai&Pitsch mechanisms.

The results show that, in absence of ozone, the LFS as a function of temperature has a similar trend with respect to the case of methane given in Figure 3.7(a): specifically, S_L increases more than linearly with temperature. With ozone addition, a similar behaviour has been obtained up to about 520 K. Above this value the LFS increases with temperature much faster. Indeed, Figure 3.8(b) shows that with 7000 ppm of ozone, in the temperature range 520-580 K, the slope of the $S_L(T)$ profile considerably increases, reaching a maximum value of 1.15 $\frac{cm}{s\,K}$ at 580 K, against 0.37 $\frac{cm}{s\,K}$ for the case in absence of ozone at the same temperature. With a decrease of the ozone concentrations, the peak of the $\frac{dS_L(T)}{dT}$ profile drops and moves towards higher temperatures, as shown in Figure 3.8(b). After the peak, a sharp decrease of the LFS derivative is observed with lower values than those obtained in absence of ozone, and then it slowly increases.

The results obtained by using the other two mechanisms for iso-octane are qualitatively similar and a comparison is shown in Figure 3.8(c) and Figure 3.8(d) in terms of absolute and relative LFS enhancements with respect to the case in absence of ozone. The results show that in the temperature range 300-520 K all the three mechanisms give approximately the same behaviour. In this range, both the relative and the absolute LFS enhancements are quantitatively similar to those obtained for methane; besides, similar trends are achieved as a function of temperature, with a linear increase of the absolute value of the LFS enhancement. Instead, for higher temperatures a different behaviour with respect to methane is obtained, since with iso-octane the enhancements are much greater in the 540-640 K range. All the three mechanisms give the same trends, even if the results quantitatively differ in this temperature range. The maximum values of both relative and absolute enhancements are different and occur at different temperatures, depending on the reaction mechanism, for each ozone concentration. Similar to Figure

3.8(b), after the peak value, the influence of ozone is reduced and the relative LFS enhancement approaches the values obtained at lower temperatures.

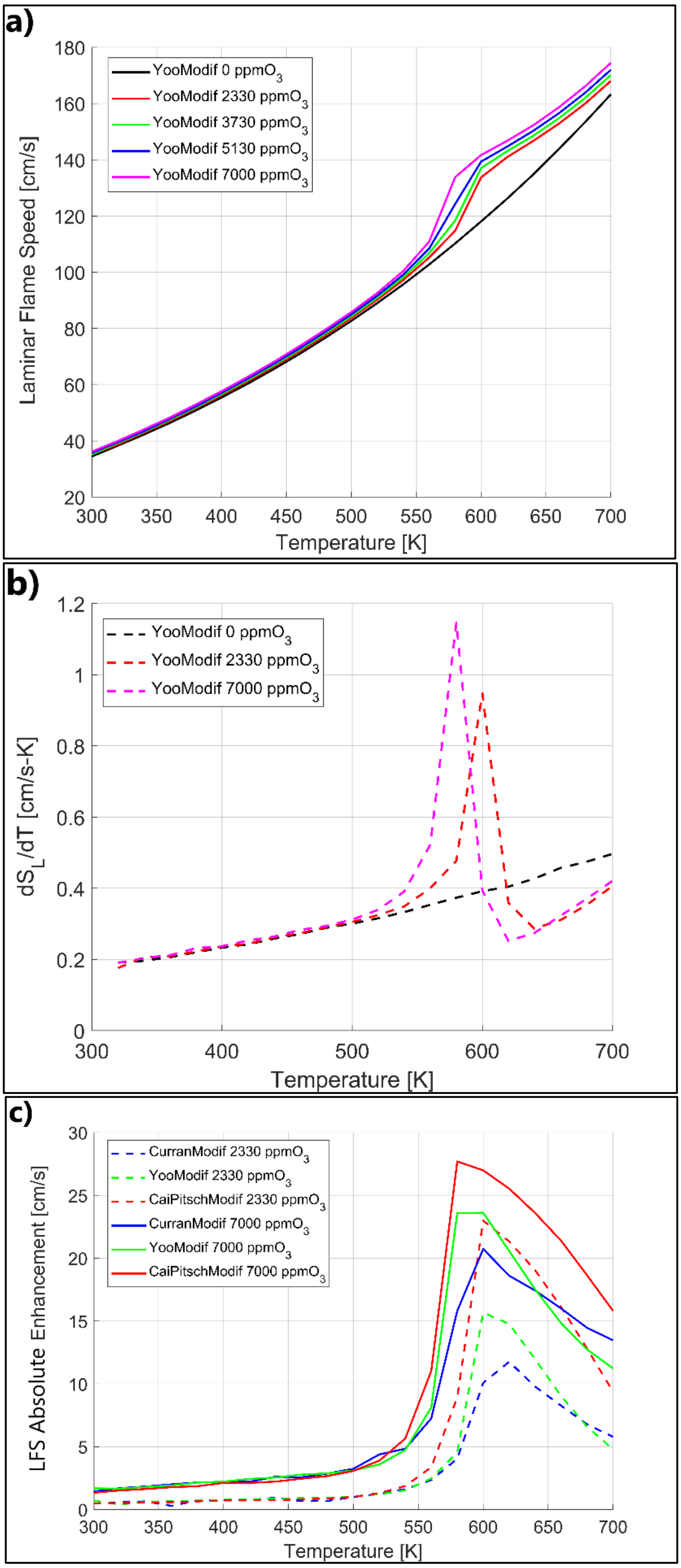

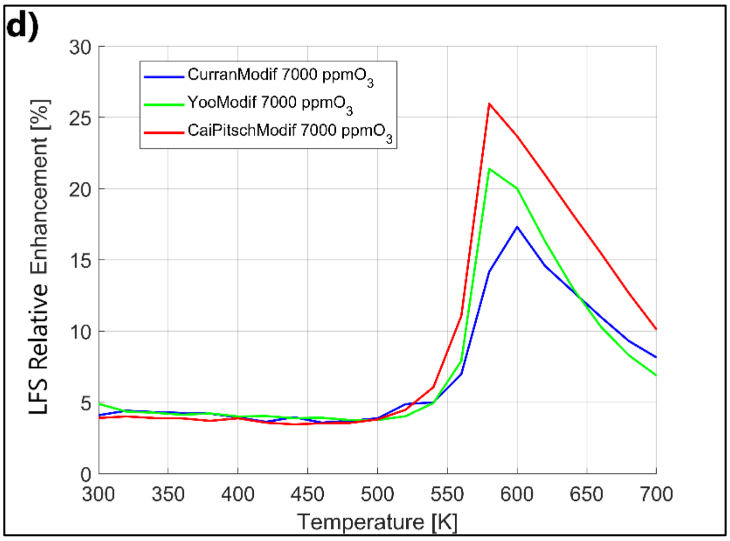

Figure 3.8. Numerical results for $C_8H_{18}/Air/O_3$ mixtures with different reaction mechanisms and ozone concentrations at P=1 bar and $\phi = 1$: a) LFS; b) derivative of LFS with respect to temperature; c) absolute enhancement of LFS; d) relative enhancement of LFS vs mixture temperature.

In order to investigate the behaviour of iso-octane/air/ozone mixtures at temperature higher than 540 K with respect to the case of methane/air/ozone mixtures, the profiles of specific quantities across the flame, i.e. temperature, ozone mole fraction and OH mole fraction, are analysed and given in Figure 3.9 for the case with 7000 ppm of ozone under stoichiometric condition and for two different reactants temperatures, i.e. 500 and 620 K. The results show that, for iso-octane with ozone addition and reactants temperature of 620 K, a cool flame occurs, in agreement with other works available in the literature [105,184-186]. Figure 3.9(a) shows that ozone decomposition depends on both the inlet temperature and the specific fuel. With a reactants temperature of 500 K, ozone is partially decomposed ahead of the high temperature flame: at the flame location, i.e. 4.94 cm, 6.2% and 10.2% of the initial amount of ozone is decomposed for the iso-octane and methane mixtures, respectively. On the other hand, with a reactants temperature of 620 K, ozone is almost completely decomposed ahead of the high-temperature flame, i.e. 98.9% and 100% of the initial amount of ozone is decomposed for methane and iso-octane mixtures, respectively.

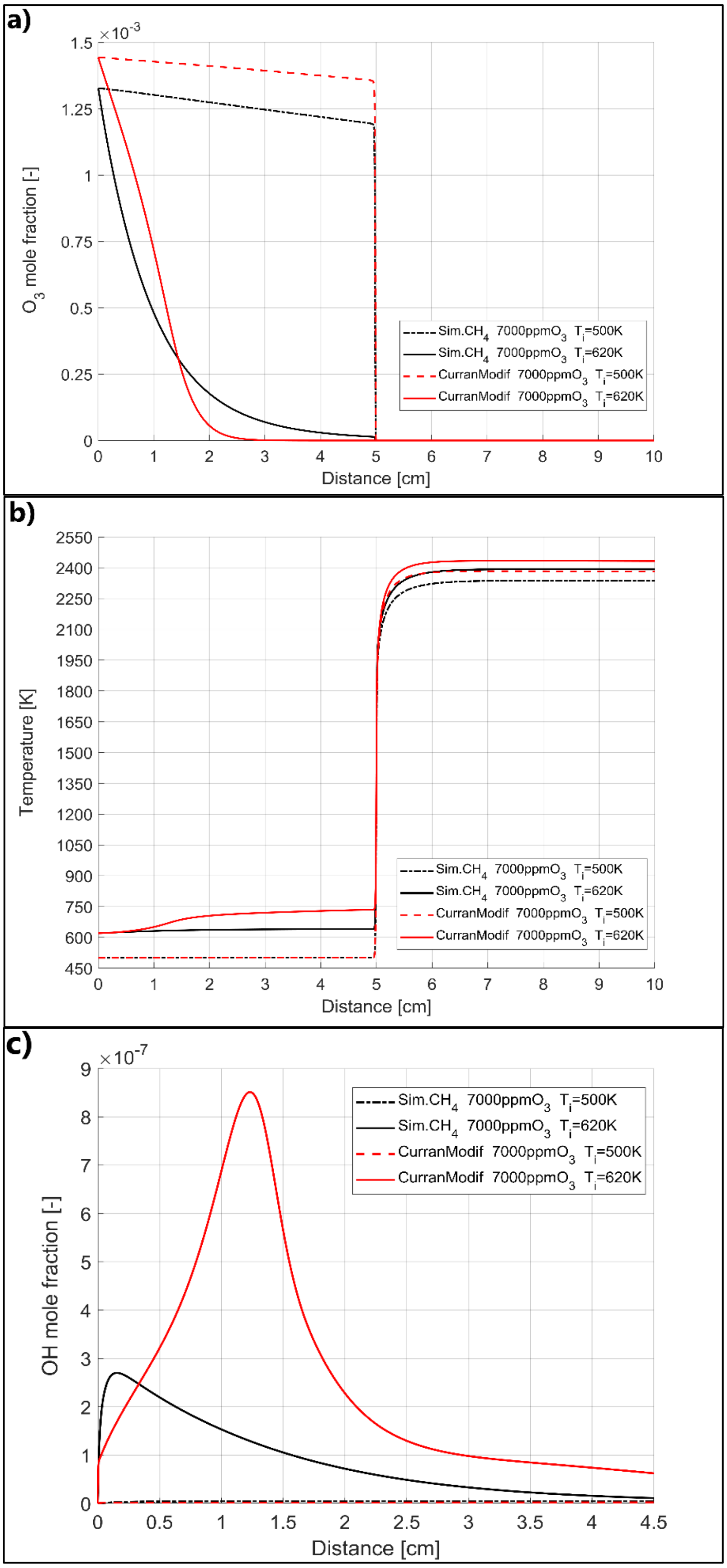

Figure 3.9. Profiles across the flame for stoichiometric $CH_4/Air/O_3$ and $C_8H_{18}/Air/O_3$ mixtures with 7000 ppm of O_3 at P=1 bar, $T_i = 500\,K$ and $T_i = 620\,K$: a) O_3 mole fraction; b) temperature; c) OH mole fraction as a function of distance across the flame.

The much faster ozone decomposition for the iso-octane mixture with an initial temperature of 620 K is due to the different temperature profile, shown in Figure 3.9(b). With a temperature of the reactants of 500 K, the flame is located approximately at 4.94 cm for both methane and iso-octane. Upstream of the flame, the temperature remains nearly the same to the initial value. On the other hand, when the temperature of the reactants is 620 K, a cool flame is established for iso-octane, therefore the fuel is consumed ahead of the high-temperature flame. At 2 cm the temperature is already 706 K (+86 K) and 38.5% of the initial amount of iso-octane is consumed. Just upstream of the high-temperature flame 47.2% of the initial amount of fuel is consumed and the temperature is 734 K. This phenomenon for methane is less evident and more gradual, so just upstream of the high temperature flame 98.4% of the fuel is present and the temperature is increased by only 20 K. Figure 3.9(c) shows the OH mole fraction in the 0 - 4.5 cm region. With a temperature of the reactants of 500 K, the OH mole fraction is of the order of 10^{-9} for both methane and iso-octane and increases very slowly with distance. On the other hand, with an initial temperature of 620 K, OH radicals are produced and, then, consumed, with a maximum in the case of iso-octane at 1.22 cm.

The trend shown in Figure 3.9 occurs with the entire set of iso-octane reaction mechanisms and with lower ozone concentrations. The cool flame location depends on the reactant temperature, on the reaction mechanism and on the ozone concentration, in agreement with the previous discussion on the increase of the LFS. In the case of methane, on the other hand, the cool flame does not occur in any of the conditions, even when the temperature of the reactants is 700 K.

As previously stated, ozone is able to activate the cool flame for iso-octane/air/ozone mixture at temperature above 560 K. To identify which reactions are involved in the cool-flame process, additional analyses have been carried out. Figure 3.10 shows the chemical reactions characterized by the highest values of the Absolute Rate of Production (ARP) of iso-octane, ozone, and atomic oxygen for the case with 7000 ppm of ozone and a temperature of the inlet mixture of 620 K, by using the modified Curran mechanism, at the distance x^* defined as:

$$x^* = x : \max\left\{\frac{dX_{OH}(x)}{dx}\right\}, \qquad 0 < x < 4.95\ cm, \qquad \text{(Eq3.3)}$$

where x is the distance from the inlet and $X_{OH}(x)$ is the molar fraction of OH. x^* is the distance corresponding to the maximum OH increase in the region ahead of the high-temperature flame. In the case under consideration, x^* is about 1 cm. The corresponding temperature is $T_{x^*} = 650\ K$, i.e. 30 K higher than the temperature of the mixture at the inlet. By definition, the ARP is negative if the specific chemical species is consumed, otherwise it is positive. Figure 3.10 also shows the main reaction pathways leading to the formation of OH, together with the ARP values. As regards ozone decomposition, Figure 3.10 shows the reaction pathways with the Relative Rate of Production (RRP) greater than 0.1% and the reactants or products involved in the reaction.

Figure 3.10(a) shows the ARPs of the 10 main reactions of the ozone reaction pathways. Specifically, from the figure, it can be observed that the faster reactions are:

R3.1) $O_3 + N_2 \rightarrow O_2 + O + N_2$,

R3.2) $O_3 + H \rightarrow O_2 + OH$.

Those two reactions account together for 84.1% of the total ozone decomposition, i.e. R3.1 is responsible for 71.9% and R3.2 for 12.2%, as shown in Figure 3.10(e). Figure 3.10(b) shows the 10 fastest reactions for the fuels. These reactions are of three types:

R3.3) $C_8H_{18} + OH \rightarrow C_8H_{17} + H_2O$,

R3.4) $C_8H_{18} + O \rightarrow C_8H_{17} + OH$,

R3.5) $C_8H_{18} + H \rightarrow C_8H_{17} + H_2$.

Specifically, the sum of R3.3-type reactions is responsible for 88.7% of the total C_8H_{18} consumption, whereas R3.4-type reactions are responsible for 10.6%.

Finally, Figure 3.10(c) shows the fastest reactions that involve atomic oxygen. Some of these reactions produce O and others consume it. The production of atomic oxygen is primarily due to two reactions involving ozone: R3.1 and $O_3 + O_2 \rightarrow 2O_2 + O$. R3.1 is the fastest reaction for atomic oxygen production, followed by R3.4-type consumption reactions.

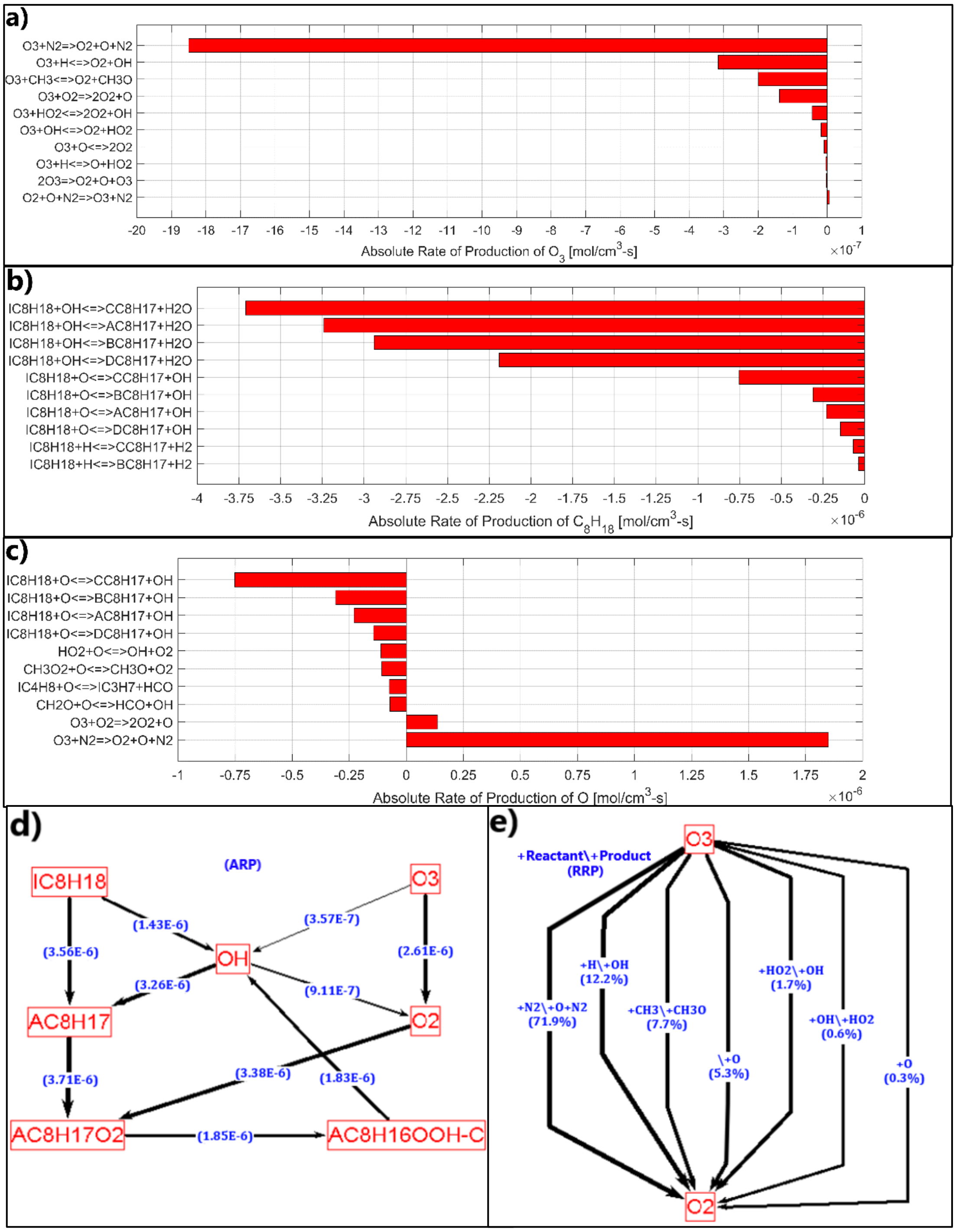

Figure 3.10. Absolute Rates of Production (ARP) and reaction paths at $x^* = 1\ cm$ for a stoichiometric $C_8H_{18}/Air/O_3$ mixture with 7000 ppm of O_3 with the modified Curran mechanism, P=1 bar, $T_i = 620\ K$. Highest ten ARPs for a) O_3; b) C_8H_{18} ; c) O. Main reaction paths for d) production of OH; e) O_3decomposition.

Therefore, ozone is decomposed very fast by R3.1 reaction producing atomic oxygen. The atomic oxygen, being highly reactive, attacks the C_8H_{18} molecules by R3.4 reaction producing OH radicals that advance the oxidation, as shown in Figure 3.10(d). As a matter of fact, at the pipe inlet ($x = 0\ cm$) with $T_i = 620\ K$ the R3.1 reaction already occurs with an ARP of $-1.73 \times 10^{-6}\frac{mol}{cm^3 s}$, i.e. with about the same rate that occurs at x^* with $T_{x^*} = 650\ K$, which is shown in Figure 3.10(a). The reactions involving iso-octane also occur very fast just after the pipe inlet. For instance, at $x = 10^{-3}\ cm$ the reaction $IC_8H_{18} + O \rightarrow CC_8H_{17} + OH$ occurs with an ARP of $-0.41 \times 10^{-6}\frac{mol}{cm^3 s}$, i.e. with the same order of magnitude corresponding to x^* and shown in Figure 3.10(c). On the other hand, for a mixture temperature equal to 500 K, ozone decomposes very slowly up to the high-temperature flame, as also shown in Figure 3.9(a). At $x = 4.95\ cm$ the R3.1 reaction proceeds with an ARP of $-3 \times 10^{-8}\frac{mol}{cm^3 s}$, i.e. about 100 times lower than the 620 K case, thus not allowing the oxidation reactions of iso-octane by atomic oxygen and OH radicals to be efficiently initiated to start the cool flame.

3.1.4 Influence of mixture pressure

In this section, the influence of the mixture pressure on the chemical kinetics of ozone and on the LFS of iso-octane/air/ozone and methane/air/ozone stoichiometric mixtures is investigated. The modified Cai&Pitsch mechanism is used for iso-octane, since it is in better agreement with the experimental data at higher pressure (Figure 3.3), especially at $\phi = 1$.

3.1.4.1 Influence of mixture pressure on ozone decomposition

The influence of pressure on the two main ozone reactions, i.e.

R3.1) $O_3 + N_2 \rightarrow O_2 + O + N_2,$

R3.2) $O_3 + H \rightarrow O_2 + OH,$

is analysed in Figure 3.11, which shows the total ozone ARP together with the ozone ARP in R3.1 and R3.2 reactions as a function of distance from the inlet of the stream tube.

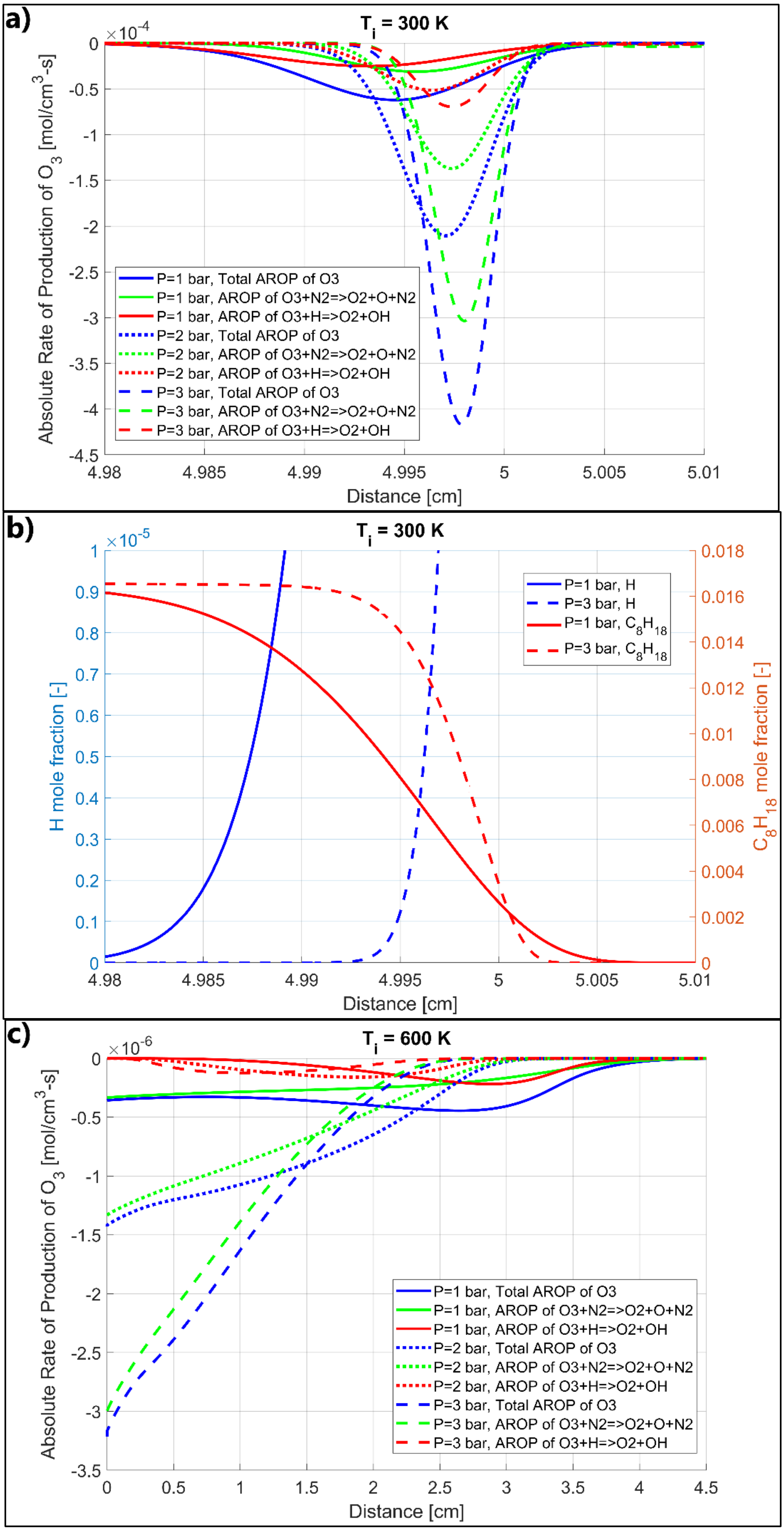
a)
T_i = 300 K
×10^-4
Absolute Rate of Production of O_3 [mol/cm^3-s]
0
-0.5
-1
-1.5
-2
-2.5
-3
-3.5
-4
-4.5
P=1 bar, Total AROP of O3
P=1 bar, AROP of O3+N2=>O2+O+N2
P=1 bar, AROP of O3+H=>O2+OH
P=2 bar, Total AROP of O3
P=2 bar, AROP of O3+N2=>O2+O+N2
P=2 bar, AROP of O3+H=>O2+OH
P=3 bar, Total AROP of O3
P=3 bar, AROP of O3+N2=>O2+O+N2
P=3 bar, AROP of O3+H=>O2+OH
4.98
4.985
4.99
4.995
5
5.005
5.01
Distance [cm]
b)
T_i = 300 K
×10^-5
H mole fraction [-]
1
0.9
0.8
0.7
0.6
0.5
0.4
0.3
0.2
0.1
0
C_8H_{18} mole fraction [-]
0.018
0.016
0.014
0.012
0.01
0.008
0.006
0.004
0.002
0
P=1 bar, H
P=3 bar, H
P=1 bar, C_8H_{18}
P=3 bar, C_8H_{18}
4.98
4.985
4.99
4.995
5
5.005
5.01
Distance [cm]
c)
T_i = 600 K
×10^-6
Absolute Rate of Production of O_3 [mol/cm^3-s]
0
-0.5
-1
-1.5
-2
-2.5
-3
-3.5
P=1 bar, Total AROP of O3
P=1 bar, AROP of O3+N2=>O2+O+N2
P=1 bar, AROP of O3+H=>O2+OH
P=2 bar, Total AROP of O3
P=2 bar, AROP of O3+N2=>O2+O+N2
P=2 bar, AROP of O3+H=>O2+OH
P=3 bar, Total AROP of O3
P=3 bar, AROP of O3+N2=>O2+O+N2
P=3 bar, AROP of O3+H=>O2+OH
0
0.5
1
1.5
2
2.5
3
3.5
4
4.5
Distance [cm]

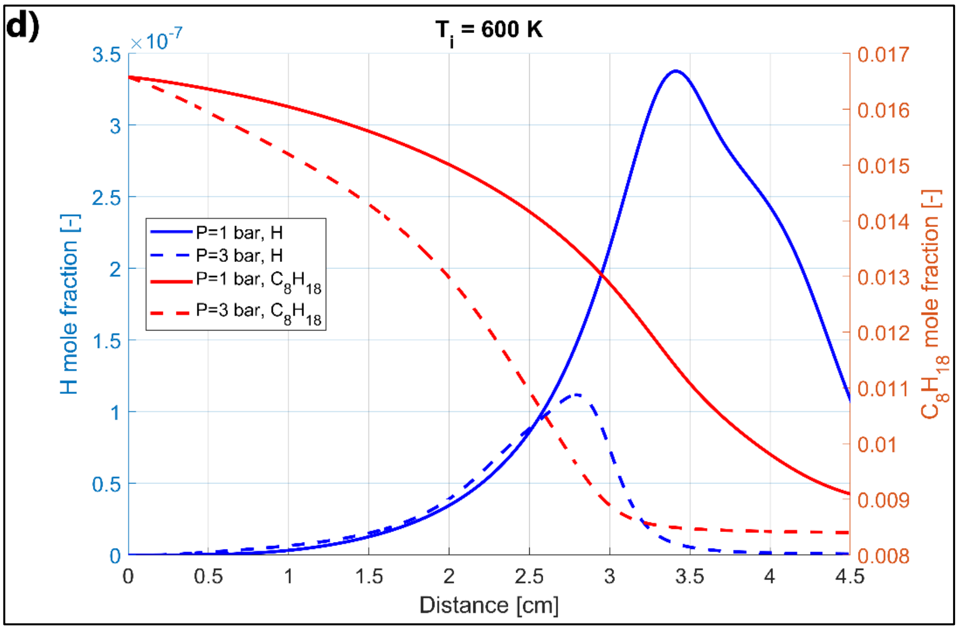

Figure 3.11. Simulations of stoichiometric $C_8H_{18}/Air/O_3$ mixtures with 2330 ppm of ozone for different values of pressure by using the modified Cai&Pitsch mechanism: a) O_3 ARPs at $T_i = 300\ K$; b) H and C_8H_{18} mole fractions at $T_i = 300\ K$; c) O_3 ARPs at $T_i = 600\ K$; d) H and C_8H_{18} mole fractions at $T_i = 600\ K$.

Three different pressures, i.e. 1, 2 and 3 bar, and two inlet temperatures, i.e. 300 K and 600 K, are considered for an iso-octane/air/ozone mixture with 2330 ppm O_3. For the case with an initial temperature of 300 K, the x-axis shows the region near the flame, whereas for the case with an initial temperature of 600 K, the region upstream the flame is also of interest since a cool flame occurs.

Figure 3.11 shows that the decomposition of ozone is very different depending on the inlet temperature of the mixture. With a temperature of 300 K, as previously discussed, only the high temperature flame is established and ozone decomposes very close to the flame. Ozone decomposition occurs earlier and is slower when the pressure is low. Specifically, the peak value of the total amount of ARP of O_3 increases by 240% and 570% for pressures of 2 bar and 3 bar, respectively, with respect to 1 bar case.

At the location where the total ozone ARP is maximum, reactions R3.1 and R3.2 contributes 88% to the total consumption of O_3 regardless of pressure. Despite this, the contribution of each reaction changes considerably as a function of pressure. When the pressure is 1 bar, the ozone starts to mainly decompose by the R3.2 reaction, which occurs due to the diffusion of hydrogen atoms from the flame region to the preheating zone, as shown in Figure 3.11(b). Furthermore, the ARP peak value of R3.1 and R3.2 reactions are similar and, at the point where the ozone ARP is maximum, R3.1 contributes 48% and R2 39%.

As the mixture pressure increases, the contribution of R3.1 increases and that of R3.2 decreases. Specifically, at the point where the ozone consumption rate is maximum, R3.1 contributes 65% and 72% at 2 bar and 3 bar, respectively, whereas the contribution of R2 decreases to 23% and 16% at 2 and 3 bar, respectively. The increase in pressure, in fact, leads to a decrease in the diffusivity of the chemical species, so the amount of H in the preheating zone is lower: for instance, where the mole fraction of C_8H_{18} is 0.014, i.e. 84.6% of the initial amount, at 1 bar the mole fraction of H is 6.28×10^{-6}, whereas at 3 bar it is only 1.93×10^{-6}, i.e. more than three times less. On the other hand, R3.1, being a third body reaction, is favoured by increasing pressure.

With a temperature of the reactants of 600 K a cool flame takes place, and, as shown in Fig. 11c, the ozone ARP has a very different route. Regardless of the pressure, the decomposition of ozone starts at the inlet of the tube, mainly due to R3.1 reaction, whose ARP represents 93% of the total. In agreement with Fig. 9a for the 620 K case, ozone is completely consumed before the high-temperature flame is established, as inferred by the total ARP. At this temperature, the sum of the ARP of R3.1 and R3.2 reactions is about 93% of the total amount and is independent of pressure and spatial location.

At 600 K, ozone decomposes much faster by increasing the pressure and this is more pronounced with respect to the case at 300 K. For instance, with a pressure of 3 bar, at 2.5 cm from the inlet the total ozone ARP is about 0, whereas at a pressure of 1 bar it is approximately equal to its maximum value. At 1 bar, the total ARP of ozone changes slightly from the pipe inlet to about 3 cm, and the maximum value is obtained at 2.64 cm, where the ARPs of R3.1 and R3.2 reactions are nearly the same and equal to 46%. On the other hand, at 2 and 3 bar the total ozone ARP monotonically decreases in the pipe, with a faster decrease in the case of high pressure. At the pipe inlet, the peak value of the total ARP of O_3, compared to the case with P =1 bar, increases by 300% and 800% with pressures of 2 and 3 bar, respectively.

Based on these results, it can be expected that for even higher pressures, with a temperature high enough to generate a cool flame, ozone should mainly decompose by means of R3.1 reaction and this will take place so fast that it will be ended in a very short distance. In this way, the reactions of fuel with atomic oxygen take place very fast, resulting in a higher LFS.

3.1.4.2 Influence of mixture pressure on LFS

In order to analyse the influence of pressure on the LFS for the two fuels, several simulations have been carried out with different operating conditions, in terms of temperature (from 500 to 600 K), pressure (from 1 to 20 bar) and ozone concentration (from 0 to 7000 ppm). Figure 3.12 summarises the results in terms of LFS as a function of pressure. Without ozone LFS decreases as pressure increases, regardless of inlet temperature, for both methane and iso-octane mixtures. With ozone addition to the mixtures, the LFS dependence on pressure is different for the two fuels.

For methane, the LFS decreases by increasing pressure, with a trend similar to the case without ozone. As expected, if ozone concentration is higher, LFS is higher, but for a given ozone concentration and temperature of the reactants, pressure only slightly affects the benefit of adding ozone. Indeed, at 600 K with 7000 ppm of ozone, the increase of the LFS, compared to the case without ozone, is 4.2%, 5.4%, 5.9%, 6.2% and 6.4% with 1, 5, 10, 15 and 20 bar, respectively.

For iso-octane mixtures, pressure has a very different influence depending on both the ozone concentration and the temperature of the reactants. Indeed, Figure 3.12 shows that, as long as the temperature of the reactant mixture is less than or equal to 540 K, the LFS decreases with increasing pressure for all the ozone concentrations. Furthermore, in this temperature range, it can be observed the influence of the cool flame on the widening of the beam of curves as the temperature increases: at 540 K the addition of ozone increases the LFS to a greater extent than in the case with 500 K. On the other hand, for higher temperatures, the trend is not monotonic as a function of pressure but, for pressures higher than a certain threshold, the LFS increases with pressure if air is ozonized. Such a threshold is lower if temperature and/or ozone concentration are higher. These results show that ozone is able to counterbalance the LFS decrease due to the increase in pressure if temperature is sufficiently high, in agreement with similar results obtained in [53] with additives (H_2, CO,O_3) addition to Haltermann gasoline.

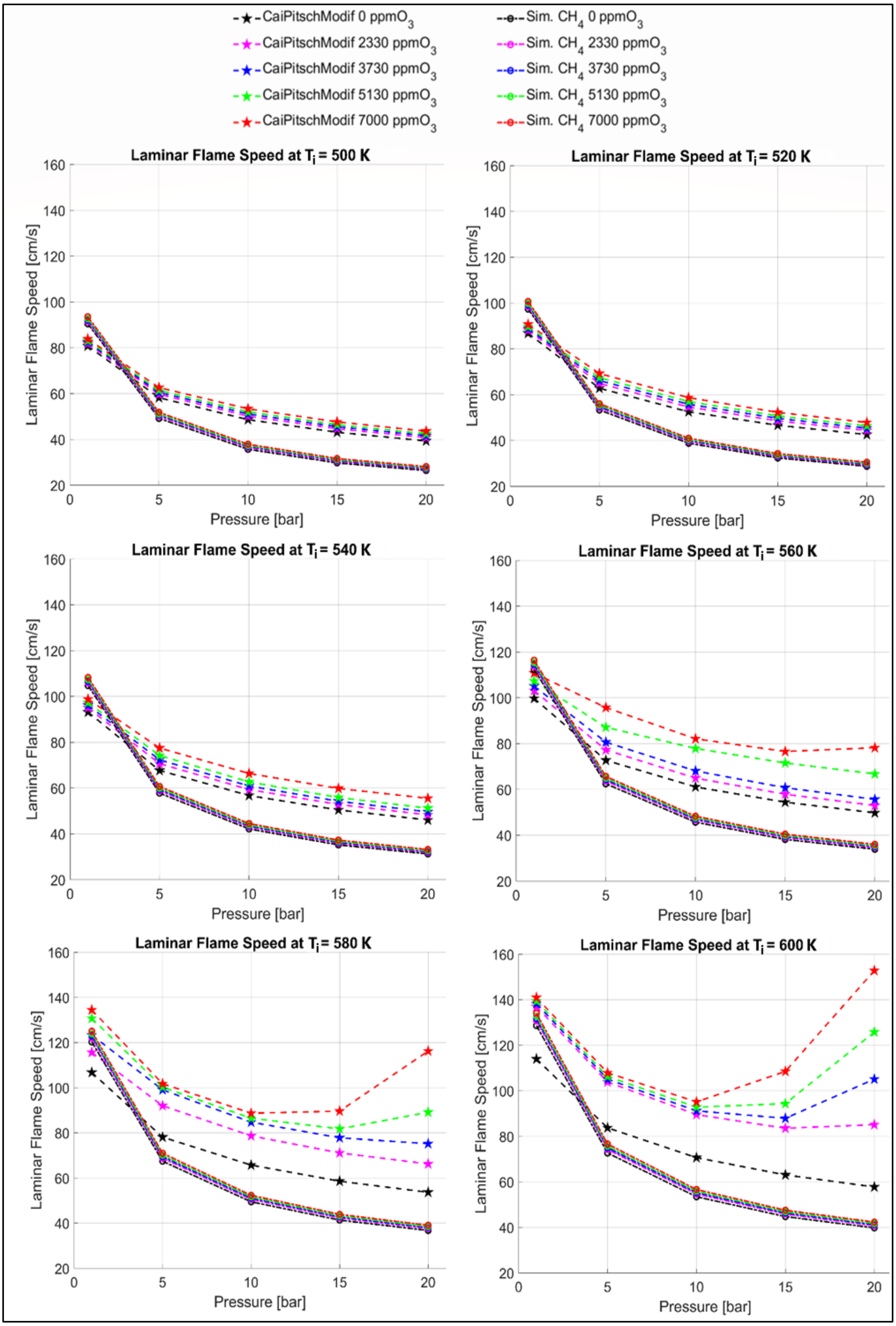

Figure 3.12. LFS as a function of pressure for stoichiometric $C_8H_{18}/Air/O_3$ and $CH_4/Air/O_3$ mixtures with different ozone concentrations and for different reactant temperatures.

The relative increases of the LFS, compared to the case without ozone, as a function of pressure are given in Table 3.1 for selected cases.

Table 3.1. Relative increase in LFS compared to the case without ozone for the stoichiometric $C_8H_{18}/Air/O_3$ mixture using the modified Cai&Pitsch mechanism.

Ozone concentration	$2330\ ppm$	$2330\ ppm$	$2330\ ppm$	$7000\ ppm$	$7000\ ppm$	$7000\ ppm$
Temperature	$500\ K$	$540\ K$	$600\ K$	$500\ K$	$540\ K$	$600\ K$
P = 1 bar	1.2%	2.0%	20.2%	3.8%	6.1%	23.7%
P = 5 bar	2.5%	4.4%	24.1%	7.5%	14.5%	28.9%
P = 10 bar	3.1%	4.6%	26.8%	9.7%	17.0%	34.7%
P = 15 bar	3.6%	4.7%	32.5%	10.5%	18.6%	72.1%
P = 20 bar	3.7%	4.8%	47.4%	10.8%	20.5%	164.6%

In order to clarify the results shown in Figure 3.12, sensitivity analyses have been carried out by using both the methane mechanism and the modified Cai&Pitsch mechanism for C_8H_{18} for three values of pressure, i.e. 1, 10 and 20 bar, both with 7000 ppm of O_3 and without ozone. The case with a reactants temperature of 600 K has been considered, since at this temperature a non-monotonic trend of LFS as a function of pressure for C_8H_{18} and ozonized air is found. Besides, this trend is more severe at 600 K with respect to the other cases at lower temperatures. The results of the sensitivity analyses are shown in Figure 3.13 and Figure 3.14. For each condition, the 10 reactions, to which the LFS is most sensitive, are given.

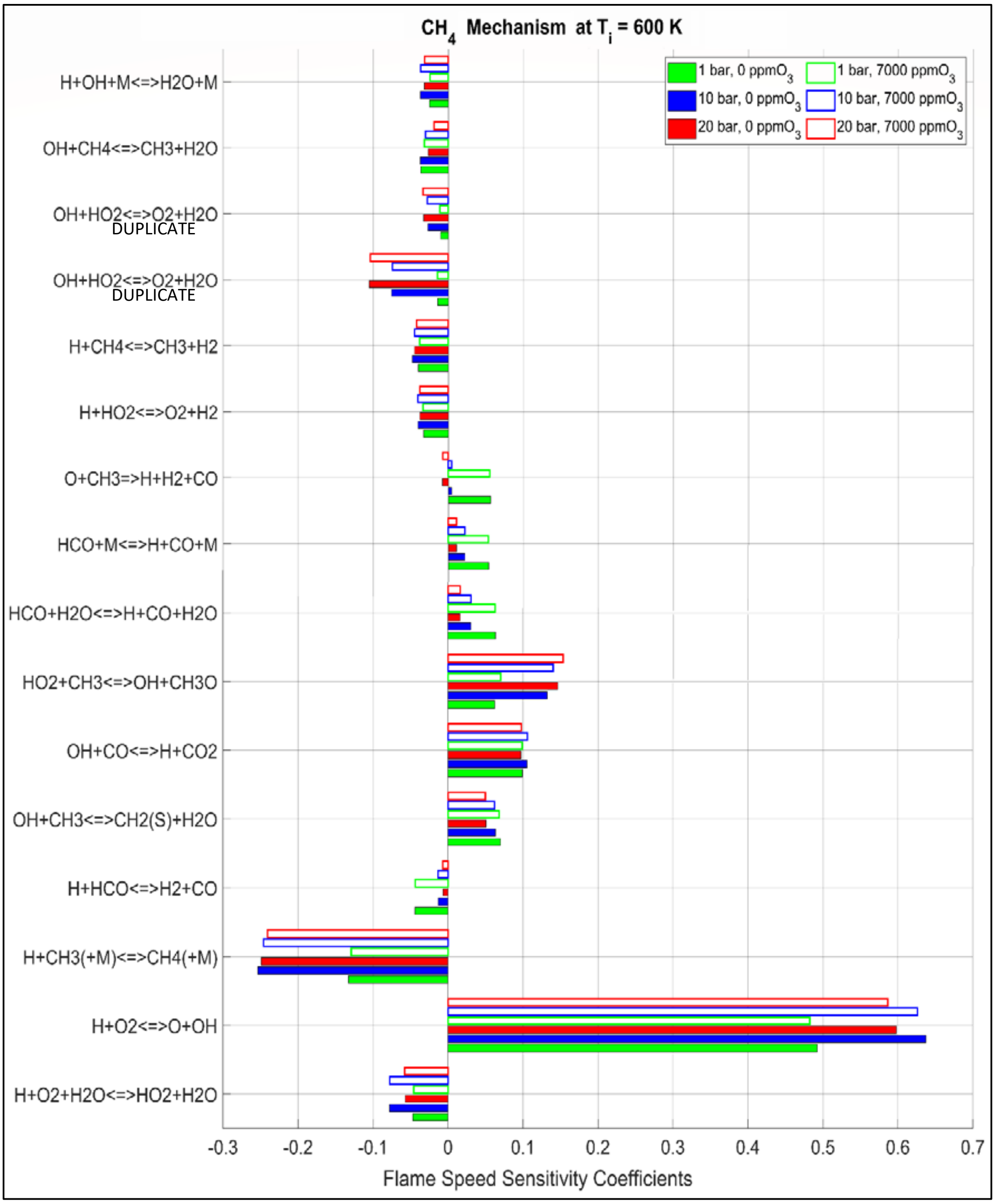

Figure 3.13. LFS sensitivity coefficients for CH_4 mechanism at $T_i = 600\ K$, with and without ozone and for different pressures.

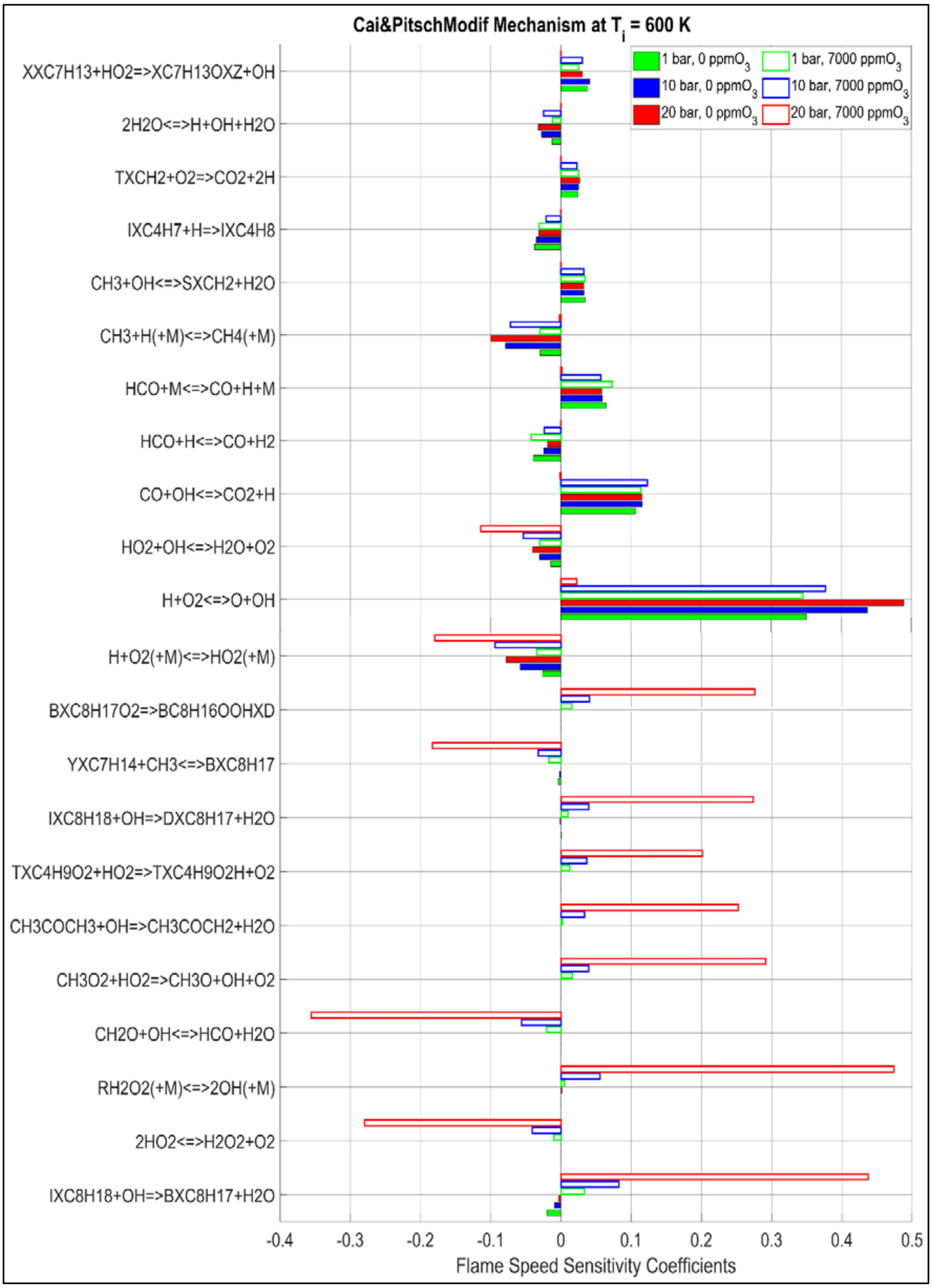

Figure 3.14. LFS sensitivity coefficients for C_8H_{18} modified Cai&Pitsch mechanism at $T_i = 600\ K$, with and without ozone and for different pressures.

As shown in Figure 3.13, the main reactions for methane are the same with and without ozone, and a slight change of the corresponding sensitivity coefficients is observed for ozonized air. Specifically, the sensitivity of the reaction $H + O_2 \rightleftarrows O + OH$

decreases with the addition of ozone, whereas the sensitivity of $HO_2 + CH_3 \rightleftarrows OH + CH_3O$ increases. This means that the increase of LFS with ozone is mainly due to the reaction pathway of HO_2. On the other hand, the reduction of LFS, as pressure increases, is mainly due to an increase of the negative sensitivity coefficients of the reactions $OH + HO_2 \rightleftarrows O_2 + H_2O;\ H + CH_3\ (+M) \rightleftarrows CH_4\ (+M)$.

As regards iso-octane, the sensitivity analysis shows large differences with and without ozone, as pressure increases (Figure 3.14). In the absence of ozone, the main reactions remain the same, regardless of pressure. This is also observed for methane. Specifically, the main reaction is $H + O_2 \rightleftarrows O + OH$, whose sensitivity coefficient shows an increase with pressure. With the addition of 7000 ppm of ozone, at low pressure, i.e. 1 bar, the sensitivity coefficients of the important reactions $CO + OH \rightleftarrows CO_2 + H$ and $HCO + M \rightleftarrows CO + H + M$ show a slight increase with respect to the case without ozone. Furthermore, the importance of the following reactions $IXC_8H_{18} + OH \rightleftarrows BXC_8H_{17} + H_2O;\ BXC_8H_{17}O_2 \rightarrow BC_8H_{16}OOHXD;\ CH_3O_2 + HO_2 \rightleftarrows CH_3O + OH + O_2$, which are in the upper kinetic chain, increase as well. It can be observed that, as the pressure increases from 10 to 20 bar, the sensitivity coefficients of the above reactions increase such that they become the most important reactions with respect to the case without ozone. Specifically, the sensitivity coefficient of the reaction $IXC_8H_{18} + OH \rightleftarrows BXC_8H_{17} + H_2O$ changes from a negative value, in the absence of ozone, to a high positive value with ozone addition. Other relevant reactions for the LFS are: $RH_2O_2\ (+M) \rightleftarrows 2OH + M;\ IXC_8H_{18} + OH \rightleftarrows DXC_8H_{17} + H_2O;\ CH_3O_2 + HO_2 \rightleftarrows CH_3O + OH + O_2$. The analysis shows that the increase of LFS with ozone addition at high pressure and temperature is mainly due to the OH reaction pathway. As shown in Figure 3.9, for the case with ozonized air, at relatively high temperatures, the production of OH radicals enables the formation of the cool flame. Figure 3.10 shows that OH radicals are mainly produced by reactions $C_8H_{18} + O \rightleftarrows (A, B, C, D)C_8H_{17} + OH$. The atomic oxygen, which reacts with fuel molecules, is produced by ozone decomposition through the reaction $O_3 + N_2 \rightarrow O_2 + O + N_2$. Such a reaction is promoted and accelerated as pressure increases, especially at higher temperatures, as shown in Figure 3.11. Hence, the increase of LFS at higher temperatures and pressures is a direct consequence of the speed up of ozone chemical kinetics in the cool flame region.

3.2 Ozone effect on ignition delay time of iso-octane/air mixtures

Similar to the approach taken in section 3.1 for LFS, the aim of the following analyses was to investigate the ozone effect on the Ignition Delay Time (IDT) of iso-octane/air/ozone mixtures. Changing the reaction pathways and enabling the LTC regime, ozone could influence the IDT of the mixture significantly for internal combustion engines applications. The IDT plays a key role in internal combustion engines, both in compression ignition engines, to achieve an optimised combustion phase, and in Spark Ignition engines, where the auto-ignition phenomena that could occur in regions not yet invested by the flame could lead to knocking or loss of performance.

Simulations were conducted using the modified kinetic mechanisms of Yoo and Curran presented in section 2.1.1.2. Specifically, the most widely used mechanism was the modified Yoo mechanism, since it is employed for the CFD calculations in order to preserve the computational cost; the modified Curran mechanism (which is the more detailed one) was only used to make a comparison between the two mechanisms.

At first the model has been validated against experimental data, then several simulations have been performed, by varying ozone concentrations, temperature, pressure and equivalence ratio of the fresh mixtures from 0 to 1000 ppm referred to the iso-octane/air/ozone mixture, from 600 K to 1250 K, from 5 bar to 40 bar, and from 0.4 to 1, respectively.

3.2.1 Model validation

The reaction mechanism is validated, in terms of IDT, by comparing the numerical results with measurements available in the scientific literature for mixtures of iso-octane and air with different equivalence ratios, since experimental results with mixtures of iso-octane and ozonized air are not available in the literature.

Figure 3.15 shows the comparison between the numerical results in terms of IDT and the experimental data available in the literature [153-155,187,188], as a function of equivalence ratio, both at ambient conditions and considering higher values of pressure and temperature. Figure 3.15(a) shows that the model is able to reproduce the experimental data with a good accuracy in the stoichiometric case at 20 bar. Specifically, the Negative Temperature Coefficient (NTC) region is reproduced very well, both in terms of temperature range and IDT values. In the lean case ($\phi = 0.4$) the numerical results are in good agreement with experimental data at 20 bar, as shown in Figure 3.15(b), even if the model underestimates the measurements in the NTC region (720-820 K), and overestimates the experimental data for T > 980 K. On the other hand, with $\phi =$ 0.4 at 40 bar, the model overestimates the available measurements in the range 640-720 K, but the trend is well captured. In summary, the model is able to predict the IDT values of an iso-octane/air mixture fairly well, under different temperature and pressure conditions, for both the stoichiometric and the lean cases.

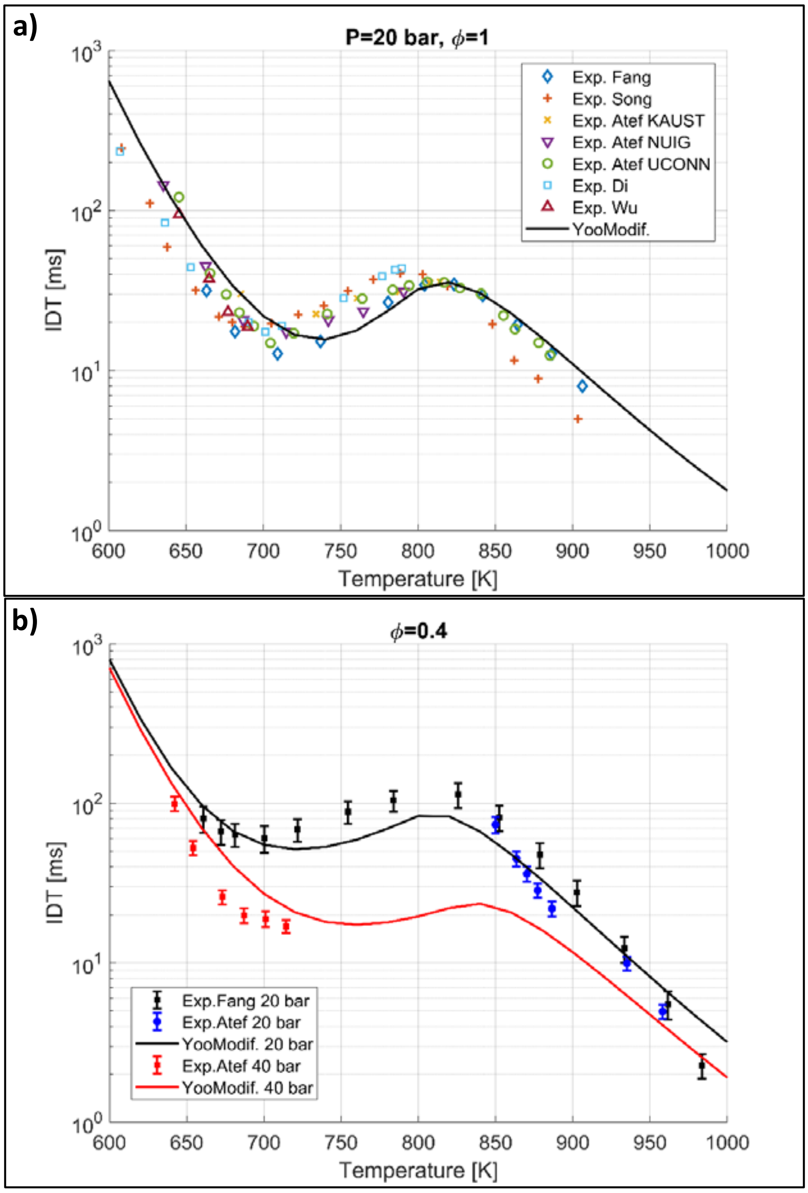

Figure 3.15. Comparison between experimental [153-155,187,188] and numerical results for iso-octane/air mixtures in terms of Ignition Delay Time for: (a) 20 bar, $\phi = 1$; (b) 20 and 40 bar, $\phi = 0.4$.

Figure 3.16 shows the comparison between the modified Yoo mechanism and the modified Curran mechanism under different pressure and temperature conditions in the stoichiometric case. The results show that the pressure increase results in a reduction of the IDT, a shift of the Negative Temperature Coefficient (NTC) region to higher temperatures and a reduction of the NTC effect. The two reaction kinetic mechanisms give similar IDT values, especially at higher pressures and in the temperature range 700-1000 K.

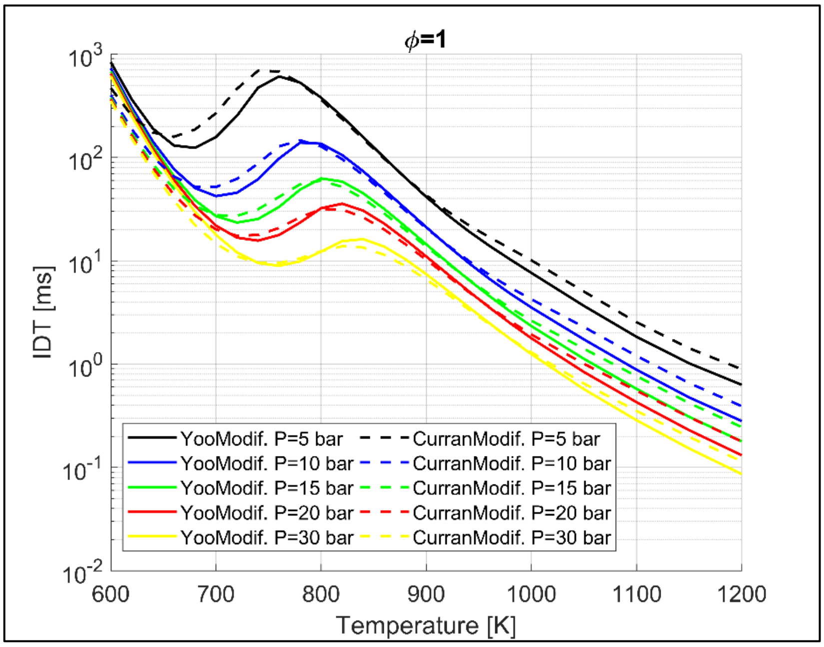

Figure 3.16. Comparison of IDT between modified Yoo and Curran mechanisms for stoichiometric iso-octane/air mixtures, for different initial temperature and pressure conditions.

3.2.2 Ozone effect on IDT

Figure 3.17 shows the ozone effect on IDT both under stoichiometric conditions and for $\phi = 0.5$. Figure 3.18, on the other hand, shows the IDT as a function of ozone concentration under different conditions of initial temperature and equivalence ratio. Finally, Figure 3.19 shows the IDT relative percentage variation with respect to the case without ozone, for stoichiometric cases and with $\phi = 0.5$, i.e.

$$\varepsilon_{IDT} = \frac{IDT_{X_{O_3}} - IDT_0}{IDT_0}, \qquad \text{(Eq3.4)}$$

where $IDT_{X_{O_3}}$ and IDT_0 are the IDT values in the case with X_{O_3} ppm of ozone and in the case without ozone, respectively.

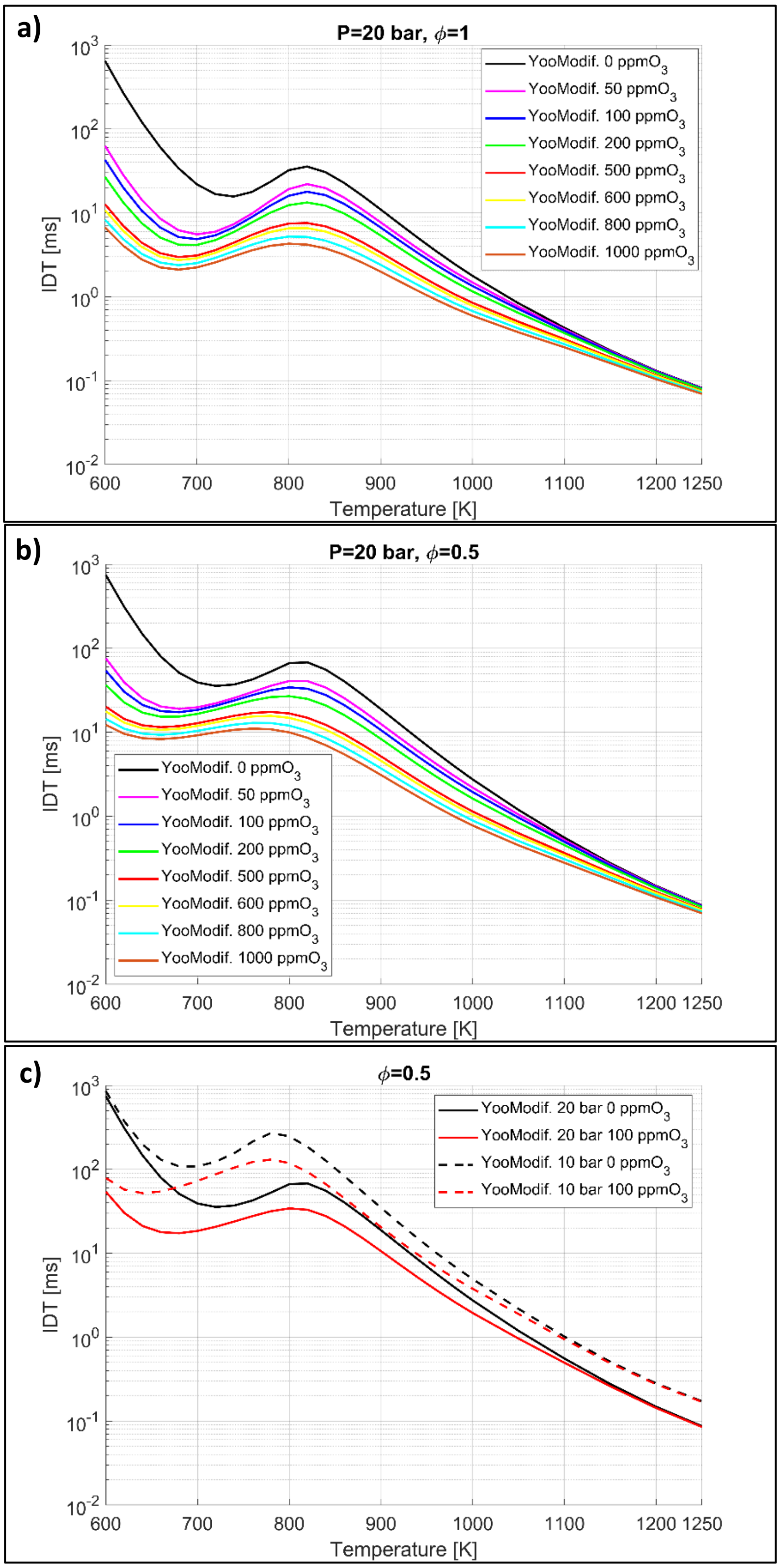

Figure 3.17. Ozone effect on Ignition Delay Time as a function of initial temperature of the mixture for different ozone concentrations in iso-octane/air/ozone mixtures: a) $P = 20\ bar, \phi = 1$; b) $P = 20\ bar, \phi = 0.5$; c) $P = 10, 20\ bar, \phi = 0.5$.

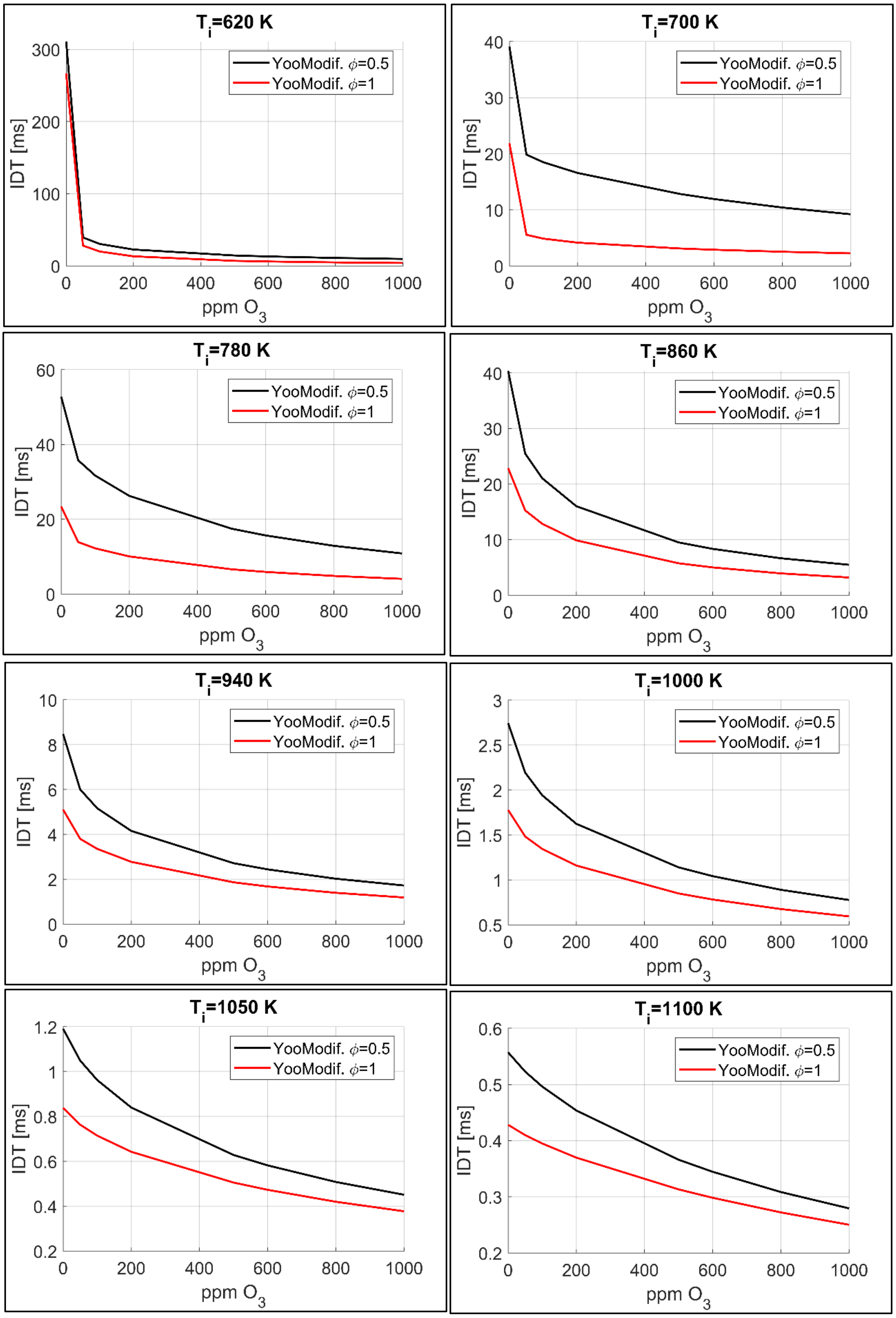

Figure 3.18. IDT as a function of ozone concentration in iso-octane/air/ozone mixtures at 20 bar for different equivalence ratios at given initial temperatures.

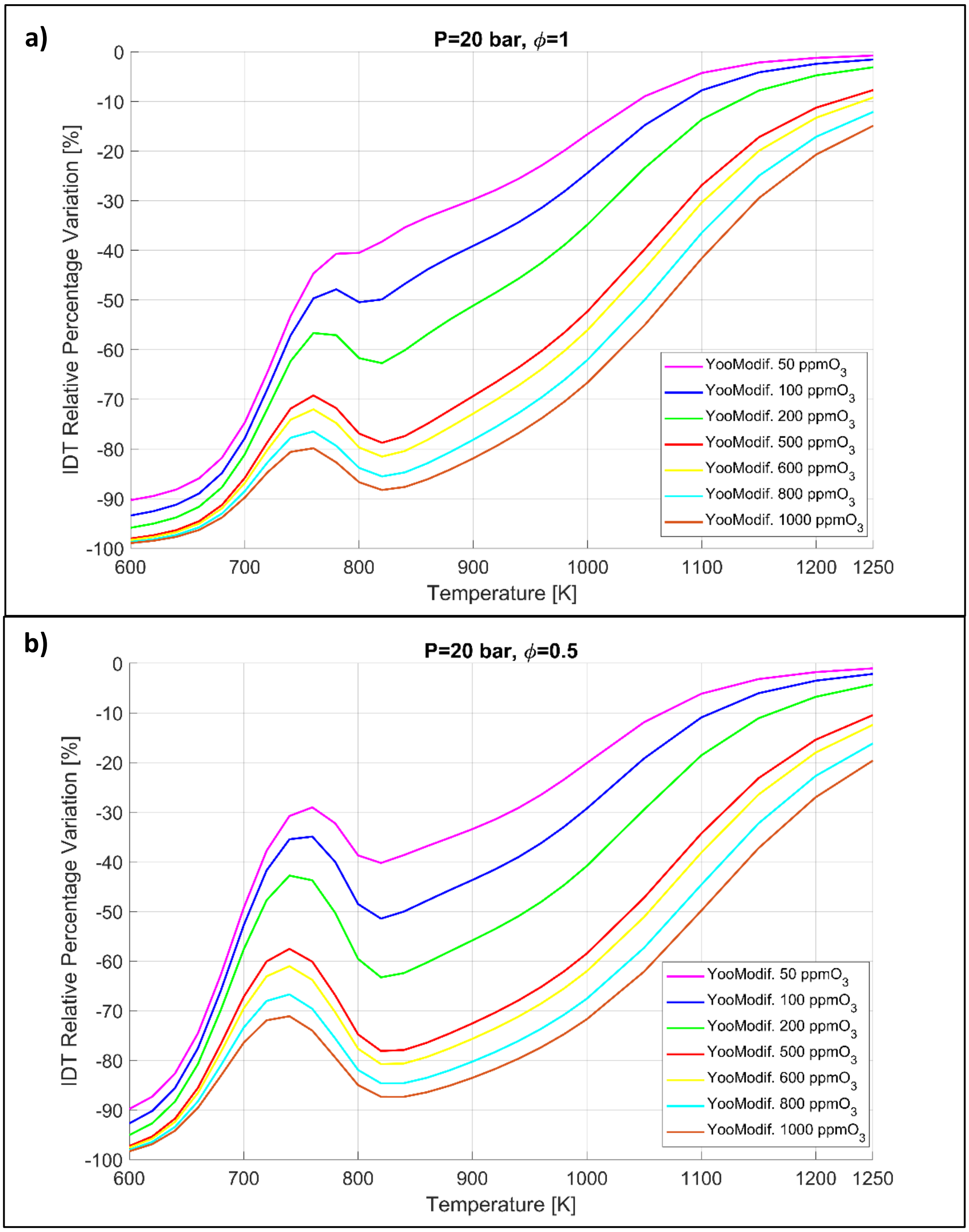

Figure 3.19. IDT relative percentage variation with respect to the case without ozone as a function of initial temperature of the mixture for different ozone concentrations in iso-octane/air/ozone mixtures at $20\ bar$: a) $\phi = 1$; b) $\phi = 0.5$.

Figure 3.17 shows that ozone reduces the IDT throughout the temperature range considered, both under stoichiometric and lean mixture conditions with a more pronounced effect as ozone concentration is increased. Furthermore, in the case $\phi = 0.5$, the increase in ozone concentration reduces the NTC effect. Figure 3.17(c) shows that, in the case $\phi = 0.5$, the addition of 100 ppm ozone in the 10 bar case reduces the IDT to significantly lower values than in the 20 bar case without ozone for temperatures below

680 K, while in the temperature range 850-950 K the IDT assumes approximately the same values in the 10 bar case with 100 ppm ozone and the 20 bar case without ozone.

Figure 3.18 shows that the ozone addition results in a reduction of the IDT with a stronger effect in the case of low temperatures: at 620 K the IDT in the case without ozone is 311 ms and 267 ms for the cases at $\phi = 0.5$ and $\phi = 1$, respectively, while with the addition of 100 ppm ozone the IDT values become 30.4 ms and 19.9 ms, respectively; at 900 K, on the other hand, the IDT is decreased from 18.84 ms and 11 ms without ozone, to 10.61 ms and 6.7 ms with the addition of 100 ppm of O_3, for the cases at $\phi = 0.5$ and $\phi = 1$, respectively. Moreover, the reduction of IDT with ozone addition is not linear, and increasing ozone concentration reduces IDT progressively slower, especially at low temperatures: for example, in the stoichiometric case at 700 K, IDT is reduced by 26.31 ms with the addition of 500 ppm ozone, whereas with 1000 ppm ozone, IDT is reduced by 29.94 ms with respect to the case without ozone, therefore the use of an additional 500 ppm of O_3 reduced IDT by only 3.63 ms.

The greater effect of ozone addition at low temperatures can also be observed in Figure 3.19. Specifically, at 600 K ozone addition reduces the ignition delay by 89-99%, depending on the specific ozone concentration, for both lean and stoichiometric cases. By increasing the initial temperature of the mixture, the effect of ozone on IDT is smaller, and increases again in the range 720–820 K, especially in the case of lean mixture and higher ozone concentrations, due to the NTC effect, which occurs mainly in the case without ozone and with $\phi = 0.5$. From 820 K to 1250 K, on the other hand, the percentage variation of IDT has a monotonic decreasing trend because the higher the temperature, the more it governs chemical kinetics almost exclusively, regardless of other factors such as the addition of ozone. Specifically, at 1200 K an ozone concentration of more than 200 ppm is required to achieve an IDT percentage reduction of more than 5%, for both the lean and stoichiometric cases. Additionally, the results show that the percentage reduction of IDT with ozone addition is greater in the stoichiometric case in the temperature range 600-800 K, especially at lower temperatures, whereas in the temperature range 820- 1250 K the percentage reduction is greater in the case $\phi = 0.5$.

These results suggest that, if the mixture temperature is high, the addition of ozone does not lead to a significant benefit in terms of percentage reduction of IDT, because temperature plays a major role in chemical kinetics. On the other hand, if temperature is relatively low, and reactions are slow, ozone is able to modify the reaction pathways, accelerating the reactions that lead to auto-ignition.

4. Chapter 4: Investigation of ozone effects in HCCI engines

This chapter will present the results obtained from simulations of possible applications of ozone in HCCI engines fuelled with iso-octane. These analyses concerned: the calculation of the Ignition Delay Time (IDT) under HCCI engine-like thermo-chemical conditions, and closed valve cycle simulations of an HCCI engine with ozone addition. Analyses were conducted covering a wide range of operating conditions depending on the aim of the investigation.

4.1 IDT of iso-octane/air/ozone mixtures under HCCI engine-like thermo-chemical conditions

In section 3.2, simulations were conducted to investigate the effect of ozone on the IDT in an iso-octane/air-ozone mixture in the case of ozone concentrations greater than 100 ppm and equivalence ratios greater than $\phi = 0.5$. In HCCI engines, on the other hand, lower equivalence ratios are generally used ($\phi \simeq 0.3$) in order to prevent the almost simultaneous auto-ignition in different spots of the chamber producing too fast heat release. In addition, it has been found in the scientific literature [102,105-107] that, in these engines, units or at most tens of ppm of ozone are sufficient to obtain a significant change in the characteristic parameters of combustion (auto-ignition timing, heat release rate, combustion duration).

In this scenario, the aim of the following analyses is to investigate the influence of ozone on IDT of a very lean iso-octane/air/ozone mixture ($\phi = 0.3$) under typical HCCI engine conditions. It is well known that the control of auto-ignition time plays a major role for the combustion development in these engines. By investigating different thermodynamic conditions, in terms of pressure, temperature and ozone concentrations, parametric analyses were conducted and the chemical evolution of the mixture was analysed. The same model described and validated in section 3.2 was used, employing the modified Yoo mechanism.

4.1.1 Ozone effect on IDT of very lean iso-octane/air/ozone mixtures

Ozone effect on IDT of iso-octane/air/ozone mixtures was investigated by considering an initial temperature ranging from 500 K to 1200 K, with a step of 20 K. Figure 4.1 shows IDT values as a function of temperature and the IDT relative percentage variation with respect to the case without ozone, computed with equation Eq3.4.

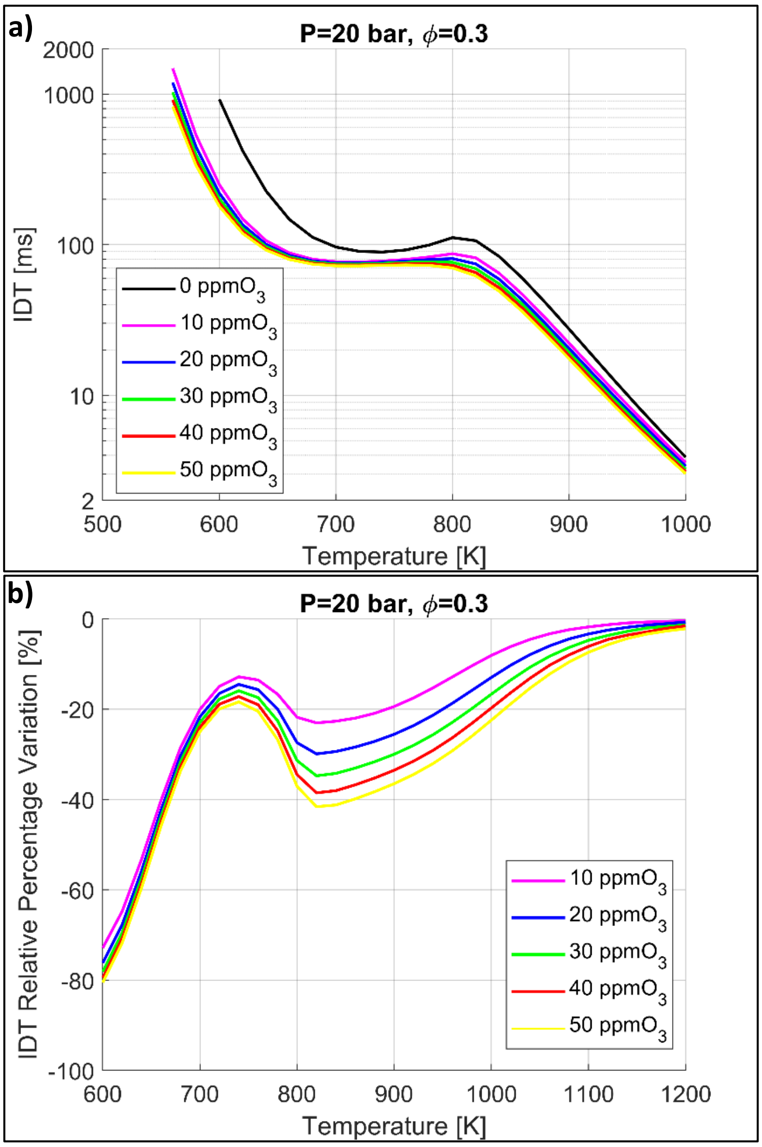

Figure 4.1. Ozone effect on Ignition Delay Time as a function of initial temperature of the mixture for different ozone concentrations in iso-octane/air/ozone mixtures at $20\ bar$ and $\phi = 0.3$, in terms of: (a) IDT; (b) IDT relative percentage variation with respect to the case without ozone.

As shown in Figure 4.1, the addition of ozone reduces the IDT throughout the temperature range considered, with a more pronounced effect as ozone concentration is increased. Furthermore, Figure 4.1(a) shows that, for all cases with ozone, the mixtures ignite at lower temperatures than those for the case without ozone. Specifically, by running a 2-second-long simulation, with the addition of ozone, auto-ignition occurs when the initial mixture temperature is equal or higher than 560 K, whereas without ozone the minimum temperature for auto-ignition is 600 K. Ozone concentration effect is more pronounced at low temperatures: at 560 K, the IDT in the case with 50 ppm of ozone is 653.8 ms lower than that for the case with 10 ppm. On the other hand, the profiles for the cases with ozone tend to converge in the temperature range 680–760 K, with a maximum difference between the case with 50 ppm and the case with 10 ppm equal to 6.5 ms.

Another effect due to ozone addition, and proportional to its concentration, is the reduction of the NTC phenomenon, which can be observed in Figure 4.1(a) in the temperature range 700–850 K. For the case with 50 ppm, IDT, as a function of temperature, shows an almost monotonic non-increasing trend, with an inflection between 700 and 780 K where IDT ranges between 72.3 and 73.3 ms. Figure 4.1(b) shows that the percentage reduction in IDT, with respect to the case without ozone, is greater at low temperatures. At 600 K, the IDT for the case without ozone is equal to 923.5 ms and ozone addition reduces the ignition delay by 70-80%, depending on the specific ozone concentration. By increasing the initial temperature of the mixture up to 740 K, the effect of ozone on IDT is smaller, and increases again in the range 740–820 K due to the NTC effect, which occurs mainly in the case without ozone. From 820 K to 1200 K, on the other hand, the percentage variation of IDT has a monotonic decreasing trend leading to zero. Specifically, at 1200 K, the percentage decrease of IDT in the cases with 10 and 50 ppm ozone is 0.4% and 2.2%, respectively.

Similar to the results obtained in section 3.2 for higher equivalence ratios and ozone concentrations, relatively low temperatures are required to achieve a significant percentage reduction in IDT. For instance, with 50 ppm of ozone at 680 K IDT is equal to 80 ms, and is comparable to the IDT in the case without ozone at a temperature of 840 K. To understand the effect of ozone on chemical kinetics, Figure 4.2 shows the profiles of temperature and mole fractions of some species as a function of time for a mixture with an initial temperature equal to 600 K and for the cases without ozone and with 30 ppm.

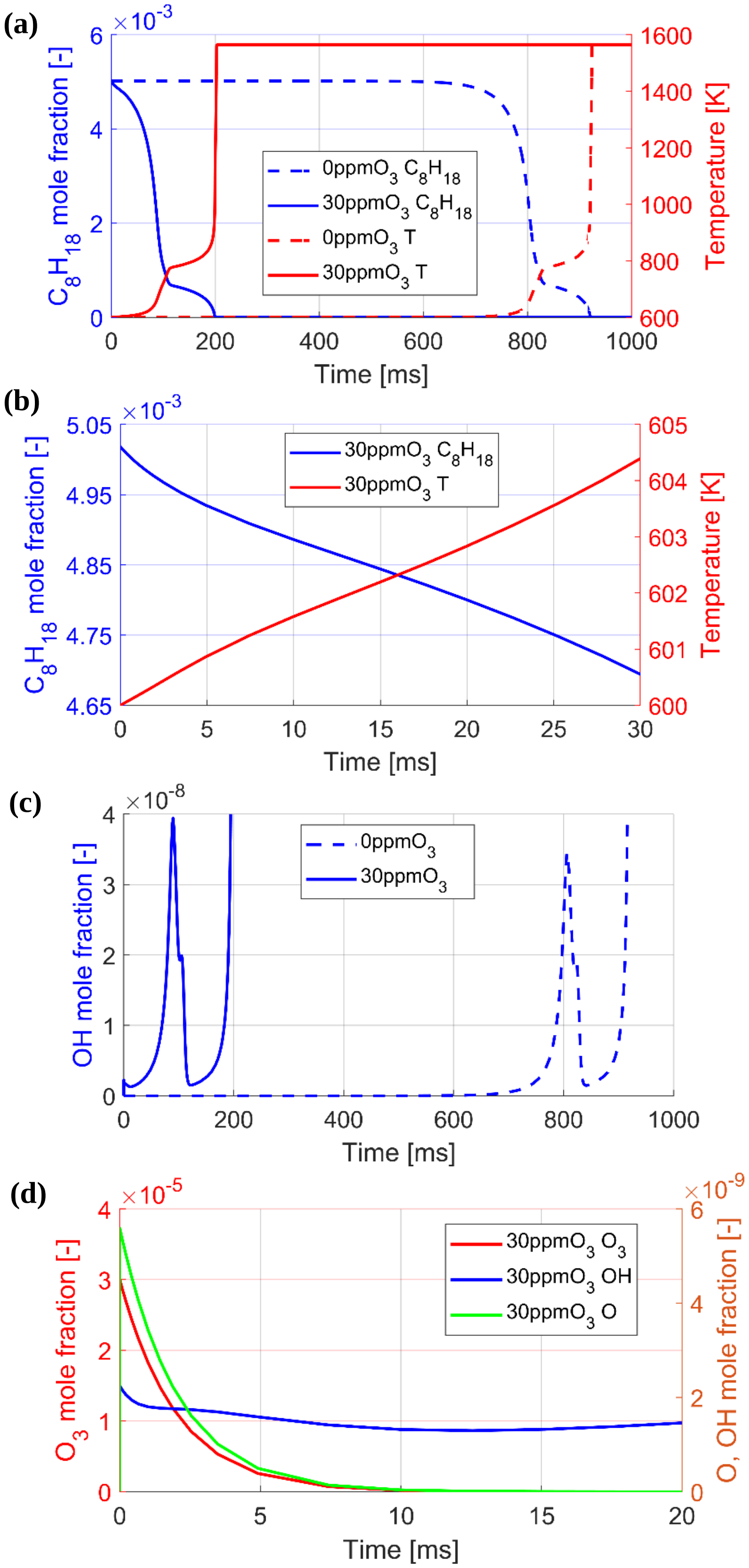

Figure 4.2. Characterization of chemical kinetics for iso-octane/air/ozone mixtures at $20\ bar, 600K$ and $\phi = 0.3$: (a) C_8H_{18} mole fraction and temperature vs time with 30 ppm of O_3 and without O_3; (b) C_8H_{18} mole fraction and temperature vs time with 30 ppm of O_3 – blow-up; (c) OH mole fraction vs time with 30 ppm of O_3 and without O_3; (d) O_3, O and OH mole fractions vs time with 30 ppm of O_3.

Figure 4.2(a) and (b) show iso-octane mole fraction and temperature as a function of time in the cases with 0 and 30 ppm of ozone and with initial temperature equal to 600 K. The auto-ignition occurs both with and without ozone with a delay equal to about 200 ms and 900 ms for the cases with 30 ppm ozone and without ozone, respectively. However, fuel consumption occurs differently for the two cases.

Figure 4.2(b), which is a blow-up of the profiles of Figure 4.2(a) for the case with ozone, reveals that both iso-octane and temperature profiles change concavity in the first 30 ms, with an inflection around 15 ms. This means that, with ozone, fuel is immediately consumed, with an initial rate that first decreases and, after the inflection, increases. In the case without ozone, on the other hand, fuel starts to slowly decompose, with the fuel profile maintaining the same concavity up to the end of the first-stage of ignition, as shown in Figure 4.2(a). This is because, with ozone addition, iso-octane consumption is due to the reaction $C_8H_{18} + O \rightleftarrows C_8H_{17} + OH$, and the reagent O is made available by the decomposition of ozone through the reaction $O_3 + N_2 \rightleftarrows O_2 + O + N_2$. Therefore, these reactions play a key role in the advance of IDT.

Figure 4.2(c) compares OH profiles for the cases without ozone and with 30 ppm of O_3 and with an initial mixture temperature equal to 600 K. The shapes of the two profiles are very similar: OH mole fraction reaches a maximum at the first-stage ignition timing, then decreases and increases once more when the main combustion occurs. However, for the case with ozone, OH production occurs earlier, and the first peak value is higher than in the case without ozone.

Figure 4.2(d) shows that, at 600 K, ozone is consumed within 10 ms, and oxygen atoms and OH radicals are immediately produced. Oxygen atoms, as ozone, are consumed very quickly, while OH smoothly decreases and then increases, following the trend of Figure 4.2(c). Such a trend could be explained by the reaction pathways of fuel oxidation: at 600 K a rapid decomposition of ozone takes place, resulting in the production of oxygen atoms that oxidize the fuel, producing OH radicals. OH is consumed by the reaction $C_8H_{18} + OH \rightleftarrows C_8H_{17} + H_2O$, which continues fuel oxidation, leading to an advance in IDT. These phenomena lead to auto-ignition even at temperatures below 600 K when ozone is added to the mixture, as shown in Figure 4.2(a).

4.1.2 Pressure effect on IDT of very lean iso-octane/air/ozone mixtures

To investigate the simultaneous effects of pressure and ozone addition on the ignition delay time of iso-octane/air/ozone mixtures, simulations were carried out by investigating the pressure range 15-40 bar, with a step of 5 bar. Ozone concentration was varied from 0 to 50 ppm, whereas the initial temperature of the mixture was changed from 500 to 1200 K.

Figure 4.3 shows the IDT as a function of temperature and the O_3 profiles as a function of time, for different cases.

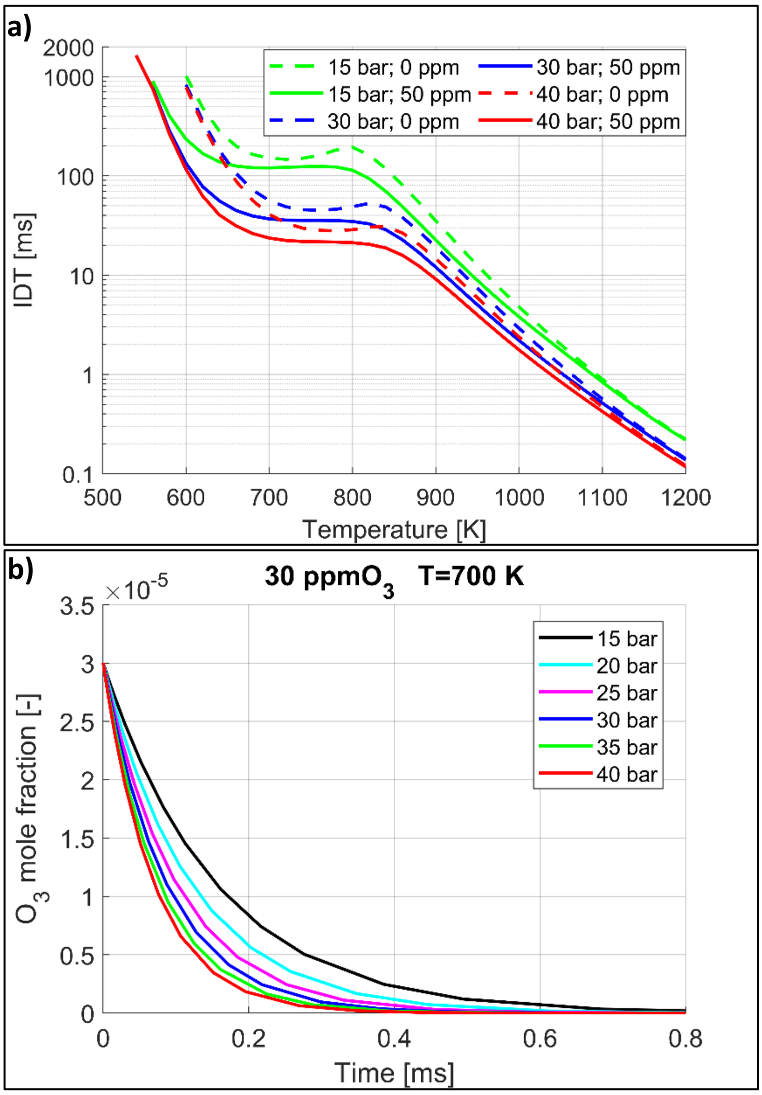

Figure 4.3. Effect of pressure and ozone addition for iso-octane/air/ozone mixtures at $\phi = 0.3$, in terms of: (a) IDT vs initial mixture temperature; (b) Ozone mole fraction vs time at $700\ K$ with $30\ ppm$ of O_3.

Figure 4.3(a) shows that, as expected, IDT decreases with increasing pressure and that higher pressures lead to a reduction in terms of NTC effect, both without ozone and with ozone. Furthermore, with the addition of 50 ppm of ozone, auto-ignition occurs at lower temperatures than for the case without ozone. For instance, for the cases with 35 and 40 bar the mixture with an initial temperature equal to 540 K auto-ignites in a 2-second-long simulation. Figure 4.3(b) shows that, at given temperature and ozone concentration, ozone decomposition is faster with increasing pressure. This is due to the decomposition of ozone by the reaction $O_3 + N_2 \rightleftarrows O_2 + O + N_2$, which, as a third-body reaction, is favoured by increasing pressure, as discussed in detail in section 3.1. Consequently, fuel oxidation and OH production, discussed in section 4.1.1, occur faster, resulting in a more pronounced reduction in terms of IDT.

Figure 4.4 shows the relative percentage variation of IDT as a function of ozone concentration and for different pressures at given temperatures. For any given pressure, the effect of ozone on the percentage reduction of IDT is higher at low temperatures.

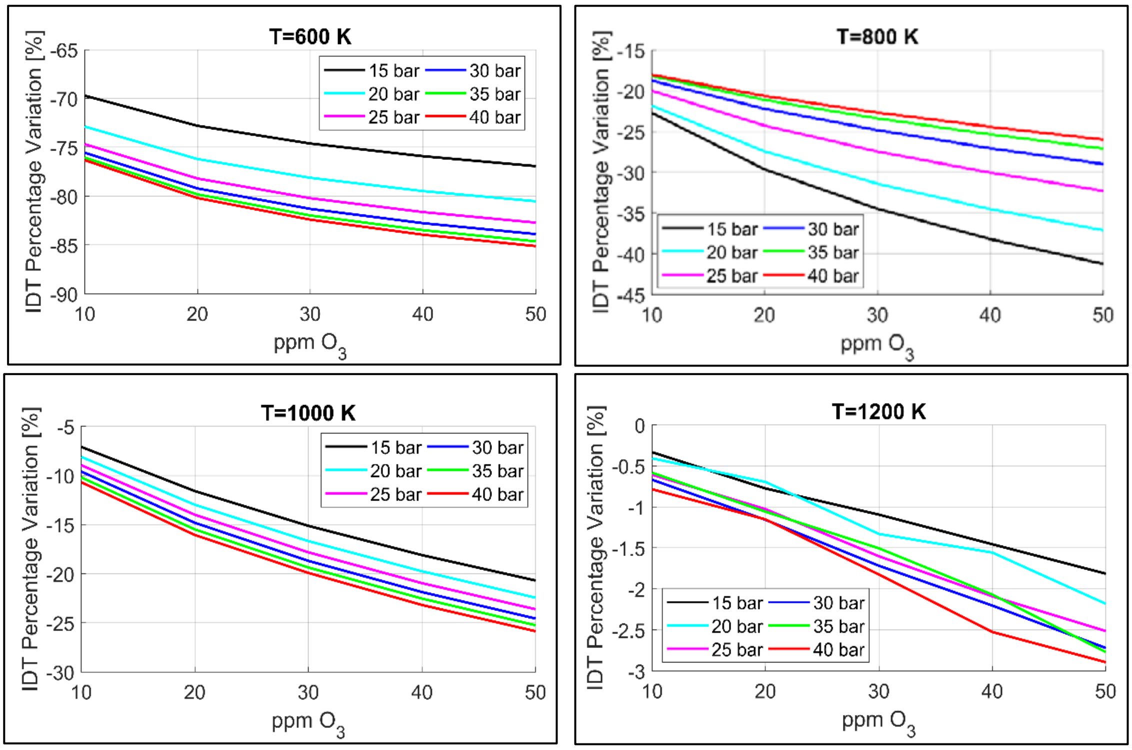

Figure 4.4. IDT relative percentage variation with respect to the case without ozone, as a function of ozone concentration, for iso-octane/air/ozone mixtures at $\boldsymbol{\phi = 0.3}$, for different pressures at given initial temperatures.

At 600 K, as shown in Figure 4.4, the percentage reduction of IDT increases with increasing pressure for all ozone concentrations. As pressure increases, however, ozone effect is progressively less important. Furthermore, from the slope of the curves, it can be seen that the effect of ozone addition tends to decrease with increasing ozone concentration.

On the other hand, at 800 K, as shown in Figure 4.4, pressure has the opposite effect on the percentage variation of IDT compared to the case at 600 K. This reversal of the pressure effect occurs in the temperature range 760-840 K, gradually appearing and disappearing, with an intersection of the various profiles at temperatures close to the limits of the range, and is due to the shift of NTC region towards higher temperatures when pressure increases. For instance, as shown in Figure 4.3(a), for the case without ozone the relative minimum and maximum values in terms of IDT as a function of temperature occur at 720 K and 800 K for the 15 bar case, respectively; whereas, at 40 bar the relative minimum and maximum occur at 780 K and 840 K, respectively.

For temperatures higher than 840 K, IDT percentage variation decreases again as pressure increases, as shown in Figure 4.4 in the case 1000 K. Finally, when the temperature is very high, as shown in Figure 4.4 in the case 1200 K, both ozone and pressure have less influence on the percentage reduction of IDT, since, as discussed in section 3.2 and section 4.1.1, it is the temperature that mainly addresses the chemical kinetics.

Therefore, with the exception of the temperature range 760-840 K and of very high temperatures, ozone has a greater impact on the percentage reduction of IDT when pressure is higher.

4.2 2-D closed-valve cycle simulations of an HCCI engine

The aim of the following analysis was to evaluate the combined effect of ozone and residual gases in an HCCI engine. As discussed in section 1.2.1, in this type of engine, auto-ignition and the entire combustion process are governed by complex chemical kinetics, which is influenced by many factors including turbulence, mixture composition and the amount of residual gases.

The simulations were carried out by considering a test case from the literature [107]. Specifically, in [107], the authors conducted an experimental campaign on a cylinder of an engine operating under HCCI conditions with the characteristics presented in Table 2.3. In the experimental campaign, vaporized iso-octane, air and ozone were mixed in a plenum located upstream of the intake duct, and maintained at a temperature of 473 K; the intake pressure was 1 bar. After the plenum, an ozone analyser measured the ozone concentration according to the capacity of the ozone generator. The experimental data were collected in terms of in-cylinder pressure, from 30 CAD BTDC to 30 CAD ATDC every 0.1 CAD, during 100 working cycles, when the ozone generator operated at capacities of 0, 5, 30 and 100% corresponding to ozone concentrations of 0, 3.1, 16 and 35 ppm, respectively. The combustion characteristics, such as the Heat Release Rate (HRR), were obtained from in-cylinder pressure profiles with thermodynamic considerations.

In this work, closed-valve numerical simulations were carried out: specifically, simulations started at Intake Valve Closing (IVC = 157° BTDC) and ended at Exhaust Valve Opening (EVO = 140° ATDC). The simulations have been performed by using the modified Yoo mechanism presented in section 2.1.1.2, with the computational grid presented in Figure 2.6. A perfectly homogeneous mixture was considered at IVC, containing iso-octane, air, ozone and residual gases with different mass percentages (0, 5 and 10%), to take into account the residuals that remained trapped in the top dead center volume between one work cycle and the next. Concerning the composition of residual gases, two cases were considered. The first one concerned the calculation of the mass fractions of residuals from both the equivalence ratio ($\phi = 0.3$) and the stoichiometry of a single global combustion reaction:

R4.1) $C_8H_{18} + \frac{25}{2\phi}O_2 + 3.76\frac{25}{2\phi}N_2 + n_{O_3}O_3 \longrightarrow 8CO_2 + 9H_2O + + \frac{25}{2\phi}(1-\phi)O_2 +$
$3.76\frac{25}{2\phi}N_2 + n_{O_3}O_3$

where n_{O_3} are the ozone moles considered non-reactive in the calculation of residual gas composition. Therefore, in this case the only species contained in the residual gases were CO_2 and H_2O. The second case concerned the computation of the residual gases mass fraction from the composition obtained at the exhaust valve opening (EVO), i.e. at the end of the simulations with the previous approach. In this case, all chemical species that had a concentration greater than 1 ppm were considered, and the following system was solved for the calculation of the residuals mass fractions:

$$\begin{cases} \sum_i Y_i' = RG, & i = 1, \dots, N_s^{EVO} \\ \dfrac{Y_i'}{Y_j'} = a_i^{EVO}, & i = 1, \dots, N_s^{EVO} \ \wedge \ i \neq j \end{cases} \tag{Eq4.1}$$

where the unknown Y_i' is the i-th mass fraction of the generic species in residuals composition, N_s^{EVO} is the number of species at EVO with a concentration greater than 1 ppm, *RG* is the normalised value of the residual gas mass with respect to the total mass, Y_j' is the mass fraction of a generic species in residual gas, and a_i^{EVO} is the ratio between the mass fractions of species *i* and *j* at EVO.

The same ozone concentrations, referred to the iso-octane/air/ozone mixture, as in the experimental campaign were considered. The swirl ratio was set to 1 with a gas velocity linearly proportional to the distance from the cylinder axis (i.e., a rigid body profile), and the initial conditions in terms of turbulent kinetic energy (k) and its dissipation rate (ε) were evaluated by using the equations Eq2.78 and Eq2.79. The initial and boundary conditions in terms of wall temperature, gas temperature at IVC and pressure at IVC are discussed in detail in section 4.2.1 concerning the validation of the model.

4.2.1 Model validation

The validation of the model was carried out by comparing the pressure profile, the heat release rate profile and the reduction, with respect to maximum values, of some polluting emissions of the simulations with the experimental ones in [107].

Figure 4.5 shows the results in terms of pressure and heat release rate. The grey areas represent the areas of variability of the experimental traces, i.e. the set of traces obtained with 100 cycles. The initial and boundary conditions, in terms of temperature at IVC T_i, wall temperature T_w, and pressure at IVC P_i, relative to each case are shown in the legends, with temperature values expressed in K and pressure values expressed in bar. For validation, 5% by mass of residual gases were considered, in terms of CO_2 and H_2O, calculated via the reaction R4.1.

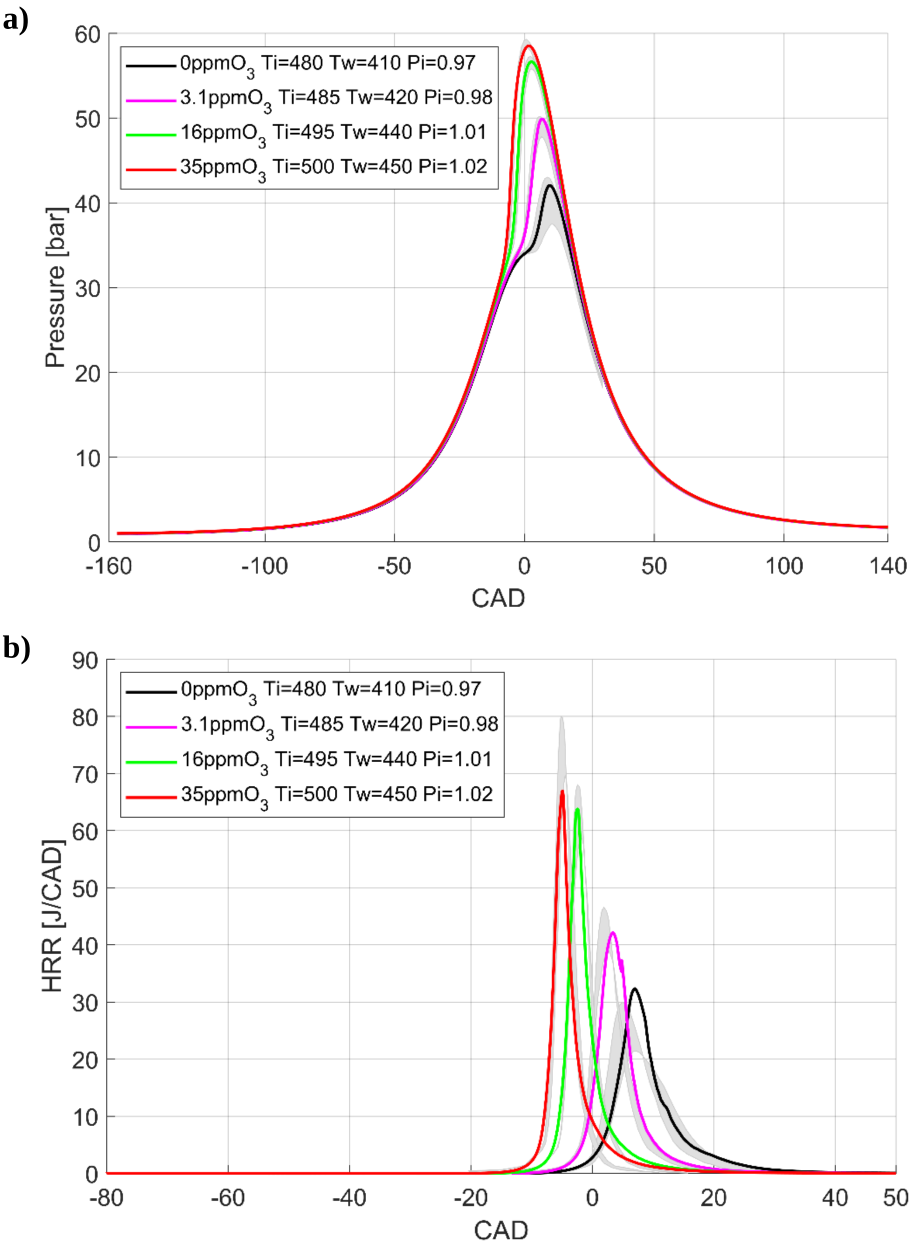

Figure 4.5. Comparison between experimental [107] (grey areas) and numerical results for the model validation, in terms of: (a) in-cylinder pressure; (b) Heat Release Rate.

As shown in Figure 4.5, slightly different values of the initial and boundary conditions were used in the cases with different ozone concentrations at IVC. Ozone, in fact, significantly modifies combustion efficiency and, consequently, the average pressure profile in the chamber. Without ozone, combustion takes place with an efficiency that varies considerably from cycle to cycle in the experimental case and is always lower than for the cases with ozonated air: the total heat released, on average, for the case without ozone is more than 16% lower than the case with 35 ppm O_3. For these reasons, it is reasonable to assume that the initial and boundary conditions were different for the different cases. Specifically, the initial pressure was set for the different cases in order to have approximately the same mass of gas mixture in the engine chamber.

The results show that, for all cases, the numerical pressure profiles fall within the experimental areas. The numerical HRR profiles are in good agreement with experiments, with slight differences for the cases with high cycle-to-cycle variability. However, it must be considered that the experimental HRR profiles were obtained from the pressure profiles on the basis of thermodynamic considerations. Numerically, without ozone the pressure peak occurs at about 9.8 CAD ATDC with a value of 42 bar; in the case with 35 ppm ozone, however, the pressure peak is advanced at 1.5 CAD ATDC, with a value of 58.5 bar. Concerning the HRR, without ozone, the peak occurs at about 7 CAD ATDC with a value of 32.3 J/CAD, and the CA50 (crank angle at which 50% of the total heat has been released) is 7.8 CAD ATDC; in the case with 35 ppm ozone, the HRR peak is obtained at 5 CAD BTDC with a value of 67.2 J/CAD, and the CA50 is 4.7 CAD BTDC. As in the experimental case, combustion efficiency is different for cases with different ozone concentrations. Specifically, the total heat released is 283 J, 293.5 J, 302.2 J and 305.4 J for the cases with 0, 3.1, 16 and 35 ppm ozone, respectively.

4.2.1.1 Effect of residual gas composition

The same simulations were carried out under the same conditions, but calculating the composition at IVC considering the composition of the residual gases that was obtained at EVO in the various cases, thus using the methodology described through the system of Equations Eq4.1. Specifically, all species with a concentration greater than 1 ppm at the EVO were considered.

The results are very similar to those obtained with the simplified composition. In particular: the pressure profiles differ by a maximum of +0.46 bar, a value that occurs for the case without ozone at 7 CAD ATDC; the HRR profiles differ by a maximum of +1.89 J, a value that occurs for the case without ozone at 5.9 CAD ATDC; the greater difference in terms of the total heat released is +2 J and occurs in the case without ozone.

Figure 4.6 shows the reductions, with respect to maximum values, of exhaust pollutants of both unburned hydrocarbons (UHCs) and nitrogen oxides (NO_x) as a function of the crank angle at which the pressure peaks occur in the experimental case, both in the simplified (R4.1) and extended (Eq4.1) mixture composition cases. The crank angle at which the pressure peak occurs ($\mathrm{CA_{Pmax}}$) is related to the capacity of the ozone generator; specifically, as the ozone concentration increases, the pressure peak advances, as shown in Figure 4.5(a).

Numerical results show good agreement with experimental results for both UHCs and NO_x, with minimal differences between the simplified and the extended mixture. With increasing ozone concentration, and thus with decreasing $\mathrm{CA_{Pmax}}$, unburned hydrocarbons decrease to about 26% and 19% of the amount obtained without ozone for experimental and numerical cases, respectively, due to more complete combustion. For example, considering only iso-octane, in the case without ozone at the exhaust remains about 4.66% and 5% of the initial mass for the cases with extended and simplified mixture, respectively, while in the case with 35 ppm of ozone only 0.47% and 0.46% remains for the same cases. This is the amount of fuel trapped in the crevices, where no combustion takes place.

On the contrary, nitrogen oxides decrease as the ozone concentration decreases, and thus with increasing $\mathrm{CA_{Pmax}}$. As NO_x are produced by the high local temperatures reached in the chamber, they are found in greater quantities where combustion has been faster and more complete. Comparison between numerical and experimental results for nitrogen oxides gives more marked differences, especially with the decrease in ozone concentration. These differences are mainly due to the positioning of the numerical curves within the experimental cycle-to-cycle variability areas: as shown in Figure 4.5(a), in the cases without ozone and with 3.1 ppm ozone, the numerical curves are in the upper portion of the respective experimental variability areas, so they are probably representative of the cases where combustion was more efficient and complete than in the cycles considered for the experimental measurements, leading to a higher NO_x production.

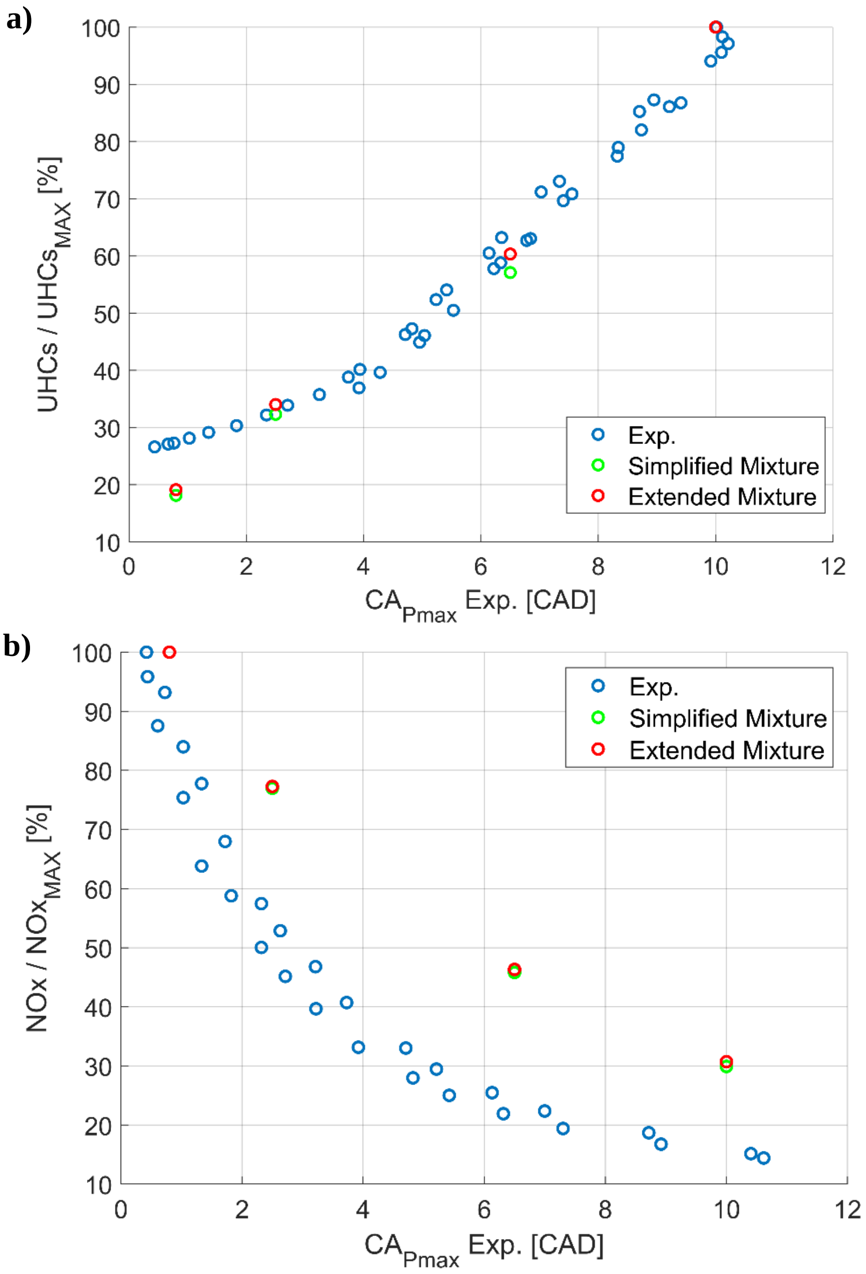

Figure 4.6. Comparison between experimental [107] and numerical results in terms of exhaust pollutants reduction, with respect to the maximum values, as a function of the crank angle at which the pressure peak occurs, both in the simplified and extended composition cases: (a) unburned hydrocarbons (UHCs); (b) nitrogen oxides (NO_x).

4.2.1.2 *Effect of ozone with the same initial and boundary conditions*

To verify that the model was indeed able to predict the effect of ozone, and therefore that the previous results were not merely the result of varying other thermodynamic conditions, simulations were also conducted by changing only the initial ozone concentration, maintaining the initial and boundary conditions of the case without ozone with simplified composition mixture at IVC. Figure 4.7 shows the results in terms of pressure, mass-averaged in-cylinder temperature, and heat release rate.

The results show a trend similar to that seen in Figure 4.5, but obviously with a smaller effect. Specifically, with 35 ppm ozone, the peak pressure increases by 10 bar and occurs 4.7 CAD earlier than in the case without ozone. In addition, the auto-ignition timing is advanced by about 5 CAD and the HRR peak is advanced by about 5.5 CAD and increases by 22 J/CAD, in agreement with the IDT reduction with ozone addition discussed and investigated in section 4.1. The average in-cylinder temperature reaches a maximum value of 1760 K with 35 ppm ozone, 150 K more than in the case without ozone.

Defining combustion duration as the difference between CA90 and CA10 (i.e. the crank angles when 10% and 90% of the total heat has been released, respectively), the combustion parameters CA10, CA50, CA90, combustion duration and total heat released are summarizes in Table 4.1. As it can be seen, in addition to advancing the mixture auto-ignition, ozone also causes a reduction of combustion duration and a more complete combustion.

Table 4.1. Combustion parameters for cases with different ozone concentrations at IVC. $T_i = 480\,K,\ T_w = 410\,K,\ P_i = 0.97\,bar.$

	$0\,ppm\,O_3$	$3.1\,ppm\,O_3$	$16\,ppm\,O_3$	$35\,ppm\,O_3$
CA10 [CAD]	3.4 ATDC	2.59 ATDC	0.52 ATDC	1.4 BTDC
CA50 [CAD]	7.98 ATDC	6.97 ATDC	4.26 ATDC	1.89 ATDC
CA90 [CAD]	17.14 ATDC	14.54 ATDC	10.02 ATDC	7.77 ATDC
CA90-CA10 [CAD]	13.74	11.95	9.5	9.17
Total heat release [J]	283	288	294	296

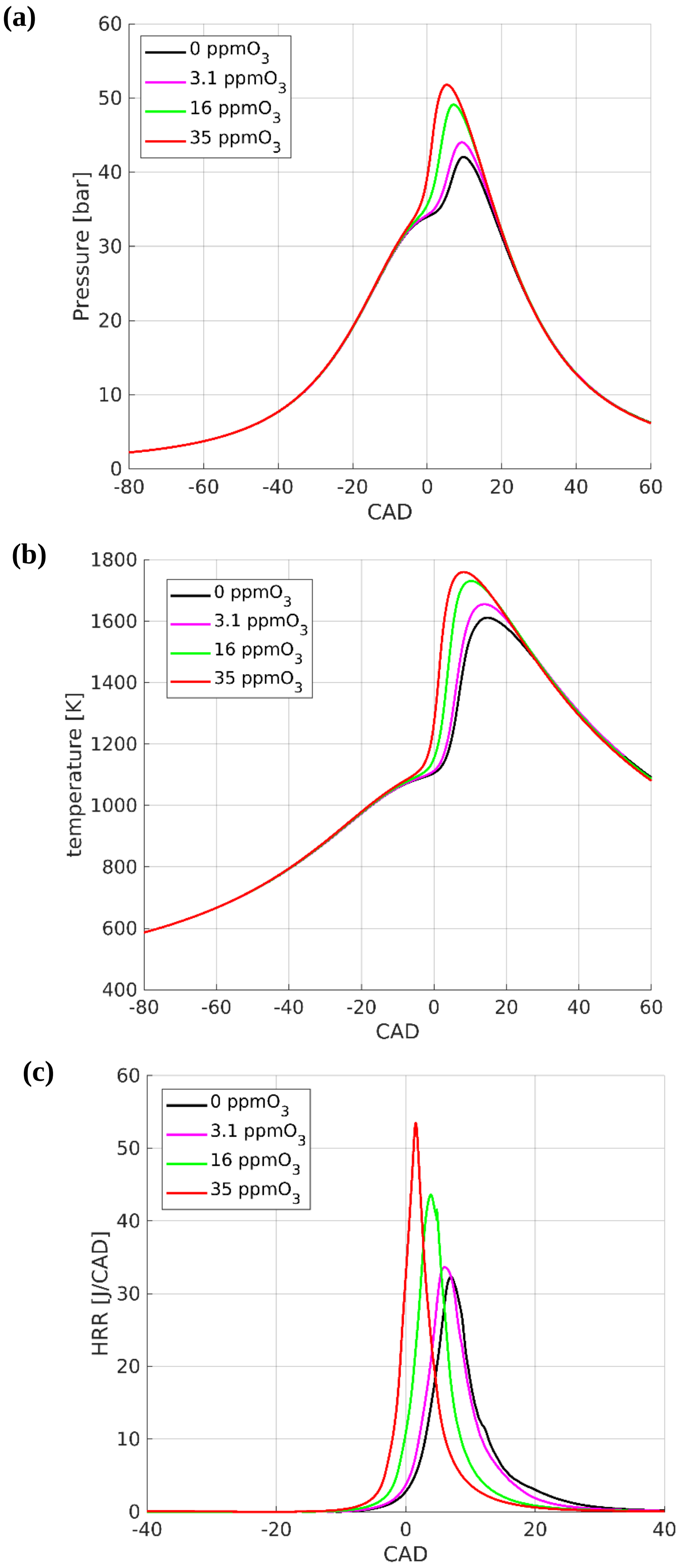

Figure 4.7. Results obtained with $T_i = 480\ K,\ T_w = 410\ K,\ P_i = 0.97\ bar$ for different ozone concentrations in terms of: (a) in-cylinder pressure; (b) in cylinder-temperature; (c) heat release rate.

In conclusion, considering that at engine regime the operating conditions vary in the cases with different ozone concentrations at IVC, and therefore it is not ozone alone that produces the results seen in Figure 4.5, it can be concluded that the model is able to predict the effect of ozone addition in HCCI engines.

4.2.2 Effect of ozone and residual gas

Considering the cases validated against experimental data (with slightly different initial and boundary conditions) but with the extended mixture composition (hereafter referred to as EM), the combined effect of ozone and the amount of residual gas in the chamber was evaluated. Figure 4.8 shows the fuel, ozone and heat release profiles for the cases with different ozone concentrations but the same amount of residual gas (5% by mass).

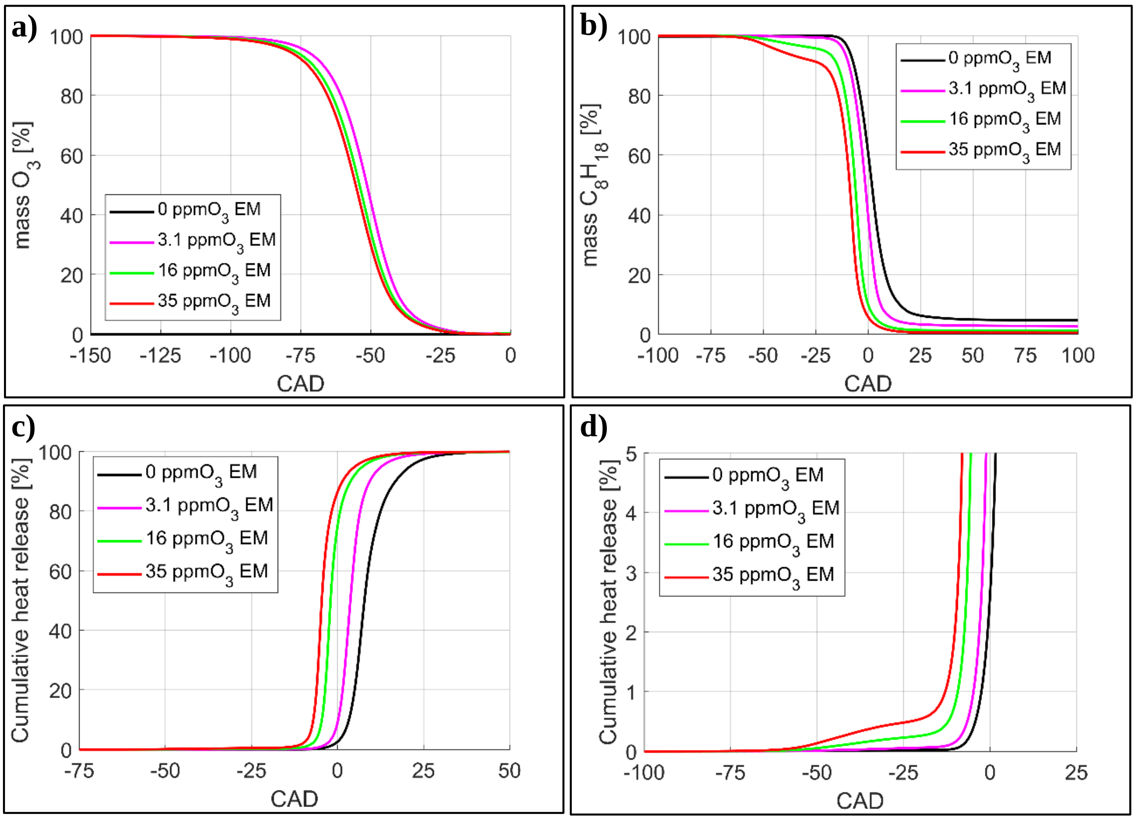

Figure 4.8. Profiles of some quantities as a function of CAD for Extended Mixture (EM) cases with 5% by mass of residual gases: a) ozone; b) iso-octane; c) cumulative heat release; d) detail of cumulative heat release.

Figure 4.8(a) and (b) show that both ozone and fuel are consumed during the compression phase. In particular, ozone decomposition is mainly due to the reaction $O_3 + N_2 \rightleftarrows O_2 + O + N_2$; since at the same CAD the temperature is slightly higher at higher ozone concentrations, the ozone decomposition reaction is favoured. Specifically, at -100 CAD (i.e. 100 CAD BTDC), ozone amount is greater than 99% of that at IVC for all cases considered; at -60 CAD (i.e. 60 CAD BTDC) the ozone levels in the chamber are 79%, 70.7% and 66.2% of that at IVC for cases with 3.1ppm, 16ppm and 35ppm ozone, respectively; finally, at -20 CAD (20 CAD BTDC), the amount of ozone is less than 1% for all cases.

The availability of oxygen atoms, produced by the ozone decomposition process, enables the reactions $C_8H_{18} + O \longrightarrow C_8H_{17} + OH$ and $C_8H_{18} + OH \longrightarrow C_8H_{17} + H_2O$, which consume the fuel before the natural auto-ignition. As shown in Figure 4.8(b), iso-octane starts to be consumed earlier and to a greater extent in the cases with higher ozone concentration. Specifically, at 20 CAD BTDC the mass of iso-octane is 89.2%, 94.7%, 99.2% and 100% of that initially available at IVC for cases with 35 ppm, 16 ppm, 3.1 ppm and 0 ppm ozone, respectively. The above chemical reactions, in addition to leading to the production of radicals and intermediate chemical species, cause an acceleration of the chemical kinetics in the initial stages of combustion, resulting in heat release. In cases with ozone addition, in fact, a small amount of heat is released before the natural combustion phase, as shown in Figure 4.8(c) and (d).

Then, using the EM composition in all cases, calculations were carried out by varying the amount of residual gas, considering cases with 0%, 5% and 10% by mass of residual gases for cases without ozone and with the addition of 35 ppm ozone. The initial and boundary conditions were the same for the cases with the same ozone concentration, and were those described in section 4.2.1 for validation. The objective was to compare the impact of ozone in cases with different amounts of residual gases with a realistic composition, which also takes into account the possible presence of reactive chemical species.

Figure 4.9 shows the results of the simulations in terms of pressure profile and heat release rate as a function of CAD, while Figure 4.10 and Figure 4.11 show the mass profiles of some chemical species, scaled to the initial fuel mass, as a function of CAD. Finally, Table 4.2 shows the combustion parameters for the different cases.

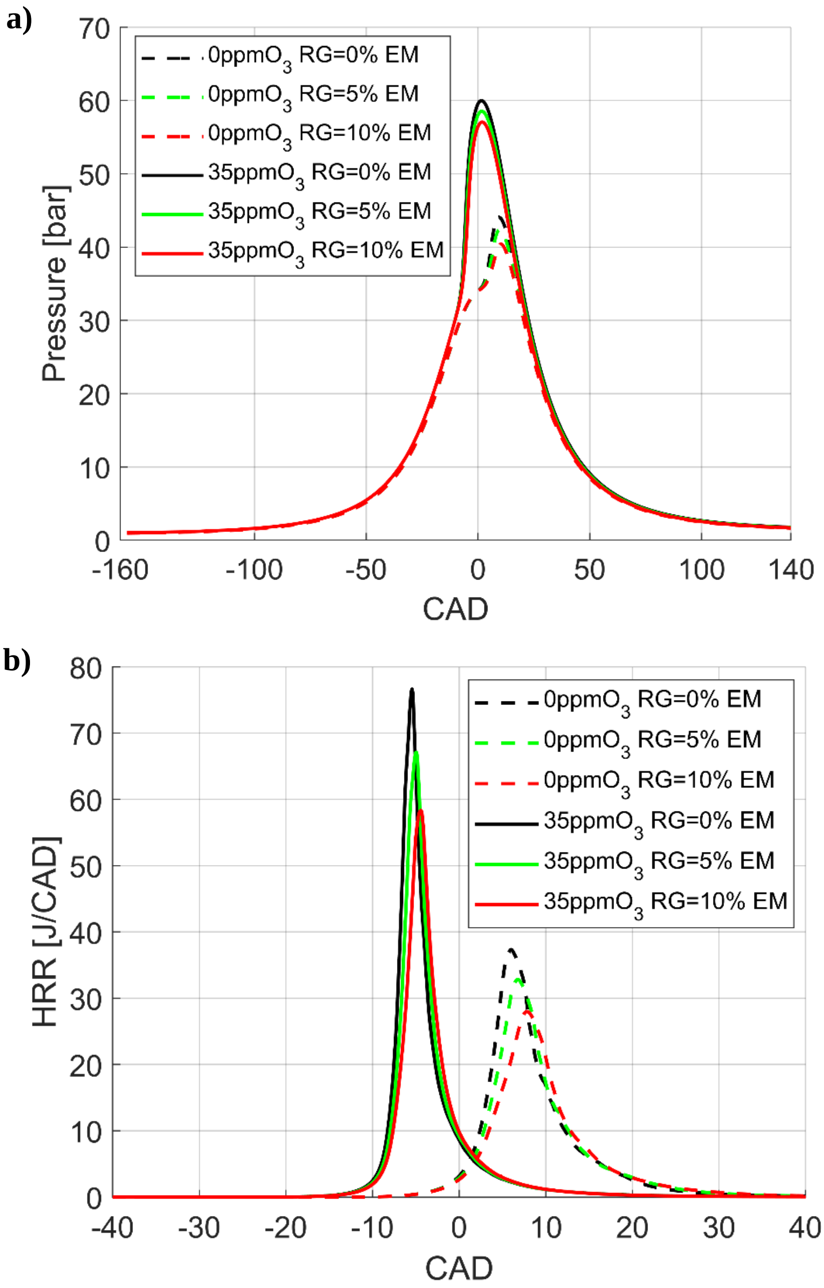

Figure 4.9. Results with different ozone concentrations and residual gases (RG) amounts, for Extended IVC Mixture cases (EM), in terms of: (a) in-cylinder pressure; (b) heat release rate.

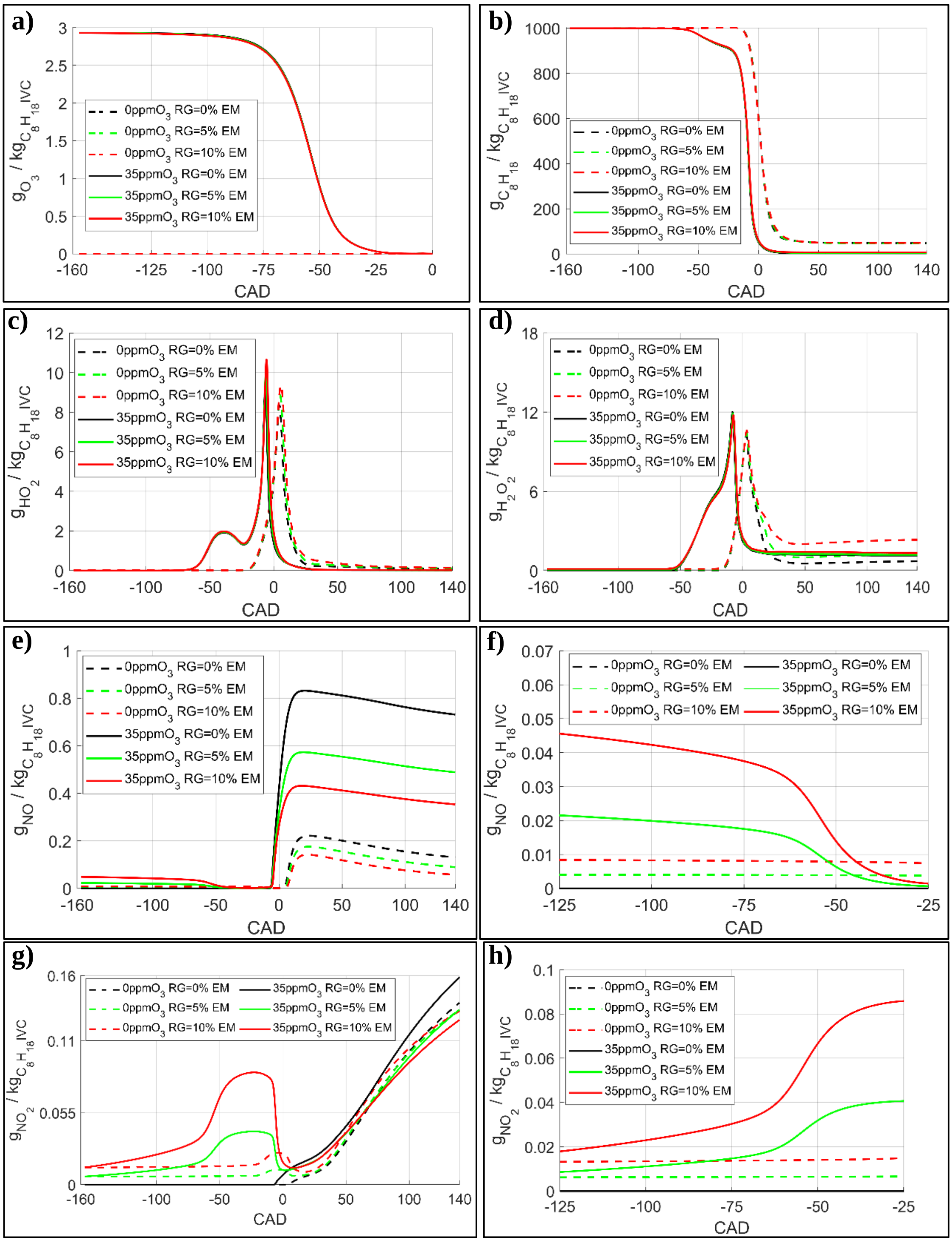

Figure 4.10. Profiles of the ratio between some chemical species mass and the initial fuel mass (C_8H_{18} at IVC) as a function of CAD for Extended IVC Mixture cases (EM): a) O_3; b) C_8H_{18}; c) HO_2; d) H_2O_2; e) NO; f) detail of NO; g) NO_2; h) detail of NO_2.

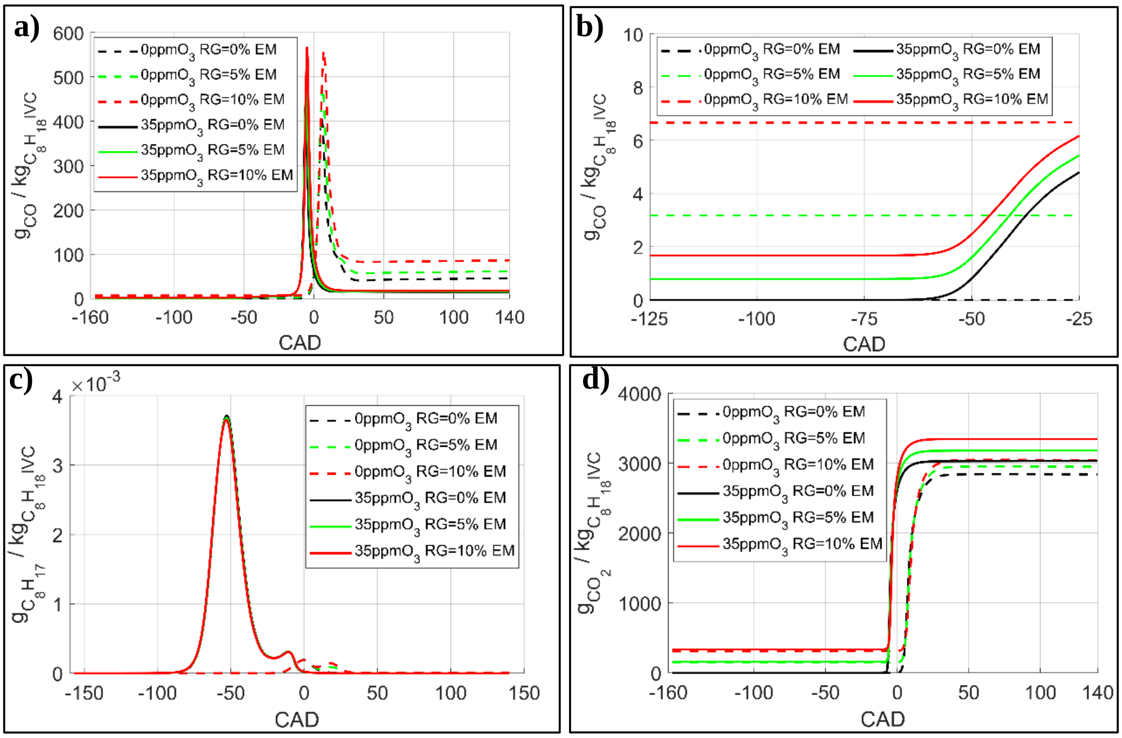

Figure 4.11. Profiles of the ratio between some chemical species mass and the initial fuel mass (C_8H_{18} at IVC) as a function of CAD for Extended IVC Mixture cases (EM): a) CO; b) detail of CO; c) C_8H_{17}; d) CO_2.

Table 4.2. Combustion parameters for cases with different ozone concentrations and Residual Gases (RG) amounts at IVC with Extended IVC Mixture cases (EM).

	$\text{Value}_{0ppm_{O_3}}$ / $\text{Value}_{35ppm_{O_3}}$		
	RG = 0%	**RG = 5%**	**RG = 10%**
CA10 [CAD]	+3.09 / -7.29	+3.30 / -7.05	+3.49 / -6.81
CA50 [CAD]	+7.16 / -5.04	+7.82 / -4.59	+8.62 / -4.09
CA90 [CAD]	+15.69 / +1.02	+16.83 / +1.44	+17.69 / +1.94
CA90-CA10 [CAD]	12.6 / 8.31	13.53 / 8.49	14.2 / 8.75
Total heat release [J]	302 / 323	286 / 306	266 / 289

Figure 4.9(a) shows that, for the same ozone concentration, increasing the percentage of residual gases at IVC reduces the peak pressure reached in the chamber due to the lower amount of fuel available at IVC, which results in less heat released, as shown in Table 4.2.

The consumption of ozone and fuel occurs almost in the same way in cases with different residual gases percentage at the same ozone concentration, as shown in Figure 4.10(a) and (b). As shown in Figure 4.10(c) and (d) in cases with 35 ppm O_3, when ozone starts to decompose, HO_2 and H_2O_2 are produced, which are typically associated with the LTC regime, leading to the advancement of mixture auto-ignition. However, ozone consumption is slightly faster in cases with a higher amount of residual gases, whereas the opposite occurs for fuel. Specifically, for the cases with 35 ppm ozone, at -90 CAD (i.e. 90 CAD BTDC), there are 2.88 and 2.86 g_{O_3}/kg_{fuel} in the chamber for the cases with no residual gases and with 10% of residual gases, respectively; in contrast, for the same cases at -30 CAD (i.e. 30 CAD BTDC), 92% and 94% of the initial fuel is in the chamber.

Ozone, in fact, in the presence of residual gases does not decompose exclusively through the reaction $O_3 + N_2 \rightleftarrows O_2 + O + N_2$, but reacts directly with certain species, such as nitrogen monoxide, through the reaction $NO + O_3 \rightarrow NO_2 + O_2$ with reactants molar ratio 1:1. By observing Figure 4.10(e),(f),(g),(h), it can be seen that, in cases without ozone, both the amount of nitrogen monoxide and nitrogen dioxide are constant up to about -20 CAD (i.e. 20 CAD BTDC); then, in the LTC regime, the nitrogen monoxide is oxidised and, when the temperature starts to rise very fast due to the increase in HRR, NO and NO_2 are produced again. On the other hand, in the cases with ozone, at IVC NO is converted immediately into NO_2, with a higher rate around -70 CAD (70 CAD BTDC), i.e. when ozone starts to be consumed faster. The $NO + O_3 \rightarrow NO_2 + O_2$ reaction reduces the amount of ozone available for the production of oxygen atoms in the pre-heating zone. However, considering the molecular weights and that, in the case with 35 ppm of ozone and 10% of residual gases, at IVC the mass of NO is about 0.32 μg, while that of ozone is about 19.25 μg, if only the $NO + O_3 \rightarrow NO_2 + O_2$ reaction took place there would still be about 97% of O_3 initially present.

The oxygen atoms that are produced by the $O_3 + N_2 \rightleftarrows O_2 + O + N_2$ reaction, being highly reactive, oxidise not only the fuel but many of the intermediate species present in the residual gases. As it can be seen in Figure 4.11(a), (b) and (c), in the CAD range in which ozone decomposes faster, there is both a production of C_8H_{17}, $C_8H_{18} + O \rightleftarrows C_8H_{17} + OH$, and a production of CO. Specifically, the peak of C_8H_{17} produced in the cases with ozone and with 10% of residual gases is 1.73% lower than in the case without residual gas, due to a lower amount of atomic oxygen reacting with iso-octane.

Finally, the following engine performance parameters were calculated, and the results are shown in Table 4.3:

- the gross indicated work per cycle, $W_{c,I}^{g}$, defined as the work delivered to the piston over the compression and expansion strokes, computed as: $W_{c,I}^{g} = \int_{IVC}^{EVO} PdV$;
- the gross Indicated Mean Effective Pressure, $IMEP^{g}$, computed as: $IMEP^{g} = \frac{W_{c,I}^{g}}{V_c}$;
- the gross indicated power output, $\dot{P}_I^{g}$, computed as: $\dot{P}_I^{g} = W_{c,I}^{g} * \frac{RPM}{60n_{rc}}$ where n_{rc} is the number of revolutions per cycle, therefore $n_{rc} = 2$;
- the gross Specific Fuel Consumption, SFC^{g}, computed as: $SFC^{g} = \frac{M_{fuel_{IVC}}}{W_{c,I}^{g}}$, where $M_{fuel_{IVC}}$ is the mass of fuel at IVC, which is related to the gross thermodynamic efficiency of the cycle by: $\eta_{th}^{g} = \frac{1}{H_{i,fuel}SFC^{g}}$ where η_{th}^{g} is the gross thermodynamic efficiency and $H_{i,fuel}$ is the lower calorific value of the fuel.

Table 4.3. Engine performance parameters for cases with different ozone concentrations and Residual Gases (RG) amounts at IVC with Extended IVC Mixture cases (EM).

	$\text{Value}_{0ppm_{O_3}}$ / $\frac{\text{Value}_{35ppm_{O_3}} - \text{Value}_{0ppm_{O_3}}}{\text{Value}_{0ppm_{O_3}}} * 100$		
	RG = 0%	**RG = 5%**	**RG = 10%**
$W_{c,I}^{g}$ **[J]**	141.5 / +2.52%	132.4 / +3.58%	122.2 / +5.7%
$IMEP^{g}$ **[bar]**	2.83 / +2.52%	2.65 / +3.58%	2.45 / +5.7%
$\dot{P}_I^{g}$ **[kW]**	1.77 / +2.52%	1.66 / +3.58%	1.53 / +5.7%
SFC^{g} **[g/kWh]**	184.26 / -1.54%	187.35 / -2.77%	192.65 / -4.96%

The results show that the ozone effect is higher in the case with a higher percentage of residual gas. Furthermore, with the addition of 35 ppm ozone, combustion duration is reduced by 34.05%, 37.25% and 38.38% for the cases with 0%, 5% and 10% residual gases. Despite the presence of chemical species that could limit the effectiveness of ozone (e.g. nitrogen monoxide), since they are contained in much smaller quantities than ozone, they had almost no impact with respect to the benefits of ozone. On the other hand, ozone addition mainly helped cases with a higher percentage of residual gases and with a lower performance, due to both the lower amount of fuel available and the residual gases, which slow down combustion.

5. Chapter 5: Investigation of ozone effects in SI engines

This chapter will present the results of the simulations of possible applications of ozone in Spark Ignition (SI) engines fuelled with iso-octane. These analyses concerned: the calculation of the Laminar Flame Speed (LFS) under engine-like thermo-chemical conditions, and the closed valve cycle simulations of a Spark Ignition engine with ozone addition. Analyses were conducted covering a wide range of operating conditions depending on the aim of the investigation.

5.1 LFS of iso-octane/air/ozone mixtures under engine-like thermo-chemical conditions: engine speed, spark advance and equivalence ratio effects

The aim of the following analyses was to calculate the laminar flame speed of an iso-octane/air/ozone mixture under Spark Ignition engine-like conditions at the ignition timing. Since ozone influences the thermo-chemical characteristics of the mixture during the compression stroke of the engine, such a mixture is analyzed up to ignition by using both 0-D and 2-D CFD model. Then, a 1-D model has been employed to calculate the LFS of the mixture under the thermo-chemical conditions reached at the end of the compression stroke, as shown in Figure 5.1.

5.1.1 0-D engine compression simulations

The 0-D engine model was used to simulate the compression stroke of the Spark Ignition engine described in section 2.2.2, whose geometric characteristics were presented in Table 2.2. Several simulations have been performed, using the modified Curran mechanism presented in section 2.1.1.2, by varying ozone concentrations, engine speed and Spark Advance (SA), from 0 to 50 ppm referred to air, from 1000 to 5000 rpm, and from 18 CAD BTDC to 3 CAD BTDC, respectively. The equivalence ratio was stoichiometric, the wall temperature was kept constant and equal to 430 K, and the temperature and pressure at IVC were set equal to 350 K and 1 bar, respectively.

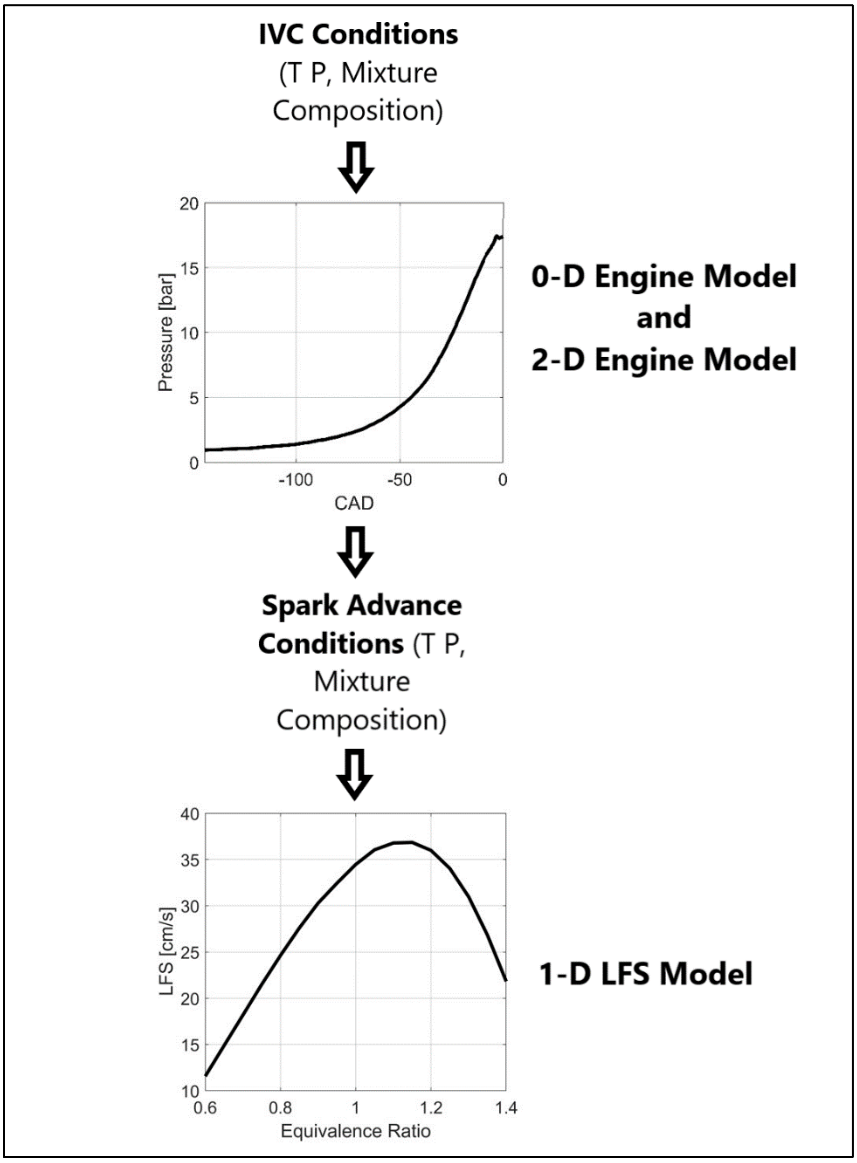

Figure 5.1. Schematic representation of the analyses conducted to calculate laminar flame speed under Spark Ignition engine like-conditions.

Table 5.1 shows the pressure and temperature values, obtained at the ignition timing, using the 0-D analysis, as a function of ozone concentration at IVC, rotation speed and Spark Advance. In all cases, pressure and temperature increase as the ozone concentration increases. However, this increment is lower with higher rpm and the earlier the ignition, as the ozone kinetics has less time to influence the mixture conditions. In accordance with the analyses discussed in section 3.1.3, calculations showed that when the temperature, during compression, reached values of around 550 K, ozone began to decompose very quickly, reacting with the fuel and producing O, OH and H, triggering the low-temperature reactions discussed above. These reactions are responsible for the slight increase in temperature and pressure obtained at the ignition timing by adding ozone.

Table 5.1. Thermodynamic conditions obtained with 0-D simulations, using the modified Curran kinetic mechanism, varying the ozone concentration at the IVC and the rotation regime, at different time instants (expressed in CAD BTDC).

	1000 rpm; 3 CAD		**3000 rpm; 3CAD**		**5000 rpm; 3 CAD**	
ppm O_3	**P [bar]**	**T [K]**	**P [bar]**	**T [K]**	**P [bar]**	**T [K]**
0	18.23	693.20	18.34	697.27	18.37	698.77
10	18.40	699.80	18.36	698.13	18.39	699.22
30	18.75	712.50	18.40	699.90	18.41	700.15
50	19.11	726.00	18.45	701.66	18.43	701.08
	1000 rpm; 8 CAD		**3000 rpm; 8 CAD**		**5000 rpm; 8 CAD**	
ppm O_3	**P [bar]**	**T [K]**	**P [bar]**	**T [K]**	**P [bar]**	**T [K]**
0	17.33	687.82	17.40	690.98	17.43	692.18
10	17.39	690.25	17.42	691.47	17.44	692.45
30	17.51	694.99	17.44	692.47	17.45	693.02
50	17.63	699.55	17.47	693.50	17.47	693.60
	1000 rpm; 13 CAD		**3000 rpm; 13 CAD**		**5000 rpm; 13 CAD**	
ppm O_3	**P [bar]**	**T [K]**	**P [bar]**	**T [K]**	**P [bar]**	**T [K]**
0	15.77	675.54	15.82	677.91	15.83	678.67
10	15.79	676.49	15.83	678.17	15.84	678.81
30	15.83	678.38	15.84	678.71	15.84	679.12
50	15.88	680.24	15.85	679.26	15.85	679.43
	1000 rpm; 18 CAD		**3000 rpm; 18 CAD**		**5000 rpm; 18 CAD**	
ppm O_3	**P [bar]**	**T [K]**	**P [bar]**	**T [K]**	**P [bar]**	**T [K]**
0	13.87	658.15	13.91	659.87	13.92	660.43
10	13.88	658.57	13.91	659.99	13.92	660.50
30	13.90	659.42	13.92	660.24	13.93	660.64
50	13.92	660.29	13.92	660.51	13.93	660.78

Figure 5.2 and Figure 5.3 show, respectively, the mass fractions of iso-octane and ppm of ozone as a function of initial ozone concentration at IVC, under different operating conditions and at different time instants.

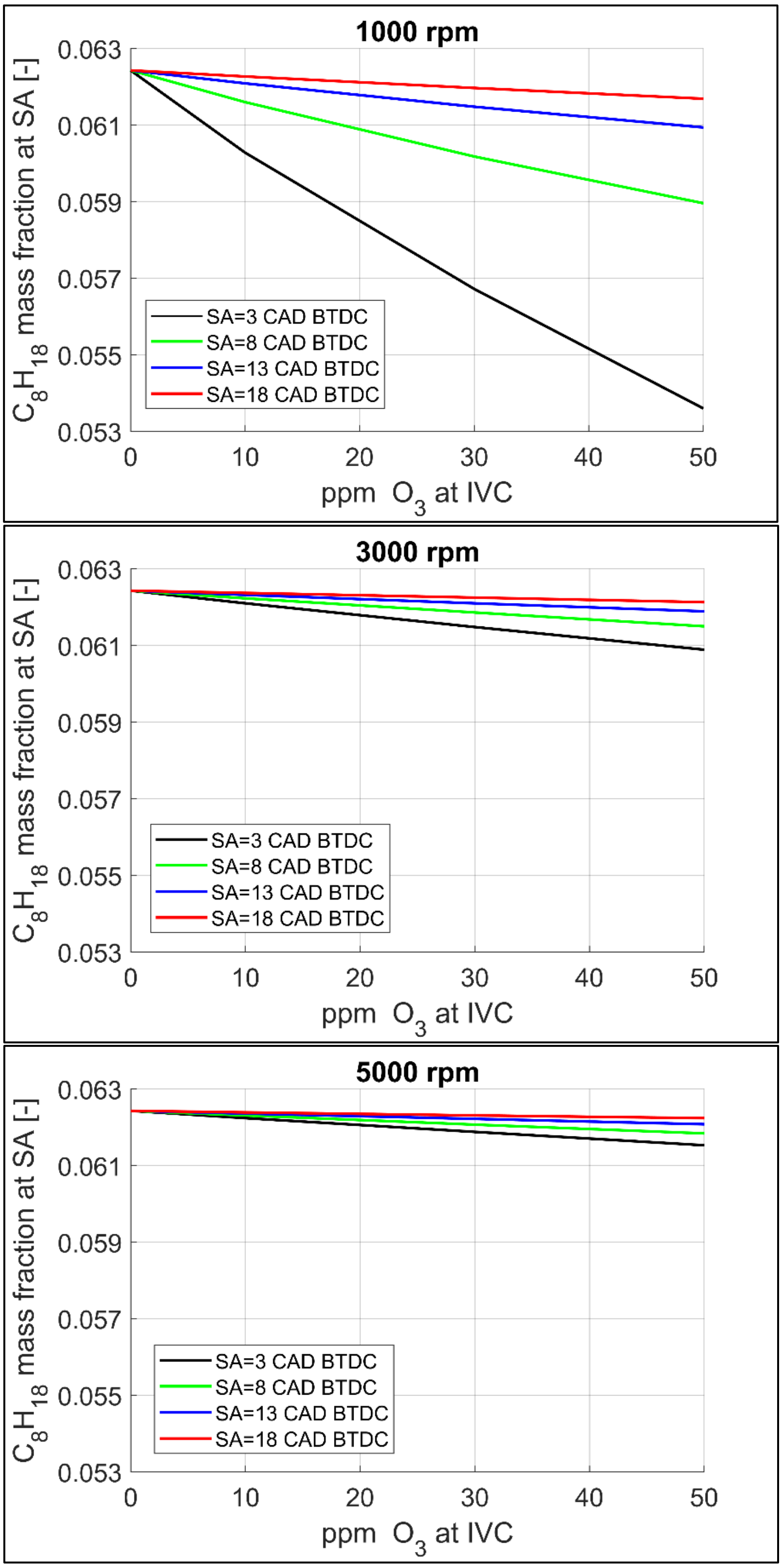

Figure 5.2. Mass fractions of iso-octane, obtained using the modified Curran kinetic mechanism, as a function of ozone concentration at IVC for different engine rotation regimes and different time instants.

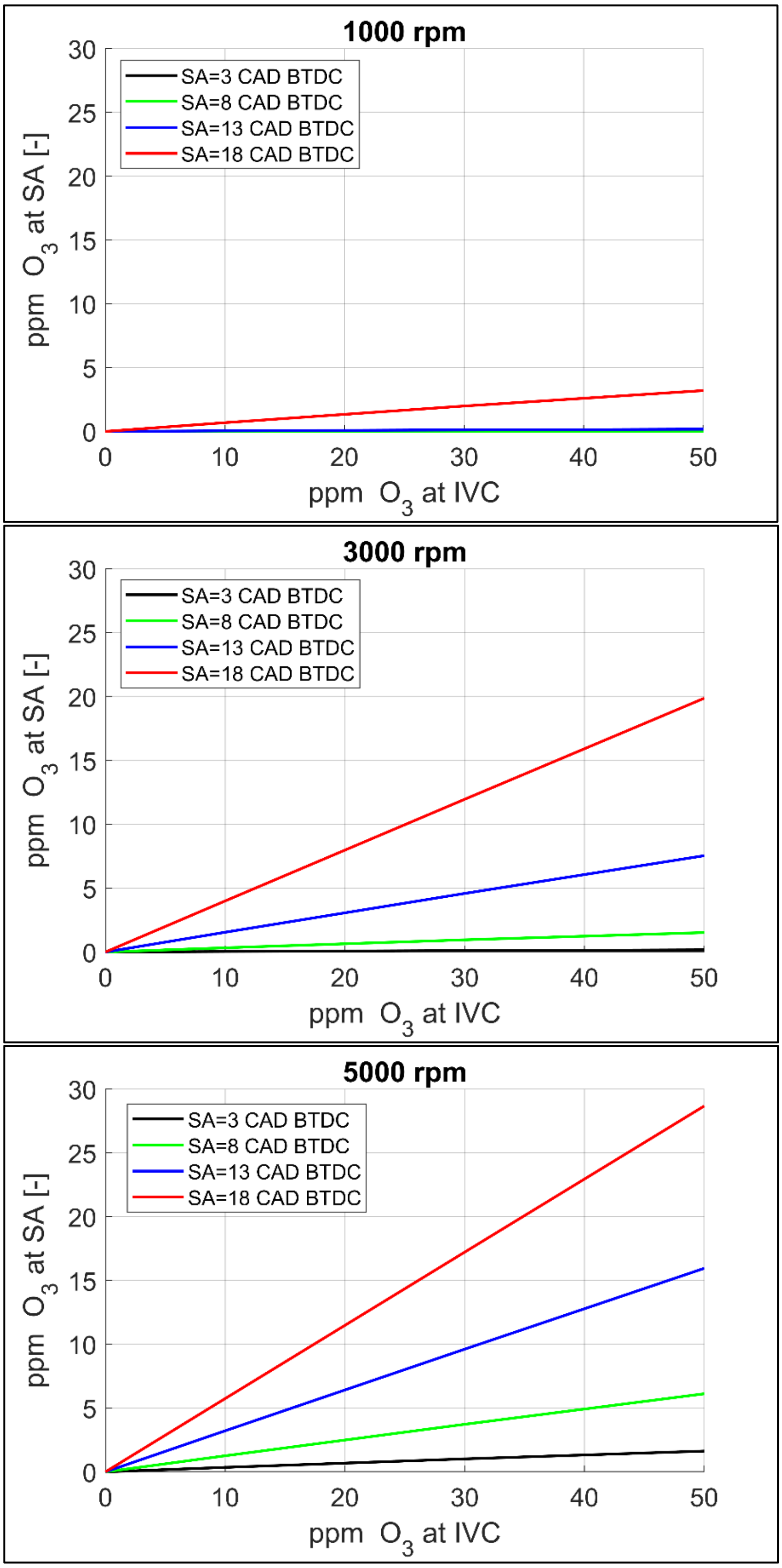

Figure 5.3. Ppm of ozone, obtained using the modified Curran kinetic mechanism, as a function of ozone concentration at IVC for different engine rotation regimes and different time instants.

Figure 5.2 shows that, given the engine speed and the ignition timing, the amount of fuel decreases linearly as the initial ozone concentration increases. In particular, in the 1000 rpm case, at the instant SA=3 CAD BTDC about 85% of the fuel initially contained in the chamber was present. The increase in rpm and the advance of the ignition timing have the effect of reducing the progression of fuel oxidation during compression. These two factors reduce the residence time of the mixture, so both the oxidation reactions with the radicals produced by ozone decomposition and the ozone decomposition reaction do not have time to take place completely. Figure 5.3 shows that at 1000 rpm only in the case of CA=18 CAD BTDC a little amount of ozone is still present, while by increasing the rpm and anticipating the ignition timing, the amount of ozone at SA increases. Specifically, in the case 5000 rpm with SA=18 CAD BTDC, with respect to the 50 ppm of ozone at the IVC, there was still almost 29 ppm at the SA.

Finally, Figure 5.4 shows the laminar flame speed calculated considering the mixture composition and thermodynamic conditions found, for different rotation regimes and time instants, from the 0-D analysis.

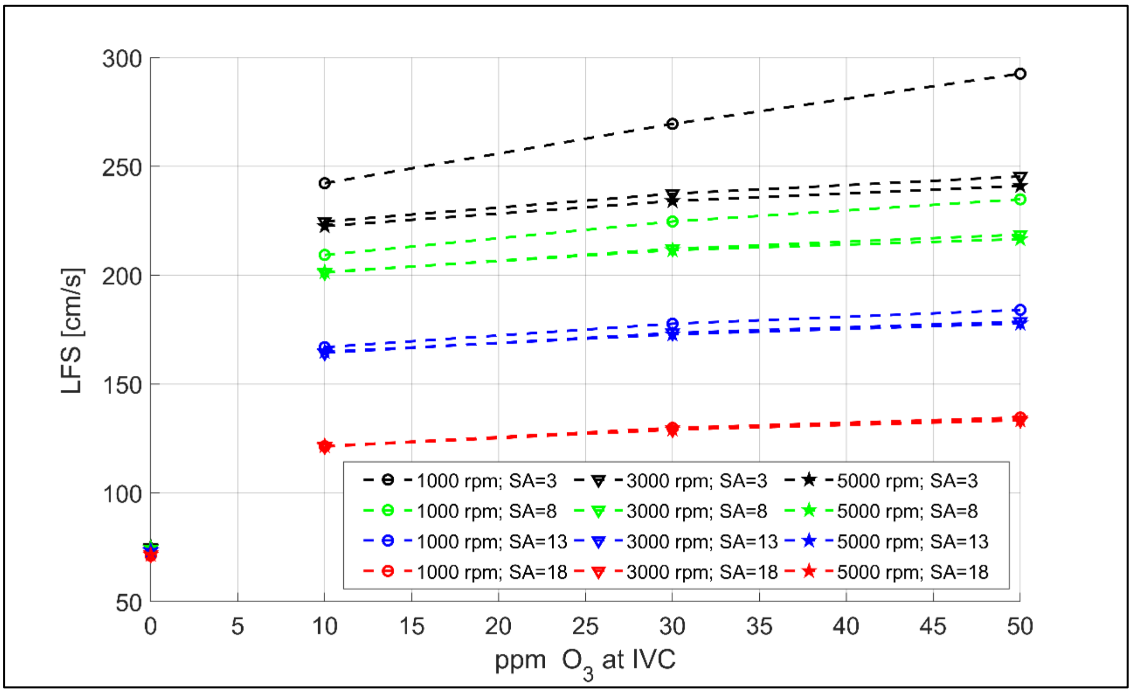

Figure 5.4. Laminar Flame Speed, obtained using the modified Curran kinetic mechanism, as a function of ozone concentration at IVC for different engine rotation regimes and different time instants.

The results show that without ozone addition, the flame propagates at approximately the same speed (72-75 cm/s) regardless of the conditions analysed. On the other hand, by adding ozone at IVC, there is a significant increase in laminar flame speed, which differs according to the conditions examined. As shown in Figure 5.4, in all cases considered, a significant increase in LFS was found already with 10 ppm of ozone compared to the case without O_3. These results are in agreement with the discussion in section 3.1.4.2: ozone, at the pressure and temperature conditions shown in Table 5.1, enables low temperature chemistry, changing the main reaction pathways responsible for the increase in LFS. The change of reaction pathways, therefore, is responsible for the discontinuity between the case without ozone and the case with ozone.

With ozone addition, the chemical kinetics, which follows the new reaction pathways, is accelerated by increasing the ozone concentration: the LFS increases approximately linearly with increasing ozone concentration at the IVC. Specifically, it is found that, given an engine speed, the laminar flame speed is higher the later the ignition occurs: this is due to the longer residence time of the mixture in the chamber, whereby the decomposition of ozone is more complete (as observed in Figure 5.3), providing more oxygen atoms and thus more OH radicals (from the fuel oxidation, as shown in Figure 5.2) responsible for the low-temperature chemistry and the cool flame. The same qualitative effect is obtained, for a constant ignition timing, by decreasing the engine speed. In this case, however, if ignition is advanced too much, the flame speed is progressively less dependent on the engine speed; for example, when ignition takes place at 18 CAD BTDC, the laminar flame speed is the same for all three values of rpm considered.

In conclusion, the greatest advantage in terms of laminar flame speed increase was obtained when the residence time of ozone in the chamber was longer; in this way, ozone decomposition was more complete and the amount of atomic oxygen, necessary to oxidise the fuel and to form OH radicals, was maximised.

5.1.2 2-D engine compression simulations

The same methodology used in the previous section is also employed to investigate the suitability of using ozone to achieve stable combustion of a very lean mixture ($\phi = 0.5$). To this end, firstly a 2-D CFD model is used to simulate the compression stroke of the same Spark Ignition engine considered in the previous section, then the LFS of iso-octane/air/ozone lean mixtures has been evaluated. The simulations have been performed by using the modified Yoo mechanism presented in section 2.1.1.2. At the start of the simulations (IVC), a perfectly homogeneous mixture containing iso-octane, air and ozone is taken into account. Two equivalence ratios, 0.5 and 1, and three ozone concentrations (in air), 0, 200 and 500 ppm, are considered. Since no experimental data with ozone addition were available in the literature, it was not possible to calibrate the EDC model during the compression stroke. For this reason, it was chosen to leave the default values of the EDC constants in order to carry out a parametric analysis. The remaining initial conditions and the boundary conditions were kept the same for all cases, to assess the influence of the initial mixture composition on the results. The initial temperature and pressure of the mixtures were 330 K and 0.97 bar, respectively, and the wall temperature was equal to 430 K during the entire simulation. The initial conditions in terms of turbulent kinetic energy (k) and its dissipation rate (ε) were evaluated by using the equations Eq2.78 and Eq2.79, thus obtaining 5 m^2/s^2 and 180 m^2/s^3 for k and ε, respectively. The thermo-chemical conditions of the mixture, in terms of temperature, pressure and composition, obtained at the end of the 2-D simulations (SA=3 CAD BTDC) in the middle of the chamber (i.e. on the axis of symmetry at the midpoint between piston and cylinder head, the place where the spark that triggers the flame is assumed to occur) were used to compute the laminar flame speed.

Table 5.2 summarizes the thermodynamic conditions, in terms of pressure and temperature, achieved in the middle of the combustion chamber at the start of ignition, i.e. 3 CAD BTDC, for all cases. For a given equivalence ratio, temperature and pressure at ignition are not influenced by the initial ozone concentration. However, under lean conditions, higher temperatures and pressures are obtained with respect to the stoichiometric case. This is due to the different specific heat of the mixture as equivalence ratio is varied. As an example, the specific heat at constant volume for $\phi = 0.5$ was 758 $\frac{J}{kgK}$ and 869 $\frac{J}{kgK}$ at IVC and SA, respectively, whereas, for the case with $\phi = 1$, was 789 $\frac{J}{kgK}$ and 926 $\frac{J}{kgK}$ at IVC and SA, respectively. Unlike the 0-D calculations shown in Table 5.1, pressure and temperature do not increase with increasing ozone concentration. However, the two results are not in contradiction considering that it is not possible to make a direct comparison between the two cases, specifically: the initial conditions of pressure and temperature are not the same; the kinetic mechanisms are different; with the

2-D model, turbulence is included, which increases the heat exchange with the walls and influences the chemical kinetics; the conditions in Table 5.2 refer to a specific point in the domain and therefore are not the average ones.

Table 5.2. Thermodynamic conditions at SA, i.e. 3 CA BTDC, in the middle of the chamber for different values of ozone concentration and equivalence ratio at IVC.

	Ozone concentration (in air) at IVC		
$\boldsymbol{\phi = 1}$ **(at IVC)**	$\boldsymbol{0\ ppm_{O_3}}$	$\boldsymbol{200\ ppm_{O_3}}$	$\boldsymbol{500\ ppm_{O_3}}$
Pressure [bar]	18.16	18.18	18.23
Temperature [K]	671	672	673
$\boldsymbol{\phi = 0.5}$ **(at IVC)**	$\boldsymbol{0\ ppm_{O_3}}$	$\boldsymbol{200\ ppm_{O_3}}$	$\boldsymbol{500\ ppm_{O_3}}$
Pressure [bar]	19.17	19.02	19.12
Temperature [K]	709	706	708

Figure 5.5 shows the mass of iso-octane, ozone, OH radicals and oxygen atoms as a function of CAD, for different ozone concentrations and equivalence ratios. If ozone is absent, fuel mass does not change up to ignition, nor O and OH radicals are produced. When ozone is added to the mixture, for stoichiometric and lean cases, both fuel and ozone decompose during the compression stroke, resulting in O and OH production. For the same initial ozone concentration, these phenomena occur more quickly with $\phi = 0.5$. The reason is that, as discussed earlier and shown in Table 5.2, at ignition, the temperature in the chamber is higher for the lean case, so chemical reactions are more favored. At the same equivalence ratio, at 3 CAD BTDC the percentage decrease in ozone is roughly the same in the cases with 200 ppm and with 500 ppm: the amount of O_3, with $\phi = 0.5$, is 42.5% and 41.4% of that at IVC for the cases with 200 e 500 ppm, respectively. However, for the case with 500 ppm, a larger amount of ozone is consumed, producing more oxygen atoms than for the case with only 200 ppm of ozone. Indeed, at about 50 CAD BTDC, ozone decomposes by the reaction $O_3 + N_2 \rightleftarrows O_2 + O + N_2$; the O atoms oxidize the fuel through the reaction $C_8H_{18} + O \rightleftarrows C_8H_{17} + OH$, producing OH radicals, which continue the oxidation through the reaction $C_8H_{18} + OH \rightleftarrows C_8H_{17} + H_2O$. For the case with $\phi = 0.5$, at 3 CAD BTDC, there is 92.1% and 97.4% of the fuel at IVC for the cases with 500 ppm and 200 ppm of ozone, respectively.

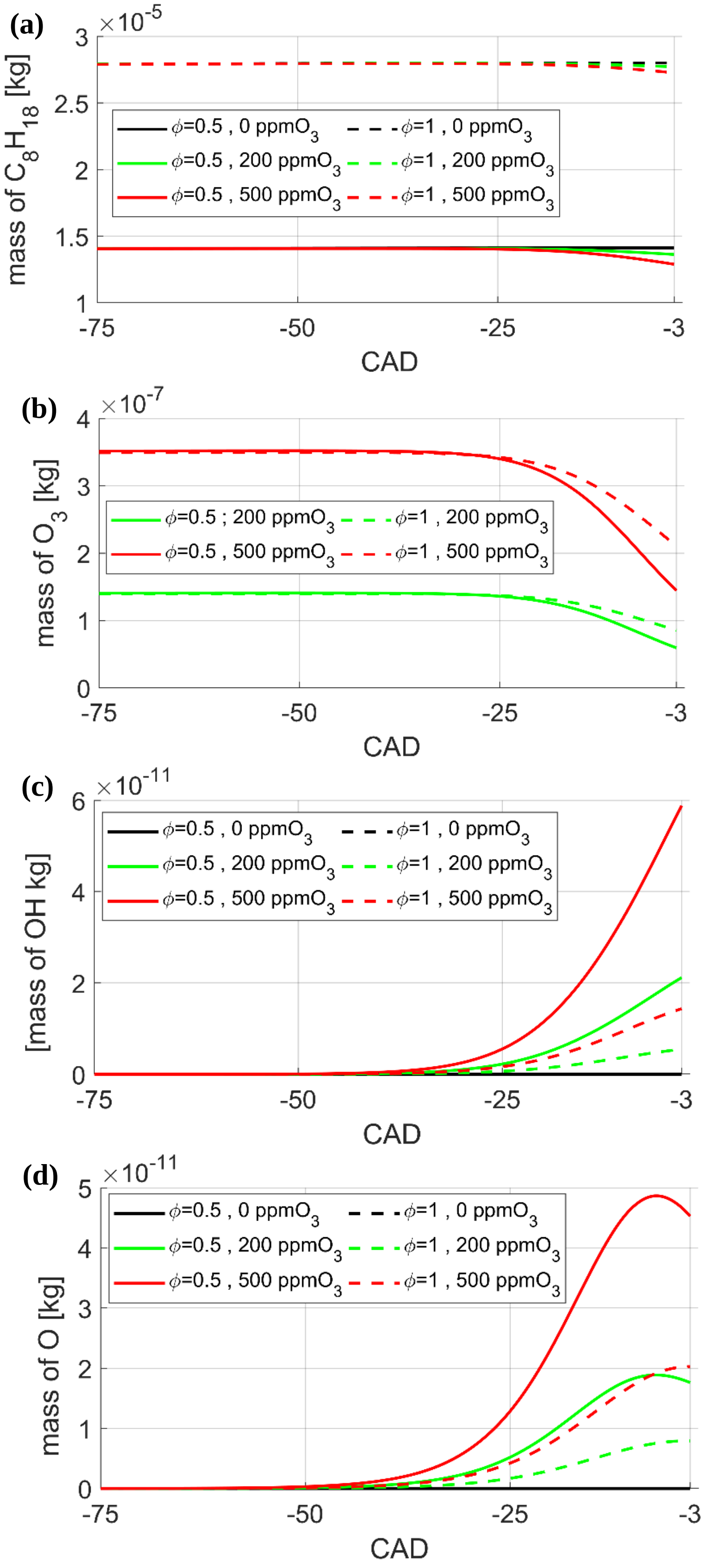

Figure 5.5. Mass of (a) C_8H_{18} , (b) O_3, (c) OH, (d) O as a function of CAD, for different ozone concentrations and equivalence ratios.

1-D simulations have been carried out to calculate the LFS by using the thermodynamic conditions and the mixture compositions achieved at the start of ignition in the combustion chamber by varying ozone concentrations and equivalence ratios. Table 5.3 shows the results in terms of LFS. As expected, with the same ozone concentration, LFS is higher in the stoichiometric than in the lean case. Moreover, LFS increases significantly with ozone concentration in both $\phi = 0.5$ and $\phi = 1$ cases. Specifically, the addition of 200 ppm of ozone at IVC in the case $\phi = 0.5$ increases LFS up to a value higher than that obtained in the stoichiometric case without ozone. Ozone influence is greater for the case of stoichiometric mixture. The LFS for the case with 200/500 ppm of ozone is about 5.3/6.4 and 7.1/9.0 times larger, compared to the case without ozone, with $\phi = 0.5$ and $\phi = 1$, respectively.

Figure 5.6 shows the temperature in the stream tube as a function of the distance from the inlet. This figure explains the reason for the significant increase of the LFS with ozone addition. Indeed, ozone changes the flame structure and leads to the formation of a cool flame. Such a flame does not occur with iso-octane/air mixtures, without ozone, under the typical thermodynamic conditions of an SI engine. Since, at the inlet of the stream tube, the temperature of the mixture is higher for the case $\phi = 0.5$ and there is a greater amount of O and OH, chemical kinetics is faster and the cool flame is generated very close to the inlet for the case of lean mixture. Hence, in agreement with the results obtained in section 3.1, ozone changes the reaction paths in the LTC region and causes the formation of a cool flame, thus leading to an increase in LFS.

Table 5.3. LFS for different equivalence ratios and ozone concentrations at IVC [cm/s].

	Ozone concentration (in air) at IVC		
	$\mathbf{0}\ \boldsymbol{ppm_{O_3}}$	$\mathbf{200}\ \boldsymbol{ppm_{O_3}}$	$\mathbf{500}\ \boldsymbol{ppm_{O_3}}$
$\boldsymbol{\phi = 0.5}$ **(at IVC)**	18.8	99.3	120.9
$\boldsymbol{\phi = 1}$ **(at IVC)**	63.5	452.0	569.6

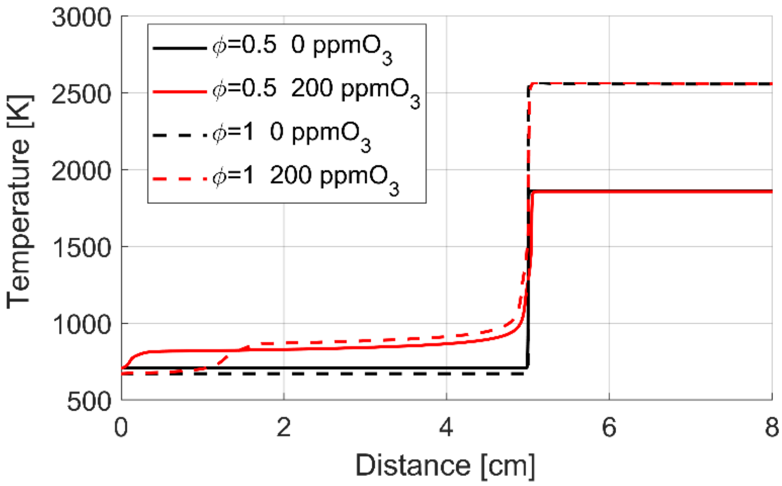

Figure 5.6. Stream tube temperature as a function of the distance from the inlet for different values of equivalence ratio and ozone concentration at IVC.

In conclusion, the results showed that ozone promotes the formation of a cool flame even under lean conditions ($\phi = 0.5$), however, the effect on the increase in LFS is greater in the stoichiometric case. The addition of ozone at IVC in the case $\phi = 0.5$ increases LFS up to values higher than that obtained for the stoichiometric case without ozone, therefore it can be concluded that ozone might be able to sustain stable combustion in the case of very lean mixtures in SI engines.

5.2 2-D closed-valve cycle simulations of an SI engine

After the evaluation of the ozone effect on the LFS under engine-like conditions, 2-D CFD simulations were carried out considering the closed-valve cycle of a Spark Ignition engine with the characteristics presented in Table 2.2. Specifically, the combustion and expansion phases of the engine up to the exhaust valve opening were also simulated in order to assess the ozone effect on engine performance, under different conditions of mixture composition and engine speed. As discussed specifically in sections 2.1.5.3 and 2.2.2, the EDC combustion model was used for these simulations in order to solve the chemical kinetics by considering the temperature, pressure, mixture composition and turbulence conditions of each specific cell in the domain.

5.2.1 Model validation

The CFD model is validated by comparing the in-cylinder pressure and Heat Release Rate (HRR) profiles with experimental results of [175]. The validation concerns with the closed-valve cycle, i.e. from IVC to EVO. As discussed in the previous section, due to the absence of experimental data with ozone addition, the values of the EDC model constants were left as the default ones during compression, while for the combustion phase the values were changed in order to validate the combustion model on the basis of experimental data. In the experimental case, the mixture is approximately stoichiometric, however, an equivalence ratio of 0.9 was considered in the present simulations. This difference between the experimental and numerical equivalence ratio can be justified by some approximations in the numerical model. In fact, the model does not take into account both the blow-by phenomenon, which reduces the fresh charge in the combustion chamber, and the crevices between the piston and cylinder, where combustion is almost absent. The mixture temperature at IVC is set to 410 K.

Figure 5.7 shows the comparison between the measurements and the simulation results. As shown in Figure 5.7(a), the model provides a good agreement with the pressure profile experiments, with some slight differences between TDC and 15 CAD ATDC, due to a faster numerical heat release in the first part of combustion, as shown in Figure 5.7(b).

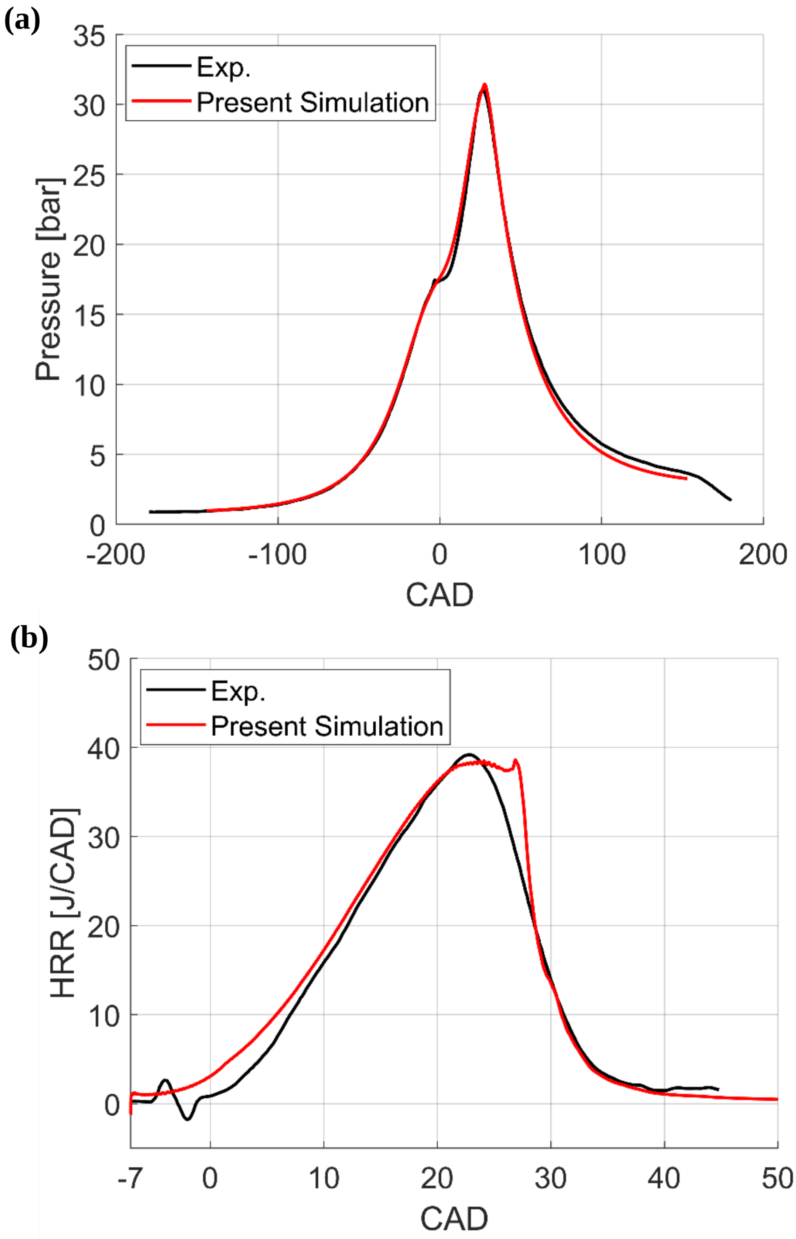

Figure 5.7. Comparison between experimental [175] and numerical results for the 2-D CFD model validation, in terms of: (a) in-cylinder pressure; (b) Heat Release Rate.

5.2.2 Ozone effect with different operating conditions

The simulations were conducted considering a perfectly homogeneous mixture at IVC containing iso-octane, air, ozone and residual gases (CO_2 and H_2O), to take into account residues trapped in the top dead center volume between consecutive work cycles. The composition of residual gases was computed by considering the stoichiometry of a single global combustion reaction as a function of the equivalence ratio (ϕ):

R5.1) $C_8H_{18} + \frac{25}{2\phi}O_2 + 3.76\frac{25}{2\phi}N_2 + n_{O_3}O_3 \longrightarrow 8CO_2 + 9H_2O + + \frac{25}{2\phi}(1-\phi)O_2 + 3.76\frac{25}{2\phi}N_2 + n_{O_3}O_3$

where n_{O_3} are the ozone moles, considered non-reactive in the calculation of residual gas composition. Therefore, the actual equivalence ratio in the chamber is slightly different from the theoretical one. The initial (at IVC) and boundary conditions of the simulations are shown in Table 5.4, with the ozone concentrations calculated with respect to the fresh intake mixture.

Table 5.4. Initial and boundary conditions of the simulations.

Pressure at IVC	0.97 bar
Temperature at IVC	410 K
Wall temperature	430 K
Equivalence ratio	$\simeq$ 0.9, 0.7
Residual gas (CO_2, H_2O) percentage	15%
Ozone concentration	0, 100, 200
Engine speed	800, 1000, 1200 rpm

The main combustion and performance parameters of a Spark Ignition engine were evaluated. Specifically, the following parameters, directly dependent on the combustion process, were evaluated:

- CA10, CA50, CA90 (i.e., the crank angles when 10%, 50% and 90% of the total heat has been released, respectively) and the combustion duration, which is defined as the difference between CA90 and CA10;
- the maximum volume-averaged in-cylinder pressure, $\bar{P}_{MAX}$, computed as: $\bar{P}_{MAX} = \max_{\theta}\left\{\frac{1}{V}\int_V PdV\right\}$ and its crank angle $\theta_{\bar{P}_{MAX}}$;
- the maximum mass-averaged in-cylinder temperature, $\bar{T}_{MAX}$, computed as: $\bar{T}_{MAX} = \max_{\theta}\left\{\frac{1}{M}\int_V \rho TdV\right\}$ and its crank angle $\theta_{\bar{T}_{MAX}}$;
- the Maximum Pressure Rise Rate, $MPRR = \max_{\theta}\left\{\frac{dP}{d\theta}\right\}$, and its crank angle θ_{MPRR}.

In addition, the following engine performance parameters were calculated:

- the gross indicated work per cycle, $W_{c,I}^{g}$, computed as: $W_{c,I}^{g} = \int_{IVC}^{EVO} PdV$;
- the gross Indicated Mean Effective Pressure, $IMEP^{g}$, computed as: $IMEP^{g} = \frac{W_{c,I}^{g}}{V_c}$;
- the gross indicated power output, $\dot{P}_I^{g}$, computed as: $\dot{P}_I^{g} = W_{c,I}^{g} * \frac{RPM}{60 n_{rc}}$ where n_{rc} is the number of revolutions per cycle, therefore $n_{rc} = 2$;
- the gross Specific Fuel Consumption, SFC^{g}, computed as: $SFC^{g} = \frac{M_{fuel_{IVC}}}{W_{c,I}^{g}}$, where $M_{fuel_{IVC}}$ is the mass fuel at IVC.

5.2.2.1 *Engine speed and ozone concentration effects*

Figure 5.8 shows the results in terms of pressure profiles for the cases $\phi \simeq 0.9$ without ozone and with the addition of 100 ppm O_3 for the different engine speeds with the same Spark Advance SA= -7 (i.e. 7 CAD BTDC); Table 5.5 shows the parameters directly dependent on the combustion process; on the other hand, Table 5.6 shows the engine performance parameters.

Table 5.5. Combustion parameters and other quantities directly dependent on the combustion process, for different cases with SA=-7 CAD with and without ozone addition at IVC.

	$\text{Value}_{0ppm_{O_3}}$ / $\text{Value}_{100ppm_{O_3}}$		
	1000rpm (base case)	**800rpm**	**1200rpm**
CA10 [CAD]	+8.22 / +5.31	+6.56 / +3.47	+9.77 / +7.01
CA50 [CAD]	+20.37 / +15.22	+16.88 / +11.70	+24.07 / +18.65
CA90 [CAD]	+29.35 / +20.34	+25.01 / +13.94	+33.77 / +26.02
CA90-CA10 [CAD]	21.13 / 15.03	18.45 / 10.47	24.00 / 19.01
$\bar{P}_{MAX}$ **[bar]**	31.44 / 41.29	35.85 / 49.96	27.45 / 34.70
$\theta_{\bar{P}_{MAX}}$ **[CAD]**	+27.67 / +20.31	+23.63 / +14.24	+31.88 / +25.29
$MPRR$ **[bar/CAD]**	0.78 / 4.01	1.21 / 17.98	0.46 / 0.96

$\boldsymbol{\theta_{MPRR}}$ **[CAD]**	+18.05 / +19.47	+14.82 / +13.24	+21.91 / +19.57
$\boldsymbol{\overline{T}_{MAX}}$ **[K]**	2326 / 2462	2361 / 2540	2296 / 2386
$\boldsymbol{\theta_{\overline{T}_{MAX}}}$ **[CAD]**	+31.27 / +21.76	+26.7 / +14.48	+35.99 / +28.09

Table 5.6. Engine performance parameters of the different cases with SA=-7 CAD with and without ozone addition at IVC.

	$\mathrm{Value}_{0ppm_{O_3}}$ / $\frac{\mathrm{Value}_{100ppm_{O_3}} - \mathrm{Value}_{0ppm_{O_3}}}{\mathrm{Value}_{0ppm_{O_3}}} * 100$		
	1000rpm (base case)	**800rpm**	**1200rpm**
$\boldsymbol{W_{c,I}^{g}}$ **[J]**	285.01 / +3.34%	286.76 / +0.86%	280.07 / +4.47%
$\boldsymbol{IMEP^{g}}$ **[bar]**	7.15 / +3.34%	7.20 / +0.86%	7.03 / +4.47%
$\boldsymbol{\dot{P}_{I}^{g}}$ **[kW]**	2.37 / +3.34%	1.91 / +0.86%	2.8 / +4.47%
$\boldsymbol{SFC^{g}}$ **[g/kWh]**	214.1 / -3.24%	212.8 / -0.86%	217.9 / -4.29%

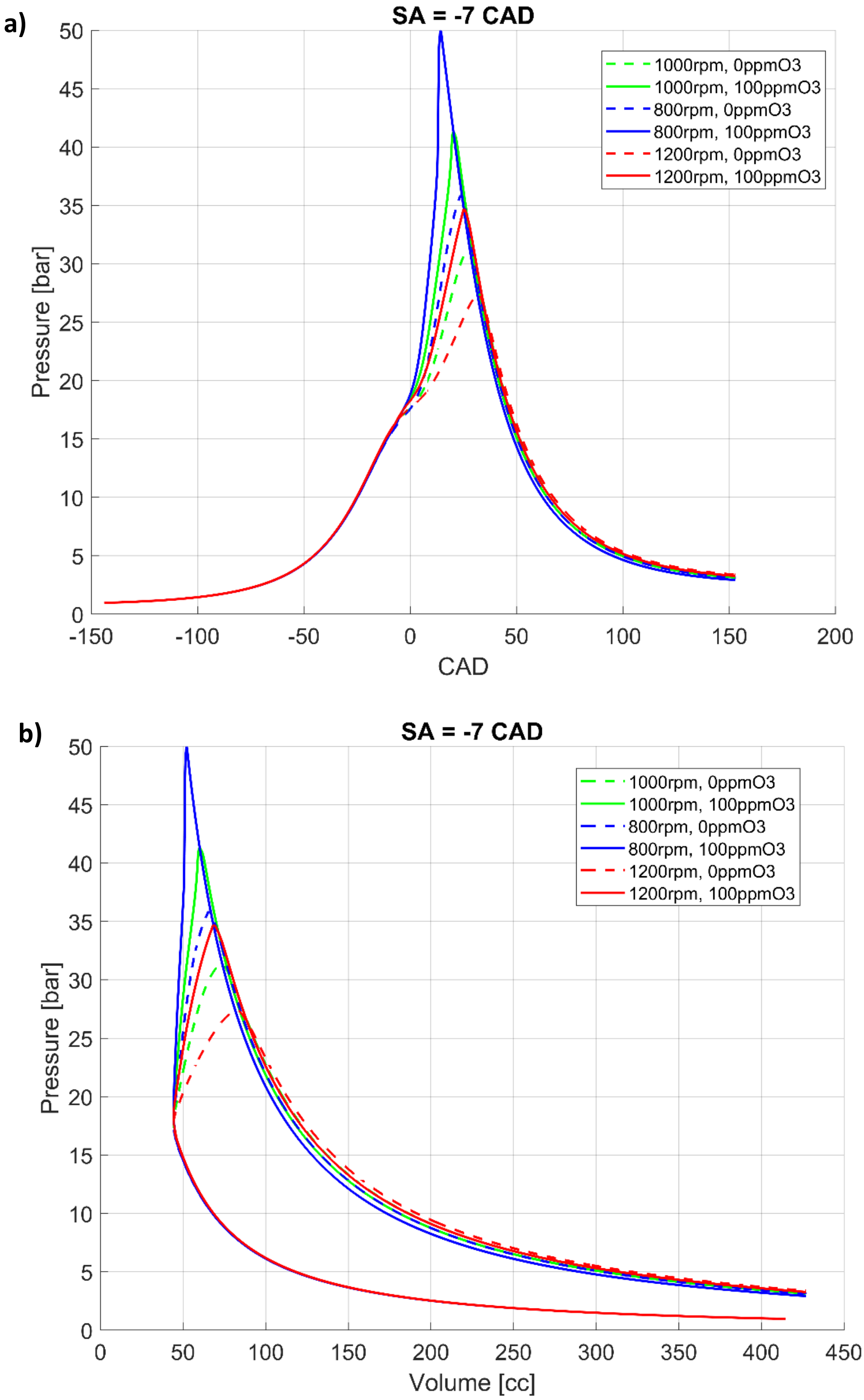

Figure 5.8. Pressure profiles with and without ozone for different rpm with SA=-7 CAD (i.e. 7 CAD BTDC): a) pressure as a function of CAD; b) pressure as a function of volume.

The results show that without ozone, at the same spark advance, the increase in rpm delays the pressure peak and reduces its value. The gross indicated work per cycle is about the same for the 800 rpm case and the 1000 rpm case, while in the 1200 rpm case it is lower due to the excessive decrease in the pressure peak reached in the chamber: as shown in Table 5.5, in fact, in the 1200 rpm case without ozone, the centre of combustion (i.e. the CA50) occurs late in the expansion phase.

The addition of 100 ppm of ozone at IVC reduces the combustion duration for all examined engine speeds, leading to an advance and an increase in the value of the pressure peak reached in the chamber. Specifically, with the addition of 100 ppm ozone, the combustion duration decreases by 43.25%, 28.87% and 20.79% for the cases at 800, 1000 and 1200 rpm respectively. With ozone addition the gross indicated work per cycle increases with respect to the relative case without ozone for all the engine speeds investigated, however in the 800 rpm case, the work gain is small due to the excessive advance of the pressure peak, which resulted in a reduction of the pressure in the expansion phase. The advancement of the pressure peak is due to auto-ignition phenomena occurring in the regions of the chamber not yet invested by the flame. These phenomena can be deduced from the analysis of the parameters shown in Table 5.5 in the cases with ozone addition at 800 and 1000 rpm, and is also evident, especially in the case at 800 rpm, by observing the change of slope in the pressure profiles in Figure 5.8. Specifically, in the case at 800 rpm without ozone, the MPRR is equal to 1.21 bar/CAD and occurs at +14.82 CAD, i.e. before 50% of the total heat has been released, while the pressure peak occurs at +23.63 CAD; furthermore, from CA50 the 40% of the total heat is released in about 8 CAD (CA90-CA50). In the case with 100 ppm ozone, on the other hand, the MPRR is increased to a value of 17.98 bar/CAD and occurs at +13.24, i.e. close to the pressure peak; the significant increase in the MPRR is due to the faster heat release in the second stage of combustion: whereas between CA50 and CA10 40% of the total heat is released in about 8 CAD, the same amount of heat, between CA50 and CA90, is released in only 2 CAD, causing a rapid increase in temperature and consequently in pressure. The auto-ignition of the mixture is also shown in Figure 5.9, which shows the in-cylinder temperature distribution, in the cases with and without the ozone addition, for the different engine speeds, at +13 CAD (i.e. 13 CAD ATDC).

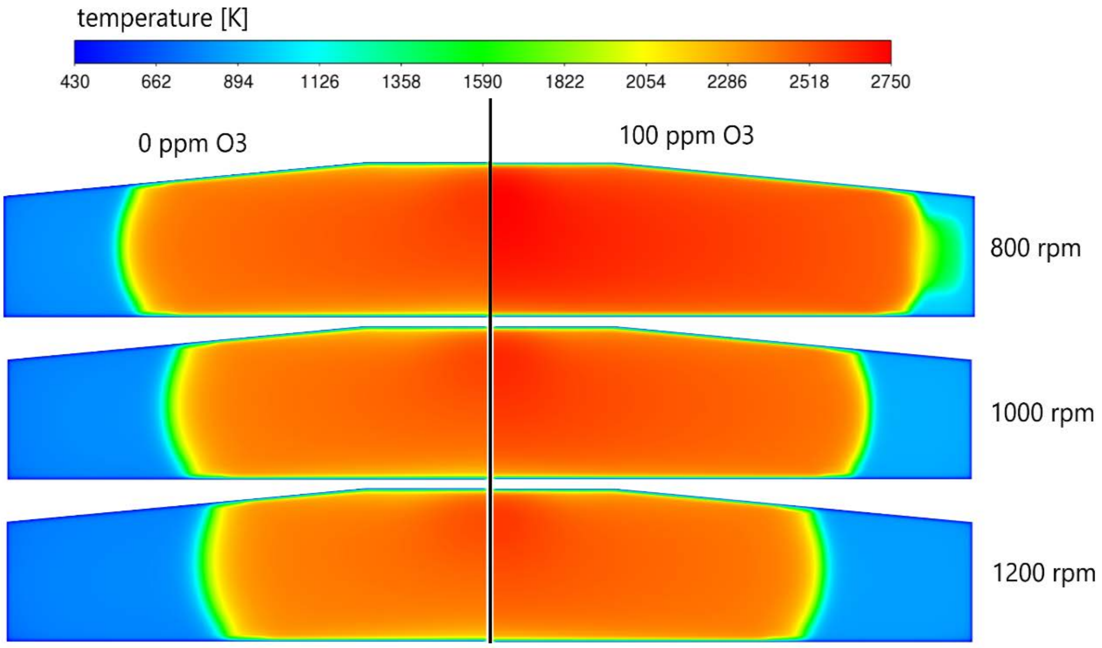

Figure 5.9. In-cylinder temperature distribution at +13CAD (i.e. 13 CAD ATDC), in the cases without ozone (left) and with addition of 100 ppm ozone (right), with SA=-7 (i.e. 7 CAD BTDC), for the different engine speeds.

As shown in Figure 5.9, at +13 CAD, given an engine speed, the flame front has swept a larger chamber region with ozone addition; while at the same ozone concentration the flame is more developed the lower the rpm. In the case at 800 rpm with 100 ppm ozone, between the flame front and the cylinder walls there is the auto-ignition of the mixture responsible for the rapid increase in pressure discussed above.

The auto-ignition of the mixture is due to the ozone that has enabled chemical reactions in the LTC regime, leading to a production of radicals and the lowering of the Ignition Delay Time (IDT) of the mixture. These auto-ignition phenomena occur earlier the lower the engine speed, because the residence time of the mixture is longer. The compression stroke from IVC to TDC occurs in 30 ms and 20 ms for the cases at 800 and 1200 rpm respectively. On the other hand, the duration from 35 CAD BTDC (point at which temperature and pressure are about 650 K and 7 bar) to 35 CAD ATDC (point at which combustion is extinguished for all cases without ozone) is equivalent to 9.72 ms and 14.58 ms for the 1200 rpm and 800 rpm cases, respectively. Considering that the pressure continues to rise due to the compression stroke and the following combustion phase, while the temperature of the end-gases is approximately 800 K, the auto-ignition is in agreement with the IDT results discussed in section 3.2 with the addition of 100 ppm ozone.

If the residence time is small, auto-ignition occurs later in terms of CAD, or does not occur at all. Specifically, in the case at 800 rpm, auto-ignition occurs at about +12.8 CAD when about 60% of the total heat has already been released; in the case at 1000 rpm, auto-ignition occurs at about +19 CAD when about 78% of the total heat has already been released; in the case at 1200 rpm, auto-ignition does not occur.

Figure 5.10 shows both the in-cylinder HO_2 mass fraction and the HO_2 mass fraction values along an axis perpendicular to the flame front, at -5 CAD for the 1200 rpm case with and without ozone; similarly Figure 5.11 shows in-cylinder temperature for the 1200 rpm case at +15 CAD. Figure 5.10 shows that in the case without ozone the hydroperoxyl (HO_2) is localized only in the end gas region, with a peak in the preheating region of the flame, i.e., in the LTC regime of combustion, characterized specifically by HO_2 production as discussed in section 2.1.1.1. With the ozone addition to the mixture, on the other hand, HO_2 is localized in the whole chamber, even in regions far away from the flame caused by the change in fuel reaction pathways due to reactions with the oxygen atom produced by ozone decomposition. Radicals and intermediate species accelerate chemical kinetics resulting in increased flame speed and temperature in the "unburnt gas" region, as shown in Figure 5.11.

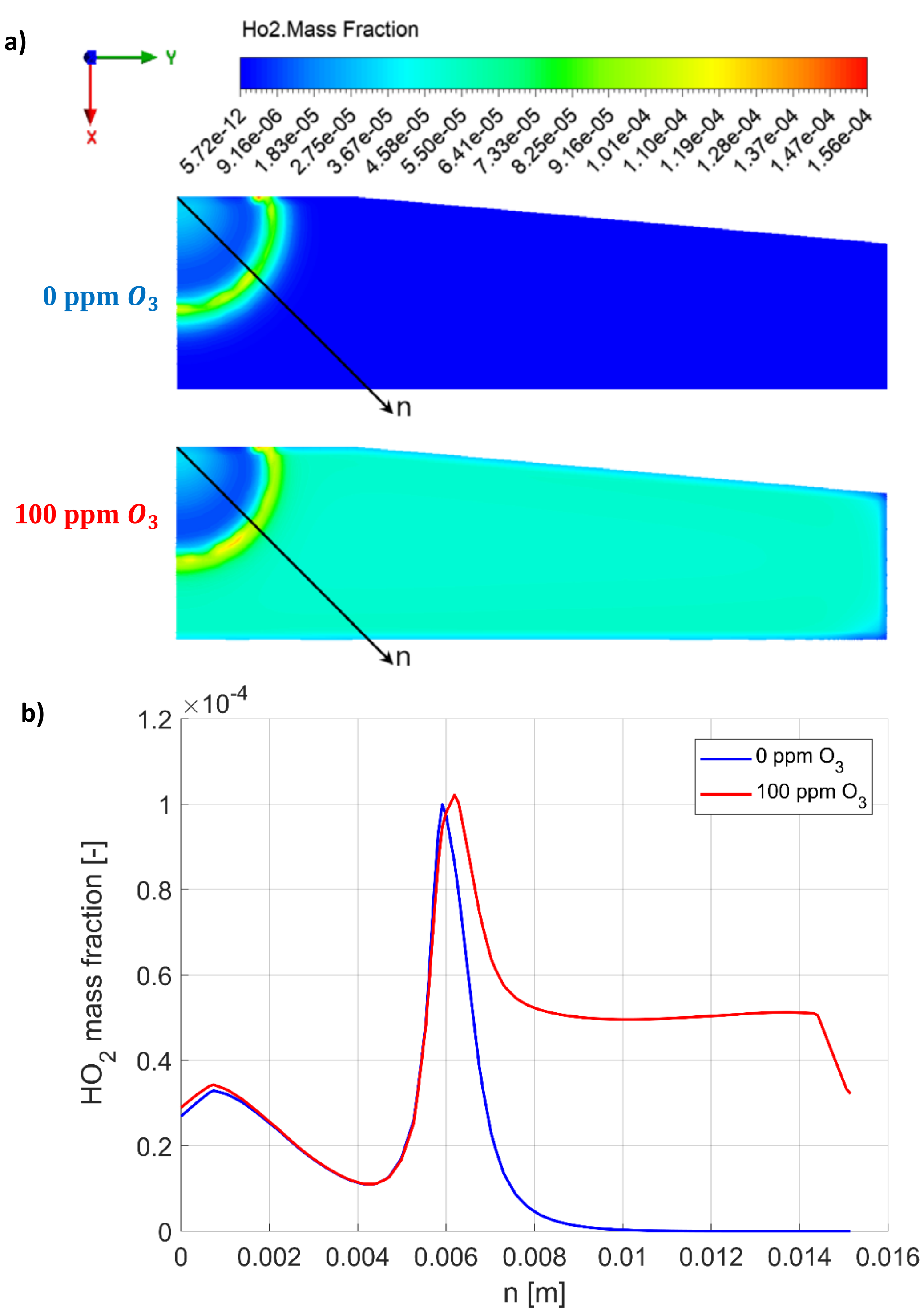

Figure 5.10. In-cylinder HO_2 mass fraction for the 1200 rpm case at -5 CAD (i.e. 5 CAD BTDC) with and without ozone: a) HO_2 mass fraction contour plot; b) HO_2 mass fraction value along the n axis.

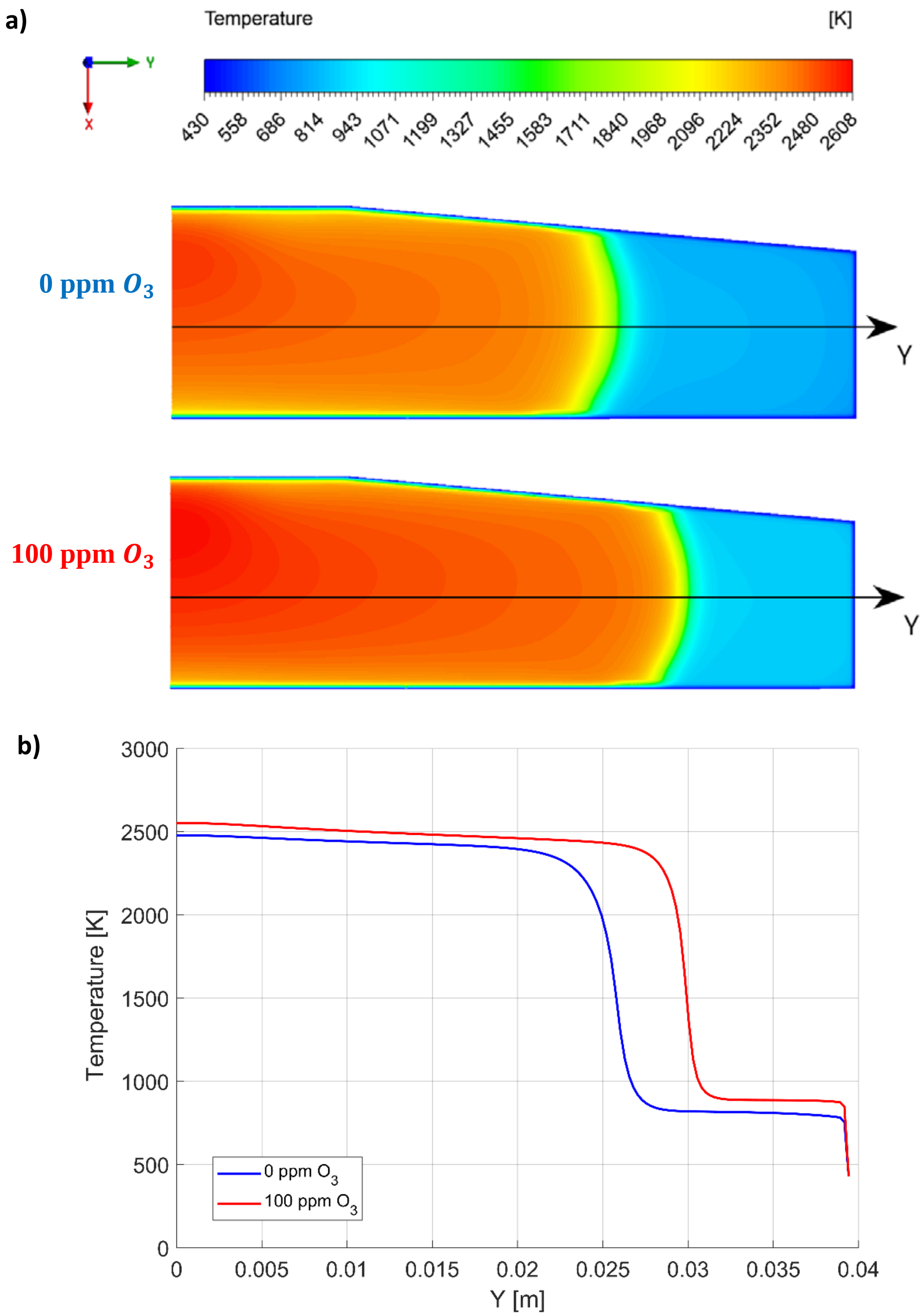

Figure 5.11. In-cylinder temperature for the 1200 rpm case at +15 CAD (i.e. 15 CAD ATDC) with and without ozone: a) temperature contour plot; b) temperature value along the Y axis.

In the 1000 rpm case, simulations were also carried out with 200 ppm of ozone at IVC, and Figure 5.12 shows the pressure profiles obtained for the cases with different ozone concentrations. The results show that with 200 ppm ozone at IVC, combustion advances even faster than in the case with 100 ppm, leading to an additional advance in auto-ignition and peak pressure. With 200 ppm ozone, CA50 advances by 2 CAD with respect to the case with 100 ppm, in agreement with the IDT results obtained in section 3.2, while the combustion duration (CA90-CA10) is 12.04 CAD, which is 6 CAD and 3 CAD less than the cases without ozone and with 100 ppm ozone, respectively. The peak pressure occurs at +16.41 CAD with a value of 47.35 bar; the *MPRR* is 13.03 bar/s and occurs at +15.3 CAD. The excessively early peak pressure, due to the early auto-ignition in the end gases, results in a faster pressure decrease during the expansion phase due to heat exchanges with the walls, compared with cases with lower ozone concentrations. Therefore, there is no additional work gain compared to the case with 100 ppm ozone. Specifically, the gross indicated work per cycle, $W_{c,I}^{g}$, and therefore also $IMEP^{g}$ and $\dot{P}_{I}^{g}$, increase by 3.36% compared to the case without ozone, which is the same value obtained in the case with 100 ppm.

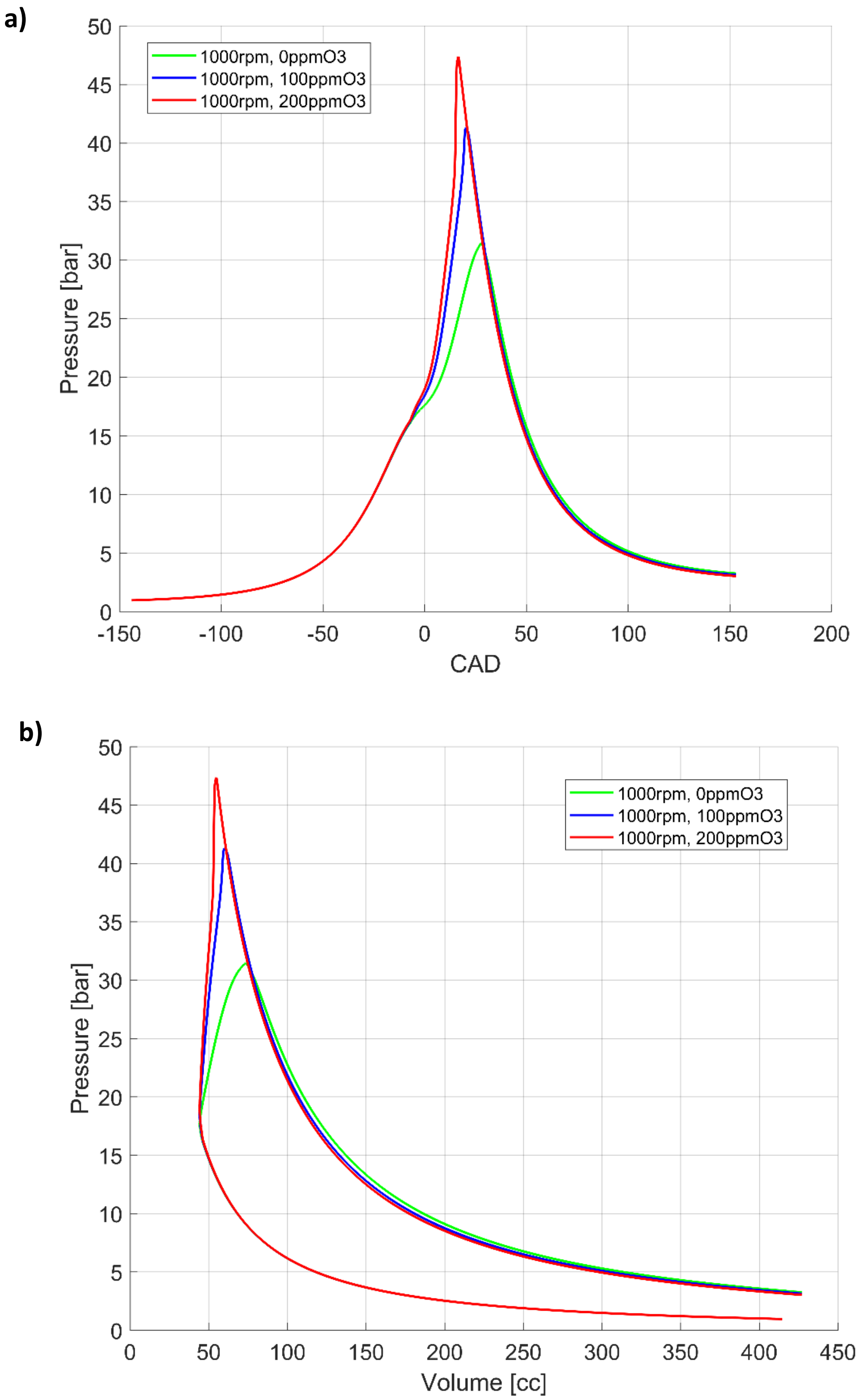

Figure 5.12. Pressure profiles with different ozone concentrations for the case at 1000 rpm with SA=-7 CAD (i.e. 7 CAD BTDC): a) pressure as a function of CAD; b) pressure as a function of volume.

5.2.2.2 Spark advance effect

The same simulations were also carried out by changing the spark advance in order to have approximately the same CA50 as in the base case (1000 rpm) in all cases without ozone at different engine speeds. In this way, it was possible to evaluate the ozone effect with the same combustion efficiency in the cases without ozone. Specifically:

- for the case at 800 rpm, the Spark Advance was SA= -5 CAD (i.e. 5 CAD BTDC);
- for the case at 1200 rpm, the Spark Advance was SA= -9 CAD (i.e. 9 CAD BTDC);

Table 5.7 and Table 5.8, similarly to Table 5.5 and Table 5.6, show the characteristic combustion and performance parameters for the different cases; Figure 5.13 shows the results in terms of pressure profiles for the cases without ozone and with the addition of 100 ppm O_3 for the different engine speeds with the same CA50≃+20 CAD (i.e. 20 CAD ATDC)

Table 5.7. Combustion parameters and other quantities directly dependent on the combustion process, for different cases with CA50≃+20 CAD with and without ozone addition at IVC.

	$\mathbf{Value}_{0ppm_{O_3}}$ / $\mathbf{Value}_{100ppm_{O_3}}$		
	1000rpm (base case)	**800rpm**	**1200rpm**
CA10 [CAD]	+8.22 / +5.31	+9.10 / +5.63	+7.3 / +4.79
CA50 [CAD]	+20.37 / +15.22	+20.32 / +14.37	+20.29 / +15.71
CA90 [CAD]	+29.35 / +20.34	+28.83 / +17.65	+29.61 / +22.28
CA90-CA10 [CAD]	21.13 / 15.03	19.73 / 12.02	22.31 / 17.49
$\bar{P}_{MAX}$ **[bar]**	31.44 / 41.29	32.02 / 45.08	31.12 / 38.85
$\theta_{\bar{P}_{MAX}}$ **[CAD]**	+27.67 / +20.31	+27.07 / +18.00	+28 / +21.90
$MPRR$ **[bar/CAD]**	0.78 / 4.01	0.94 / 10.18	0.69 / 1.48
θ_{MPRR} **[CAD]**	+18.05 / +19.47	+19.91 / +16.79	+16.84 / +21.23
$\bar{T}_{MAX}$ **[K]**	2326 / 2462	2328 / 2503	2324 / 2426
$\theta_{\bar{T}_{MAX}}$ **[CAD]**	+31.27 / +21.76	+30.44 / +18.53	+31.86 / +24.23

Table 5.8. Engine performance parameters of the different cases with CA50≃+20 CAD with and without ozone addition at IVC.

	$\mathbf{Value}_{0ppm_{O_3}}$ / $\frac{\mathbf{Value}_{100ppm_{O_3}} - \mathbf{Value}_{0ppm_{O_3}}}{\mathbf{Value}_{0ppm_{O_3}}} * \mathbf{100}$		
	1000rpm (base case)	**800rpm**	**1200rpm**
$\boldsymbol{W^g_{c,I}}$ **[J]**	285.01 / +3.34%	280.72 / +2.9%	288.7 / +3.17%
$\boldsymbol{IMEP^g}$ **[bar]**	7.15 / +3.34%	7.04 / +2.9%	7.24 / +3.17%
$\boldsymbol{\dot{P}^g_I}$ **[kW]**	2.37 / +3.34%	1.87 / +2.9%	2.88 / +3.17%
$\boldsymbol{SFC^g}$ **[g/kWh]**	214.1 / -3.24%	217.4 / -2.83%	211.4 / -3.08%

Without ozone, at the same CA50, both the maximum pressure reached in the cylinder and the relative crank angle are approximately the same. The work obtained differs between the different cases mainly due to the different duration of heat exchange with the walls during expansion: in the case at 800 rpm the average temperature at the end of expansion is 1332 K, while in the case at 1200 rpm it is 1382 K. With the addition of 100 ppm ozone, as in the case with constant SA, combustion accelerates and combustion duration is decreased, with a greater effect in the case of lower rpm. Similarly to the case with constant SA, auto-ignition of the mixture in the end gases zone occurs, but in this case this phenomenon also affects the 1200 rpm case. With respect to the cases with SA=-7 CAD, in fact, in these cases the Spark Advance for the 1200 rpm case was advanced, resulting in an increased residence time, while in the 800 rpm case the residence time decreased. Specifically, in the case at 800 rpm, auto-ignition occurs at about +16.1 CAD when about 64% of the total heat has already been released; in the case at 1200 rpm, auto-ignition occurs at about +20.75 CAD when about 81% of the total heat has already been released.

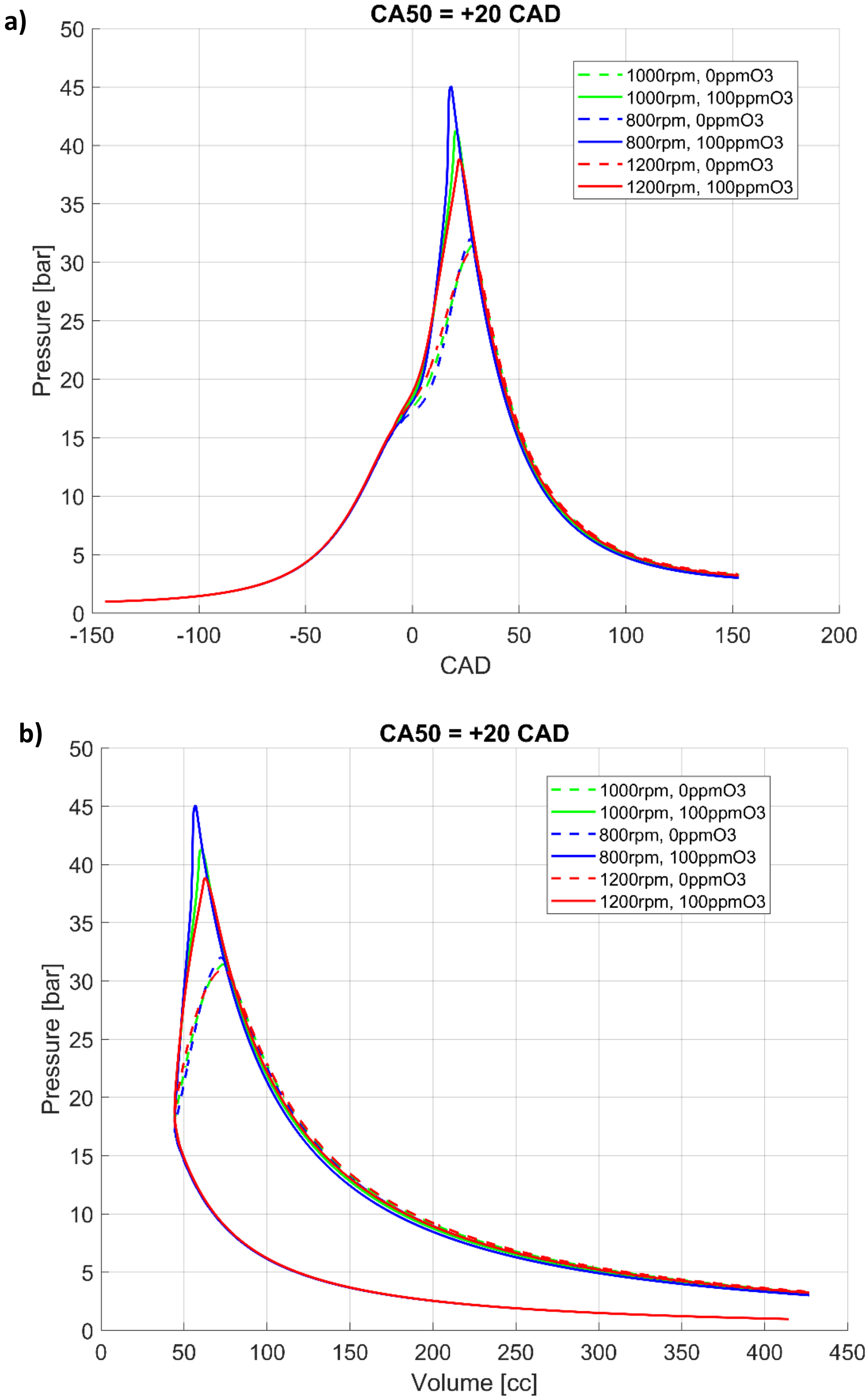

Figure 5.13. Pressure profiles with and without ozone for different rpm with CA50≃+20 CAD (i.e. 20 CAD ATDC): a) pressure as a function of CAD; b) pressure as a function of volume.

5.2.2.3 Equivalence ratio effect

The effect of ozone addition was also evaluated by lowering the equivalence ratio, using $\phi \simeq 0.7$. Simulations were carried out in the 1000 rpm case, both with the same Spark Advance as the base case (1000 rpm, SA=-7 CAD, without ozone), and with the same combustion efficiency as the base case (i.e. with same CA50), which was obtained by advancing the Spark Advance to SA=-11 CAD (i.e. 11 CAD BTDC). The simulations covered both cases without ozone and cases with 100 ppm ozone at IVC. Table 5.9 and Table 5.10 show the characteristic combustion and performance parameters for the different cases, while Figure 5.14 shows the pressure profiles and Heat Release Rate (HRR) as function of CAD. Finally, Figure 5.15 shows the comparison between the cases with different equivalence ratios at 1000 rpm, in terms of closed-valve cycle. Obviously, in the case with the lower equivalence ratio, there is less fuel in the chamber, so the total heat that can be released, and therefore the work that can be obtained is lower. However, a comparison can be made considering the Specific Fuel Consumption SFC^g.

The results show that, in the case of lean mixture with SA=-7 CAD, combustion proceeds very slowly such that the CA50 and CA90 are +32.85 CAD and +53.43 CAD respectively, and the combustion duration is 42.35 CAD. The peak pressure only exceeds the pressure reached at TDC by 0.7 bar, resulting in an increase in Specific Fuel Consumption and therefore a loss of work compared to the case with SA=-11 CAD, as shown in Figure 5.15 and Table 5.10. The addition of 100 ppm ozone in the case with $\phi = 0.7$, in contrast to the case with $\phi = 0.9$, does not lead the mixture auto-ignition for either SA=-7 CAD or SA=-11 CAD. Reducing the equivalence ratio, in fact, increased the IDT of the mixture, in agreement with the results discussed in section 3.2.

Table 5.9. Combustion parameters and other quantities directly dependent on the combustion process, for the cases at 1000 rpm and $\phi = 0.7$, with and without ozone addition at IVC.

$\text{Value}_{0ppm_{O_3}}$ / $\text{Value}_{100ppm_{O_3}}$		
	SA=-7 CAD	**SA=-11 CAD**
CA10 [CAD]	+11.08 / +7.53	+6.05 / +3.11
CA50 [CAD]	+32.85 / +20.70	+21.51 / +14.11
CA90 [CAD]	+53.43 / +29.00	+30.02 / +19.50
CA90-CA10 [CAD]	42.35 / 21.47	23.97 / 16.39
$\bar{P}_{MAX}$ **[bar]**	18.39 / 27.31	26.37 / 36.73
$\theta_{\bar{P}_{MAX}}$ **[CAD]**	+11.69 / +28.4	+28.87 / +19.63
$MPRR$ **[bar/CAD]**	0.38 / 0.52	0.38 / 1.4
θ_{MPRR} **[CAD]**	-18.12 / 24.84	-18.10 / +17.52
$\bar{T}_{MAX}$ **[K]**	1790 / 2077	2041 / 2178
$\theta_{\bar{T}_{MAX}}$ **[CAD]**	+54.31 / +31.34	+32.56 / +21.73

Table 5.10. Engine performance parameters for the cases at 1000 rpm and $\phi = 0.7$, with and without ozone addition at IVC.

$\text{Value}_{0ppm_{O_3}}$ / $\frac{\text{Value}_{100ppm_{O_3}} - \text{Value}_{0ppm_{O_3}}}{\text{Value}_{0ppm_{O_3}}} * 100$		
	SA=-7 CAD	**SA=-11 CAD**
$W^g_{c,I}$ **[J]**	202.62 / +13.5%	230.6 / +4.17%
$IMEP^g$ **[bar]**	5.08 / +13.5%	5.78 / +4.17%
$\dot{P}^g_I$ **[kW]**	1.69 / +13.5%	1.92 / +4.17%
SFC^g **[g/kWh]**	235.28 / -11.9%	206.73 / -4.02%

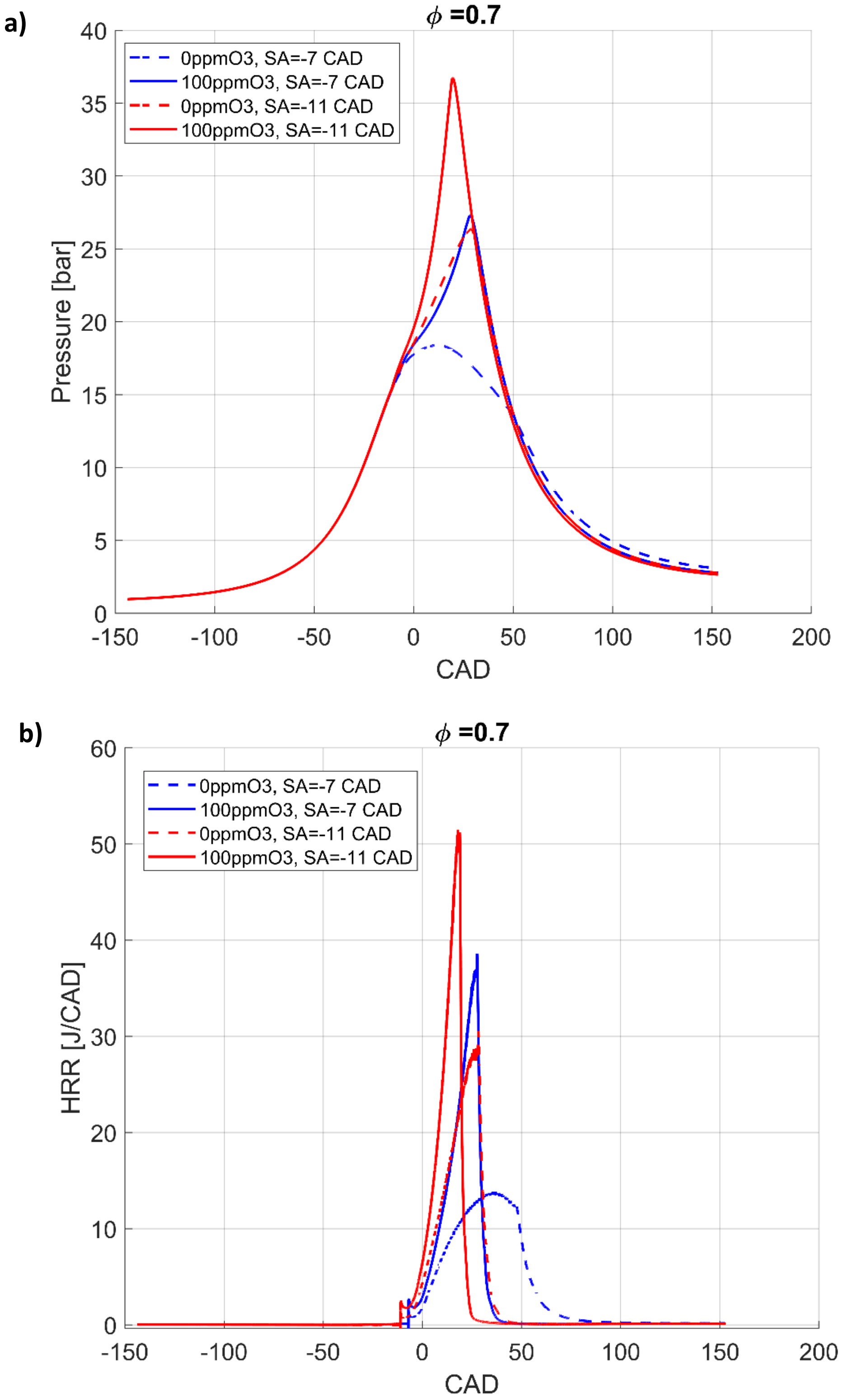

Figure 5.14. Results as function of CAD with different ozone concentrations and spark advance, for the case at 1000 rpm with $\phi \simeq 0.7$: a) pressure; b) Heat Release Rate.

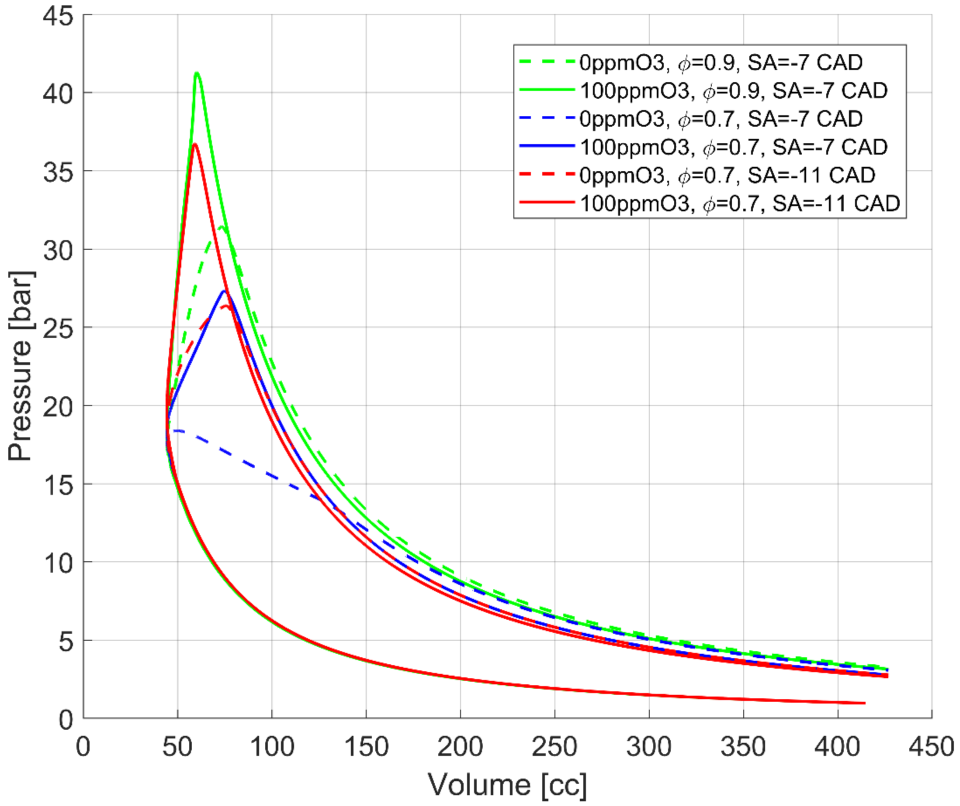

Figure 5.15. Pressure as function of CAD for cases at 1000 rpm, for different ozone concentrations, equivalence ratio and spark advance.

In the case with SA=-7 CAD, the ozone addition resulted in a greater increase in performance than in the case with SA=-11 CAD, as shown in Table 5.10. Specifically, with the addition of 100 ppm of O_3, the gross work per cycle increased by 13.5% and 4.17%, while the combustion duration decreases by 49.3% and 31.62% for cases with SA=-7 CAD and SA=-11 CAD respectively. Ozone, in fact, by enabling LTC reactions leads both to a slight increase in the end gases temperature, and to the production of radicals that promote the flame propagation speed, resulting in a more pronounced effect in the cases where combustion without ozone is slower, less optimised or with self-sustaining difficulties.

Considering only the case with SA=-11 CAD, which has approximately the same CA50 as the base case with $\phi = 0.9$, the reduction in the equivalence ratio results in a small increase in the combustion duration, which is 23.97 CAD and 21.13 CAD for $\phi = 0.7$ and $\phi = 0.9$ respectively; however, compared to the case without ozone, the combustion duration with ozone addition was reduced by 7.58 CAD and 6.1 CAD in the $\phi = 0.7$ and $\phi = 0.9$ cases respectively. These results are in agreement with those presented in section 3.1.2, which showed that for the same ozone concentration, by lowering the equivalence ratio leads to a reduction in LFS, but a greater percentage increase compared to the case without ozone.

Conclusions

The main objectives of engineering research concerning internal combustion engines are to increase efficiency, fuel economy and reduce pollutant emissions. One common aspect of these factors is the combustion process, in particular the control and maximisation of its efficiency. In this context, the aim of this thesis was to investigate ozone-assisted combustion for possible applications in both unconventional engines, in particular HCCI engines, and conventional Spark Ignition engines.

First, the influence of ozone addition on the combustion of methane and iso-octane in air has been investigated. Specifically, 1-D simulations have been carried out to compute the laminar flame speed under different conditions of pressure, temperature, equivalence ratio and ozone concentration, by using a reaction mechanism for methane and three different mechanisms for iso-octane. Each mechanism has been modified with the addition of an ozone sub-mechanism. Final considerations are:

- the three modified mechanisms used for iso-octane provide similar results for all the simulations. The greatest discrepancies are found at high reactant temperatures (T>540 K) even if, qualitatively, the mechanisms are always in agreement;

- at ambient conditions (P = 1bar, T=300 K), ozone addition has the same impact on both mixtures with methane and iso-octane for all the equivalence ratios investigated;

- as the temperature of the reactants increases, ozone addition has a different influence on the two fuels. In the case of iso-octane, O_3 enables a cool flame. This phenomenon occurs at temperature equal to or higher than about 540 K when 7000 ppm ozone is added to the mixture, leading to an increase of the laminar flame speed;

- for mixture temperatures below 520-540 K, ozone mainly decomposes near the high-temperature flame. For higher temperatures, ozone is already almost completely consumed upstream the flame. In the case of iso-octane, the atomic oxygen, produced by the decomposition of ozone for temperatures higher than about 540 K, oxidises the fuel, thus producing

OH-radicals, which advance the oxidation. These reactions are fast enough to generate the cool flame;

- for high mixture pressures, ozone decomposition by the reaction $O_3 + N_2 \rightarrow O_2 + O + N_2$ is greatly favoured and a different behaviour occurs for methane/air/ozone and for iso-octane/air/ozone mixtures. For methane, the laminar flame speed decreases as pressure increases, regardless of temperature. For iso-octane, the influence of ozone addition is the same as for methane with a temperature of the reactants below 540 K. For higher temperatures, i.e. in the presence of a cool flame, the laminar flame speed increases with pressure, to a greater extent for higher ozone concentrations and/or temperatures;
- as regards methane, LFS sensitivity analyses performed at 600 K show that, with and without ozone, the main reactions are the same regardless of pressure. Furthermore, the values of the sensitivity coefficients with and without ozone are comparable and present the same variations with pressure. As regards iso-octane, the sensitivity analyses at 600 K show that, in the presence of ozone, the laminar flame speed is mainly influenced by reactions that do not correspond to those in the absence of ozone. Specifically, the most important reactions are those involved in the cool flame and activated by ozone kinetics. This is especially true at high pressure.

Then, parametric analyses were carried out concerning the effect of ozone on Ignition Delay Time under different conditions of temperature, pressure, equivalence ratio and ozone concentration. The main results concerning the analyses with ozone concentrations between 100 and 1000 ppm and equivalence ratios $\phi = 0.5$ and $\phi = 1$ show:

- a reduction in terms of IDT with the addition of ozone over the entire temperature range examined, with a greater effect at low temperatures. Moreover, the reduction of IDT with ozone addition is not linear, and increasing ozone concentration reduces IDT progressively slower, especially at low temperatures. Specifically, at 600 K ozone addition reduces the ignition delay by 89-99%, depending on the specific ozone concentration (50-1000 ppm), for both lean ($\phi = 0.5$) and stoichiometric cases. On the other hand, at 1200 K an ozone concentration of more than 200 ppm is required to achieve an IDT percentage reduction of more than 5%, for both $\phi = 0.5$ and stoichiometric cases;

- a greater percentage reduction of IDT with ozone addition in the stoichiometric case in the temperature range 600-800 K, especially at lower temperatures, whereas in the temperature range 820-1250 K the percentage reduction is greater in the case $\phi = 0.5$.

On the other hand, in the cases with lower equivalence ratio ($\phi = 0.3$) and ozone concentrations (10-50 ppm) the results show that:

- at pressure equal to 20 bar, with the addition of ozone, auto-ignition occurs in mixtures with an initial temperature higher than or equal to 560 K in a 2-second simulation, whereas without ozone a temperature of at least 600 K is required. The reason for the strong IDT decrease for the cases with ozone is due to the chemical decomposition of O_3, which leads to the formation of oxygen atoms that oxidise fuel and produce more OH in the pre-heating zone than for the case without ozone;
- with increasing pressure, the percentage reduction of IDT with ozone addition, compared to the case without ozone, increases at almost all temperatures considered. Exceptions are the temperature range [760-840 K], where the opposite effect occurs due to the shift of NTC region towards higher temperatures with increasing pressure, and temperatures equal to or higher than 1200 K. Besides, at both 35 bar and 40 bar and with 50 ppm of ozone, the influence of both high pressure and ozone concentration enables auto-ignition in a mixture with an initial temperature equal to 540 K.

Following the investigation of the ozone effect on the combustion chemistry kinetics, simulations were carried out concerning ozone applications in internal combustion engines. Since HCCI engines, which are one of the most interesting types of unconventional engines from the perspective of fuel economy and high thermal efficiency, have the difficulty of combustion control as a major limitation, the potential use of ozone was investigated. In particular, CFD simulations of an HCCI engine containing air, ozone, iso-octane and residual gases were carried out. The objective was to understand the thermo-fluid-dynamic evolution of the mixture and the effects on combustion performance considering different ozone concentrations and different compositions and percentages of residual gases. The main results show that:

- the ozone addition (3 to 30 ppm) anticipates the mixture auto-ignition and reduces the combustion duration, which is also more complete, leading to a reduction in UHCs but an increase in NO_x due to the higher temperatures reached in the chamber;
- using both a simplified (carbon dioxide and water) and an extended (considering all species present at the exhaust with a concentration greater than 1 ppm) composition of the residual gases, approximately the same results are obtained;
- ozone decomposes during the engine compression stroke, releasing oxygen atoms, which oxidise the fuel and other intermediate species. This enables Low-Temperature Combustion with the release of species such as OH, HO_2 and H_2O_2. Reactions in the LTC regime also result in a small amount of heat being released before the instant of auto-ignition;
- as the percentage of residual gas increases, more ozone is consumed by reacting with the nitrogen oxide in the chamber through the reaction $NO + O_3 \rightarrow NO_2 + O_2$. In addition, some of the oxygen atoms produced by the $O_3 + N_2 \rightleftarrows O_2 + O + N_2$ reaction react with other intermediate species instead of the fuel. However, despite the presence of chemical species that could limit the effectiveness of ozone, since they are contained in much smaller quantities than ozone, they had almost no impact with respect to the benefits of ozone;
- the ozone effect is higher in the case with a higher percentage of residual gas. With the addition of 35 ppm ozone at IVC the gross work per cycle increases by 2.52%, 3.58% and 5.7% compared to the case without ozone for the cases with 0%, 5% and 10% by mass of residual gases; on the other

hand, the specific fuel consumption is reduced by 1.54%, 2.77% and 4.96% for the same cases.

Finally, simulations were conducted to understand the effect of ozone in the case of Spark Ignition engine applications. First, simulations of the compression stroke of the engine were conducted under both lean and stoichiometric conditions, with the aim of identifying the conditions reached at the end of compression and of evaluating the LFS by considering different engine speeds and different ignition timings. Next, CFD simulations, from IVC to EVO, of a Spark Ignition engine were carried out in order to assess the effect of ozone on engine performance. The main results concerning the LFS simulations are the following:

- without ozone addition, the laminar flame propagates at approximately the same speed (72-75 cm/s) regardless of the conditions analysed (ignition timing between 18 and 3 CAD BTDC, and engine speed between 1000 and 5000 rpm). On the other hand, by adding ozone at IVC, there is a significant increase in laminar flame speed, which differs according to the conditions examined;
- the LFS increases approximately linearly with increasing ozone concentration at the IVC. Specifically, it is found that, given an engine speed, the laminar flame speed is higher the later the ignition occurs: this is due to the longer residence time of the mixture in the chamber. The same qualitative effect is obtained, for a constant ignition timing, by decreasing the engine speed. In this case, however, if ignition is advanced too much, the flame speed is progressively less dependent on the engine speed;
- during the compression stroke of the engine, ozone decomposes and promotes the formation of a cool flame, leading to an increase in the LFS. The higher the ozone concentration, the greater the LFS increase and ozone effect on LFS is stronger for the case of stoichiometric mixtures with respect to $\phi = 0.5$. The addition of ozone at IVC in the case $\phi = 0.5$ increases LFS up to values higher than that obtained for the stoichiometric case without ozone.

Instead, the main considerations that can be drawn from CFD simulations of the Spark Ignition engine are:

- in the near-stoichiometric case with the same spark advance (SA=7 CAD BTDC), the addition of 100 ppm of ozone at IVC reduces the combustion duration for all examined engine speeds, leading to an advance and an increase in the value of the pressure peak reached in the chamber. Specifically, with the addition of 100 ppm ozone, the combustion duration decreases by 43.25%, 28.87% and 20.79% for the cases at 800, 1000 and 1200 rpm respectively.
- in the near-stoichiometric case with the same spark advance (SA=7 CAD BTDC), with ozone addition the gross indicated work per cycle increases with respect to the relative case without ozone for all the engine speeds investigated. However, in the 800 rpm case, the work gain is small due to the excessive advance of the pressure peak, which resulted in a reduction of the pressure in the expansion phase. The advancement of the pressure peak is due to auto-ignition phenomena, occurring in the regions of the chamber not yet invested by the flame, where ozone has enabled chemical reactions in the LTC regime, leading to a production of radicals and a reduction of the Ignition Delay Time of the mixture. These auto-ignition phenomena occur earlier the lower the engine speed, because the residence time of the mixture is longer;
- in the near-stoichiometric case with the same spark advance (SA=7 CAD BTDC), with the addition of 200 ppm of ozone at IVC there is no additional work gain compared to the case with 100 ppm ozone. Specifically, the gross indicated work per cycle increases by 3.36% compared to the case without ozone, which is the same value obtained in the case with 100 ppm. This is due to the excessively early peak pressure, due to the early auto-ignition in the end gases;
- without ozone, at the same CA50 (CA50=20 CAD ATDC), both the maximum pressure reached in the cylinder and the relative crank angle are approximately the same for the cases with different engine speed. The work obtained differs in the various cases mainly due to the different

duration of the heat exchange with the walls during expansion. With the addition of 100 ppm ozone, as in the case with constant SA, combustion accelerates and combustion duration is decreased, with a greater effect in the case of lower rpm;

- in the cases with the same CA50 (CA50=20 CAD ATDC), similarly to the case with constant SA, auto-ignition of the mixture in the end gases zone occurs with ozone addition, but in this case this phenomenon also affects the 1200 rpm case due to the higher residence time;
- in the cases with the same SA (SA=7 CAD BTDC) the gross indicated work per cycle with 100 ppm of ozone increases by 0.86%, 3.34% and 4.47% with respect to the relative cases without ozone addition at 800, 1000 and 1200 rpm, respectively; on the other hand, the specific fuel consumption is reduced by 0.86%, 3.24% and 4.29% for the same cases.
- in the cases with the same CA50 (CA50=20 CAD ATDC) the gross indicated work per cycle with 100 ppm of ozone increases by 2.9%, 3.34% and 3.17% with respect to the relative cases without ozone addition at 800, 1000 and 1200 rpm, respectively; on the other hand, the specific fuel consumption is reduced by 2.83%, 3.24% and 3.08% for the same cases.
- in the case of lean mixture ($\phi = 0.7$), at 1000 rpm, with SA= 7 CAD BTDC and without ozone, combustion proceeds very slowly. The peak pressure only exceeds the pressure reached at TDC by 0.7 bar, resulting in an increase in Specific Fuel Consumption and therefore a loss of work compared to the case with SA=11 CAD BTDC (CAD allowing the same CA50 as the case with $\phi = 0.9$, 1000 rpm, SA=7 CAD BTDC, without ozone);
- the addition of 100 ppm ozone in the case with $\phi = 0.7$, at 1000 rpm in contrast to the case with $\phi = 0.9$, does not lead the mixture auto-ignition for either SA=7 CAD BTDC or SA=11 CAD BTDC. Reducing the equivalence ratio, in fact, increases the IDT of the mixture;
- in the case with $\phi = 0.7$, at 1000 rpm, the gross indicated work per cycle with 100 ppm of ozone increases by 13.5% and 4.17% with respect to the

cases without ozone addition at SA=7 CAD BTDC and SA=11 CAD BTDC, respectively; on the other hand, the specific fuel consumption is reduced by 11.9% and 4.02% for the same cases.

References

[1] H. Ritchie, M. Roser, P. Rosado, Energy, Published online at OurWorldInData.org. 2022, https://ourworldindata.org/energy. Accessed January 2023.

[2] International Energy Outlook (IEO) 2021, [Online Resource] https://www.eia.gov/outlooks/ieo/. Accessed January 2023.

[3] https://unfccc.int/resource/docs/convkp/kpeng.pdf. Accessed January 2023.

[4] https://unfccc.int/process-and-meetings/the-paris-agreement/the-paris-agreement. Accessed January 2023.

[5] https://climate.ec.europa.eu/eu-action/climate-strategies-targets/2020-climate-energy-package_en. Accessed January 2023.

[6] https://climate.ec.europa.eu/eu-action/climate-strategies-targets/2030-climate-energy-framework_en. Accessed January 2023.

[7] https://climate.ec.europa.eu/eu-action/climate-strategies-targets/2050-long-term-strategy_en. Accessed January 2023.

[8] H. Ritchie, M. Roser, P. Rosado, CO2 and Greenhouse Gas Emissions, Published online at OurWorldInData.org. 2020, https://ourworldindata.org/co2-and-other-greenhouse-gas-emissions. Accessed January 2023.

[9] IEA, Transport sector CO2 emissions by mode in the Sustainable Development Scenario, 2000-2030, IEA, Paris https://www.iea.org/data-and-statistics/charts/transport-sector-co2-emissions-by-mode-in-the-sustainable-development-scenario-2000-2030, IEA. Licence: CC BY 4.0.

[10] W. Sun, X. Gao, B. Wu, T. Ombrello, The effect of ozone addition on combustion: Kinetics and dynamics, Prog. Energy Combust. Sci. 73 (2019) 1-25.

[11] J. McClurkin, D. Maier, Half-life time of ozone as a function of air conditions and movement, Julius-Kühn-Archiv 25 (2010) 381.

[12] U. Kogelschatz, B. Eliasson, W. Egli, Dielectric-barrier discharges. Principle and applications. Le Journal de Physique IV 7 (1997) C4-47.

[13] B. Eliasson, U. Kogelschatz, P. Baessler, Dissociation of O2 in N2 /O2 mixtures. J. Phys. B At. Mol. Phys. 17 (1984) L797.

[14] Z. Wang, J. Zhou, Y. Zhu, Z. Wen, J. Liu, K. Cen. Simultaneous removal of NOx, SO2 and Hg in nitrogen flow in a narrow reactor by ozone injection: experimental results, Fuel Process. Technol. 88 (2007) 817–23.

[15] Y.S. Mok, H-J Lee, Removal of sulfur dioxide and nitrogen oxides by using ozone injection and absorption–reduction technique. Fuel Process. Technol. 87 (2006) 591–7.

[16] R. Sandri, On the decomposition flame of liquid ozone-oxygen mixtures in a tube, Combust. Flame 2 (1958) 348–52.

[17] A.G. Streng, A.V. Grosse, The quenching diameter of ozone flames, Combust. Flame 5 (1961) 81-6.

[18] F. Cramarossa, G. Dixon-Lewis, Ozone decomposition in relation to the problem of the existence of steady-state flames, Combust. Flame 16 (1971) 243-51.

[19] J.M. Heimerl, T.P. Coffee, The detailed modeling of premixed, laminar steady-state flames. I. Ozone, Combust. Flame 39 (1980) 301-15.

[20] B. Rogg, A. Liñán, F.A. Williams, Deflagration regimes of laminar flames modeled after the ozone decomposition flame, Combust. Flame 65 (1986) 79-101.

[21] S.W. Benson, A.E. Axworthy Jr, Mechanism of the gas phase, thermal decomposition of ozone. J. Chem. Phys. 26 (1957) 1718-26.

[22] J.A. Zaslowsky, H.B. Urbach, F. Leighton, R.J. Wnuk, J.A. Wojtowicz, The Kinetics of the Homogeneous Gas Phase Thermal Decomposition of Ozone, J. Am. Chem. Soc. 82 (1960) 2682–6.

[23] W.M. Jones, N. Davidson, The thermal decomposition of ozone in a shock tube, J. Am. Chem. Soc. 84 (1962) 2868-78.

[24] H. Endo, K. Glänzer, J. Troe, Shock wave study of collisional energy transfer in the dissociation of nitrogen dioxide, nitrosyl chloride, ozone, and nitrous oxide, J. Chem. Phys. 83 (1979) 2083-90.

[25] J.M. Heimerl, T.P. Coffee, The unimolecular ozone decomposition reaction, Combust. Flame 35 (1979) 117-23.

[26] S. Toby, E. Ullrich, Reaction of carbon monoxide with ozone: Kinetics and chemiluminescence, Int. J. Chem. Kinet. 12 (1980) 535-46.

[27] B. Lunin, O. Kuricheva, Y.N. Zhitnev, Determination of the Arrhenius parameters of the ozone thermal decomposition reaction initiated by pulsed infrared laser radiation, Zh. Fiz. Khim. 60 (1986) 2050.

[28] S. Peukert, R. Sivaramakrishnan, J. Michael, High temperature shock tube studies on the thermal decomposition of O3 and the reaction of dimethyl carbonate with O-Atoms, J. Phys. Chem. A. 117 (2013) 3729-38.

[29] J. Drugman, The oxidation of hydrocarbons by ozone at low temperatures, J. Chem. Soc. Trans. 89 (1906) 939–45.

[30] C.C. Schubert, S.J. Schubert, R.N. Pease, The Oxidation of lower paraffin hydrocarbons. I. Room temperature reaction of methane, propane, n-butane and isobutane with ozonized oxygen, J. Am. Chem. Soc. 78 (1956) 2044–8.

[31] R.J. Morrissey, C. Schubert, The reactions of ozone with propane and ethane, Combust. Flame 7 (1963) 263–8.

[32] R. Atkinson, D.L. Baulch, R.A. Cox, J.N. Crowley, R.F. Hampson Jr, J.A. Kerr et al. Summary of evaluated kinetic and photochemical data for atmospheric chemistry; IUPAC subcommittee on gas kinetic data evaluation for atmospheric chemistry, Web Version December 2001.

[33] W.B. DeMore, S.P. Sander, D.M. Golden, R.F. Hampson, M.J. Kurylo, C.J. Howard et al. Chemical kinetic and photochemical data for use in stratospheric modeling: evaluation no. 11 of the NASA panel for data evaluation, JPL Publication (1994) 94-26.

[34] R. Wegener, T. Brauers, R. Koppmann, S. Rodríguez Bares, F. Rohrer, R. Tillmann et al. Simulation chamber investigation of the reactions of ozone with shortchained alkenes. J. Geophys. Res. Atmos. 112 (2007).

[35] D. Lucas, D. Dunn-Rankin, K. Hom, N.J. Brown, Ignition by excimer laser photolysis of ozone, Combust. Flame 69 (1987) 171–84.

[36] F. Liu, H. Furutani, J. Hama, S. Takahashi, The Ignition of H2-O2-O3 / H2-O2-O3-Ar Mixture Induced by the Photolysis of Ozone, JSME Int. J. Ser. B 41 (1998) 951–8.

[37] T. Nomaguchi, S. Koda, Spark ignition of methane and methanol in ozonized air, Symp. (Int.) Combust. 22 (1989) 1677–82.

[38] T. Ombrello, S.H. Won, Y. Ju, S. Williams, Flame propagation enhancement by plasma excitation of oxygen. Part I: effects of O3, Combust. Flame157 (2010) 1906–15.

[39] F. Halter, P. Higelin, P. Dagaut, Experimental and Detailed Kinetic Modeling Study of the Effect of Ozone on the Combustion of Methane, Energy Fuels 25 (2011) 2909-16.

[40] Z.H. Wang, L. Yang, B. Li, Z.S. Li, Z.W. Sun, M. Aldén, K.F. Cen, A.A. Konnov, Investigation of combustion enhancement by ozone additive in CH4/air flames using direct laminar burning velocity measurements and kinetic simulations, Combust. Flame 159 (2012) 120–9.

[41] S. Ji, Y. Li, G. Tian, M. Shu, G. Jia, S. He, X. Lan, Y. Cheng, Investigation of laminar combustion characteristics of ozonized methane-air mixture in a constant volume combustion bomb, Energy 226 (2021) 120349.

[42] S. Ji, X. Lan, J. Lian, H. Xu, Y. Wang, Y. Cheng, Y. Liu, Influence of Ozone on Ignition and Combustion Performance of a Lean Methane/Air Mixture, Energy Fuels, 31 (2017) 14191-200.

[43] W. Xie, S. Drost, R. Schiebl, U. Maas, 2022 Preprint SSRN: https://papers.ssrn.com/sol3/papers.cfm?abstract_id=4109908. Accessed January 2023.

[44] C. Jiang, J. Pan, H. Yu, Y. Zhang, Q. Lu, E.K Quaye, Effects of mixing ozone on combustion characteristics of premixed methane/oxygen in meso-scale channels, Fuel 312 (2022) 122792.

[45] X. Gao, Y. Zhang, S. Adusumilli, J. Seitzman, W. Sun, T. Ombrello, C. Carter, The effect of ozone addition on laminar flame speed, Combust. Flame 162 (2015) 3914-24.

[46] M.E. Gluckstein, R.B. Morrison, T.B. Khammash, Combustion with ozone-modification of flame speeds C2 hydrocarbon-air mixtures, University of Michigan 1955.

[47] M. Pinchak, T. Ombrello, C. Carter, E. Gutmark, V. Katta, The effect of hydrodynamic stretch on the flame propagation enhancement of ethylene by addition of ozone. Philos. Trans. R. Soc. A 373 (2015) 20140339.

[48] M. Pinchak, T. Ombrello, C. Carter, E. Gutmark, V. Katta, Flame propagation enhancement of ethylene by addition of ozone in: the 51st AIAA Meeting on Aerospace Sciences Including the New Horizons Forum and Aerospace Exposition, Grapevine (Dallas/Ft. Worth Region), Texas, 2013.

[49] T.M. Vu, S.H. Won, T. Ombrello, M.S. Cha, Stability enhancement of ozone-assisted laminar premixed Bunsen flames in nitrogen co-flow, Combust. Flame 161 (2014) 917-26.

[50] Y. Zhang, M. Zhu, Z. Zhang, R. Shang, D. Zhang, Ozone effect on the flammability limit and near-limit combustion of syngas/air flames with N2, CO2, and H2O dilutions, Fuel 186 (2016) 414–21.

[51] W. Weng, E. Nilsson, A. Ehn, J. Zhu, Y. Zhou, Z. Wang, Z. Li, M. Aldén, K. Cen, Investigation of formaldehyde enhancement by ozone addition in CH4/air premixed flames, Combust. Flame 162 (2015) 1284–93.

[52] A. Ehn, J.J. Zhu, P. Petersson, Z.S. Li, M. Aldén, C. Fureby, T. Hurtig, N. Zettervall, A. Larsson, J. Larfeldt, Plasma assisted combustion: Effects of O3 on large scale turbulent combustion studied with laser diagnostics and Large Eddy Simulations, Proc. Combust. Inst. 35 (2015) 3487–95.

[53] F. Khan, A. Elbaz, A. Katoch, J. Badra, V. Costanzo, W. Roberts, A Comprehensive Experimental Study to Measure Laminar and Turbulent Burning Velocity of Haltermann Gasoline with Ternary Additives (O3, H2, and CO), SAE Tech. Paper 2021-01-0473.

[54] C.B. Reuter, T. Ombrello, Numerical Simulations of Ozone Addition to Strained Flames, Combust. Sci. Technol. 194 (2022) 3225-45.

[55] H. Li, W. Liang, C.K. Law, Role of ozone addition on premixed hydrogen/oxygen flames: Multi-zone structure and multi-regime dynamics, Combust. Flame 242 (2022) 112188.

[56] W. Liang, Y. Wang, C.K. Law, Role of ozone doping in the explosion limits of hydrogen-oxygen mixtures: Multiplicity and catalyticity, Combust. Flame 205 (2019) 7-10.

[57] J. Crane, X. Shi, A.V. Singh, Y. Tao, H. Wang, Isolating the effect of induction length on detonation structure: Hydrogen–oxygen detonation promoted by ozone, Combust. Flame 200 (2019 44-52.

[58] W. Han, W. Liang, C. Wang, J.X. Wen, C.K. Law, Spontaneous initiation and development of hydrogen–oxygen detonation with ozone sensitization, Proc. Combust. Inst. 38 (2021) 3575-83.

[59] Y. Ju, C.B. Reuter, O.R. Yehia, T.I. Farouk, S.H. Won, Dynamics of cool flames, Prog. Energy Combust. Sci. 75 (2019) 100787.

[60] S.H. Won, B. Jiang, P. Diévart, C.H. Sohn, Y. Ju, Self-sustaining n-heptane cool diffusion flames activated by ozone, Proc. Combust. Inst. 35 (2015) 881-8.

[61] M.Q. Brown, E.L. Belmont, Effects of ozone on n-heptane low temperature chemistry and premixed cool flames, Combust. Flame 225 (2021) 20-30.

[62] C.B. Reuter, M. Lee, S.H. Won, Y. Ju, Study of the low-temperature reactivity of large n-alkanes through cool diffusion flame extinction, Combust. Flame 179 (2017) 23–32.

[63] J. Liu, R. Yu, B. Ma, Effect of Ozone Addition on the Cool Flame and Negative Temperature Coefficient Regions of Propane–Oxygen Mixtures, ACS Omega 27 (2020) 16448-54.

[64] O.R. Yehia, C.B. Reuter, Y. Ju, Low-temperature multistage warm diffusion flames, Combust. Flame 195 (2018) 63-74.

[65] Y. Ju, C.B. Reuter, S.H. Won, Numerical simulations of premixed cool flames of dimethyl ether/oxygen mixtures, Combust. Flame 162 (2015) 3580–8.

[66] C.B. Reuter, S.H. Won, Y. Ju, Experimental study of the dynamics and structure of self-sustaining premixed cool flames using a counterflow burner, Combust. Flame 166 (2016) 125-132.

[67] J.B. Heywood, Internal Combustion Engine Fundamentals, McGraw-Hill Inc.: New York, NY, USA, 1988.

[68] R. Stone, Introduction to Internal Combustion Engines, Palgrave Macmillan, 1992.

[69] F. Zhao, M.C. Lai, D.L. Harrington, Automotive spark-ignited direct-injection gasoline engines, Prog. Energy Combust. Sci. 25 (1999) 437–562.

[70] A.C. Alkidas, Combustion advancements in gasoline engines, Energy Convers. Manag. 48 (2007) 2751–61.

[71] J.M. Bergthorson, M.J. Thomson, A review of the combustion and emissions properties of advanced transportation biofuels and their impact on existing and future engines, Renewable Sustainable Energy Rev. 42 (2015) 1393-417.

[72] R.D. Reitz, Directions in internal combustion engine research, Combust. Flame 160 (2013) 1-8.

[73] S. Imtenan, M. Varman, H.H. Masjuki, M.A. Kalam, H. Sajjad, M.I. Arbab, I.M. Rizwanul Fattah, Impact of low temperature combustion attaining strategies on diesel engine emissions for diesel and biodiesels: A review, Energy Convers. Manag. 80 (2014) 329-56.

[74] H. Bendu, S. Murugan, Homogeneous Charge Compression Ignition (HCCI) Combustion: Mixture Preparation and Control Strategies in Diesel Engines, Renew. Sustain. Energy Rev, 38 (2014) 732–46.

[75] M.M. Hasan, M.M. Rahman, Homogeneous Charge Compression Ignition Combustion: Advantages Over Compression Ignition Combustion, Challenges and Solutions, Renew. Sustain. Energy Rev. 57 (2016) 282–91.

[76] T.K. Sharma, G.A.P. Rao, K.M. Murthy, Homogeneous Charge Compression Ignition (HCCI) Engines: A Review, Arch. Comput. Method. E 23 (2016) 623–57.

[77] J.E. Dec, M. Sjöberg, Isolating the Effects of Fuel Chemistry on Combustion Phasing in an HCCI Engine and the Potential of Fuel Stratification for Ignition Control, SAE Tech. Paper 2004.

[78] M. Yao, Z. Zheng, H. Liu, Progress and Recent Trends in Homogeneous Charge Compression Ignition (HCCI) Engines, Prog. Energy Combust. 35 (2009) 398–437.

[79] S. Saxena, I.D. Bedoya, Fundamental phenomena affecting low temperature combustion and HCCI engines, high load limits and strategies for extending these limits, Prog. Energy Combust. 39 (2013) 457–88.

[80] S. Gowthaman, A.P. Sathiyagnanam, Analysis the Optimum Inlet air Temperature for Controlling Homogeneous Charge Compression Ignition (HCCI) Engine, Alex. Eng. J. 57 (2018) 2209–14.

[81] D. Jung, N. Iida, Closed-loop control of HCCI combustion for DME using external EGR and rebreathed EGR to reduce pressure-rise rate with combustion-phasing retard, Appl. Energy 138 (2015) 315–30.

[82] M. Sjoberg, J.E. Dec, W. Hwang, Thermodynamic and chemical effects of EGR and its constituents on HCCI autoignition, SAE Tech. Paper 2007-01- 0207.

[83] B. Prasad, C. Sharma, T. Anand, R. Ravikrishna, High Swirl-Inducing Piston Bowls in Small Diesel Engines for Emission Reduction, Appl. Energy 88 (2011) 2355–67.

[84] S.C. Kong, R.D. Reitz, M. Christensen, B. Johansson, Modeling the Effects of Geometry Generated Turbulence on HCCI Engine Combustion. SAE Tech. Paper 2003-01-1088.

[85] M. Christensen, B. Johansson, A. Hultqvist, The Effect of Combustion Chamber Geometry on HCCI Operation, SAE Tech. Paper 2002-01-0425.

[86] E. Distaso, R. Amirante, G. Calò, P. De Palma, P. Tamburrano, R.D. Reitz, Predicting lubricant oil induced pre-ignition phenomena in modern gasoline engines: The reduced GasLube reaction mechanism, Fuel 281 (2020) 118709.

[87] Z. Peng, H. Zao, T. Ma, N. Ladommatos, Characteristics of Homogeneous Charge Compression Ignition (HCCI) Combustion and Emissions of n-Heptane, Combust. Sci. Technol. 177 (2005) 2113–50.

[88] S. Tanaka, F. Ayala, J.C. Keck, J.B. Heywood, Two-stage ignition in HCCI combustion and HCCI control by fuels and additives, Combust. Flame 132 (2003) 219–39.

[89] R. Herold, J.M. Krasselt, D.E. Foster, J.B. Ghandhi, D.L. Reuss, P.M. Najt, Investigations into the Effects of Thermal and Compositional Stratification on HCCI Combustion–Part II: Optical Engine Results, SAE Int. J. Engines 2 (2009) 1034-53.

[90] A. Viggiano, V. Magi, An Investigation on the Performance of Partially Stratified Charge CI Ethanol Engines, SAE Tech. Paper 2011-01-0837.

[91] J.M. Krasselt, D.E. Foster, J.B. Ghandhi, R. Herold, D.L. Reuss, P.M. Najt, Investigations into the Effects of Thermal and Compositional Stratification on HCCI Combustion—Part I: Metal Engine Results, SAE Tech. Paper 2009-01-1105.

[92] R. Yu, T. Joelsson, X. Bai, B. Johansson, Effect of Temperature Stratification on the Auto-ignition of Lean Ethanol/Air Mixture in HCCI engine, SAE Tech. Paper 2008-01-1669.

[93] M.P.B. Musculus, P.C. Miles, L.M. Pickett, Conceptual models for partially premixed low-temperature diesel combustion, Prog. Energy Combust. Sci. 39 (2013) 246-83.

[94] C.A. Idicheria, L.M. Pickett, Soot formation in diesel combustion under high-EGR conditions, SAE Tech. Paper 2005–01-3834.

[95] T. Urushihara, K. Yamaguchi, K. Yoshizawa, T. Itoh, A Study of a Gasoline-fueled Compression Ignition Engine - Expansion of HCCI Operation Range Using SI Combustion as a Trigger of Compression Ignition, SAE Tech. Paper 2005-01-0180.

[96] H. Xie, L. Li, T. Chen, W. Yu, X. Wang, H. Zhao, Study on spark assisted compression ignition (SACI) combustion with positive valve overlap at medium–high load, Appl. Energy 101 (2013) 622-33.

[97] D. Robertson, R. Prucka, A Review of Spark-Assisted Compression Ignition (SACI) Research in the Context of Realizing Production Control Strategies, SAE Tech. Paper 2019-24-0027.

[98] D.L. Reuss, T.W. Kuo, G. Silvas, V. Natarajan, V. Sick, Experimental metrics for identifying origins of combustion variability during spark-assisted compression ignition, Int. J. Engine Res. 9 (2008) 409–34.

[99] J.B. Martz, R.J. Middleton, G.A. Lavoie, A. Babajimopoulos, D.N. Assanis, A computational study and correlation of premixed isooctane-air laminar reaction front properties under spark ignited and spark assisted compression ignition engine conditions, Combust. Flame 158 (2011) 1089–96.

[100] T. Tachibana, K. Hirata, H. Nishida, H. Osada, Effect of ozone on combustion of compression ignition engines, Combust. Flame 85 (1991) 515-9.

[101] H. Nishida, T. Tachibana, Homogeneous charge compression ignition of natural gas/air mixture with ozone addition, J. Propul. Power 22 (2006) 151–7.

[102] F. Foucher, P. Higelin, C. Mounaïm-Rousselle, P. Dagaut, Influence of ozone on the combustion of n-heptane in a HCCI engine, Proc. Combust. Inst. 34 (2013) 3005-12.

[103] J.-B. Masurier, F. Foucher, G. Dayma, P. Dagaut, Ozone applied to the homogeneous charge compression ignition engine to control alcohol fuels combustion, Appl. Energy 160 (2015) 566-80.

[104] H. Yamada, M. Yoshii, A. Tezaki, Chemical mechanistic analysis of additive effects in homogeneous charge compression ignition of dimethyl ether, Proc. Combust. Inst. 30 (2005) 2773–80.

[105] J-B Masurier, F. Foucher, G. Dayma, P. Dagaut, Homogeneous charge compression ignition combustion of primary reference fuels influenced by ozone addition, Energy Fuels 27 (2013) 5495-505.

[106] J-B Masurier, F. Foucher, G. Dayma, P. Dagaut, Investigation of iso-octane combustion in a homogeneous charge compression ignition engine seeded by ozone, nitric oxide and nitrogen dioxide, Proc. Combust. Inst. 35 (2015) 3125-32.

[107] J-B Masurier, F. Foucher, G. Dayma, C. Rousselle, P. Dagaut, Application of an Ozone Generator to Control the Homogeneous Charge Compression Ignition Combustion Process, SAE Tech. Paper 2015-24-2456.

[108] P.M. Pinazzi, F. Foucher, Influence of Injection Parameters, ozone seeding and residual NO on a Gasoline Compression Ignition (GCI) engine at low load, Proc. Combust. Inst. 36 (2017) 3659-68.

[109] P.M. Pinazzi, F. Foucher, Potential of Ozone to Enable Low Load Operations of a Gasoline Compression Ignition (GCI) Engine, SAE Tech. Paper 2017-01-0746.

[110] N. Seignour, A. Khacef, F. Foucher, Experimental Understanding of Ozone Decomposition inside a Low Temperature Combustion Engine, Combust. Sci. Technol. 194 (2022) 292-303.

[111] N. Seignour, J. Masurier, B. Johansson, G. Dayma, P. Dagaut, F. Foucher, Ozone-assisted combustion of hydrogen: A comparison with isooctane, Int. J. Hydrog. Energy, 44 (2019) 13953-63.

[112] S. Biswas, I. Ekoto, Detailed Investigation into the Effect of Ozone Addition on Spark Assisted Compression Ignition Engine Performance and Emissions Characteristics, SAE Tech. Paper 2019-01-0966.

[113] S. Biswas, I. Ekoto, Ozone Added Spark Assisted Compression Ignition, Advanced Combustion Techniques and Engine Technologies for the Automotive Sector. Energy, Environment, and Sustainability (2020).

[114] C.M. Gong, X.K. Si, K. Wang, F.X. Wei, F.H. Liu, Numerical analysis of carbon monoxide, formaldehyde and unburned methanol emissions with ozone addition from a direct-injection spark-ignition methanol engine, Energy 144 (2018) 432-42.

[115] C.M. Gong, J. Yu, K. Wang, J. Liu, W. Huang, X. Si, F. Wei, F. Liu, Y. Han, Numerical study of plasma produced ozone assisted combustion in a direct injection spark ignition methanol engine, Energy 153 (2018) 1028-37.

[116] D. Golke, M. Rohrig, T.D.M. Lanzanova, M.E.S. Martins, F. Windlin, G. Alegre, Potential of ozone addition on dethrottling of a gasoline/ethanol blend-fueled direct injection spark ignition engine in part load, Int. J. Engine Research (2022).

[117] Y. Ju, W. Sun, Plasma assisted combustion: Dynamics and chemistry, Prog. Energy Combust. Sci. 48 (2015) 21-83.

[118] A. Starikovskiy, N. Aleksandrov, Plasma-assisted ignition and combustion, Prog. Energy Combust. Sci. 39 (2013) 61-110.

[119] J. Lefkowitz , Y. Ju, R. Tsuruoka, Y. Ikeda, A studies of plasma-assisted ignition in a small internal combustion engine, AIAA Paper-2012-1133.

[120] T. Shiraishi, T. Urushihara, Fundamental Analysis of Combustion Initiation Characteristics of Low Temperature Plasma Ignition for Internal Combustion Gasoline Engine, SAE Tech. Paper 2011-01-0660.

[121] J. Hwang, W. Kim, C. Bae, Influence of plasma-assisted ignition on flame propagation and performance in a spark-ignition engine, Prog. Energy Combust. Sci. 6 (2021) 100029.

[122] H.J. Curran, P. Gaffuri, W.J. Pitz, C.K. Westbrook, A comprehensive modeling study of n-heptane oxidation, Combust. Flame 114 (1998) 149-77.

[123] H.J. Curran, P. Gaffuri, W.J. Pitz, C.K. Westbrook, A comprehensive modeling study of iso-octane oxidation, Combust. Flame 129 (2002) 253-80.

[124] P. Dagaut, M. Reuillon, M. Cathonnet, High Pressure Oxidation of Liquid Fuels From Low to High Temperature. 1. n-Heptane and iso-Octane, Combust. Sci. Technol. 95 (1994) 233-60.

[125] G.P. Smith, D.M. Golden, M. Frenklach, N.W. Moriarty, B. Eiteneer, M. Goldenberg, C.T. Bowman, R.K. Hanson, S. Song, W.C. Gardiner Jr., V.V. Lissianski, Z. Qin. http://combustion.berkeley.edu/gri-mech/version30/text30.html#thefiles. Accessed January 2023.

[126] M.B. Luong, Z. Luo, T.F. Lu, S.H. Chung, C.S. Yoo, Direct numerical simulations of the ignition of lean primary reference fuel/air mixtures with temperature inhomogeneities, Combust. Flame 160 (2013) 2038–47.

[127] L. Cai, H. Pitsch, Optimized chemical mechanism for combustion of gasoline surrogate fuels, Combust. Flame 162 (2015) 1623-37.

[128] P. Saxena, F.A. Williams, Numerical and Experimental Studies of Ethanol Flames, Proc. Combust. Inst. 31 (2007) 1149–56.

[129] T. Ombrello, S.H. Won, Y. Ju, S. Williams, Flame propagation enhancement by plasma excitation of oxygen. Part I: Effects of O3, Combust. Flame 157 (2010) 1906-15.

[130] S.P. Sander, R.R. Friedl, D.M. Golden, M.J. Kurylo, G.K. Moortgat, P.H. Wine, A.R. Ravishankara, C.E. Kolb, M.J. Molina, B.J. Finlayson-Pitts, R.E. Huie, V.L. Orkin, Chemical Kinetics and Photochemical Data for Use in Atmospheric Studies: Evaluation Number 15, JPL Publication 06-2, Jet Propulsion Laboratory, Pasadena, CA, USA, 2006.

[131] R. Atkinson, D.L. Baulch, R.A. Cox, J.N. Crowley, R.F. Hampson, R.G. Hynes, M.E. Jenkin, M.J. Rossi, J. Troe, Evaluated kinetic and photochemical data for

atmospheric chemistry: Volume I - gas phase reactions of Ox, HOx, NOx and SOx species, Atmos. Chem. Phys. 4 (2004) 1461-738.

[132] A. Mansergas, J.M. Anglada, The Gas-Phase Reaction between O3 and HO Radical: A Theoretical Study, ChemPhysChem 8 (2007) 1534-9.

[133] S. Hatakeyamat, M.T. Leu, Rate constants for reactions between atmospheric reservoir species. 2. Water, J. Phys. Chem. 93 (1989) 5784-9.

[134] R. Atkinson, D.L. Baulch, R.A. Cox, R.F. Hampson, J.A. Kerr, J. Troe, Evaluated Kinetic and Photochemical Data for Atmospheric Chemistry: Supplement III. IUPAC Subcommittee on Gas Kinetic Data Evaluation for Atmospheric Chemistry, J. Phys. Chem. Ref. Data 18 (1989) 881.

[135] C.J. Howard, B.J. Finlayson-Pitts, Yields of HO2 in the reaction of hydrogen atoms with ozone, J. Chem. Phys. 72 (1980) 3842-3.

[136] A.M. Starik, V.E. Kozlov, N.S. Titova, On the influence of singlet oxygen molecules on the speed of flame propagation in methane–air mixture, Combust. Flame 157 (2010) 313-27.

[137] A.A. Konnov, A. Mohammad, V.R. Kishore, N.I. Kim, C. Prathap, S. Kumar, A comprehensive review of measurements and data analysis of laminar burning velocities for various fuel+air mixtures, Prog. Energy Combust. Sci. 68 (2018) 197-267.

[138] K.J. Bosschaart, L.P.H. deGoey, The laminar burning velocity of flames propagating in mixtures of hydrocarbons and air measured with the heat flux method, Combust. Flame 136 (2004) 261–9.

[139] T. Tahtouh, F. Halter, C. Mounaïm-Rousselle, Measurement of laminar burning speeds and Markstein lengths using a novel methodology, Combust. Flame 156 (2009) 1735-43.

[140] S. Jerzembeck, N. Peters, P. Pepiot-Desjardins, H. Pitsch, Laminar burning velocities at high pressure for primary reference fuels and gasoline: Experimental and numerical investigation, Combust. Flame 156 (2009) 292-301.

[141] B. Galmiche, F. Halter, F. Foucher, Effects of high pressure, high temperature and dilution on laminar burning velocities and Markstein lengths of iso-octane/air mixtures, Combust. Flame 159 (2012) 3286–99.

[142] E. Fanelli, A. Viggiano, G. Braccio, V. Magi, On laminar flame speed correlations for H2/CO combustion in premixed spark ignition engines, Applied Energy 130 (2014) 166-80.

[143] M. Metghalchi, J.C. Keck, Burning velocities of mixtures of air with methanol, isooctane, and indolene at high pressure and temperature, Combust. Flame 48 (1982) 191–210.

[144] R.J. Kee, J.F. Grcar, M.D. Smooke, J.A. Miller, E. Meeks, PREMIX: a fortran program for modelling steady laminar one-dimensional premixed flames, Report No. SAND85-8249, Sandia National Laboratories, CA, USA, 1985.

[145] D.G. Goodwin, H.K. Moffat, R.L. Speth, Cantera: An object-oriented software toolkit for chemical kinetics, thermodynamics, and transport processes, Pasadena, CA, Caltech, 2009.

[146] C.M. Vagelopoulos, F.N. Egolfopoulos, Direct experimental determination of laminar flame speeds, Symp. (Int.) Combust. 27 (1998) 513-9.

[147] X.J. Gu, M.Z. Haq, M. Lawes, R. Woolley, Laminar burning velocity and Markstein lengths of methane–air mixtures, Combust. Flame 121 (2000) 41-58.

[148] M. Reyes, F.V. Tinaut, A. Camaño, Experimental Study of Premixed Gasoline Surrogates Burning Velocities in a Spherical Combustion Bomb at Engine Like Conditions, Energies 13 (2020) 3430.

[149] S.G. Davis, C.K. Law, Determination of and fuel structure effects on laminar flame speeds of C1 to C8 hydrocarbons, Combust. Sci. Technol. 140 (1998) 427–49.

[150] J.O Hirschfelder, C.F. Curtiss, R.B. Bird, Molecular Theory of Gases and Liquids, John Wiley and Sons, New York, 1954.

[151] S. Chapman, T.G. Cowling, The Mathematical Theory of Non-Uniform Gases, Cambridge, University Press, Cambridge, 1970.

[152] T.P. Coffee, J.M. Heimerl, Transport algorithms for premixed, laminar steady-state flames, Combust. Flame 43 (1981) 273-289.

[153] Y. Song, Y. He, Y. Yu, B. Moreau, F. Foucher, Effect of Exhaust Gas Recirculation and NO on Ignition Delay Times of Iso-octane in a Rapid Compression Machine, Energy Fuels 34 (2020) 8788-95.

[154] N. Atef, G. Kukkadapu, S.Y. Mohamed, M. Al Rashidi, C. Banyon, M. Mehl, K.A. Heufer, E.F. Nasir, A. Alfazazi, A.K. Das, C.K. Westbrook, W.J. Pitz et al., A comprehensive iso-octane combustion model with improved thermochemistry and chemical kinetics, Combust. Flame 178 (2017) 111-34.

[155] H. Di, X. He, P. Zhang, Z. Wang, M.S. Wooldridge, C.K. Law, C. Wang, S. Shuai, J. Wang, Effects of buffer gas composition on low temperature ignition of iso-octane and n-heptane, Combust. Flame 161 (2014) 2531-8.

[156] W.J.D. Annand, Heat Transfer in the Cylinders of Reciprocating Internal Combustion Engines, Proc. Instn Mech. Engrs 177 (1963) 973-90.

[157] G. Woschni, A Universally Applicable Equation for Instantaneous Heat Transfer Coefficient in the Internal Combustion Engine, SAE Tech. Paper 670931 (1967).

[158] G. Hohenberg, Advanced Approaches for Heat Transfer Calculations, SAE Tech. Paper 790825 (1979).

[159] T. LeFeuvre, P.S. Myers, O.A. Uyehara, Experimental Instantaneous Heat Fluxes in a Diesel Engine and Their Correlation, SAE Tech. Paper 690464 (1969).

[160] H.A. McGee, Molecular Engineering, McGraw-Hill, New York, 1991.

[161] A.N. Kolmogorov, 1941 The local structure of turbulence in incompressible viscous fluid for very large Reynolds numbers, C.R. Acad. Sci. USSR 30 (1941) 301.

[162] T. Poinsot, D. Veynante, Theoretical and Numerical Combustion, R.T. Edwards, Inc., Philadelphia, PA, USA 2005.

[163] B.E. Launder, D.B. Spalding, Lectures in Mathematical Models of Turbulence, Academic Press, London, England, 1972.

[164] B. E. Launder and D. B. Spalding, The Numerical Computation of Turbulent Flows, Comput. Methods Appl. Mech. Eng. 3 (1974) 269–89.

[165] B.F. Magnussen, On the structure of turbulence and a generalized Eddy Dissipation Concept for chemical reaction in turbulent flow. Inn Proceedings of the 19th Aerospace Sciences Meeting, St. Louis, MO, USA, 12–15 January 1981.

[166] M. Bösenhofer, E.M. Wartha, C. Jordan, M. Harasek, The Eddy Dissipation Concept—Analysis of Different Fine Structure Treatments for Classical Combustion, Energies 11 (2018) 1902.

[167] I.S. Ertesvåg, B.F. Magnussen, The Eddy Dissipation Turbulence Energy Cascade Model, Combust. Sci. Technol.159 (2007) 213–35.

[168] B.F. Magnussen, The Eddy Dissipation Concept—A Bridge Between Science and Technology, In Proceedings of the ECCOMAS Thematic Conference on Computational Combustion, Lisbon, Portugal, 21–24 June 2005.

[169] I.R. Gran, B.F. Magnussen, A Numerical Study of a Bluff-Body Stabilized Diffusion Flame. Part 2. Influence of Combustion Modeling and Finite-Rate Chemistry, Combust. Sci. Technol. 119 (1996) 191–217.

[170] A. Parente, M.R. Malik, F. Contino, A. Cuoci, B.B. Dally, Extension of the Eddy Dissipation Concept forturbulence/chemistry interactions to MILD combustion, Fuel 163 (2016) 98–111

[171] H. Bao, Development and Validation of a New Eddy Dissipation Concept (EDC) Model for MILD Combustion. Master’s Thesis, Delft University of Technology, Delft, The Netherlands, 2017.

[172] Ansys® Academic Research Chemkin-Pro, Release 20.1, ANSYS, Inc.

[173] V. Magi, REC-2000: a multidimensional code for transient, two-phase, turbulent reacting flows, Engine Research Laboratory Report, School of Mechanical Engineering, Purdue University, 2000.

[174] Ansys® Academic Research Fluent, Release 20.1, ANSYS, Inc.

[175] G. D'Errico, T. Lucchini, A. Onorati, S. Merola, B. M. Vaglieco, M. Mehl, T. Faravelli, E. Ranzi, Development and Experimental Validation of a Combustion Model with Detailed Chemistry for Knock Predictions, SAE Tech. Paper 2007-01-0938.

[176] S.G. Davis, C.K. Law, Laminar flame speeds and oxidation kinetics of iso-octane-air and n-heptane-air flames, Symp. (Int.) Combust. 27 (1998) 521-7.

[177] Y. Huang, C.J. Sung, J.A. Eng, Laminar flame speeds of primary reference fuels and reformer gas mixtures, Combust. Flame 139 (2004) 239-51.

[178] K. Kumar, J.E. Freeh, C.J. Sung, Y. Huang, Laminar Flame Speeds of Preheated iso-Octane/O2/N2 and n-Heptane/O2/N2 Mixtures, J. Propuls. Power 23 (2007).

[179] J.PJ. Lipzig, E.J.K. Nilsson, L.P.H. de Goey, A.A. Konnov, Laminar burning velocities of n-heptane, iso-octane, ethanol and their binary and tertiary mixtures, Fuel 90 (2011) 2773-81.

[180] A.P. Kelley, W. Liu, Y.X. Xin, A.J. Smallbone, C.K. Law, Laminar flame speeds, non-premixed stagnation ignition, and reduced mechanisms in the oxidation of iso-octane, Proc. Combust. Inst. 33 (2011) 501-8.

[181] J.X. Zhou, M. Cordier, C. Mounaïm-Rousselle, F. Foucher, Experimental estimate of the laminar burning velocity of iso-octane in oxygen-enriched and CO2-diluted air, Combust. Flame 158 (2011) 2375-83.

[182] D. Bradley, R.A. Hicks, M. Lawes, C.G.W. Sheppard, R. Woolley, The Measurement of Laminar Burning Velocities and Markstein Numbers for Iso-octane–Air and Iso-octane–n-Heptane–Air Mixtures at Elevated Temperatures and Pressures in an Explosion Bomb, Combust. Flame 115 (1998) 126-44.

[183] C. Mandilas, M.P. Ormsby, C.G.W. Sheppard, R. Woolley, Effects of hydrogen addition on laminar and turbulent premixed methane and iso-octane–air flames. Proc. Combust. Inst 31 (2007) 1443-50.

[184] K. Fieweger, R. Blumenthal, G. Adomeit, Self-ignition of S.I. engine model fuels: A shock tube investigation at high pressure, Combust. Flame 109 (1997) 599-619.

[185] R. Minetti, M. Carlier, M. Ribaucour, E. Therssen, L.R. Sochet, Comparison of oxidation and autoignition of the two primary reference fuels by rapid compression, Symp. (Int.) Combust. 26 (1996) 747-53.

[186] F. Contino, J-B Masurier, F. Foucher, T. Lucchini, G. D’Errico, P. Dagaut, CFD simulations using the TDAC method to model iso-octane combustion for a large range of

ozone seeding and temperature conditions in a single cylinder HCCI engine, Fuel 137 (2014) 179-84.

[187] R. Fang, C. Saggese, S.W. Wagnon, A.B. Sahu, H.J. Curran, W.J. Pitz, C.-J. Sung, Effect of nitric oxide and exhaust gases on gasoline surrogate autoignition: iso-octane experiments and modeling, Combust. Flame 236 (2022) 111807.

[188] Y. Wu, M. Yang, C. Tang, Y. Liu, P. Zhang, Z. Huang, Promoting “adiabatic core” approximation in a rapid compression machine by an optimized creviced piston design, Fuel 251 (2019) 328-40.